frontiers | Research Topics

Microenvironmental stimuli-responsive nanomedicine for biomedical application

Edited by
Yong Hu, Jingwei Xie and Donglin Xia

Published in
Frontiers in Bioengineering and Biotechnology

ISSN 1664-8714
ISBN 978-2-8325-2453-4
DOI 10.3389/978-2-8325-2453-4

About Frontiers

Frontiers is more than just an open access publisher of scholarly articles: it is a pioneering approach to the world of academia, radically improving the way scholarly research is managed. The grand vision of Frontiers is a world where all people have an equal opportunity to seek, share and generate knowledge. Frontiers provides immediate and permanent online open access to all its publications, but this alone is not enough to realize our grand goals.

Frontiers journal series

The Frontiers journal series is a multi-tier and interdisciplinary set of open-access, online journals, promising a paradigm shift from the current review, selection and dissemination processes in academic publishing. All Frontiers journals are driven by researchers for researchers; therefore, they constitute a service to the scholarly community. At the same time, the *Frontiers journal series* operates on a revolutionary invention, the tiered publishing system, initially addressing specific communities of scholars, and gradually climbing up to broader public understanding, thus serving the interests of the lay society, too.

Dedication to quality

Each Frontiers article is a landmark of the highest quality, thanks to genuinely collaborative interactions between authors and review editors, who include some of the world's best academicians. Research must be certified by peers before entering a stream of knowledge that may eventually reach the public - and shape society; therefore, Frontiers only applies the most rigorous and unbiased reviews. Frontiers revolutionizes research publishing by freely delivering the most outstanding research, evaluated with no bias from both the academic and social point of view. By applying the most advanced information technologies, Frontiers is catapulting scholarly publishing into a new generation.

What are Frontiers Research Topics?

Frontiers Research Topics are very popular trademarks of the *Frontiers journals series*: they are collections of at least ten articles, all centered on a particular subject. With their unique mix of varied contributions from Original Research to Review Articles, Frontiers Research Topics unify the most influential researchers, the latest key findings and historical advances in a hot research area.

Find out more on how to host your own Frontiers Research Topic or contribute to one as an author by contacting the Frontiers editorial office: frontiersin.org/about/contact

Microenvironmental stimuli-responsive nanomedicine for biomedical application

Topic editors

Yong Hu — Nanjing University, China

Jingwei Xie — University of Nebraska Medical Center, United States

Donglin Xia — Nantong University, China

Citation

Hu, Y., Xie, J., Xia, D., eds. (2023). *Microenvironmental stimuli-responsive nanomedicine for biomedical application*. Lausanne: Frontiers Media SA. doi: 10.3389/978-2-8325-2453-4

Table of contents

frontiers | Frontiers in Bioengineering and Biotechnology

TYPE Editorial
PUBLISHED 04 May 2023
DOI 10.3389/fbioe.2023.1206895

OPEN ACCESS

EDITED AND REVIEWED BY
Hasan Uludag,
University of Alberta, Canada

*CORRESPONDENCE
Yong Hu,
hvyong@nju.edu.cn

RECEIVED 16 April 2023
ACCEPTED 24 April 2023
PUBLISHED 04 May 2023

CITATION
Xia D, Xie J and Hu Y (2023), Editorial: Microenvironmental stimuli-responsive nanomedicine for biomedical application.
Front. Bioeng. Biotechnol. 11:1206895.
doi: 10.3389/fbioe.2023.1206895

Editorial: Microenvironmental stimuli-responsive nanomedicine for biomedical application

Donglin Xia[1], Jingwei Xie[2] and Yong Hu[3]*

[1]College of Engineering and Applied Sciences, Nanjing University, Nanjing, China, [2]School of Public Health, Nantong University, Nantong, China, [3]Department of Surgery-Transplant College of Medicine, University of Nebraska Medical Center, Omaha, NE, United States

KEYWORDS

nanomedcine, stimuli-reponsive, nanoparticles, tumor, targeting

Editorial on the Research Topic
Microenvironmental stimuli-responsive nanomedicine for biomedical application

The purpose of this Research Topic, *Microenvironmental stimuli-responsive nanomedicine for biomedical application*, is to bring together the latest developments from researchers working on smart nanomaterials for biosensing and therapy applications. The guest editorial team would like to thank all colleagues who submitted their reviews and research articles for the Research Topic.

The releasing of a microenvironment-responsive drug in the morbid site is one of the most effective therapeutic approaches, especially nanoparticles, for enhanced therapeutic outcomes for tumor therapy. That is because the compromised potency of nanomedicines has been attributed to its limited delivery efficiency into tumors, with less than ~1% of the nanoparticle dose reaching the solid tumors. Shen et al. analyzed the clinical value of magnetic resonance-guided microwave ablation in lung cancer. It showed that MRI-guided percutaneous ablation had significant prospects for the treatment of lung tumors and provided a satisfactory outcome. This suggested that local drug delivery could achieve favorable therapeutic efficacy. As it could not only significantly increase the local drug concentration but also decreased the number of drug administrations, it improved compliance and minimized side effects.

Stimuli-responsive drug delivery systems are promising for the control of drug release *in vivo*. Various responsive systems triggered by microenvironment stimuli have been widely reported in the literature for controlled drug release studies. Among all types of stimuli-responsive drug delivery systems, pH-sensitive releasing has received increasing attention. Unlike the direct response to pH, Yang et al. developed an indirect pH-responsive insulin release system, which regulated insulin release behavior for diabetes therapy. In this work, glucose oxidase was employed as the microenvironment-responsive switch and converted a change in the hyperglycemic environment to a pH-stimulus to control the insulin releasing behavior. Furthermore, the regulation of the local microenvironment by ultrasound altered the release behavior of the insulin, because ultrasound can generate reactive oxygen species (ROS) and regulate the pharmacological effects in a timely manner. Inspired by this, Chen et al. showed a remote ultrasound-induced lidocaine delivery system for postoperative pain management. Under remote stimulation, drugs were released into the bloodstream because

of the high-concentration ROS microenvironment. These results suggest an effective strategy to spatiotemporally control the release of drugs.

As increasing attention has been paid to the treatment of tumors, research in microenvironmental stimuli-responsive nanomedicine has become active, and a wide range of work has been executed to enhance tumor treatment efficacy. Yang et al. reviewed the recent advances in potentiating the oxygenation in tumor tissue with nanomaterials and highlighted the superiority of microenvironmental stimuli-responsive nanomaterials in enhancing the therapeutic effect in tumor treatment. In order to strengthen the mitochondrial respiration suppression efficacy of atovaquone, Li et al. developed a targeting strategy with RGD-modified silk fibroin-based nanocarriers. An increased inhibition efficacy, enhanced chemotherapy effect, and strikingly suppressed tumor development was observed in the tumor models treated by the RGD-modified silk fibroin-based nanocarriers due to the targeting ability of RGD. These results suggest that an RGD-based targeted drug carrier could reverse the hypoxia microenvironment *in vivo* for enhancing chemotherapy, thereby suggesting a promising candidate for tumor therapy. Moreover, therapeutic specificity might also be achieved by targeting tumor cell-specific metabolic alterations. Previous studies suggested that most of the cancer cells exhibited the phenomenon of glutamine (GL) addiction, that is, the tumor cells actively absorb and accumulate GL in tumor tissues for growth. Zhang et al. showed an oxygen-deficient TiO_{2-x} coated with a GL layer for targeted delivery with the joint application of sonodynamic therapy and photothermal therapy. This study presented a nanomedicine with high target efficacy to the tumor.

The studies about microenvironmental stimuli-responsive nanomedicine for biomedical application are not limited to abovementioned research. Recently, Zhang et al. summarized the mechanism of action, administration methods, and engineered production for exosomes in medical aesthetics. However, exosomes used as drug delivery vehicles still face many challenges in clinical practice. Shi et al.studied the nasopharyngeal carcinoma immune microenvironment through ferroptosis-related genes. The results show that ATG5 has potential as a significant independent prognostic marker and might be used to attain drug targeting. Zhao et al. studied the role of Notch signaling and fluid shear stress in regulating osteogenic differentiation. The results reveal new information concerning the osteogenic differentiation of hMSCs under shear stress and the regulatory role of Notch signaling. Enhancing targeting efficiencies for drug delivery applications could be pursued by considering those findings as microenvironmental stimuli-responsive candidate switches.

In summary, this Research Topic has collected diverse aspects of microenvironmental stimuli-responsive nanomedicine for biomedical applications. More specifically, it illustrates a variety of microenvironmental stimuli-responsive switches with different stimuli-responsive properties, and relevant stimuli-responsive mechanisms are systematically investigated and presented. The development of microenvironmental stimuli-responsive nanomedicine is a fascinating subject, and the current Research Topic is anticipated to provide a valuable reference for the exploration of this hot research field.

Author contributions

DX drafted the manuscript, and the other authors discussed and revised the manuscript.

Acknowledgments

The authors acknowledge the financial support from the National Natural Science Foundation of China (52173128, 51973091) and the Science and Technology R&D Fund of Nantong City (No. MS12021033, MS22022096).

Conflict of interest

The authors declare that the research was conducted in the absence of any commercial or financial relationships that could be construed as a potential conflict of interest.

Publisher's note

frontiers | Frontiers in Bioengineering and Biotechnology

ORIGINAL RESEARCH
published: 11 July 2022
doi: 10.3389/fbioe.2022.925047

Ultrasound-Triggered on Demand Lidocaine Release Relieves Postoperative Pain

Xiaohong Chen[1,2†], Jianfeng Zhang[2†], Yan Yu[2], Haoran Wang[2], Genshan Ma[2], Di Wang[2], Hanzhong Cao[2] and Jianping Yang[1]**

[1]The Frist Affiliated Hospital of Soochow University, Suzhou, China, [2]Nantong Tumor Hospital, Tumor Hospital Affiliated to Nantong University, Nantong, China

Safe and non-invasive on-demand relief is a crucial and effective treatment for postoperative pain because it considers variable timing and intensity of anesthetics. Ultrasound modulation is a promising technique for this treatment because it allows convenient timed and non-invasive controlled drug release. Here, we created an ultrasound-triggered lidocaine (Lido) release platform using an amino acid hydrogel functioning as three-dimensional (3D) scaffold material (Lido-PPIX@ER hydrogel). It allows control of the timing, intensity and duration of lidocaine (Lido) to relieve postoperative pain. The hydrogel releases Lido due to the elevated reactive oxygen species (ROS) levels generated by PPIX under ultrasound triggering. The Lido-PPIX@ER hydrogel under individualized ultrasound triggering released lidocaine and provided effective analgesia for more than 72 h. The withdrawal threshold was higher than that in the control group at all time points measured. The hydrogel showed repeatable and adjustable ultrasound-triggered nerve blocks *in vivo*, the duration of which depended on the extent and intensity of insonation. On histopathology, no systemic effect or tissue reaction was observed in the ultrasound-triggered Lido-PPIX@ER hydrogel-treated group. The Lido-PPIX@ER hydrogel with individualized (highly variable) ultrasound triggering is a convenient and effective method that offers timed and spatiotemporally controlled Lido release to manage postoperative pain. This article presents the delivery system for a new effective strategy to reduce pain, remotely control pain, and offer timed and spatiotemporally controlled release of Lido to manage postoperative pain.

Keywords: ultrasound-triggered drug release, postoperative pain, lidocaine, on-demand release, erythrocytes

OPEN ACCESS

Edited by:
Jingwei Xie,
University of Nebraska Medical Center, United States

Reviewed by:
Lesan Yan,
Wuhan University of Technology, China
Xiangzhong Chen,
ETH Zürich, Switzerland

****Correspondence:***
Hanzhong Cao
chz-zp@163.com
Jianping Yang
YangJP1956@126.com

†These authors have contributed equally to this work and share first authorship

Specialty section:
This article was submitted to Biomaterials, a section of the journal Frontiers in Bioengineering and Biotechnology

Received: *21 April 2022*
Accepted: *15 June 2022*
Published: *11 July 2022*

Citation:
Chen X, Zhang J, Yu Y, Wang H, Ma G, Wang D, Cao H and Yang J (2022) Ultrasound-Triggered on Demand Lidocaine Release Relieves Postoperative Pain. Front. Bioeng. Biotechnol. 10:925047. doi: 10.3389/fbioe.2022.925047

INTRODUCTION

Postoperative pain management, particularly acute postoperative pain analgesia, remains a leading clinical problem (Gao et al., 2021; Joseph et al., 2021). Without personalized, adjustable, and convenient regional anesthesia, many patients experience intolerable pain. Studies have reported that 10%–50% of patients undergoing surgery experience postoperative pain lasting more than 1 month, and 2%–10% of these patients continue to experience moderate to severe chronic pain (Wang et al., 2020). Although many new devices for postoperative pain have been developed, inadequate postoperative analgesia occurs because the anesthetic cannot meet the on-demand requirements (Tobe et al., 2010; Wang et al., 2016; Rwei et al., 2017; Chen et al., 2020). Inadequate management of postoperative pain can lead to severe consequences, such as poor immediate postoperative effects,

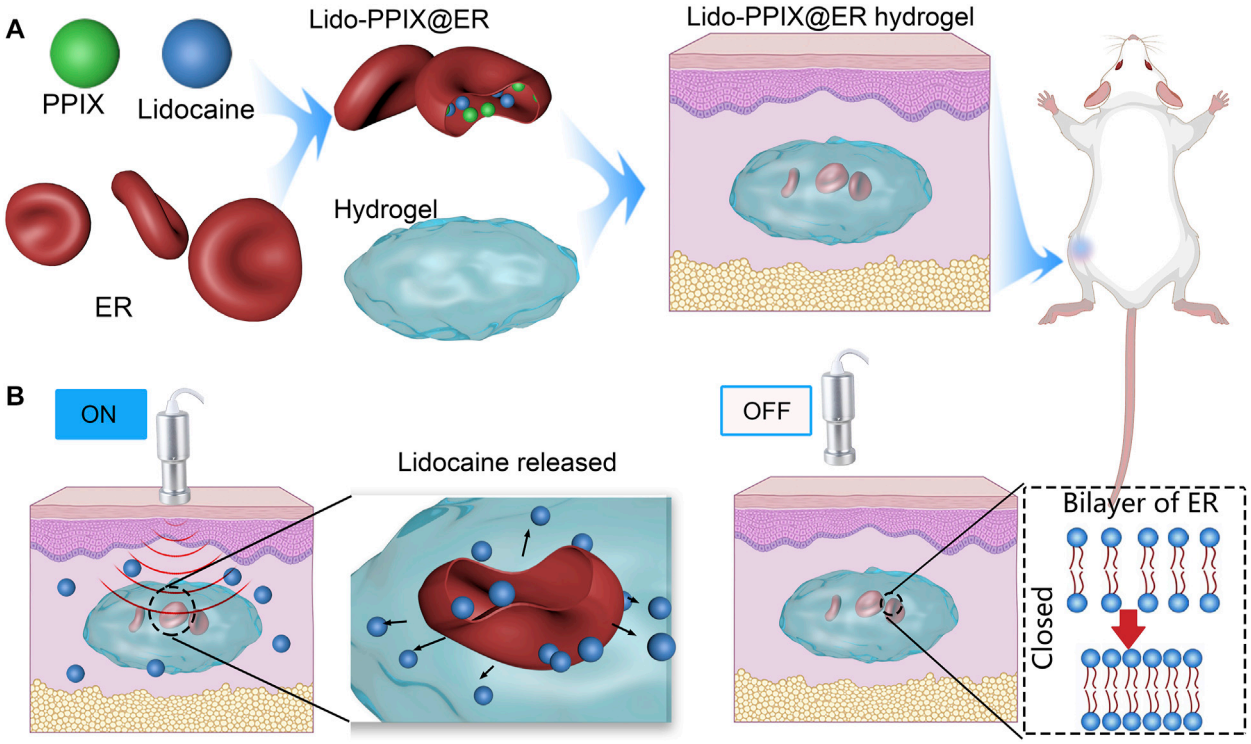

SCHEME 1 | Schematic representation of erythrocyte-inspired and ultrasound-triggered Lido on demand release platform. **(A)** Formation of the Lido-PPIX@ER hydrogel in which ultrasound (0.3 W/cm^2, 30 s) triggers the release of lidocaine (Lido). ERs (erythrocytes) were selected as the lidocaine and PPIX carrier. The amino acid hydrogel functions as a hydrogel 3D scaffold material, which offers increased subcutaneous ER stability. **(B)** A schematic representation showing the ultrasound-regulated Lido release from the Lido-PPIX@ER hydrogel. After surgery, following ultrasound irradiation (0.3 W/cm^2), PPIX improves active oxygen production, promoting pore formation on the erythrocyte membrane, and allowing lidocaine release. Turning off the ultrasound leads to closure of the pores on the ER membrane, suppressing lidocaine release. The Lido-PPIX@ER hydrogel allows on-demand lidocaine release from the subcutaneous lidocaine reservoir by remote control.

prolonged hospital stays, poor patient satisfaction, and increased burden on patients and health systems (Beaulieu, 2021; Joseph et al., 2021; Park et al., 2021). Thus, variability in the patients' ability to modulate pain has clinical application in the control of postoperative pain.

Remotely triggered drug release systems have been developed that can meet the need to regulate pharmacological effects in a timely manner (Raoof et al., 2013; Park et al., 2019; Pedersen et al., 2020; Yao et al., 2021). Ultrasound is already commonly used in both hospital and family therapy for diagnostic and therapeutic practice (Tharkar et al., 2019; van Rooij et al., 2021). Ultrasound is non-invasive and can penetrate deep into tissues (Rwei et al., 2017). It can be applied in a focused manner to minimize the energy applied to the surrounding, non-targeted tissues. Many of the current ultrasound-triggerable drug release systems, such as micelles, liposomes, composites, and hybrid materials are responsive to the thermal and mechanical effects of ultrasound waves (Song et al., 2016; Singh et al., 2018; Jing et al., 2019; Kuls et al., 2020). To improve the effect of sonodynamic therapy, more sonosensitizers have been developed, such as protoporphyrin IX (PPIX) (Rwei et al., 2017). Ultrasound can induce sonochemistry—that is, the use of ultrasonic waves for chemical reactions in which sound sensitizers are activated by acoustic energy to generate reactive oxygen species (ROS). Remote-controlled ROS generation has been widely explored to trigger drug release (Xia et al., 2019).

Erythrocytes (ER), which can deliver various drugs, are attractive systems with adequate lifespans, large internal capacities, and good biocompatibility (Al-Achi and Greenwood, 1998; Hamidi et al., 2007; Favretto et al., 2013). Remote laser-controlled drug delivery systems, showing spatiotemporally controlled drug release, allow on-demand drug release without invasive injury (Wang et al., 2021). Photosensitisers generate reactive oxygen species (ROS) by laser irradiation, working as optical switches to be used in remote laser-controlled drug delivery systems (Strauss et al., 2017). Under remote stimulation, drugs are released into the bloodstream from the laser-regulated drug release system because of ROS generation, opening the ER phospholipid bilayer and triggering drug release. Once the remote stimulation disappears, ROS is no longer produced, and the generated ROS is scavenged by superoxide dismutase and catalase, leading to ROS exhaustion in the hydrogel (Xia et al., 2019). The pores on the ER membrane are then closed to terminate the release behavior.

Inspired by the characteristics of sonodynamic therapy and erythrocytes as drug carriers, an injectable erythrocyte-inspired,

ultrasound-activated hydrogel (Lido-PPIX@ER hydrogel) was reported (**Scheme 1**). In this system, ERs are used as reservoirs for both Lido and PPIX (**Scheme 1A**), and the deformed hydrogel can be subcutaneously injected into the body and function as a 3D scaffold containing Lido- and PPIX-loaded ER to improve their subcutaneous stability. This Lido-PPIX@ER hydrogel releases Lido because of the elevated content of reactive oxygen species (ROS) generated by PPIX under ultrasound. Conversely, ROS are scavenged without ultrasound irradiation and stop Lido release from the Lido-PPIX@ER hydrogel (**Scheme 1B**). Thus, an ultrasound-triggered anesthetic release system with remote-controlled timing and intensity is obtained to regulate postoperative pain on demand. Collectively, we highlight the potential of this ER-enabled on-demand nerve block system, which can use off-the-shelf ultrasound clinical equipment and may ease the clinical transformation of on-demand drug delivery systems in postoperative pain management.

MATERIALS AND METHODS

Materials and Animals

Lidocaine hydrochloride (5 ml: 0.1 g) was obtained from Tiancheng Pharmaceutical (Hebei, China). Protoporphyrin IX (PPIX) and dialysis bags (molecular cutoff, 0.5 kDa) were obtained from Bomei Biotechnology (Hefei, China). Fluorescein isothiocyanate lidocaine (FITC-Lido) was provided by Qiyue Biological Technology (Xi'an, China). Fmoc-Phe and Phe2 were purchased from Yuanye Biotechnology (Shanghai, China). *Lipase* from *Pseudomonas fluorescens* (PFL) was provided by Aladdin Industrial Corporation (Shanghai, China). An malondialdehyde (MDA) kit was obtained from Nanjing Jiancheng Bioengineering Institute (Nanjing, China). All other reagents were of reagent grade.

SPF Sprague–Dawley (SD) rats were purchased from the Experimental Animal Center of Nantong University. All the animals were housed at 24 ± 2°C, 40%–70% humidity, and a 12 h photoperiod. The procedures used in our study were approved by the Committee of the Animal Research of Nantong University (20210421-072), and followed the guidelines the Use of Animals in Research of the International Association for the Study of Pain and the directive of the European Parliament (2010/63/EU).

Preparation of the Lido-PPIX@ER hydrogel

Fresh blood was collected from SD rats using an appropriate anticoagulant (heparin). ERs were normally centrifuged at 4°C and then washed with 10–15 ml of PBS solution at least three times. The hypotonic dialysis method was adopted to prepare the Lido-PPIX@ER. Briefly, PPIX was dissolved in 1 ml of dimethyl sulfoxide (DMSO). Next, lidocaine hydrochloride and PPIX were added to the ER suspension. The mixture was subjected to dialysis (molecular cut off, 0.5 kDa) before immersion in hypotonic buffer (72 mOsm/kg, pH 8) at 4°C for a set time and resealing buffer (550 mOsm/kg, pH 8) for 30 min at 37°C. Finally, free lidocaine hydrochloride and PPIX were removed using repeated centrifugation.

Hypotonic buffer was used to prepare Lido-PPIX@ER, comprising 15 mM $NaH_2PO_4{\cdot}2H_2O$, 15 mM $NaHCO_3$, 2 mM ATP, 3 mM glutathione, 20 mM glucose, and 5 mM NaCl in 100 ml of distilled water, and the resealing buffer included 250 mM NaCl, 12.5 mM glucose, 12.5 mM sodium pyruvate, 12.5 mM inosine, 12.5 mM $NaH_2PO_4{\cdot}2H_2O$, 0.63 mM adenine, and 550 mOsm/kg in 100 ml of distilled water (Millán et al., 2004).

The deformable peptide hydrogel was prepared as described previously (Chronopoulou et al., 2012). Briefly, the substrates Fmoc-Phe and Phe2 were suspended in 420 μL of 0.5 M NaOH. The final concentrations of the Fmoc-Phe derivative and Phe2 were 11.3 and 8.5 mg/ml, respectively. Next, 500 μL of Lido-PPIX@ER, 0.1 M catalase, and SOD were added and dispersed in the suspension using a magnetic stirrer. The pH (7.0) was adjusted using 0.1 M HCl, and a final volume of 3.5 ml was obtained. Next, 100 μL of 50 mg/ml of lipase solution was added to the substrate suspension, and incubation was performed in a controlled temperature bathtub (37°C) for up to 30 min.

Characterization of the Lido-PPIX@ER hydrogel

For SEM analysis, Lido-PPIX@ER, and Lido-PPIX@ER hydrogel samples were prepared as follows. The samples were treated with 2.5% (v/v) glutaraldehyde in PBS (0.1 M, pH 7.4) for 3 h at 4°C. Next, after washing with PBS, the samples were mixed with different ethanol solutions (60%–100%) for 15 min at room temperature. All the samples were coated with a 10 nm thick gold film using a sputter coater, and the coated samples were examined using a JSM-6700F microscope (JEOL, Japan) in the secondary scattering and backscattering electron modes at a 10 keV electron acceleration voltage.

FITC-labeled lidocaine was tested *in vitro*. Images of ER-encapsulated FITC-Lido (green) and PPIX (red) were obtained using a Leica DM400 B LED (Leica, Germany) fluorescence microscope. LasX and Huygens were used for microscopy operation and data analysis, respectively.

The Lido-PPIX@ER was mixed with the amino acid hydrogel under stirring for 30 s using a vortex mixer, and then PFL was added. Photographs were taken at 2 and 8 min. The rheology experiment was performed using a rheometer at 37°C to determine the elastic modulus (G') of the formed gel. The inflammatory activity of the Lido-PPIX@ER hydrogel was evaluated as follows: 1.0 ml of Lido-PPIX@ER hydrogel was subcutaneously injected into the back of the rat, and blocks of skin tissue from the injection site were collected on the third day and sliced. The anti-inflammatory activity was evaluated by imaging macrophages stained with rabbit anti-F4-80 fluorescent antibody. The sections were analyzed using a Leica SP8 STED instrument.

The weight fraction in percent vs. time and volume change of peptide hydrogel was tested as follows: After freeze-drying, the hydrogel was immediately weighed (W_0), the volume was measured (V_0), and the water absorption capacity of the samples was obtained. The wet specimens were weighed (W)

and the volume (V) was measured at specified intervals after immersion in PBS at room temperature. The weight change was calculated as follows: weight fraction % = $W/W_0 \times 100\%$. The volume change was calculated as follows: volume fraction % = $V/V_0 \times 100\%$.

In Vitro Release Behavior of the Lido-PPIX@ER hydrogel

The lidocaine concentration was determined by LC-2030 series HPLC (Shimadzu Corporation, Japan). The analysis was performed using a Hypersil OD S2 C18 5 μm column (250 × 4.6 mm, Å). The mobile phase was methanol/ammonium dihydrogen phosphate 0.01 M ($NH_4H_2PO_4$) (25:75, v/v). The flow rate was set to 1.0 ml/min, and the detection was monitored at 220 nm.

The release behavior of the Lido-PPIX@ER hydrogel under different ultrasound powers (0–1 W/cm^2 for 60 s) was monitored. The lidocaine concentration was monitored because the Lido@ER hydrogel (without PPIX) and Lido-PPIX@ER hydrogel (with 10 mg/ml of lidocaine in the ER) were triggered by ultrasound (0.3 W/cm^2) for approximately 180 s. The spatiotemporally controlled release behavior of the Lido-PPIX@ER hydrogel was examined as 0.3 W/cm^2 for repeated 30 s irradiation, and the assay was replicated a minimum of five times. HPLC was used to measure the PPIX concentration in the supernatant.

Singlet Oxygen and MDA Determination

To analyze the laser irradiation-dependent release mechanism of the Lido-PPIX@ER hydrogel, singlet oxygen was labeled using a chemical probe (DCFH-DA; BestBio, Shanghai, China). The release at different time points was monitored based on fluorescence using a Leica DM400 B LED fluorescence microscope.

The malondialdehyde (MDA) concentration was measured using an MDA kit. The OD values of the measuring tube (ODm), control tube (ODc), standard tube (ODs) and blank tube (ODb) were measured at 533 nm.

The MDA concentration of Lido-PPIX@ER at different glucose concentrations was calculated as follows:

$$\text{MDA (nmol/L)} = \frac{\text{ODm} - \text{ODc}}{\text{ODs} - \text{ODb}} \times \frac{\text{standard substance concentration}}{\text{protein concentration}}$$

Postoperative Pain Model

The surgery was performed according to the procedure described by Brennan et al. (1996). In this model, a 1 cm incision was made on the plantar surface of the left hind paw under isoflurane anesthesia (2% isoflurane in 100% oxygen). The incision was started immediately beginning at the distal end of the heel and extended to the proximal end of the first set of footpads. Forceps were used to elevate the plantar muscle, and the incision was lengthwise. The wound was sutured with two mattress sutures using 5-0 silk. After surgery, the rats recovered from anesthesia in their cages. Wounds were checked for signs of dehiscence before the behavioral test.

In Vivo Behavioral Testing

To assess the *in vivo* management of postoperative pain, Lido-PPIX@ER hydrogel was subcutaneously injected around the created wound in the postoperative pain model rats before solidifying. The rats were divided into two groups (n = 10 per group)—namely, the free Lido group (6 mg) and 1 ml Lido-PPIX@ER hydrogel (with 5.6 mg lidocaine) + ultrasound group (0.3 W/cm^2, 30 s).

The rats were placed in individual plastic chambers with a plastic mesh floor and allowed to acclimate to the environment for 30 min. The mechanical withdrawal threshold was measured using calibrated von Frey filaments (Stoelting, Wood Dale, IL, United States). The filaments were applied vertically in the area adjacent to the wound for 5–6 s with slight bending of the filament. Withdrawal of the hind paw from the stimulus was scored as a positive response. As described previously, the up-down method was used to identify tactile stimuli with a 50% likelihood of producing a withdrawal threshold (Chaplan et al., 1994).

Long-term postoperative pain management was administered as 30 s ultrasound irradiation (0.3 W/cm^2, 30 s) every 2 h within 12 h after surgery, every 4 h from 12 to 48 h, and every 6 h from 48 to 72 h after surgery. The withdrawal threshold was determined after ultrasound triggering.

Histological Observation

For histological evaluations, the postoperative pain model, treated with Lido-PPIX@ER hydrogel + ultrasound, was sacrificed to collect the skin tissue at the injection site and key organs, including heart, liver, kidney, lung, and spleen.

Blood Biochemistry Index

Following the administration of Lido-PPIX@ER hydrogel + ultrasound for 5 and 15 days, an automated biochemical analyzer (Trilogy, France) was used to determine liver function indices, including alkaline phosphatase (ALP), alanine aminotransferase (ALT), and aspartate aminotransferase (AST). Likewise, the kidney function markers blood urea nitrogen (BUN), creatinine (Cr), and globulin (GLB) were also evaluated (Wang et al., 2019).

Statistical Analysis

All values were reported as means ± SD unless stated otherwise. Statistical analysis was performed using SPSS 18.0 software. Multiple variables were compared using ANOVA, while two groups were compared using two-sample t-test. $p < 0.05$ was considered statistically significant.

RESULTS

Preparation of Lido-PPIX@ER

In the present study, ERs were used as lidocaine carriers because of their high drug loading capacities and long *in vivo* circulation features in vessels (Xia et al., 2018). The lidocaine content inside Lido-PPIX@ER is a key factor that affects the therapeutic efficiency in postoperative pain. During the preparation of

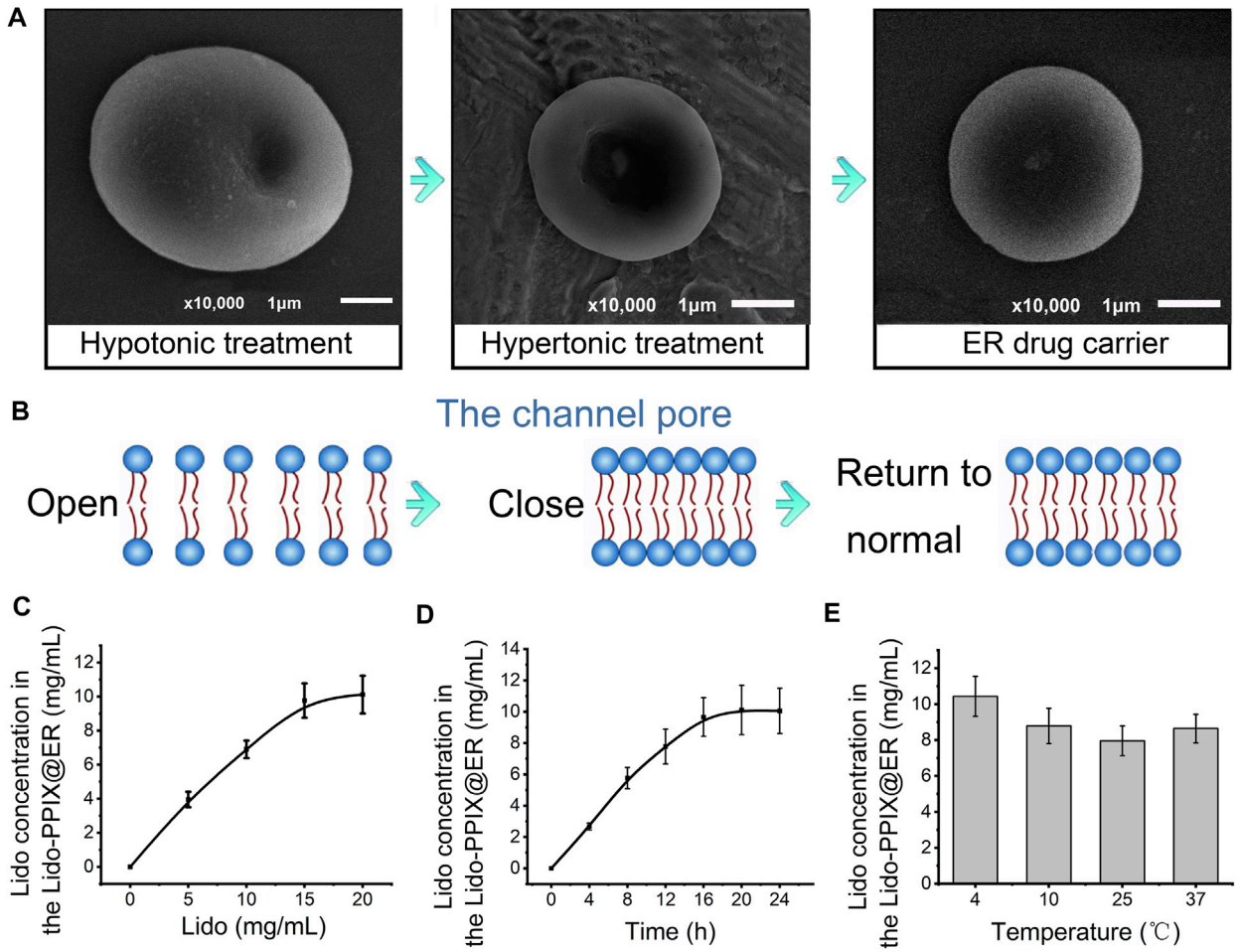

FIGURE 1 | Construction of Lido-PPIX@ER. **(A)** SEM images of Lido-PPIX@ER during hypotonic, hypertonic or PBS treatment. **(B)** Schematic diagram of phospholipid bilayer changes during hypotonic, hypertonic or PBS treatment. **(C)** Relationship between the initial Lido concentration and loading content. **(D)** Effect of dialysis duration on the Lido loading content. **(E)** Relationship between the temperature and loading content.

Lido-PPIX@ER, the ERs were first dispersed in a hypotonic solution to achieve a pre-swelling status to facilitate drug loading (**Figure 1A**). The ER carriers bulged and became enlarged, but maintained their original shape (concave disk-like). Subsequently, the Lido-PPIX@ER was dispersed in a hypertonic solution for reannealing. The ER carriers became smaller, and the fovea of the ERs became enlarged. Finally, the Lido-PPIX@ER was dispersed in isotonic solution for resealing. Because the ER cell membrane comprises phospholipid bilayers, the high tension (hypoosmotic conditions) loosened the bilayers and allowed the drugs to enter (**Figure 1B**). Similarly, the bilayers became compact under hypertonic reannealing and returned to normal under isotonic resealing. Thus, we established a practical lidocaine-loaded ER system.

To achieve a practical lidocaine-loaded erythrocyte system, the optimal loading condition was first challenged using a procedure involving the lidocaine concentration, dialysis time and temperature. The loading content of lidocaine increased with increasing Lido concentration until it approached 15 mg/ml (**Figure 1C**). Extending the incubation time also resulted in more Lido entering ERs to reach equilibrium (**Figure 1D**). The temperature of 4°C was selected as the best reaction temperature in hypotonic dialysis (**Figure 1E**).

In the present study, PPIX was loaded inside the ER to act as an ultrasound-activated switch to control lidocaine release. The resulting decrease in the lidocaine concentration in ERs (**Figure 2A**) indicated that PPIX and ER bind competitively to lidocaine. An optimized PPIX concentration (0.3%) was adopted to achieve a high lidocaine loading content without compromising the Lido-loading efficiency. To further demonstrate that lidocaine and PPIX were enclosed within ERs, the loading of lidocaine and PPIX was characterized by fluorescence imaging (**Figure 2B**). FITC-labeled PPIX (green) and lidocaine (red) were both observed in ERs. The overlapping image of Lido and PPIX demonstrated the successful encapsulation of lidocaine and PPIX inside Lido-PPIX@ER.

Even after the loading of lidocaine and PPIX, ERs maintained their original shape (concave disk-like) and size. Additionally,

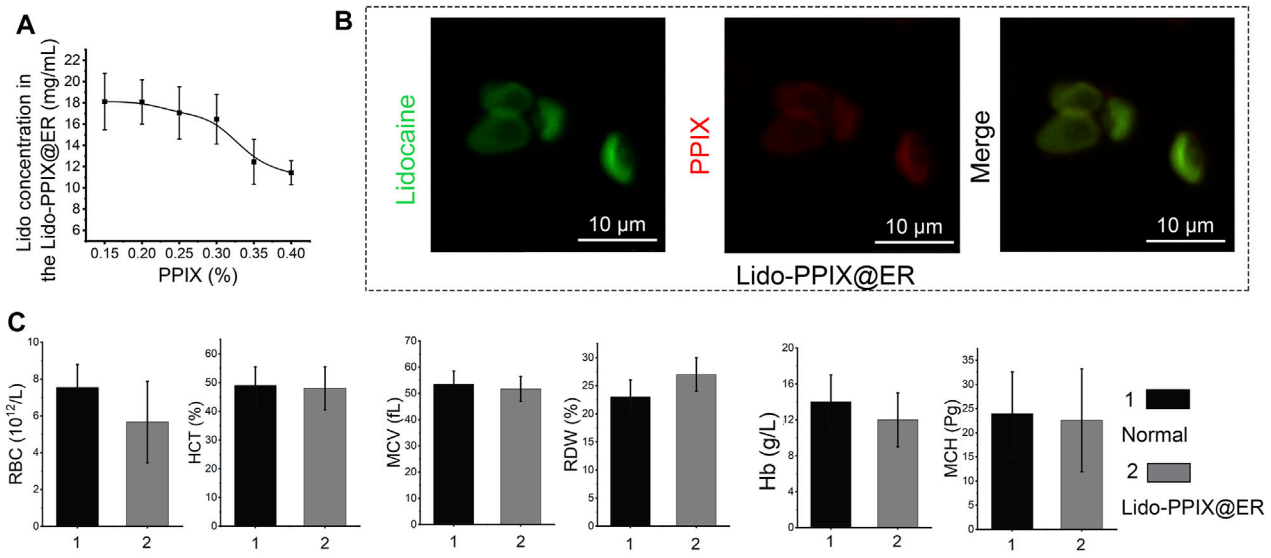

FIGURE 2 | Structure of Lido-PPIX@ER. **(A)** Relationship between the initial PPIX concentration and loading content. **(B)** Confocal images of FITC-labeled Lido (green), PPIX (red), and merged fluorescence. **(C)** Hematological parameters of normal blood and Lido-PPIX@ER, including red blood cells (RBCs), hematocrit (HCT), mean corpuscular volume (MCV), red cell distribution width (RDW), hemoglobin (Hb), and mean corpuscular hemoglobin (MCH).

hematological parameters showed no significant differences between the native ER and Lido-PPIX@ER, such as the RBC number (RBC), hematocrit (HCT), mean corpuscular volume (MCV), red blood cell distribution width (RDW), hemoglobin (Hb), and mean corpuscular hemoglobin (MCH) (**Figure 2C**). These results suggested that the encapsulation of Lido and PPIX did not alter the biological properties of the ERs. The stabilities of Lido-PPIX@ER were examined as the size, morphology, and stability in PBS or culture medium (**Supplementary Figures S1, S2**). These results demonstrated that the Lido-PPIX@ER were stable during storage, and provided a possible favorable condition for preparing in advance.

Preparation of the Lido-PPIX@ER Hydrogel

The ER drug carriers were administered subcutaneously and scavenged by macrophages (Millán et al., 2004). To extend their lifetime *in vivo*, the Lido-PPIX@ER were embedded in a stable scaffold comprising an amino acid hydrogel, which could be subcutaneously implanted. *Pseudomonas fluorescens* (PFL) was used to catalyze the formation of a peptide bond between Fmoc-Phe and Phe2 at 37°C. The mechanical properties of this hydrogel obtained at different reaction times are shown in **Figure 3A** and **Supplementary Figure S2A**. After 8 min, the highest rheological property was reached and maintained a constant value for at least 4 days. The effect of PLF on the mechanical of hydrogel cured was investigated (**Supplemantary Figure S2B**). We observed a rapid rise in compressive strength of hydrogel and it was maintained on subsequent days. The lipase-catalyzed reaction rapidly changed the reaction medium from solution to gel, enhancing the mechanical properties. When the reaction was completed, the hydrogel was no longer formed, resulting in a constant mechanical property.

Mixing Lido-PPIX@ER and amino acids (1:1, vol/vol) formed a cohesive network (Lido-PPIX@ER hydrogel) following the addition of lipase (PFL). After lipase addition, the mixture of Lido-PPIX@ER and PFL shifted from liquid to a homogeneous gel state (**Figure 3B**). Next, the changes from liquid to gel *in vivo* were examined. The peptide hydrogel was subcutaneously injected within 2 min. Ten minutes later, the mixture and PFL also shifted from liquid to a homogeneous gel state *in vivo* (**Figure 3C**).

The hydrogel worked as a scaffold to support the Lido-PPIX@ER and prolonged the action time. We hypothesized that the hydrogel could support the structure of Lido-PPIX@ER because a small change in the volume of the Lido-PPIX@ER hydrogel was observed during the following 3 days (**Figure 3D**). The hydrogel swelled in PBS, resulting in a slight increase in weight in the first 6 h. Next, it reached weight balance and maintained a constant weight for more than 3 days (**Figure 3E**).

This transforming ability ensured that the Lido-PPIX@ER hydrogel was injected into a mold to obtain a stable 3D structure. The SEM image in **Figure 3F** illustrates the porous structure of this obtained amino acid hydrogel comprising a 3D network with microchannels. ERs, exhibiting a typical concave disk structure similar to normal ERs, were still clearly observed in this hydrogel. As envisioned, the Lido in the Lido-PPIX@ER hydrogel exhibited excellent stability *in vitro* because most of the Lido still exited the ERs (**Figure 3G**). Combining the results in **Figure 1**, we confirm the successful loading of ERs.

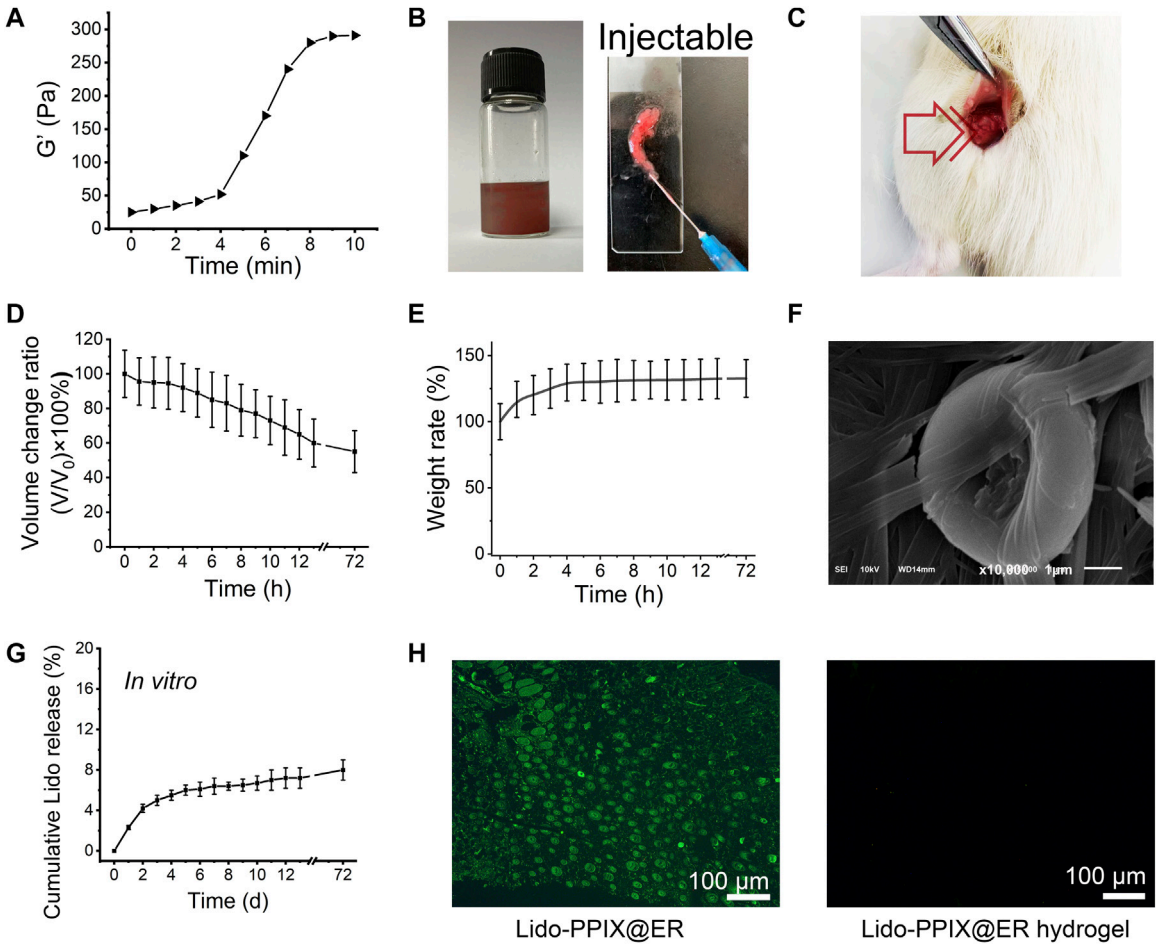

FIGURE 3 | Characterization of the Lido-PPIX@ER hydrogel. **(A)** Rheology properties of PFL-catalyzed Fmoc-Phe_3. **(B)** Photographs showing the gelation behavior of the Lido-PPIX@ER hydrogel after adding PFL for 2 and 10 min and photograph of the injectable Lido-PPIX@ER hydrogel. **(C)** Photograph of peptide hydrogel *in vivo*. The peptide hydrogel was subcutaneously injected within 2 min. Ten minutes later, the mixture and PFL could also shift from liquid to a homogeneous gel state *in vivo*. **(D)** Volume change curve of the Lido-PPIX@ER hydrogel in PBS at 37°C. **(E)** Weight fraction in precent vs. time of Lido-PPIX@ER hydrogel in PBS at 37°C. **(F)** The SEM imge of Lido-PPIX@ER hydrogel. **(G)** Stability of Lido-PPIX@ER hydrogel *in vitro*. **(H)** Immunohistochemical staining for f4/80 to identify infiltrated macrophages in the subcutaneous tissues. The experiment was repeated at least three times.

Good compatibility, without an inflammatory-like response, is a vital feature of subcutaneous scaffolds to prevent macrophage infiltration, preventing the early destruction of drug-loaded ER (Rose and Currow, 2009). The infiltrated macrophages in the subcutaneous tissues after the hydrogel implant were labeled with f4/80 (green) and are shown in **Figure 3H**. Compared with the direct injection of Lido-PPIX@ER, the injection of Lido-PPIX@ER hydrogel did not induce significant infiltration of macrophages even after 5 days. This finding partly demonstrated that the Lido-PPIX@ER hydrogel would not induce inflammation *in vivo*.

Ultrasound-Triggered *In Vitro* Release of Lido From Lido-PPIX@ER Hydrogel

We expected that when the Lido-PPIX@ER hydrogel is triggered by ultrasound, PPIX will produce ROS, which consequently destroy the integrity of the ER membrane, leading to Lido release. To confirm the ultrasound-triggerable response leakage of Lido, the release of Lido from the Lido-PPIX@ER hydrogel was monitored by ultrasound from 0 to 1 W/cm^2 for 60 s (**Figure 4A**). The burst release of Lido was observed when the ultrasound power was greater than 0.3 W/cm^2 ($p > 0.01$), while almost no Lido was released when the power was off. This result demonstrated that ultrasound (0.3 W/cm^2) was effective in regulating Lido release from the Lido-PPIX@ER hydrogel.

By contrast, almost no Lido was released from the Lido@ER hydrogel (without PPIX) with/without ultrasound or the Lido-PPIX@ER hydrogel without ultrasound (**Figure 4B**). Interestingly, Lido release from the Lido-PPIX@ER hydrogel could be accelerated with the extension of ultrasound (**Figure 4C**). To evaluate the responsible release behavior of the Lido-PPIX@ER hydrogel, the Lido concentration was monitored when the ultrasound was cyclically turned on and

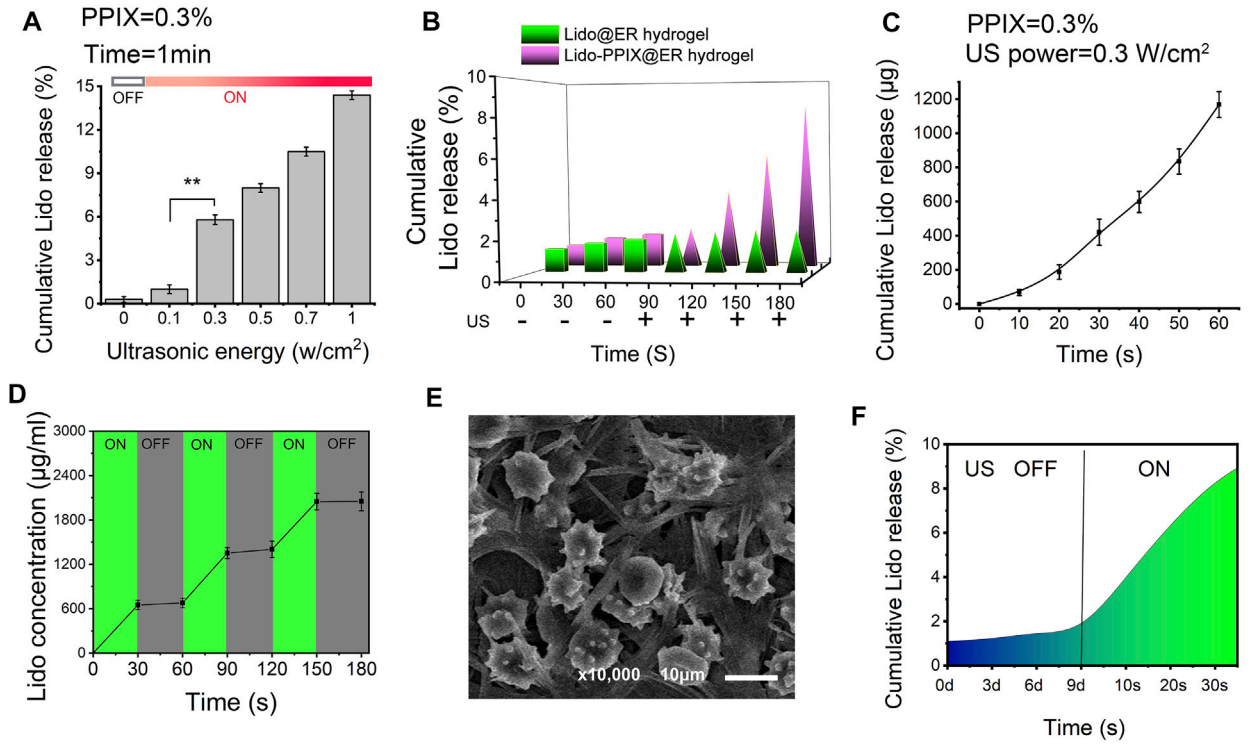

FIGURE 4 | Ultrasound-triggered release behavior of the Lido-PPIX@ER hydrogel. **(A)** *In vitro* lidocaine release from the Lido-PPIX@ER hydrogel at increasing ultrasound power at 37°C. **(B)** *In vitro* lidocaine release from the Lido@ER hydrogel or Lido-PPIX@ER hydrogel with or without laser intensities at 37°C (0.3 W/cm^2, 60 s). **(C)** Release profile of lidocaine from 1.0 ml of Lido-PPIX@ER hydrogel during continuous ultrasound triggering. **(D)** *In vitro* release profile of lidocaine when the ultrasound was cyclically varied between on and off for several repetitions. **(E)** Morphological changes of Lido-PPIX@ER during "on-off" lidocaine release. **(F)** Ultrasound-triggered release behavior of the Lido-PPIX@ER hydrogel after storage in PBS at 4°C for 9 days.

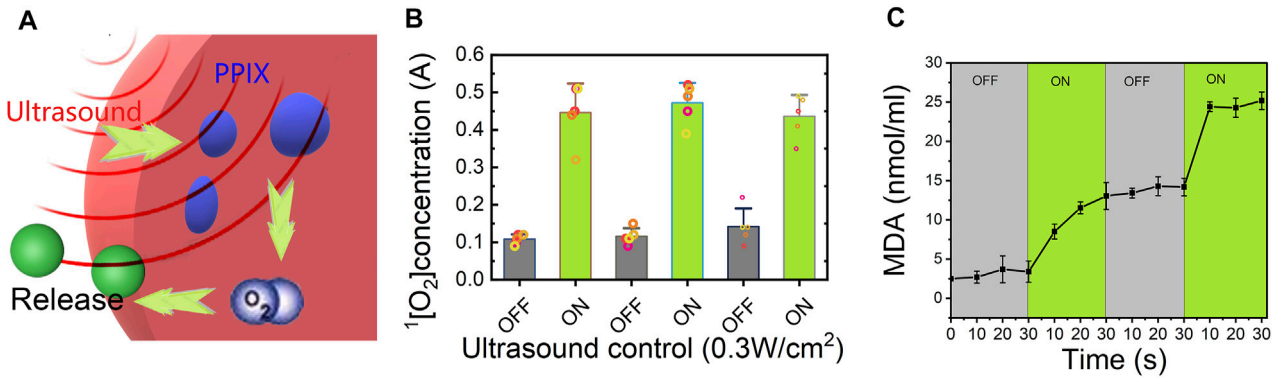

FIGURE 5 | Release mechanism of the Lido-PPIX@ER hydrogel under ultrasound. **(A)** Schematic representation showing the ultrasound-regulated release of lidocaine from the Lido-PPIX@ER hydrogel. **(B)** Concentration profile of singlet oxygen with ultrasound (0.3 W/cm^2) in the on/off state. **(C)** MDA concentration changes of the Lido-PPIX@ER hydrogel under ultrasound regulation (on-off state) at 37°C.

off every 30 s. Lido released from the 1 ml Lido-PPIX@ER hydrogel responded to 0.3 W/cm^2 ultrasound irradiation for 30 s (**Figure 4D**). The concentration of lidocaine increased as the ultrasound was turned on, while lidocaine was no longer released from the Lido-PPIX@ER hydrogel when the power was turned off. The effect of ultrasound on the morphology change of Lido-PPIX@ER was examined by SEM (**Figure 4E**). With the power on, the Lido-PPIX@ER showed an irregular morphology, and morphological changes of ER were observed facilitating lidocaine release.

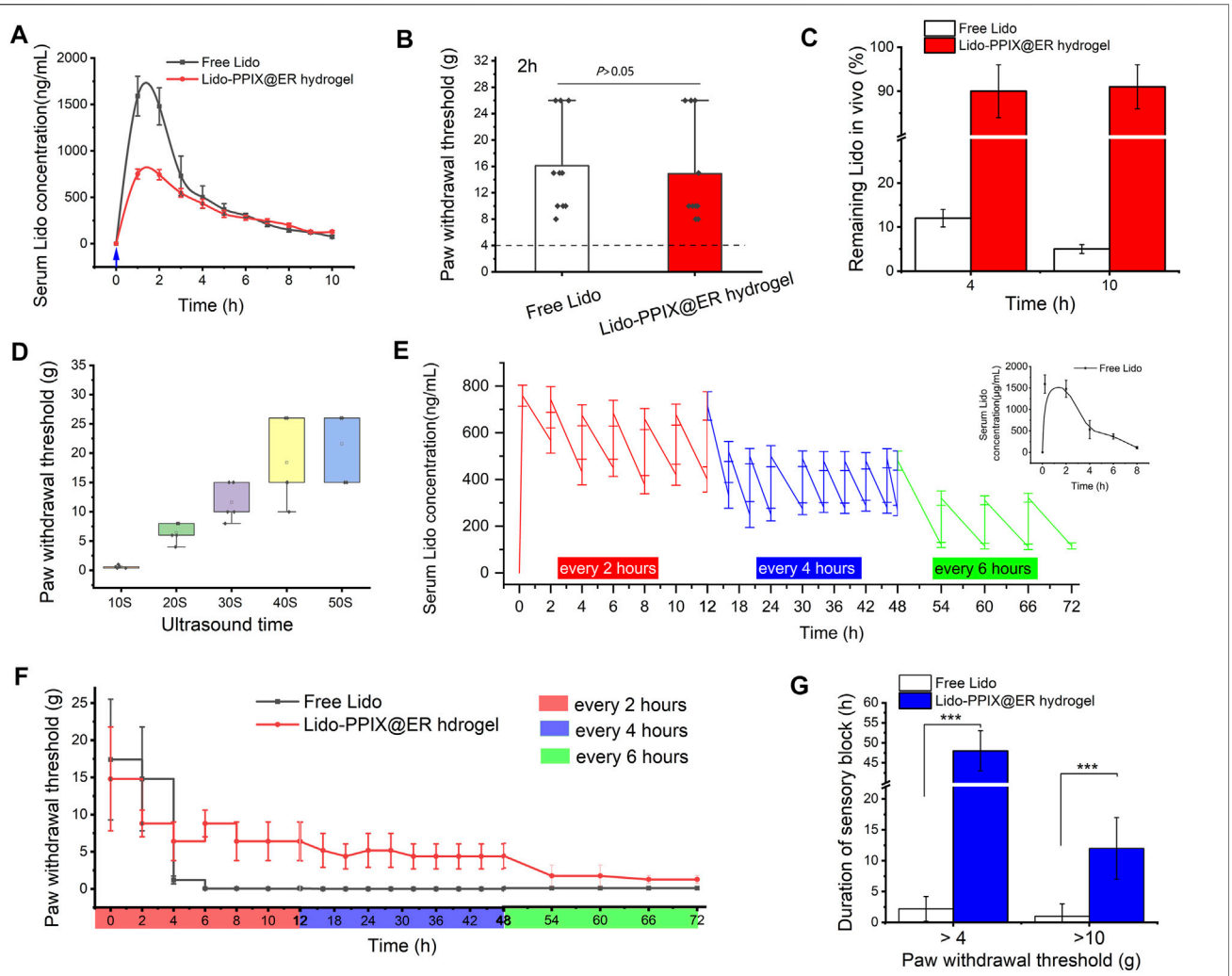

FIGURE 6 | Effects of managing postoperative pain *in vivo*. **(A)** Change curve of the serum Lido concentration and **(B)** paw withdrawal threshold (2 h after surgery) after one ultrasound trigger. **(C)** Ratio of the remaining lidocaine in free lidocaine and Lido-PPIX@ER hydrogel after one ultrasound-triggered removal from the administration site in rats. **(D)** Duration of ultrasound-triggered lidocaine release and effect of pain relief application in the rat model of postoperative pain in the Lido-PPIX@ER hydrogel-treated group. **(E)** Change curve of the serum Lido concentration and **(F)** the hind paw withdrawal thresholds after on-demand ultrasound triggering in the Lido-PPIX@ER hydrogel group (triggered for every 2 h in the first 12 h and every 4 h for the next 36 h, and then every 6 h until 72 h after surgery). **(G)** Effective time at different paw withdrawal thresholds in the ultrasound-triggered Lido-PPIX@ER hydrogel group. ***, $p < 0.001$.

Unsurprisingly, the Lido-PPIX@ER hydrogel maintained its bioactivity even after 9 days in PBS, representing a crucial property of Lido-PPIX@ER for postoperative pain management (**Figure 4F**). The Lido concentration in the supernatant was very low in the first 9 days, indicating that most of the Lido was stored inside the ERs and would not be released into PBS. On Day 9, the remaining Lido-PPIX@ER hydrogel was treated with ultrasound. The Lido concentration in the suspension increased rapidly after 30 s.

Releasing Mechanism of the Lido-PPIX@ER Hydrogel

We expected that when the Lido-PPIX@ER hydrogel is irradiated by ultrasound, PPIX will produce ROS, which consequently destroy the integrity of the ER membrane, leading to Lido release. To confirm the ultrasound-triggered leakage of Lido, Lido release from the Lido-PPIX@ER hydrogel was monitored following ultrasound treatment (0.3 W/cm^2, 30 s) (**Figure 5A**). Given that the lipid bilayer membrane of ERs would be damaged in the presence of accumulated ROS to release the packed drugs (Xia et al., 2018), the relationship between ultrasound treatment and ROS production was studied and is shown in **Figure 5B**.

The ROS concentration was directly related to ultrasound because PPIX generated singlet oxygen after triggering. Once the ultrasound was turned off, ROS were no longer produced, and the residual ROS could be scavenged by SOD and CAT, leading to ROS exhaustion in the hydrogel. Therefore, the ROS concentration showed pulsate changes with the laser on and off. The accumulated ROS promoted pore formation in the ER

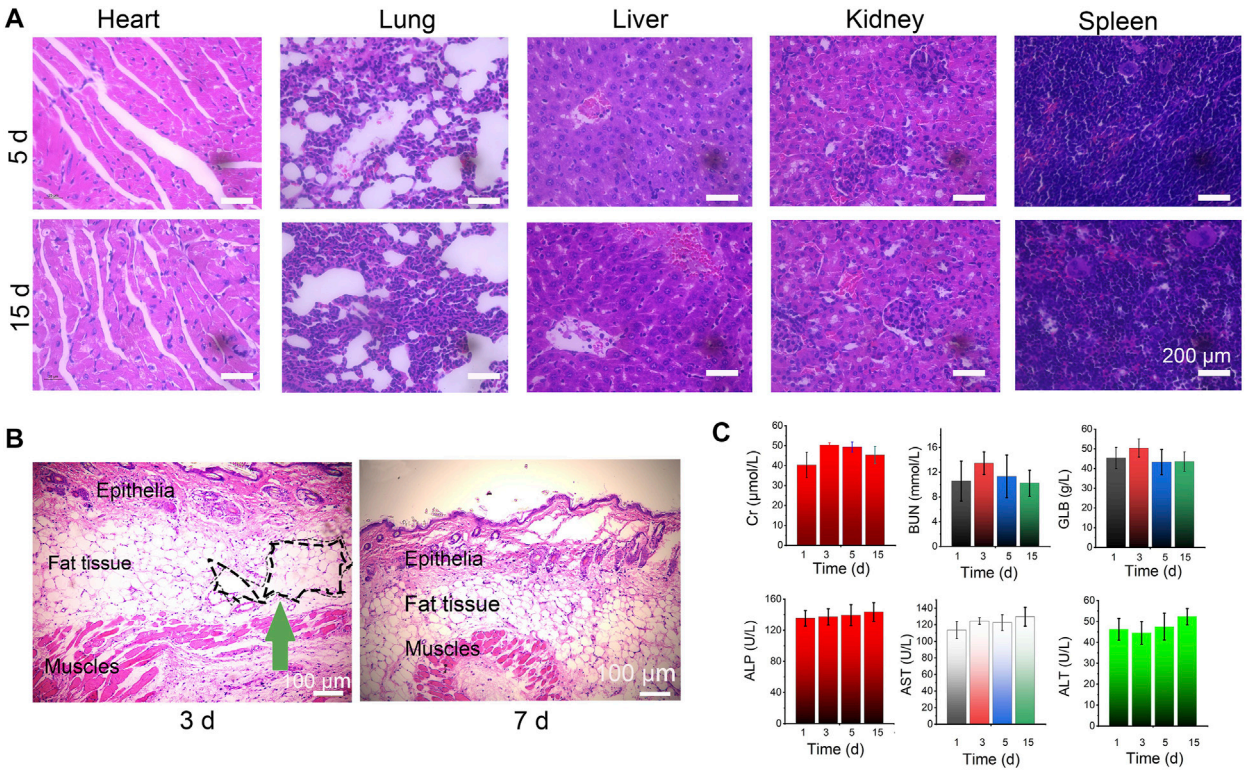

FIGURE 7 | Biosafety of the Lido-PPIX@ER hydrogel *in vivo*. **(A)** Images of H&E staining after treatment with the Lido-PPIX@ER hydrogel. **(B)** H&E-stained sections of surrounding tissues at the site of subcutaneously injected Lido-PPIX@ER hydrogel. Scale bar = 100 μm. **(C)** Kidney function (BUN, Cr, and GLB) and the levels of liver (ALP, ALT, and AST) markers on Days 1, 3, 5, and 15 in the control and Lido-PPIX@ER hydrogel treatment groups.

membrane, allowing Lido release. Likewise, ROS generation was stopped when ultrasound was turned off, leading to closure of the pores in the ER membrane and inhibited PPIX release.

Additionally, we evaluated changes in the malondialdehyde (MDA) levels in Lido-PPIX@ER as an indicator of oxidative stress (**Figure 5C**). The changes in the MDA and H_2O_2 levels were consistent, reflecting ultrasound triggering.

Postoperative Pain Management *In Vivo*

To investigate the possibility of the Lido-PPIX@ER hydrogel controlling postoperative pain with ultrasound triggering, we treated a postoperative pain rat model with the Lido-PPIX@ER hydrogel. First, the mean serum Lido concentration after free Lido (6 mg) or 1 ml of Lido-PPIX@ER hydrogel (containing 5.6 mg/ml of lidocaine) treatment must be evaluated. In the lidocaine (6 mg)-treated group, the mean serum lidocaine concentration steadily increased to 1,790 ng/ml at 2 h after subcutaneous administration (**Figure 6A**). In the Lido-PPIX@ER hydrogel-treated group, the serum lidocaine concentration did not show a burst increase after ultrasound triggering (0.3 W/cm^2, 30 s).

To further prove that the ultrasound-triggered Lido-PPIX@ER hydrogel could be used in postoperative pain management, mechanical hypersensitivity was observed 2 h after paw incision (**Figure 6B**). Subcutaneous administration of the Lido-PPIX@ER hydrogel produced antihypersensitivity effects compared with the control group ($p > 0.05$). We confirmed that the ultrasound course of lidocaine released by the Lido-PPIX@ER hydrogel *in vivo* was similar to that of free Lido to manage postoperative pain in the first 4 h.

As expected, examination of the residual Lido-PPIX@ER hydrogel removed from rats after one ultrasound-triggered (0.3 W/cm^2, 30 s) *in vivo* treatment revealed that approximately 91% and 90% of the administered lidocaine remained at 4 and 10 h, respectively (**Figure 6C**). Conversely, approximately 11 and 6% of the administered lidocaine remained at 4 and 10 h, respectively, in the free Lido-treated group. Thus, sufficient subcutaneous storage of the Lido-PPIX@ER hydrogel provides a favorable condition for long-term ultrasound-triggered postoperative pain management.

The on-demand release of Lido in postoperative pain management meets the needs of the most acute care. We next tested the on-demand release behavior of the Lido-PPIX@ER hydrogel under different ultrasound-triggered times. With increasing ultrasound-triggered time, the Lido concentration increased as expected (**Figure 6D**).

Ultrasound at 0.3 W/cm^2 for 30 s for triggered release in the Lido-PPIX@ER hydrogel was optimal because it achieved a stable plasma concentration (**Figure 6E**). After surgery, severe pain continued for approximately 12 h and was relieved. To address this issue, ultrasound was triggered every 2 h in the first 12 h, every 4 h for the next 36 h, and then every 6 h until 72 h after

surgery. Thus, the mean serum lidocaine concentration was steadily high initially and then decreased from 592 ng/ml at 12 h to 487 ng/ml at 18 h after the administration of the ultrasound-triggered time interval. Unsurprisingly, the mean serum lidocaine concentration from 48 to 72 h after surgery decreased to a lower level. Naked Lido without protection, by contrast, can be cleared from organisms by 4–8 h after subcutaneous administration.

The paw withdrawal threshold changed with the mean serum lidocaine concentration (**Figure 6F**). The group treated perineurally with repeatedly ultrasound-triggered Lido-PPIX@ER hydrogel showed stable withdrawal thresholds at various time periods, higher concentrations at all time points after paw incision than the free Lido-treated group, and lasted approximately 72 h. However, the free lidocaine treatment group disappeared 4 h after paw incision, and the paw withdrawal thresholds were decreased to less than 4 g.

To better fit the needs of men with different pain thresholds, the effective time at different paw withdrawal thresholds was examined (**Figure 6G**). The Lido-PPIX@ER hydrogel controlled the paw withdrawal thresholds over 4 g or 10 g for approximately 48 and 12 h compared with the free lidocaine-treated group ($p < 0.001$). Therefore, repeated administration of the Lido-PPIX@ER hydrogel meets the requirement to ensure sustained postoperative pain management.

Safety Analysis

Next, to evaluate the potential health risks after treatment with the Lido-PPIX@ER hydrogel plus laser irradiation, the treated mice were euthanized on Day 5 and 15. The main organs, including the heart, liver, kidney, lung, and spleen tissues, were stained with hematoxylin and eosin (H&E) (**Figure 7A**).

To evaluate the *in vivo* degradability of the Lido-PPIX@ER hydrogel, the size of the resultant subcutaneous skin lump was monitored over time (not shown). We noticed that 15 days post-injection, no obvious skin protrusion was noticed, illustrating the complete degradation of the Lido-PPIX@ER hydrogel. From the H&E staining results of surrounding tissues at the site of subcutaneously injected Lido-PPIX@ER hydrogel, the lesion region was covered with connective tissue after 15 days (**Figure 7B**). Collectively, the hydrogel provided structural support and exhibited self-degradation *in vivo*.

Furthermore, analysis of liver function (ALP, ALT, and AST) and kidney function (BUN, Cr, and GLB) markers (**Figure 7C**) revealed that Lido-PPIX@ER hydrogel + ultrasound treatment did not cause hepatic or kidney damage. Therefore, the Lido-PPIX@ER hydrogel exhibits good biocompatibility *in vivo*.

DISCUSSION

To maximize postoperative pain relief, enhance patient satisfaction, and facilitate postoperative rehabilitation, pain management is essential. Lidocaine has been used in clinical medicine for more than half a century, and multimodal lidocaine-containing products have proven effective to treat postoperative pain. However, lidocaine may induce nerve demyelination and contribute to the neurotoxicity of lidocaine, and multiple dosing delivery was used in the clinic using conventional intravenous administration. This presents a challenge, such as the requirement of skilled professionals, a situation that is not easily achievable for families. Studies specifically designed to address this issue are required. Sustained-release local anesthetics have been reported to treat postoperative pain (Wang et al., 2016). The liposomal bupivacaine injectable suspension (EXPAREL®; Pacira Pharmaceuticals, Inc., United States) has received FDA Approval for infiltration into a surgical site to provide postoperative analgesia in adults based on clinical trials in which subjects had undergone bunion reaction (Golf et al., 2011) and hemorrhoidectomy (Gorfine et al., 2011), demonstrating efficacy for 36 and 72 h, respectively. Furthermore, clinical trials of liposomal bupivacaine for epidural block (Viscusi et al., 2012), femoral nerve block (Surdam et al., 2015), transversus abdominis plane block (Fayezizadeh et al., 2016) and interscalene block (Namdari et al., 2017) have been reported previously. However, different people have different pain thresholds or pain tolerance scores. Therefore, an effective treatment for postoperative pain should consider variable timing and intensity of anesthetics.

Generally, men show severe pain on the day after the operation. With the extension of the treatment time, the postoperative pain is reduced over time. Different people have different pain thresholds or pain tolerance scores. Relieving local pain as needed, allowing patients to control the timing and intensity, would be the excellent choice to maximize personalized postoperative pain. An ultrasound-triggerable, on-demand nerve block system allows control of the duration and intensity of nerve block simply using the duration and intensity of the ultrasound (Rwei et al., 2017). In the present study, ultrasound-triggered on-demand local anesthesia was reported, and the intensity and duration of local anesthesia were controlled by adjusting the intensity and duration of the ultrasound. The Lido-PPIX@ER hydrogel described here allowed an on-demand release of lidocaine from the subcutaneous lidocaine reservoir by remote ultrasound control without frequent injection. Thus, additional time for on-demand nerve blocks is allowed, leading to personalized anesthesia-free pain management.

Alternatively, a sufficient action time must be considered in its clinical application because patients undergoing major spine surgery frequently experience severe postoperative pain lasting more than 3 days. Here, we designed a large capacity lidocaine vector that controls the timing, intensity and duration of lidocaine to relieve postoperative pain. Recently, the erythrocyte membrane has been extensively studied to develop novel drug delivery systems to prolong the cyclic persistence of drugs. As "innate carriers," ER have many unique characteristics, such as perfect biocompatibility, a long circulation half-life (approximately 120 days in humans), membrane flexibility and stability. In the present study, ER were used as lidocaine carriers because of their high drug loading capacities and long *in vivo* circulation features in vessels (Xia et al., 2018). Furthermore, the presence of accumulated H_2O_2 caused the pores in the erythrocyte membrane to open rapidly. Considering that PPIX

produces H_2O_2 when triggered by ultrasound, we describe the development of an ultrasound-triggered drug release platform (Lido-PPIX@ER hydrogel) for postoperative pain management. From the results in **Figure 3**, the drug release platform was very stable *in vivo*, providing a prerequisite to obtain ultrasound-triggered on-demand release behavior.

Ultrasound, as an integral part of drug-delivery modalities, has many attractive features, including simplicity and cost-effectiveness (Covotta et al., 2020). Sonication can be performed non-invasively, and ultrasound waves can be directed to deep locations for precise energy-deposition patterns (de la Fuente et al., 2021; Mi et al., 2021). In early studies, microbubbles, which are clinically recognized as ultrasound contrast agents, were used to load therapeutic agents for effective tumor chemotherapy. However, the shortcomings of these gas-filled microbubbles prevent their widespread use in drug delivery. In the present study, the hypothesis that sonochemistry and ROS production played a major role in ultrasound-triggered cargo release is supported by the observation that PPIX-loaded ER produced more ROS, opening the ER phospholipid bilayer and triggering drug release. Ultrasound-induced cavitation can produce light (sonoluminescence), which activates the photosensitizer PPIX to produce ROS. Implosion of ultrasound-induced cavitation bubbles can also induce the formation of sonosensitizer-derived free radicals that generate ROS. These effects depend on inertial cavitation following insonation, which may be caused by the ultrasound conditions used here (0.3 W/cm^2). Therefore, we designed a novel multimode osmotic analgesia scheme for wound infiltration.

In this study, we report an injectable, remote ultrasound-induced lidocaine delivery system for postoperative pain management. The Lido-PPIX@ER hydrogel exhibited high lidocaine loading capacity with efficient ultrasound-triggered release of lidocaine, making it a potential delivery system for well-regulated postoperative pain. *In vivo* experiments in a postoperative pain model showed that a single injection of Lido-PPIX@ER hydrogel can effectively control the duration and intensity of nerve block by simply adjusting the duration and intensity of ultrasound. Therefore, we suggest that this delivery system is an effective strategy to reduce pain, remotely control pain, and offer timed and spatiotemporally controlled release of Lido to manage postoperative pain. Although, this kind of ultrasound-triggered on demand release system cannot be applied clinic in present form due to limited source of ER, we hope this Lido delivery stratagem can provide new insights for the management of postoperative pain.

DATA AVAILABILITY STATEMENT

The original contributions presented in the study are included in the article/**Supplementary Material**, further inquiries can be directed to the corresponding authors.

ETHICS STATEMENT

The procedures used in our study were approved by the Committee of the Animal Research of Nantong University (20210421-072), and followed the guidelines the use of Animals in Research of the International Association for the Study of Pain and the directive of the European Parliament (2010/63/EU).

AUTHOR CONTRIBUTIONS

JY and XC conceived the idea and designed the experiments. JZ and YY, did the synthesis and characterization. HW and GM conducted the *in vitro* experiments. XC, DW, and HC did the *in vivo* analyses. XC, JZ, HC, and JY analyzed all the data and wrote the manuscript. All the authors have proof-read this article and approved its publication.

FUNDING

This study was funded by the Clinical Frontier Technology Project of China Jiangsu Provincial Department of Science and Technology (No. BE2018669), the Health Research Funds of Nantong, China (No. 2020JCC046), General program from Nantong Commission of Health (No. MB2021050).

ACKNOWLEDGMENTS

The authors would like to acknowledge Dr. Donglin Xia for his statistical help with the analysis.

SUPPLEMENTARY MATERIAL

The Supplementary Material for this article can be found online at: https://www.frontiersin.org/articles/10.3389/fbioe.2022.925047/full#supplementary-material

REFERENCES

Al-Achi, A., and Greenwood, R. (1998). Erythrocytes as Oral Delivery Systems for Human Insulin. *Drug Dev. Industrial Pharm.* 24 (1), 67–72. doi:10.3109/03639049809082354

Beaulieu, P. (2021). Cannabinoids and Acute/postoperative Pain Management. *Pain* 162 (8), 2309. doi:10.1097/j.pain.0000000000002294

Brennan, T. J., Vandermeulen, E. P., and Gebhart, G. F. (1996). Characterization of a Rat Model of Incisional Pain. *Pain* 64 (3), 493–502. doi:10.1016/0304-3959(95)01441-1

Chaplan, S. R., Bach, F. W., Pogrel, J. W., Chung, J. M., and Yaksh, T. L. (1994). Quantitative Assessment of Tactile Allodynia in the Rat Paw. *J. Neurosci. Methods* 53 (1), 55–63. doi:10.1016/0165-0270(94)90144-9

Chen, J., Jin, T., and Zhang, H. (2020). Nanotechnology in Chronic Pain Relief. *Front. Bioeng. Biotechnol.* 8, 682. doi:10.3389/fbioe.2020.00682

Chronopoulou, L., Togna, A. R., Guarguaglini, G., Masci, G., Giammaruco, F., Togna, G. I., et al. (2012). Self-assembling Peptide Hydrogels Promote Microglial Cells Proliferation and NGF Production. *Soft Matter* 8 (21), 5784. doi:10.1039/c2sm25528f

Covotta, M., Claroni, C., Costantini, M., Torregiani, G., Pelagalli, L., Zinilli, A., et al. (2020). The Effects of Ultrasound-Guided Transversus Abdominis Plane Block on Acute and Chronic Postsurgical Pain After Robotic Partial Nephrectomy: A Prospective Randomized Clinical Trial. *Pain Med.* 21 (2), 378–386. doi:10.1093/pm/pnz214

Favretto, M. E., Cluitmans, J. C. A., Bosman, G. J. C. G. M., and Brock, R. (2013). Human Erythrocytes as Drug Carriers: Loading Efficiency and Side Effects of Hypotonic Dialysis, Chlorpromazine Treatment and Fusion with Liposomes. *J. Control. Release* 170 (3), 343–351. doi:10.1016/j.jconrel.2013.05.032

Fayezizadeh, M., Majumder, A., Neupane, R., Elliott, H. L., and Novitsky, Y. W. (2016). Efficacy of Transversus Abdominis Plane Block with Liposomal Bupivacaine during Open Abdominal Wall Reconstruction. *Am. J. Surg.* 212 (3), 399–405. doi:10.1016/j.amjsurg.2015.12.026

Fuente, J., Aramendi, J. F., Ibañez, J. M., Blasi, M., Vazquez, A., Aurrekoetxea, J. J., et al. (2021). Minimally Invasive Ultrasound-guided vs Open Release for Carpal Tunnel Syndrome in Working Population : A Randomized Controlled Trial. *J. Clin. Ultrasound* 49 (7), 693–703. doi:10.1002/jcu.23019

Gao, X., Xin, X., Li, Z., and Zhang, W. (2021). Predicting Postoperative Pain Following Root Canal Treatment by Using Artificial Neural Network Evaluation. *Sci. Rep.* 11 (1), 17243. doi:10.1038/s41598-021-96777-8

Golf, M., Daniels, S. E., and Onel, E. (2011). A Phase 3, Randomized, Placebo-Controlled Trial of DepoFoam Bupivacaine (Extended-release Bupivacaine Local Analgesic) in Bunionectomy. *Adv. Ther.* 28 (9), 776–788. doi:10.1007/s12325-011-0052-y

Gorfine, S. R., Onel, E., Patou, G., and Krivokapic, Z. V. (2011). Bupivacaine Extended-Release Liposome Injection for Prolonged Postsurgical Analgesia in Patients Undergoing Hemorrhoidectomy: a Multicenter, Randomized, Double-Blind, Placebo-Controlled Trial. *Dis. Colon Rectum* 54 (12), 1552–1559. doi:10.1097/DCR.0b013e318232d4c1

Hamidi, M., Zarei, N., Zarrin, A. H., and Mohammadi-Samani, S. (2007). Preparation and *In Vitro* Characterization of Carrier Erythrocytes for Vaccine Delivery. *Int. J. Pharm.* 338 (1-2), 70–78. doi:10.1016/j.ijpharm.2007.01.025

Jing, Y., Xiu-Juan, Z., Hong-Jiao, C., Zhi-Kui, C., Qing-Fu, Q., En-Sheng, X., et al. (2019). Ultrasound-targeted Microbubble Destruction Improved the Antiangiogenic Effect of Endostar in Triple-Negative Breast Carcinoma Xenografts. *J. Cancer Res. Clin. Oncol.* 145 (5), 1191–1200. doi:10.1007/s00432-019-02866-7

Joseph, J. M., Gori, D., Curtin, C., Hah, J., Ho, V. T., Asch, S. M., et al. (2022). Gaps in Standardized Postoperative Pain Management Quality Measures: A Systematic Review. *Surgery* 171 (2), 453–458. doi:10.1016/j.surg.2021.08.004

Küls, N., Trujanovic, R., Otero, P. E., and Larenza-Menzies, M. P. (2020). Ultrasound-Guided Transversus Abdominis Plane Block in Shetland Ponies: A Description of a Three-Point Injection Technique and Evaluation of Potential Analgesic Effects. *J. Equine Veterinary Sci.* 90, 102994. doi:10.1016/j.jevs.2020.102994

Mi, X., Zou, B., Rashidi, P., Baharloo, R., Fillingim, R. B., Wallace, M. R., et al. (2021). Effects of Patient and Surgery Characteristics on Persistent Postoperative Pain. *Clin. J. Pain* 37 (11), 803–811. doi:10.1097/AJP.0000000000000979

Millán, C. G., Marinero, M. L. S., Castañeda, A. Z., and Lanao, J. M. (2004). Drug, Enzyme and Peptide Delivery Using Erythrocytes as Carriers. *J. Control. Release* 95 (1), 27–49. doi:10.1016/j.jconrel.2003.11.018

Namdari, S., Nicholson, T., Abboud, J., Lazarus, M., Steinberg, D., and Williams, G. (2017). Randomized Controlled Trial of Interscalene Block Compared with Injectable Liposomal Bupivacaine in Shoulder Arthroplasty. *J. Bone Jt. Surg.* 99 (7), 550–556. doi:10.2106/JBJS.16.00296

Park, J. K., Nan, K., Luan, H., Zheng, N., Zhao, S., Zhang, H., et al. (2019). Remotely Triggered Assembly of 3D Mesostructures Through Shape-Memory Effects. *Adv. Mat.* 31 (52), 1905715. doi:10.1002/adma.201905715

Park, S. J., Kim, H. S., and Yim, G. W. (2021). Comparison of Vaginal Natural Orifice Transluminal Endoscopic Surgery (vNOTES) and Laparoendoscopic Single-Site (LESS) Hysterectomy on Postoperative Pain Reduction: A Randomized Pilot Study. *Pain Ther.* 10, 1401–1411. doi:10.1007/s40122-021-00300-w

Pedersen, S. L., Huynh, T. H., Pöschko, P., Fruergaard, A. S., Jarlstad Olesen, M. T., Chen, Y., et al. (2020). Remotely Triggered Liquefaction of Hydrogel Materials. *ACS Nano* 14 (7), 9145–9155. doi:10.1021/acsnano.0c04522

Qi, F., Wang, Z., Huang, H., Yang, S., Huang, S., Guo, J., et al. (2016). Long-term Effect of Ropivacaine Nanoparticles for Sciatic Nerve Block on Postoperative Pain in Rats. *Ijn* 11, 2081–2090. doi:10.2147/IJN.S101563

Raoof, M., Cisneros, B. T., Guven, A., Phounsavath, S., Corr, S. J., Wilson, L. J., et al. (2013). Remotely Triggered Cisplatin Release from Carbon Nanocapsules by Radiofrequency Fields. *Biomaterials* 34 (7), 1862–1869. doi:10.1016/j.biomaterials.2012.11.033

Rose, M., and Currow, D. C. (2009). The Need for Chemical Compatibility Studies of Subcutaneous Medication Combinations Used in Palliative Care. *J. Pain & Palliat. Care Pharmacother.* 23 (3), 223–230. doi:10.1080/15360280903098382

Rwei, A. Y., Paris, J. L., Wang, B., Wang, W., Axon, C. D., Vallet-Regí, M., et al. (2017). Ultrasound-triggered Local Anaesthesia. *Nat. Biomed. Eng.* 1, 644–653. doi:10.1038/s41551-017-0117-6

Singh, T., Castellanos, I. S., Haar, S., Klimas, A., Entcheva, E., Salvador, T., et al. (2018). Ultrasound-Induced Insulin Release as a Potential Novel Treatmentfor Type 2 Diabetes Mellitus. *Conf. Proc. IEEE Eng. Med. Biol. Soc.* 2018, 6060–6063. doi:10.1109/EMBC.2018.8513687

Song, X., Feng, L., Liang, C., Yang, K., and Liu, Z. (2016). Ultrasound Triggered Tumor Oxygenation with Oxygen-Shuttle Nanoperfluorocarbon to Overcome Hypoxia-Associated Resistance in Cancer Therapies. *Nano Lett.* 16 (10), 6145–6153. doi:10.1021/acs.nanolett.6b02365

Strauss, C., Brix, E., Anker, A., Prantl, L., Brébant, V., and Aung, T. (2017). Perfusion Control of a Partial Revascularized Hand via Application of Indocyanine Green (ICG) and Near-Infrared Fluorescence Imaging. *Clin. Hemorheol. Microcirc.* 67 (3-4), 215–219. doi:10.3233/CH-179202

Surdam, J. W., Licini, D. J., Baynes, N. T., and Arce, B. R. (2015). The Use of Exparel (Liposomal Bupivacaine) to Manage Postoperative Pain in Unilateral Total Knee Arthroplasty Patients. *J. Arthroplasty* 30 (2), 325–329. doi:10.1016/j.arth.2014.09.004

Tharkar, P., Varanasi, R., Wong, W. S. F., Jin, C. T., and Chrzanowski, W. (2019). Nano-Enhanced Drug Delivery and Therapeutic Ultrasound for Cancer Treatment and Beyond. *Front. Bioeng. Biotechnol.* 7, 324. doi:10.3389/fbioe.2019.00324

Tobe, M., Obata, H., Suto, T., Yokoo, H., Nakazato, Y., Tabata, Y., et al. (2010). Long-term Effect of Sciatic Nerve Block with Slow-Release Lidocaine in a Rat Model of Postoperative Pain. *Anesthesiology* 112 (6), 1473–1481. doi:10.1097/ALN.0b013e3181d4f66f

van Rooij, T., Skachkov, I., Beekers, I., Lattwein, K. R., Voorneveld, J. D., Kokhuis, T. J. A., et al. (2021). Corrigendum to "Viability of Endothelial Cells after Ultrasound-Mediated Sonoporation: Influence of Targeting, Oscillation, and Displacement of Microbubbles" [Journal of Controlled Release 238 (2016) 197-211]. *J. Control Release* 332, 502. doi:10.1016/j.jconrel.2021.03.011

Viscusi, E. R., Candiotti, K. A., Onel, E., Morren, M., and Ludbrook, G. L. (2012). The Pharmacokinetics and Pharmacodynamics of Liposome Bupivacaine Administered via a Single Epidural Injection to Healthy Volunteers. *Regional Anesth. Pain Med.* 37 (6), 616–622. doi:10.1097/AAP.0b013e318269d29e

Wang, J., Yao, C., Shen, B., Zhu, X., Li, Y., Shi, L., et al. (2019). Upconversion-Magnetic Carbon Sphere for Near Infrared Light-Triggered Bioimaging and Photothermal Therapy. *Theranostics* 9 (2), 608–619. doi:10.7150/thno.27952

Wang, L., Ren, C., Li, Y., Gao, C., Li, N., Li, H., et al. (2021). Remote Ischemic Conditioning Enhances Oxygen Supply to Ischemic Brain Tissue in a Mouse Model of Stroke: Role of Elevated 2,3-biphosphoglycerate in Erythrocytes. *J. Cereb. Blood Flow. Metab.* 41 (6), 1277–1290. doi:10.1177/0271678X20952264

Wang, Y., Wang, X., and Zhang, K. (2020). Effects of Transversus Abdominis Plane Block versus Quadratus Lumborum Block on Postoperative Analgesia: a Meta-Analysis of Randomized Controlled Trials. *BMC Anesthesiol.* 20 (1), 103. doi:10.1186/s12871-020-01000-2

Xia, D., He, H., Wang, Y., Wang, K., Zuo, H., Gu, H., et al. (2018). Ultrafast Glucose-Responsive, High Loading Capacity Erythrocyte to Self-Regulate the Release of Insulin. *Acta Biomater.* 69, 301–312. doi:10.1016/j.actbio.2018.01.029

Xia, D., Xu, P., Luo, X., Zhu, J., Gu, H., Huo, D., et al. (2019). Overcoming Hypoxia by Multistage Nanoparticle Delivery System to Inhibit Mitochondrial Respiration for Photodynamic Therapy. *Adv. Funct. Mat.* 29 (13), 1807294. doi:10.1002/adfm.201807294

Yao, J., Zhu, C., Peng, T., Ma, Q., and Gao, S. (2021). Injectable and Temperature-Sensitive Titanium Carbide-Loaded Hydrogel System for Photothermal Therapy of Breast Cancer. *Front. Bioeng. Biotechnol.* 9, 791891. doi:10.3389/fbioe.2021.791891

Conflict of Interest: The authors declare that the research was conducted in the absence of any commercial or financial relationships that could be construed as a potential conflict of interest.

Publisher's Note: All claims expressed in this article are solely those of the authors and do not necessarily represent those of their affiliated organizations, or those of the publisher, the editors and the reviewers. Any product that may be evaluated in this article, or claim that may be made by its manufacturer, is not guaranteed or endorsed by the publisher.

frontiers | Frontiers in Bioengineering and Biotechnology

ORIGINAL RESEARCH
published: 22 July 2022
doi: 10.3389/fbioe.2022.960501

Biodegradable Silk Fibroin Nanocarriers to Modulate Hypoxia Tumor Microenvironment Favoring Enhanced Chemotherapy

Li Bin[1], Yuxiao Yang[1], Feiyu Wang[1], Rong Wang[1], Hongxin Fei[1], Siliang Duan[1], Linling Huang[2], Na Liao[1], Shimei Zhao[2]* and Xinbo Ma[1]**

[1]Department of Biochemistry and Molecular Biology, Medical College, Guangxi University of Science and Technology, Liuzhou, China, [2]Second Clinical Medical College, Medical College, Guangxi University of Science and Technology, Liuzhou, China

Biopolymer silk fibroin (SF) is a great candidate for drug carriers characterized by its tunable biodegradability, and excellent biocompatibility properties. Recently, we have constructed SF-based nano-enabled drug delivery carriers, in which doxorubicin (Dox) and atovaquone (Ato) were encapsulated with Arg-Gly-Asp-SF-Polylactic Acid (RSA) to form micellar-like nanoparticles (RSA-Dox-Ato NPs). The RGD peptide was decorated on micellar-like nanoparticles, promoting tumor accumulation of the drug. Meanwhile, Ato, as a mitochondrial complex III inhibitor inhibiting mitochondrial respiration, would reverse the hypoxia microenvironment and enhance chemotherapy in the tumor. *In vitro*, the biopolymer alone showed extremely low cytotoxicity to 4T1 cell lines, while the RSA-Dox-Ato demonstrated a higher inhibition rate than other groups. Most significantly, the ROS levels in cells were obviously improved after being treated with RSA-Dox-Ato, indicating that the hypoxic microenvironment was alleviated. Eventually, SF-based targeted drug carrier provides biocompatibility to reverse hypoxia microenvironment *in vivo* for enhancing chemotherapy, strikingly suppressing tumor development, and thereby suggesting a promising candidate for drug delivery system.

Keywords: biocompatibility, hypoxia, chemotherapy, atovaquone, breast cancer

OPEN ACCESS

Edited by:
Donglin Xia,
Nantong University, China

Reviewed by:
Chao Zhang,
Southern Medical University, China
Swati Biswas,
Birla Institute of Technology and Science, India

****Correspondence:***
Na Liao
43283280@qq.com
Shimei Zhao
974791041@qq.com
Xinbo Ma
16869050@qq.com

Specialty section:
This article was submitted to Biomaterials, a section of the journal Frontiers in Bioengineering and Biotechnology

Received: *03 June 2022*
Accepted: *24 June 2022*
Published: *22 July 2022*

Citation:
Bin L, Yang Y, Wang F, Wang R, Fei H, Duan S, Huang L, Liao N, Zhao S and Ma X (2022) Biodegradable Silk Fibroin Nanocarriers to Modulate Hypoxia Tumor Microenvironment Favoring Enhanced Chemotherapy. Front. Bioeng. Biotechnol. 10:960501. doi: 10.3389/fbioe.2022.960501

INTRODUCTION

While the 5-year survival outcome in traditional antitumor modalities has clinical progress, the mortality in patients with advanced tumors remained undiminished owing to metastasis and recurrence (Zhang et al., 2016; Zhang et al., 2017; Zhang et al., 2018a; Zhang et al., 2020a; Cai et al., 2022). Hypoxic tumor microenvironment (TME) is gradually recognized as an essential factor in tumor progression, especially in multidrug resistance, radiosensitivity, immunologic escape, and metastasis (Jiang et al., 2020; Jin et al., 2021). According to previously described, the lower oxygen levels in locally advanced tumors (less than 2.5 mm Hg) compared with that in normal tissue (20–150 mm Hg) (Vaupel et al., 2007). Obviously, the difference is mainly caused by high oxygen consumption for tumor proliferation and abnormal angiogenesis in the hypoxic tumor, resulting imbalance in oxygen supply and depletion (Ye et al., 2018). Against this background, probing a robust TME-modulating nanocarrier as preludes for tumor combination therapies is extremely crucial.

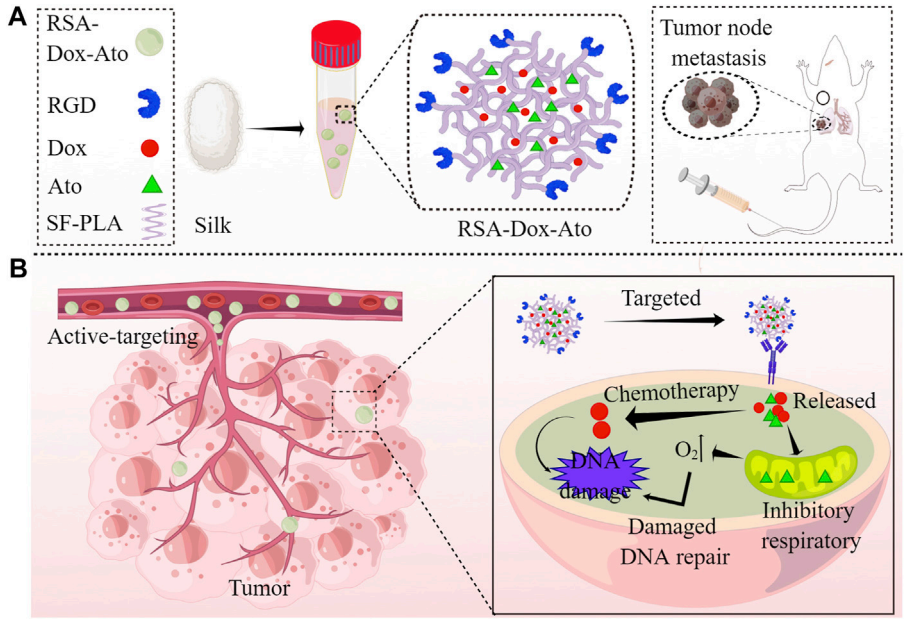

SCHEME 1 | Schematics demonstration the RSA-Dox-Ato alleviating tumor hypoxia and improving the antitumor efficacy (by Figdraw). **(A)** Scheme illustrating the synthesis of RSA-Dox-Ato NPs; **(B)** The mechanism of RSA-Dox-Ato NPs alleviate tumor hypoxia *in vivo*.

To reverse the oxygen imbalance, a series of therapeutic strategies have been proposed around the hypoxic tumor microenvironment for improving chemotherapy efficiency. For instance, oxygen-carrying and oxygen-generating with multifunctional nanodrug delivery systems were performed to overcome tumor hypoxia (Zhang et al., 2018b; Zhao et al., 2018; Zuo et al., 2018; Zhang et al., 2020b; Huang et al., 2020; Zhao et al., 2020). Such strategies may still have restricted therapeutic effects, especially toward unlimited proliferation of tumor cells with rapid oxygen consumption (Li et al., 2018; Wang et al., 2019; Li et al., 2020; Xia et al., 2020). Recently, the mitochondria-targeted metabolism strategy may be a promising treatment to inhibit proliferation and hypoxia in tumor. The mechanism of mitochondria-targeted strategy is inhibition of mitochondrial complex III in Krebs (TCA) cycle which deplete the oxygen to produce ATP for energy metabolism and the cell proliferation (Jeena et al., 2019; Frattaruolo et al., 2020). To date, atovaquone (Ato), known as an FDA-approved antimicrobial agent, competitively replaced the ubiquinol to occupy the active center of mitochondrial complex III, interrupting the respiratory chain in breast cancer cells (Xia et al., 2019; Cheng et al., 2020). In addition, mitochondria-targeted atovaquone increases tumor-infiltrating $CD4^+$ T cells in PD-1 blockade immunotherapy (Huang et al., 2022). However, circulation time, targeted effect, and hydrophilia featured in small molecular drugs have limited the clinical antitumor and therapeutic effect.

Silk fibroin (SF), a promising biomaterial that has attracted substantial attention, is a natural biopolymeric protein with good biocompatibility and drug-loading capability (Zhao et al., 2015; Hu et al., 2018; Mao et al., 2018). Under low pH conditions, doxorubicin-loaded silk nanoparticles readily release the payloads due to changes in surface properties (Seib et al., 2013; Xia et al., 2014; Montalbán et al., 2018). What's more, SF as a protein nanoparticle could be decomposed in the lysosome and rapidly eliminated by kidneys (Nguyen et al., 2019; Li et al., 2021). Compared with inorganic nano-delivery systems, the biodegradable SF nanocarriers have no long-term toxicity problems *in vivo* applications (Mathur and Gupta, 2010; Subia et al., 2015). In addition, TME-responsive SF-based nanocarriers with outcoming biocompatibility enable efficient therapeutics to realize the lysosomes targeting and escape (Tan et al., 2019; Zhang et al., 2020c; Yu et al., 2022). Considering off-target toxicity in normal tissues, nanocarrier was modified by an active targeting agent (RGD) to enhance the injected doses of drugs end up in tumor tissue. According to previously reports, RGD is a targeted small molecule peptide that specifically interacts with integrin αvβ3 overexpressed on tumor cells (Meyer et al., 2006; Subia et al., 2014; Mao et al., 2018; Bari et al., 2021). The surprising case of RGD decorated polymer-based nano-micelles encouraged us to investigate whether the SF-based nanocarriers decorated with RGD as multifunctional nanoplatforms enables low side-effect and efficacy in chemotherapy treatment.

Herein, we therefore custom-constructed SF-based biocompatible nanoplatform as a nano-enabled drug delivery system for targeting the tumor in a highly-efficient manner, realizing TME-responsive drug release to enhance chemotherapy by reversing hypoxia in the tumor (as shown in **Scheme 1A**). For this system, SF proteins were FDA-approved natural materials in medical applications with outstanding biodegradability under weakly acidic environments and

proteases. Therefore, payloads of silk nanoparticles would be dissociated to release Dox for enhanced chemotherapy upon encountering a lower pH environment. Meanwhile, the released atovaquone competitively banded to mitochondrial complex III, obstructing mitochondrial respiration and oxygen consumption to modulate hypoxia in the tumor (as shown in **Scheme 1B**). Therefore, this work focuses on the reversal of hypoxic tumor microenvironment by promising SF-based nano-systems to improve the chemotherapy efficacy, providing a new angle in fighting tumors.

MATERIALS AND METHODS

Materials

All reagents in this study were purchased from commercial suppliers without further purification. The paraformaldehyde (4%), sodium chloride (NaCl), disodium hydrogen phosphate (Na_2HPO_4), sodium dihydrogen phosphate (NaH_2PO_4), potassium chloride (KCl), potassium hydroxide (KOH) were purchased from Sigma-Aldrich (Shanghai, China). RPMI-1640 incomplete medium with 1% (v/v) penicillin-streptomycin, trypsin-EDTA digestion supplemented with 0.25% trypsin and 0.02% EDTA were purchased from KeyGen Biotech Co., Ltd., (Nanjing, China). The reactive oxygen level in tumor cells was observed by CM-H2DCFDA reagent kit under laser scanning confocal microscope. About 10% (v/v) serum (FBS) was supplemented in cell culture media (RPMI-1640). Dimethyl sulfoxide (DMSO) and thiazolyl blue (MTT) were obtained from Solarbio Technology Ltd (Beijing, China). Doxorubicin (DOX) was obtained from Titan technology Co. Ltd (Shanghai, China). The mitochondrial respiratory chain was competitively inhibited by atovaquone (Marck KGaA, Shanghai, China). Silk protein (SF) and SF-polylactic acid (SF-PLA) was bought from Hongxin Liyu Fine Chemical Ltd (Wuhan, Hubei, China). RGD peptide (The purity >90%) was purchased from PeptideValley (Nanjing, China). Hoechst 33,342 was obtained from Beyotime Biotechnology Ltd (Shanghai, China). The mouse-derived 4T1 cancer cells were incubated in RPMI-1640 complete media containing with 10% FBS, and obtained from Shanghai Institute of Cells (Shanghai, China). All-female BLAB/c mice (SPF, 5-weeks-old, weighing 16–19 g, Animal Certificate NO: SCXK (Beijing) 2019–0010) were purchased from SPF Biotechnology Co., Ltd., (Beijing, China), and housed under room temperature with the pathogen-free environment. All mice experiments were approved by the Institutional Animal Ethics Committees of Guangxi University of Science and Technology (Liuzhou, China). All experiments in this study were performed with deionized water (Persee, 18.2 MΩ cm-1).

Preparation of SF-Based Nanocarriers

SF-based nanocarriers were synthesized by the oil-in-water emulsion solvent diffusion method as described in previously reported (Qiao et al., 2015; Mao et al., 2018; Wei et al., 2021). Firstly, the EDC and NHS were successively added with RGD solution to activate the carboxyl group. The NH_2-SF-PLA (SA) was added to synthesize the RSA under pH 5.0 at room temperature. RSA was collected after freeze-drying and stored at 4°C. Then, the fabrication process includes dissolution, filtration, agitation, centrifugation, sonication, and lyophilization. For instance, 2.0 mg of doxorubicin (Dox) and 1.9 mg of atovaquone (Ato) were firstly dissolved using 5 ml of chloroform. The dissolved solution was then dropped into 25 ml of SF-based micelles (the concentration of SF-based micelles was 0.5 mg/ml in deionized water) at the speed of six drops/minute. Ultrasound continued for 25 min after the solution was added. The mixture was then dialyzed in deionized water. After lyophilization, the SA-Dox-Ato and RSA-Dox-Ato nano micelles were collected and saved at 4°C.

Characterization

To observe the RSA-Dox-Ato NPs, the morphology was visualized with a transmission electron microscope (HC-1, Hitachi, Japan). The UV-vis spectrophotometer UV-2600 (Shimadzu, Japan) was successfully performed to record the absorption spectra of Ato, Dox, RSA, and RSA-Dox-Ato. To investigate the release behavior under different pH environment, the RSA-Dox-Ato NPs were resuspended in PBS (1 ml) with pH 5.0 and pH 7.4, respectively. Then, the sediment of RSA-Dox-Ato NPs was collected at a fixed time after centrifugation, while the precipitate was redispersed with PBS under different pH conditions. Then, the absorbance of Ato and free Dox were respectively monitored by UV-vis spectrophotometer UV-2600 (SHIMADZU, Japan) at room temperature.

Cell Culture

The mouse breast cancer cells (4T1) were cultured for cytotoxicity studies *in vitro*. First, the 4T1 cells were cultured with a complete medium (prepared with 100 U/ml penicillin, 10% (v/v) fetal bovine serum (FBS), 100 μg/ml streptomycin, and RPMI-1640 incomplete medium) in a cell incubator (BPN-80CH, Blue Pard, Shanghai) at 37°C with 5% CO_2 under a humidified atmosphere. When the 4T1 cells reached 80% confluence, discarded the medium and washed all dishes with PBS (pH 7.4) three times. Then, the cells were digested with trypsin-EDTA under 37°C and collected in 15 ml sterile centrifugal tubes for subculturing in a fresh RPMI-1640 medium.

Cytotoxicity Assay

The MTT assay was employed to investigate the cytotoxicity of RSA-Dox-Ato for 4T1 cells *in vitro*. Firstly, 4T1 cells were seeded under standard protocol and subcultured in a multi-well plate with 100 μL of RPMI-1640 medium at a density of 5×10^3 cells/well. After 12 h, all groups were respectively treated with PBS, Dox, RSA-Dox, and RSA-DOX-Ato at different concentrations ($n = 3$) as an experimental procedure. Then, the time-dependence effect of cell viability was respectively evaluated within 12 and 24 h. Subsequently, the medium of all groups was removed and washed three times with PBS for 5 min, re-incubated with MTT solution (100 μL) at a concentration of 5 mg/ml for 4 h according to cytotoxicity protocol. All these processed 4T1 cells were incubated under a humidified environment at 37°C with 5% CO_2. Meanwhile, 150 μL of DMSO was applied to dissolve the

solid crystals following washed by PBS (pH 7.4) in each well. After that, the absorbance of samples in each well was reported using a microplate reader at 490 nm (Victor Nivo 3S, US). The cytotoxicity (%) of nanodrugs was evaluated and calculated as OD treatment/OD control × 100%.

Evaluation of Endocytosis

The receptor-mediated endocytosis in 4T1 cells of RSA-Dox-Ato NPs was assessed utilizing confocal laser scanning microscopy (CLSM, Nikon). The laser confocal dish was seeded with 5×10^4 cells per well and placed in a cell incubator (37°C, 5% CO_2) for 24 h. These tumor cells were seeded with RPMI-1640 medium contained 100 U/ml penicillin, 10% (v/v) serum (FBS), 100 μg/ml streptomycin. After 24 h incubation, RSA-Dox-Ato (500 μL, 100 μg/ml) and Dox (500 μL, 100 μg/ml) were respectively added and co-cultured with 4T1 cells at 37°C with 5% CO_2. Later, the supernatant of each dish was removed, and the 4T1 cells in each dish were washed three times with PBS. Subsequently, 4% paraformaldehyde (1 ml) in PBS (pH 7.4) was added to dishes to fixed tumor cells for 20 min. Then, triton X-100 (1 ml, 0.1% v/v) was employed to wash cells three times. Afterward, the cell nucleus was stained using Hoechst 33,342 (blue) in the dark field for 20 min. Finally, the cells were washed with PBS (pH 7.4) three times, and the fluorescence images were obtained by confocal microscopy.

The Oxygen Consumption Rate

The oxygen consumption rate (OCR) was detected as the previous methods (Diepart et al., 2012; Xia et al., 2019; Xia et al., 2020). Briefly, the 4T1 cells were seeded in a 12-well plate within 24 h at a cell concentration of about 3 × 104 cells/well. All cells in the 12-well plate were incubated with RPMI-1640 medium containing 100 U/ml penicillin, 10% (v/v) fetal bovine serum (FBS), and 100 μg/ml streptomycin. To test the oxygen concentration in the medium, all groups treated with nanodrugs were placed in the anaerobic environment with AnaeroPack system. Then, the oxygen concentration in the medium was continuously evaluated for 4 h at a multi-time-point using a dissolved oxygen instrument (Huihe intelligent Electronic Instrument Co., Ltd., China). The OCR level (%) was calculated after oxygen concentration normalized.

ROS Detection *In Vitro*

Inspired by the oxygen consumption under medium, the ROS in 4T1 cells treated with reactive oxygen species detection assay kit (CM-H2DCFDA) was furtherly observed under fluorescence microscopy. All operations follow the protocol. Rosup as a ROS activator was used to induce ROS production. Firstly, 4T1 cells with a density of 5×10^4 cells/well were incubated in a 12-well plate under complete RPMI 1640 medium at 37°C with 5% CO_2. DCFH-DA After an incubation of 24 h, all groups were respectively treated with RSA-Dox (500 μL, Dox concentration is 12.5 μg/ml) + Rosup (50 μg/ml) and RSA-Dox-Ato (500 μL, Dox concentration is 12.5 μg/ml) + Rosup (50 μg/ml) for 2 h. The control group was added with PBS in plate. The H2DCFDA was diluted in RPMI 1640 medium without serum and injected into chambers of the 12-well plate. After incubated for 15 min in a cell incubator (37°C, 5% CO_2), the culture media was respectively removed, and 4T1 cells were further added with PBS (pH 7.4) to wash the H2DCFDA. Then, the cells were co-stained with Hoechst 33,342 in the dark field for 15 min. Subsequently, 4T1 cells were fixed with 4% paraformaldehyde (1 ml) in PBS (pH 7.4) for 20 min. Finally, the cells were washed three times with PBS and observed with an inverted fluorescence microscope (IX73, OLYMPUS). The generated fluorescence was visualized under 495/529 nm and analyzed by ImageJ software.

Scratch Assay

In order to assess the influence of RSA-Dox-Ato in cell migration, the scratch assay as a direct and economical approach was adopted *in vitro*. In short, the cells were incubated into each well of a 6-well plate and co-incubated with RPMI 1640 medium with 100 U/ml penicillin, 10% FBS containing, and 100 μg/ml streptomycin. Afterward, the sterile pipette was used to wound the monolayer 4T1 cells, and the cell debris was removed by washing three times with PBS. Subsequently, all treatment groups were incubated with Dox (1 ml, Dox concentration is 5 μg/ml), RSA-Dox (1 ml, Dox concentration is 5 μg/ml) and RSA-Dox-Ato (1 ml, Dox concentration is 5 μg/ml), while the control group was injected with 1 ml of PBS (pH 7.4). After incubation for 24 h, the images of 4T1 cells were observed using an inverted microscope and analyzed by ImageJ software.

The 4T1 Tumor-Bearing Mice Models

About 5 weeks old healthy female Balb/c mice (About 20 g/mouse) were obtained and housed under pathogen-free conditions. After a week, the 4T1 tumor-bearing mice models were built by subcutaneous injection with 4T1 cells (5×10^6 cells/mouse, 100 μL) into the right forelimb. Then, the tumor volume on mouse was monitored and measured by a vernier caliper after 6 days. Meantime, the tumor volumes were calculated as length × width2 × 1/2. Then, the 4T1 tumor-bearing mice models were divided randomly after the tumor volume reached about 100 mm^3.

Antitumor Efficacy *In Vivo*

The 4T1 tumor-bearing mice models were divided randomly into the following five groups, including the PBS group, RSA group, Dox group, RSA-Dox, and RSA-Dox-Ato. The treatment groups were injected intravenously with RSA, Dox, RSA-Dox, and RSA-Dox-Ato, while the PBS group as control was treated with PBS every other day. Meanwhile, the tumor-volume change and mouse weight were recorded to assess the therapeutic effects. Finally, all treated mice were weighted and humanely sacrificed, and tumors were collected to assess the inhibition effect. In addition, the major organs were isolated and saved in 4% paraformaldehyde for further histopathology experiments.

Inhibition of Metastasis

To further investigate tumor metastasis, the xenograft-bearing mice were treated with nanodrugs *in vivo*. The lungs in mice were collected and washed three times in PBS. The metastasis nodules in the lung were counted and calculated to analyze the

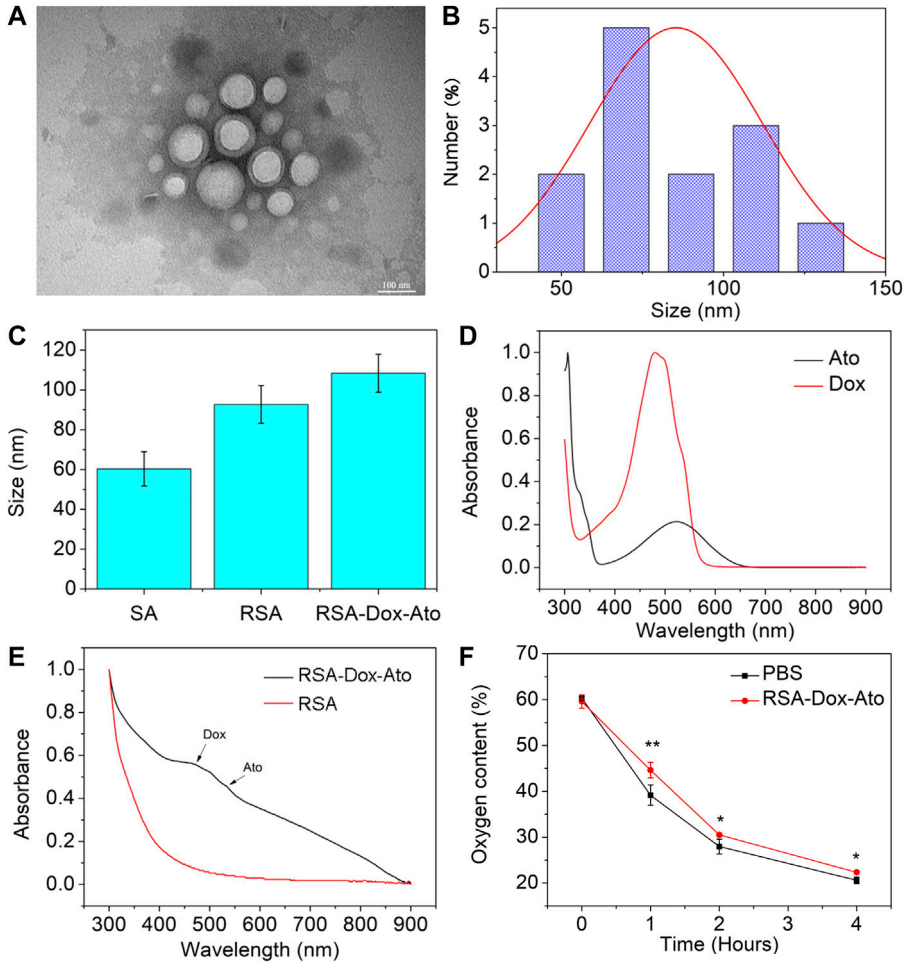

FIGURE 1 | Characterization of SF-based nanoparticles. **(A)** TEM images of the RSA-Dox-Ato NPs. **(B)** The size distribution of the RSA-Dox-Ato NPs; **(C)** The mean hydrodynamic diameter distribution of RSA NPs (92.67 ± 9.50 nm) and RSA-Dox-Ato NPs (114.67 ± 14.29 nm); **(D)** UV-vis spectra of Ato and Dox; **(E)** UV-vis spectra of RSA-Dox-Ato NPs and SA NPs; **(F)** Oxygen concentration in the cell medium after treatment with and without Ato under an anaerobic environment.

suppression efficiency of nanodrugs. Afterward, the lungs were obtained from mice and fixed in 4% (w/v) paraformaldehyde solution for metastasis evaluation in histopathology.

Histopathology Analysis

The major organs (heart, liver, spleen, lung, and kidney) and tumors from the treated mice in the antitumor experiment were collected and were fixed in 4% paraformaldehyde solution, followed by paraffin embedding. After that, the tumors and the major organs were co-stained for immunohistochemical analyses. All of the sections from mice were collected and imaged by an inverted microscope for histopathology analysis.

Statistical Analysis

All statistical analyses were conducted with a t-test in Excel with no outliers (two-sided tests). All data in pictures were presented as means ± standard deviation ($n > 2$, $^*p < 0.05$, which represented the significant differences).

RESULTS

Characterization of the RSA-Dox-Ato Nano-Micelles

According to the previous reports, SF-based nano-carries were fabricated utilizing the oil-in-water emulsion solvent diffusion method (Qiao et al., 2015; Mao et al., 2018; Wei et al., 2021). The Dox and Ato were firstly enveloped with RGD-SF-PLA (RSA) amphiphilic polymers (as shown in **Scheme 1**). Then, the synthesized RSA-Dox-Ato nano-micelles were furtherly characterized using a TEM micrograph. The nanoparticles of RSA-Dox-Ato had a uniformly dispersed spherical morphology, as indicated in the TEM micrograph illustrated in **Figure 1A**. The mean diameters were 85.38 ± 26.75 nm, as displayed in **Figure 1B**, indicating an excellent blood circulation time for Dox and Ato *in vivo*. In **Figure 1C**, the mean hydrodynamic diameter of RSA NPs was 92.67 ± 9.50 nm, which was investigated utilizing dynamic light scattering. For RSA-Dox-

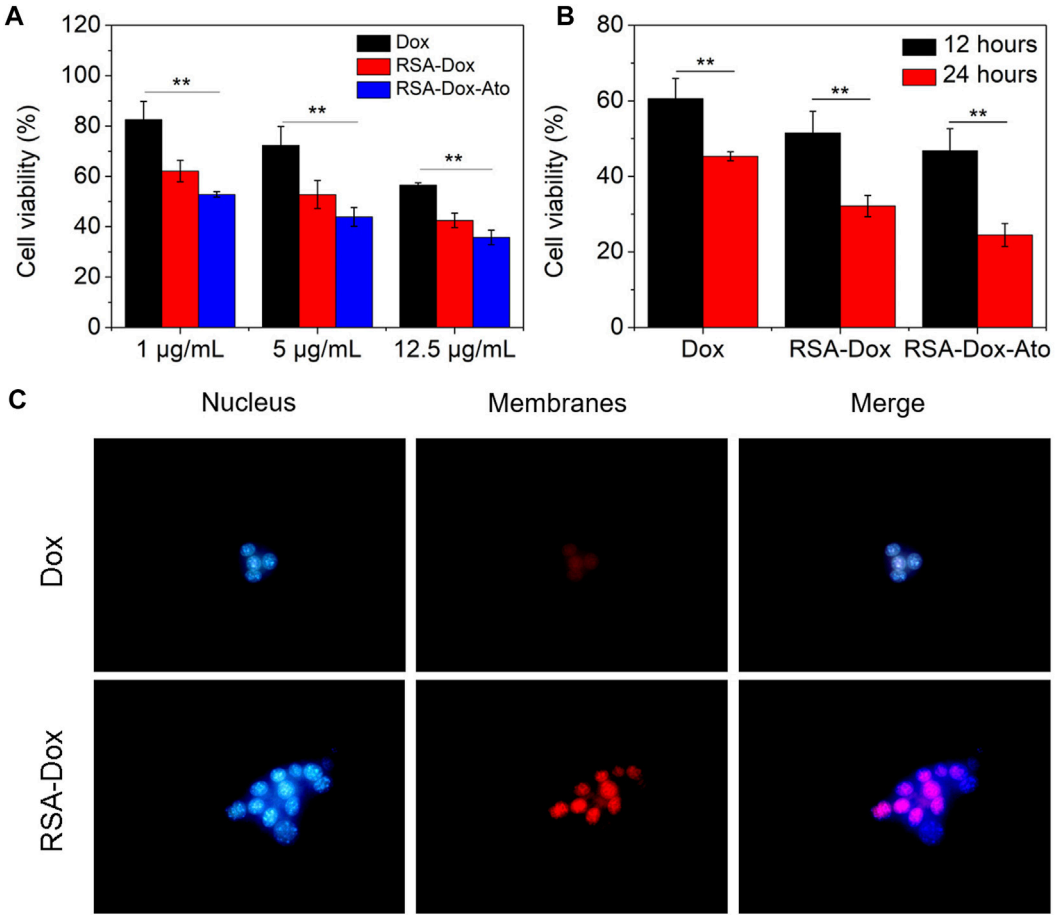

FIGURE 2 | The cell cytotoxicity and endocytosis were evaluated *in vitro*. **(A)** The cell cytotoxicity of 4T1 cells in a dose-dependent manner was recorded by MTT assay *in vitro* (Dox, RSA-Dox, RSA-Dox-Ato). **(B)** The cell cytotoxicity of 4T1 cells in a time-dependent manner was recorded by MTT assay *in vitro* (Dox, RSA-Dox, RSA-Dox-Ato). **(C)** The endocytosis of 4T1 cells was observed by microscope with a ×40 objective *in vitro*. ($n = 5$, $*p < 0.05$, $**p < 0.01$).

Ato NPs, the mean hydrodynamic diameter was detected to be 114.67 ± 14.29 nm, which was higher than that of RSA NPs. The mean hydrodynamic diameter of RSA-Dox-Ato NPs had no obvious changes for 6 days, preliminary indicating the stability under room temperature (as shown in **Supplementary Figure S1**). The zeta potential of the RSA NPs was -24.73 ± 1.98 mV (as shown in **Supplementary Figure S2**). To further evaluate the RSA-Dox-Ato NPs, the absorption spectra of Dox and Ato presented, respectively, strong unimodal pink at 480 and 524 nm, as depicted in **Figure 1D**. After synthesizing nanomicelles, two absorption peaks were observed with the RSA-Dox-Ato NPs, which correspond to the Dox and Ato spectrograms, as shown in **Figure 1E**. According to the pioneering reports, the silk protein-based nanocarriers were observed with excellent drug release behavior under an acidic environment. Notably, the acidic microenvironment appeared in the most tumors due to alter tumor vascularization and insufficient oxygen supply for glucose metabolism. Triggered and controlled SF-based nanomicelles release system was an essential factor for nanomedicine. Therefore, the release behavior of SF-based nanoparticles was evaluated under different pH conditions. As illustrated in **Supplementary Figure S3**, the release ratio of Dox under an acidic environment was higher than that in a slightly alkaline environment (pH 7.4), evidencing a pH-dependent release behavior. As the Ato serves as a mitochondrial inhibitor, we envisioned that hypoxia in the tumor environment could be alleviated to enhance the chemotherapy. To this end, the oxygen consumption rate (OCR) in the medium was monitored utilizing a dissolved oxygen instrument under an anaerobic environment with AnaeroPack system. As shown in **Figure 1F**, the treatment group with Ato revealed a higher mean dissolved oxygen concentration in medium (44.63 ± 1.69%) than the PBS group (39.17 ± 2.23%) within 1 h, indicating inhibition of the oxygen consumption in mitochondrial could be conducive to hypoxia alleviation.

Cytotoxicity *In Vitro*

To evaluate the cytotoxicity of Dox and Ato released by the prepared nanoparticles on 4T1 cells. The SF drug-loaded nanoparticles were incubated with 4T1 cancer cells for 12 h or 24 h with different concentrations, and cell viability was

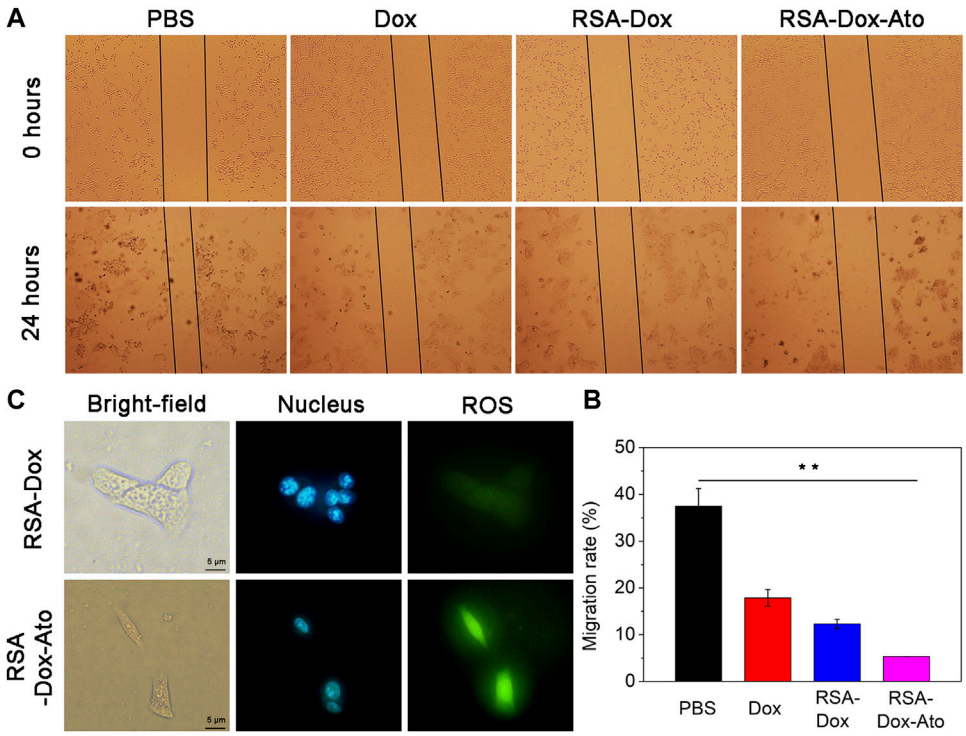

FIGURE 3 | The effects of SF-based nanomicelles on cell migration and hypoxia. **(A)** The effects of drugs on cell migration in 4T1 cells after treatment within 0 hour and 24 hours (all cells were observed by microscope with a 4× objective); **(B)** The migration rate was calculated after various therapies; **(C)** The images of SF-based NPs against 4T1 cells hypoxia after various treatments.

measured by MTT assay. As indicated in **Figure 2A** and **Figure 2B**, the cell viability of 4T1 cells was gradually decreased after treatment with nanodrugs under 37°C (5% CO_2), indicating a dose-dependent relationship. **Figure 2A** shows that when cells were treated with a concentration drug of 1 μg/ml for 12 h, the cell survival rate was 82.6% in the Dox group, 62.1% in the RSA-Dox group, and 59.9% in the RSA-Dox-Ato group, and there was a significant difference. The results revealed that SF-based nanocarriers with RGD could enhance drug concentration in cells, and Ato could contribute to improved toxicity. What's more, the cell viability demonstrated a time-dependent manner after treatment with nanodrugs at different times. As shown in **Figure 2B**, groups treated respectively with varying drugs for 24 h, including Dox, RSA-Dox, and RSA-Dox-Ato, displayed a higher antitumor effect than that in 12 h. Meanwhiles, the survival rate of 4T1 cells with high concentration drug treatment within 24 h, could be seen that the RSA-Dox group had a higher inhibition rate than the Dox group at the same concentration, regardless of whether the drug was treated within 12 h or 24 h. The increased inhibition efficacy of RSA-Dox was observed due to the RGD plays a better targeting ability to enable Dox enrichment in cells. It was worth noting that the RSA-Dox-Ato group exhibited the lowest cell viability than other treatment groups, even at a low concentration of 1 μg/ml, implying the outstanding antitumor efficacy of SF-based nanocarriers.

The Evaluation of Endocytosis

Considering the internalization as a major biological barrier, the targeting strategy of RGD modified with SF-based nanocarriers was furtherly evaluated to improve endocytosis. To confirm the hypothesis, 4T1 cells were firstly treated with RSA-Dox and free Dox, then stained with Hoechst 33,342 and photographed. As depicted in **Figure 2C**, the RSA-Dox NPs group had stronger fluorescence than those in the DOX group, demonstrating that RGD modified SF-based nanocarrier contributed to Dox internalization by 4T1 cells. Therefore, SF-based drug-loaded nanoparticles modified with RGD enabled drugs to specifically bind with tumor cells, realizing targeted drug aggregation in tumors and off-target toxicity reduction.

The Wound Healing Assays

Given the inhibition of nanodrugs loaded-Dox for tumor cells in previous reporters, the scratch assays, as an economical and easy processing method, were carried out to evaluate further the cell migration. In this study, the healing of scratch in cell plates by treating SF-based nanocarriers with the same concentration of Dox was observed and imaged. As shown in **Figures 3A,B**, the wound area of the PBS group without nano-drug treatment was narrowest, indicating that 4T1 cells had the fastest wound healing within 24 h. While wound healing of the 4T1 cells treated with Dox and silk fibroin nanodrugs was slower. It was worth noting that 4T1 cells were treated with RSA-Dox-Ato, resulting the extremely slow speed of wound healing after 24 h. That was to say, the RSA nanocarriers were capable of inhibiting tumor migration *in vitro*.

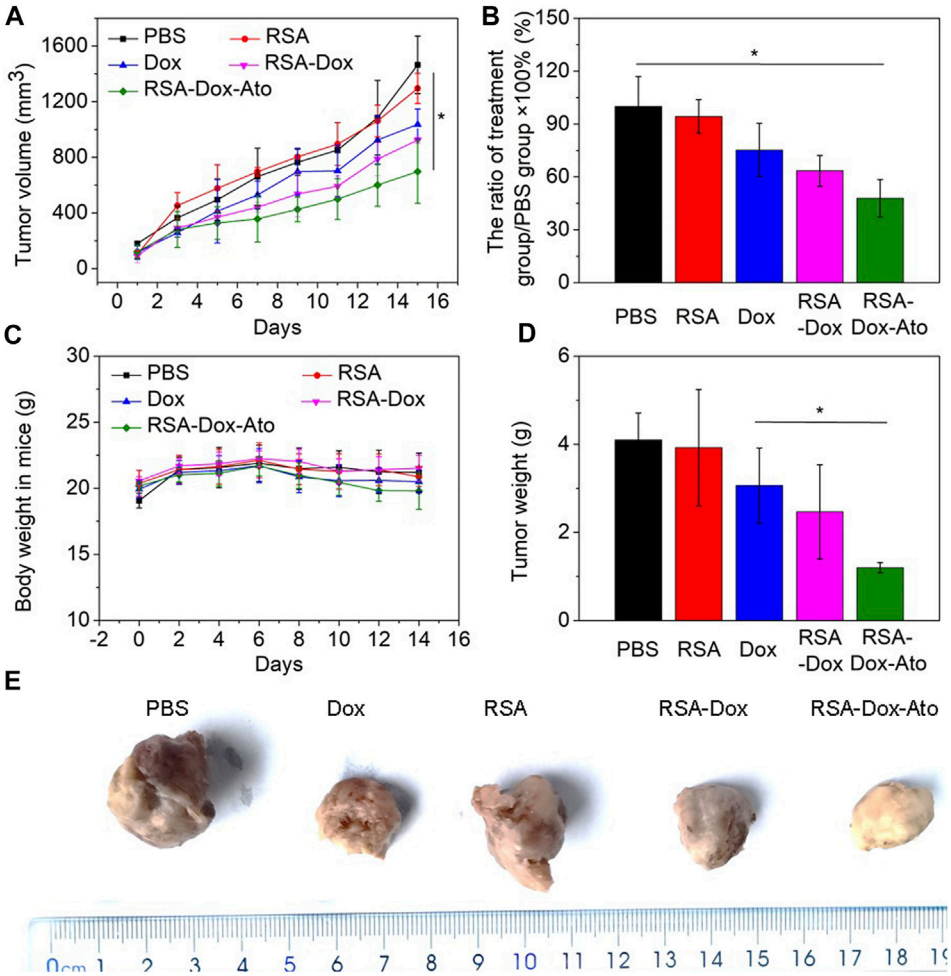

FIGURE 4 | The behavior of RSA-Dox-Ato NPs post-i.v. injection *in vivo*. **(A)** The tumor volume growth curves of 4T1 tumor-bearing mice injected with nanodrugs for 14 days. The data were represented as the mean ± SD ($n = 5$, $*p < 0.05$, $**p < 0.01$); **(B)** The tumor growth inhibition ratio of each group; **(C)** The body weight curve of 4T1 tumor-bearing mice upon the period of treatment; **(D)** The tumor weight curve of 4T1 tumor-bearing mice upon the period of treatment; **(E)** Representative photos of tumor-bearing mice from different treatment groups at the end of the study.

Intracellular ROS Detection

ROS levels with appropriate improvement often favor cell proliferation, whereas an excessive number of ROS inhibit cell viability. Tumor cells lack oxygen owing to proliferation too fast, leading to large amounts of ROS intracellular production, so it is prone to trigger oxidative stress response leading to cell damage and apoptosis (Mirzaei et al., 2021). Recently, it has been reported that Ato alleviated tumor hypoxia by intervening in the function of mitochondrial complex III and increasing the level of intracellular ROS (Zhao et al., 2020). Consequently, we prepared RGD modified SF-based nanoparticles enveloped with Ato to evaluate the hypoxia *in vitro*. Encouraged by the surprising OCR in the RSA-Dox-Ato treatment group, its triggered ROS level was visually monitored by using reactive oxygen species (ROS) analysis kit. ROS production was indicated as green fluorescence (490/525 nm), and the cell nucleus was marked with blue fluorescence (Hoechst 33,342). In addition, the Rosup was an induced agent to activate ROS *in vitro*. As shown in **Figure 3C**, under a fluorescence microscope, stronger blue and green fluorescence were observed in RSA-Dox-Ato + Rosup group. In contrast, the RSA-DOX + Rosup group had weaker fluorescence. The fluorescence intensity of the RSA-Dox-Ato + Rosup group was higher than that of the other groups, as shown in **Figure 3C** and **Supplementary Figure S4**. These results demonstrated that Ato enabled the mitochondrial respiratory to inhibit for alleviating tumor hypoxia, which is consistent with previous investigations (as seen in **Figure 1F**). Collectively, RSA-Dox-Ato NPs prepared in this experiment could reduce oxygen consumption by inhibiting the function of mitochondrial complex, further improving ROS level for alleviating tumor hypoxia, which is helpful against tumor chemotherapy.

Antitumor Effect *In Vivo*

Encouraged by the satisfactory therapeutic effect *in vitro*, RSA nanoparticles had a very high probability of achieving effective

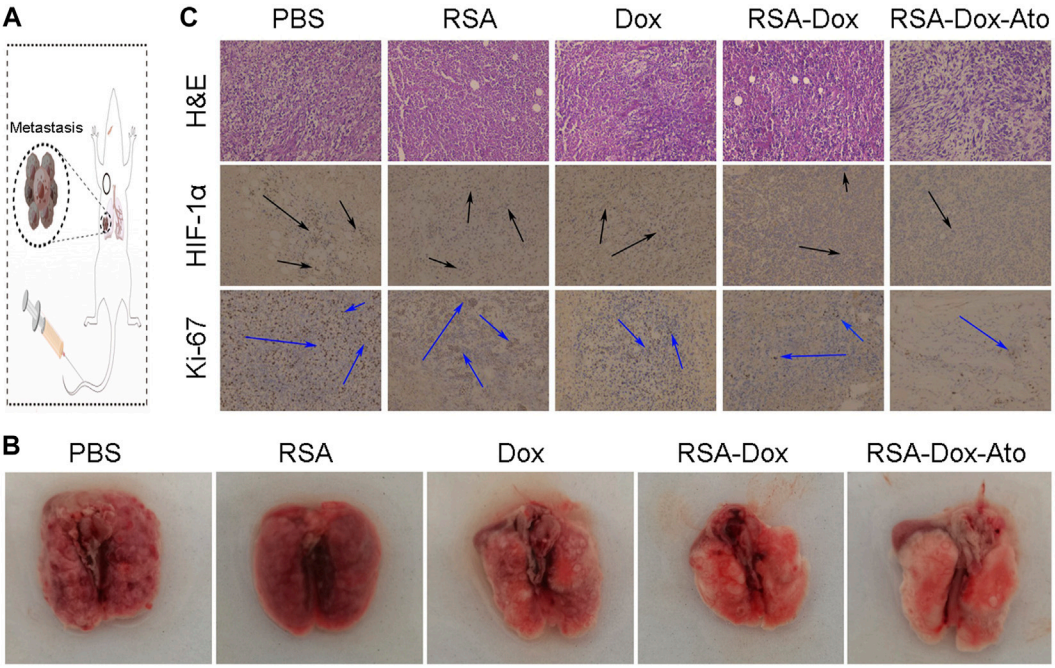

FIGURE 5 | The pathological analysis and lung metastasis of mice received RSA-Dox- Ato NPs with the intravenous injection ($n = 3$). **(A)** Scheme of RSA-Dox-Ato NPs against tumors. **(B)** Representative images of tumor metastasis were collected from mice after treatments with RSA-Dox-Ato NPs. **(C)** The pathological sections were analyzed by unitizing H &E staining, HIF-1α, and Ki-67 (×10 objective).

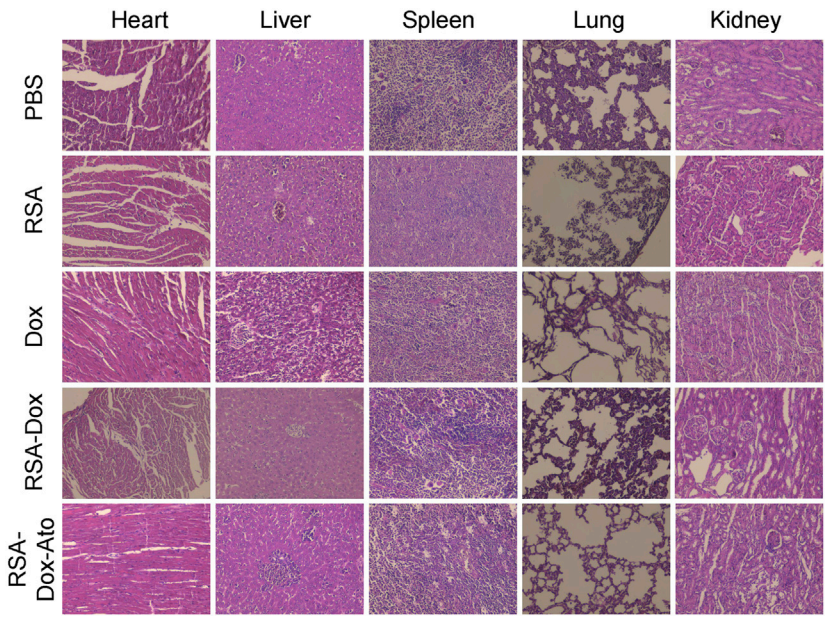

FIGURE 6 | The primary safety was evaluated by H&E staining of major organs from treatment mice (×10 objective).

cancer treatment for breast cancer. In order to verify the remarkable anti-tumor effect of RSA nanodrugs, further 4T1 tumor-bearing mice were prepared to investigate the behavior of RSA-Dox-Ato *in vivo*. As shown in **Figure 4A**, the mice were injected with PBS as the control group, and other mice treated intravenously with the Dox, RSA NPs, RSA-Dox

NPs, and RSA-Dox-Ato NPs, respectively. The RSA-Dox group exhibited a retarded tumor development within 14 days, compared with PBS and RSA groups. Importantly, it was confirmed by the significant inhibition ratio for the tumor volume in the RSA-Dox-Ato NPs treated mice when compared to the other treatment groups, indicating the RSA-Dox-Ato contributed to retard tumor development as a promising drug delivery system (as seen in **Figure 4A** and **Figure 4B**). By monitoring the weight of mice within the treatment period, it was found that the weight change of the mice treated with nanodrugs was unobvious (**Figure 4C**). Meanwhile, the tumors were weighted for evidencing the inhibition of RSA-Dox-Ato NPs as shown in **Figure 4D**. Then, the mice were dissected, and the tumors were harvested and fixed in 4% (w/v) paraformaldehyde solution (as displayed in **Figure 4E**). There was a significant suppression for the tumor weight of treatment groups in comparison with the control group, indicating the excellent antitumor efficacy of the SF-based nanocarriers. As a result, the inhibition tendency of tumor weight was consistent with **Figure 4A**.

Alleviation of Tumor Hypoxia and the Inhibition of Lung Metastasis

Dox, as an inducer of immunogenic cell death ICD, activated the immune system by abscopal effect to inhibit tumor metastasis. Enhanced chemotherapy of RSA-Dox-Ato NPs were enable Dox to enhance ICD occurrence *in vivo*, which was beneficial to inhibit tumor metastasis. As a proof-of-concept, the metastasis inhibition of 4T1 tumor-bearing mice was investigated by injected intravenously with RSA-Dox-Ato NPs. As exhibited in **Figures 5A,B**, there were the most significant lung metastases in the PBS group than the other groups. It was noted that the RSA-Dox-Ato group had the least lung metastasis, indicating that SF-based nanocarriers loaded with Dox and Ato had a better inhibition effect on tumor metastasis. Given the outstanding therapeutic efficacy of RSA-Dox-Ato NPs compared with other treatment mice, tumor hypoxia as an important factor was evaluated *in vivo*. When an imbalance between oxygen supply and consumption, the hypoxia-inducible factor 1α (HIF-1α) was often induced to overexpress in the tumor cell. Based on this, the hypoxia-inducible factor 1α (HIF-1α) in the tumor section was stained with an immunohistochemical method to carried out for evaluation of tumor hypoxia *in vivo*. Compared to other treatment groups, the expression of HIF-1α in the RSA-Dox-Ato group was significantly lower (as exhibited in **Figure 5C**). Furtherly, all samples from 4T1 tumor-bearing mice after *in vivo* treatment with SF-based nanocarriers were evaluated utilizing pathological analysis. As shown in **Figure 5C**, the tumor sections stained with hematoxylin and eosin (H&E) from the RSA-Dox-Ato group showed obvious necrotic areas, while no significant damage was observed in the PBS group. From the result of the Ki-67 stained, the RSA-Dox-Ato group revealed the most negligible proliferation factor than that in other groups. Together with H&E staining analysis, the relief of hypoxia (HIF-1α), and low levels of proliferation marker Ki-67, the RSA-Dox-Ato NPs had excellent behavior *in vivo*.

The Evaluation of Safety *In Vivo*

Silk fibroin, as drug delivery materials, was often applied in the clinic owing to its excellent biocompatibility and biodegradability. Therefore, the primary safety assessment was employed using H&E staining of major organs from mice, as indicated in **Figure 6**. Compared with the PBS group, there were ignorable changes in heart, liver, spleen, lung, and kidney in the RSA-Dox-Ato group, indicating that the RSA-Dox-Ato had better biocompatibility as a promising value for antitumor application in the future.

DISCUSSION

In summary, the RGD modified SF-based nanocarriers were successfully custom-designed, which could suppress mitochondrial respiration to alleviate the hypoxia microenvironment. This versatile platform played a significant role in drug delivery and active targeting to improve antitumor efficacy. Significantly, the tumor hypoxia microenvironment had been alleviated by biodegradable SF-based nanomicelles, eventually rendering systematic chemotherapy against tumor metastasis. As expected, RGD modified SF-based nanomicelles as a biodegradable drug delivery platform inhibited primary tumor and metastasis, lighting up an alternative biomaterial in clinical application.

DATA AVAILABILITY STATEMENT

The original contributions presented in the study are included in the article/**Supplementary Material**, further inquiries can be directed to the corresponding authors.

ETHICS STATEMENT

The animal study was reviewed and approved by the Institutional Animal Ethics Committees of Guangxi University of Science and Technology.

AUTHOR CONTRIBUTIONS

All authors listed have made a substantial, direct, and intellectual contribution to the work and approved it for publication.

FUNDING

This work was supported in part by Basic Ability Improvement Project for Young and Middle-Aged Teachers in Guangxi Province (2021KY0351); in part by Doctoral Research Start-up Fund of Guangxi University of Science and Technology (Xiaokebo21Z31); in part by Guangxi Science and Technology Bases and Talents

(AD21238014); in part by the National Natural Science Foundation of China (No. 82003250); in part by the Self-funded Scientific Research Project of Guangxi Health Commission (Z20190607); in part by Liuzhou Science and Technology Plan Project (2020PAAA0605).

REFERENCES

Bari, E., Serra, M., Paolillo, M., Bernardi, E., Tengattini, S., Piccinini, F., et al. (2021). Silk Fibroin Nanoparticle Functionalization with Arg-Gly-Asp Cyclopentapeptide Promotes Active Targeting for Tumor Site-specific Delivery. *Cancers* 13, 1185. doi:10.3390/cancers13051185

Cai, Y. W., Shao, Z. M., and Yu, K. D. (2022). De-escalation of Five-Year Adjuvant Endocrine Therapy in Patients with Estrogen Receptor-low Positive (Immunohistochemistry Staining 1%-10%) Breast Cancer: Propensity-matched Analysis from a Prospectively Maintained Cohort. *Cancer-Am. Cancer Soc.* 128, 1748–1756. doi:10.1002/cncr.34155

Cheng, G., Hardy, M., Topchyan, P., Zander, R., Volberding, P., Cui, W., et al. (2020). Potent Inhibition of Tumour Cell Proliferation and Immunoregulatory Function by Mitochondria-Targeted Atovaquone. *Sci. Rep.* 10, 17872–17914. doi:10.1038/s41598-020-74808-0

Diepart, C., Karroum, O., Magat, J., Feron, O., Verrax, J., Calderon, P. B., et al. (2012). Arsenic Trioxide Treatment Decreases the Oxygen Consumption Rate of Tumor Cells and Radiosensitizes Solid Tumors. *Cancer Res.* 72, 482–490. doi:10.1158/0008-5472.can-11-1755

Frattaruolo, L., Brindisi, M., Curcio, R., Marra, F., Dolce, V., and Cappello, A. R. (2020). Targeting the Mitochondrial Metabolic Network: A Promising Strategy in Cancer Treatment. *Ijms* 21, 6014. doi:10.3390/ijms21176014

Hu, D., Li, T., Xu, Z., Liu, D., Yang, M., and Zhu, L. (2018). Self-stabilized Silk Sericin-Based Nanoparticles: *In Vivo* Biocompatibility and Reduced Doxorubicin-Induced Toxicity. *Acta Biomater.* 74, 385–396. doi:10.1016/j.actbio.2018.05.024

Huang, H., Zhang, C., Wang, X., Shao, J., Chen, C., Li, H., et al. (2020). Overcoming Hypoxia-Restrained Radiotherapy Using an Erythrocyte-Inspired and Glucose-Activatable Platform. *Nano Lett.* 20, 4211–4219. doi:10.1021/acs.nanolett.0c00650

Huang, M., Xiong, D., Pan, J., Zhang, Q., Wang, Y., Myers, C. R., et al. (2022). Prevention of Tumor Growth and Dissemination by *In Situ* Vaccination with Mitochondria-Targeted Atovaquone. *Adv. Sci.* 9, 2101267. doi:10.1002/advs.202101267

Jeena, M. T., Kim, S., Jin, S., and Ryu, J.-H. (2019). Recent Progress in Mitochondria-Targeted Drug and Drug-free Agents for Cancer Therapy. *Cancers* 12, 4. doi:10.3390/cancers12010004

Jiang, W., Han, X., Zhang, T., Xie, D., Zhang, H., and Hu, Y. (2020). An Oxygen Self-Evolving, Multistage Delivery System for Deeply Located Hypoxic Tumor Treatment. *Adv. Healthc. Mat.* 9, 1901303. doi:10.1002/adhm.201901303

Jin, Z., Zhao, Q., Yuan, S., Jiang, W., and Hu, Y. (2021). Strategies of Alleviating Tumor Hypoxia and Enhancing Tumor Therapeutic Effect by Macromolecular Nanomaterials. *Macromol. Biosci.* 21, 2100092. doi:10.1002/mabi.202100092

Li, C., Zheng, X., Chen, W., Ji, S., Yuan, Y., and Jiang, X. (2020). Tumor Microenvironment-Regulated and Reported Nanoparticles for Overcoming the Self-Confinement of Multiple Photodynamic Therapy. *Nano Lett.* 20, 6526–6534. doi:10.1021/acs.nanolett.0c02272

Li, J., Khalid, A., Verma, R., Abraham, A., Qazi, F., Dong, X., et al. (2021). Silk Fibroin Coated Magnesium Oxide Nanospheres: A Biocompatible and Biodegradable Tool for Noninvasive Bioimaging Applications. *Nanomaterials* 11, 695. doi:10.3390/nano11030695

Li, X., Kwon, N., Guo, T., Liu, Z., and Yoon, J. (2018). Innovative Strategies for Hypoxic-Tumor Photodynamic Therapy. *Angew. Chem. Int. Ed.* 57, 11522–11531. doi:10.1002/anie.201805138

Mao, B., Liu, C., Zheng, W., Li, X., Ge, R., Shen, H., et al. (2018). Cyclic cRGDfk peptide and chlorin e6 functionalized silk fibroin nanoparticles for targeted drug delivery and photodynamic therapy. *Biomaterials* 161, 306–320. doi:10.1016/j.biomaterials.2018.01.045

SUPPLEMENTARY MATERIAL

The Supplementary Material for this article can be found online at: https://www.frontiersin.org/articles/10.3389/fbioe.2022.960501/full#supplementary-material

Mathur, A. B., and Gupta, V. (2010). Silk Fibroin-Derived Nanoparticles for Biomedical Applications. *Nanomedicine* 5, 807–820. doi:10.2217/nnm.10.51

Meyer, A., Auernheimer, J., Modlinger, A., and Kessler, H. (2006). Targeting RGD Recognizing Integrins: Drug Development, Biomaterial Research, Tumor Imaging and Targeting. *Cpd* 12, 2723–2747. doi:10.2174/138161206777947740

Mirzaei, S., Hushmandi, K., Zabolian, A., Saleki, H., Torabi, S. M. R., Ranjbar, A., et al. (2021). Elucidating Role of Reactive Oxygen Species (ROS) in Cisplatin Chemotherapy: a Focus on Molecular Pathways and Possible Therapeutic Strategies. *Molecules* 26, 2382. doi:10.3390/molecules26082382

Montalbán, M., Coburn, J., Lozano-Pérez, A., Cenis, J., Víllora, G., and Kaplan, D. (2018). Production of Curcumin-Loaded Silk Fibroin Nanoparticles for Cancer Therapy. *Nanomaterials* 8, 126. doi:10.3390/nano8020126

Nguyen, T. P., Nguyen, Q. V., Nguyen, V.-H., Le, T.-H., Huynh, V. Q. N., Vo, D.-V. N., et al. (2019). Silk Fibroin-Based Biomaterials for Biomedical Applications: a Review. *Polymers* 11, 1933. doi:10.3390/polym11121933

Qiao, X., Wang, L., Shao, Z., Sun, K., and Miller, R. (2015). Stability and Rheological Behaviors of Different Oil/water Emulsions Stabilized by Natural Silk Fibroin. *Colloids Surfaces A Physicochem. Eng. Aspects* 475, 84–93. doi:10.1016/j.colsurfa.2015.01.094

Seib, F. P., Jones, G. T., Rnjak-Kovacina, J., Lin, Y., and Kaplan, D. L. (2013). pH-Dependent Anticancer Drug Release from Silk Nanoparticles. *Adv. Healthc. Mater.* 2, 1606–1611. doi:10.1002/adhm.201300034

Subia, B., Chandra, S., Talukdar, S., and Kundu, S. C. (2014). Folate Conjugated Silk Fibroin Nanocarriers for Targeted Drug Delivery. *Integr. Biol.* 6, 203–214. doi:10.1039/c3ib40184g

Subia, B., Dey, T., Sharma, S., and Kundu, S. C. (2015). Target Specific Delivery of Anticancer Drug in Silk Fibroin Based 3D Distribution Model of Bone-Breast Cancer Cells. *ACS Appl. Mat. Interfaces* 7, 2269–2279. doi:10.1021/am506094c

Tan, M., Liu, W., Liu, F., Zhang, W., Gao, H., Cheng, J., et al. (2019). Silk Fibroin-Coated Nanoagents for Acidic Lysosome Targeting by a Functional Preservation Strategy in Cancer Chemotherapy. *Theranostics* 9, 961–973. doi:10.7150/thno.30765

Vaupel, P., Höckel, M., and Mayer, A. (2007). Detection and Characterization of Tumor Hypoxia Using pO2 Histography. *Antioxidants Redox Signal.* 9, 1221–1236. doi:10.1089/ars.2007.1628

Wang, D., Wu, H., Lim, W. Q., Phua, S. Z. F., Xu, P., Chen, Q., et al. (2019). A Mesoporous Nanoenzyme Derived from Metal-Organic Frameworks with Endogenous Oxygen Generation to Alleviate Tumor Hypoxia for Significantly Enhanced Photodynamic Therapy. *Adv. Mat.* 31, 1901893. doi:10.1002/adma.201901893

Wei, J., Sun, X.-Q., and Hou, B.-X. (2021). Evaluation of Silk Fibroin-RGD-Stem Cell Factor Scaffold Effect on Adhesion, Migration, and Proliferation of Stem Cells of Apical Papilla. *Stem Cells Int.* 2021, 1–10. doi:10.1155/2021/6612324

Xia, D., Hang, D., Li, Y., Jiang, W., Zhu, J., Ding, Y., et al. (2020). Au-Hemoglobin Loaded Platelet Alleviating Tumor Hypoxia and Enhancing the Radiotherapy Effect with Low-Dose X-Ray. *ACS Nano* 14, 15654–15668. doi:10.1021/acsnano.0c06541

Xia, D., Xu, P., Luo, X., Zhu, J., Gu, H., Huo, D., et al. (2019). Overcoming Hypoxia by Multistage Nanoparticle Delivery System to Inhibit Mitochondrial Respiration for Photodynamic Therapy. *Adv. Funct. Mat.* 29, 1807294. doi:10.1002/adfm.201807294

Xia, X.-X., Wang, M., Lin, Y., Xu, Q., and Kaplan, D. L. (2014). Hydrophobic Drug-Triggered Self-Assembly of Nanoparticles from Silk-elastin-like Protein Polymers for Drug Delivery. *Biomacromolecules* 15, 908–914. doi:10.1021/bm4017594

Ye, I. C., Fertig, E. J., DiGiacomo, J. W., Considine, M., Godet, I., and Gilkes, D. M. (2018). Molecular Portrait of Hypoxia in Breast Cancer: a Prognostic Signature and Novel HIF-Regulated Genes. *Mol. Cancer Res.* 16, 1889–1901. doi:10.1158/1541-7786.mcr-18-0345

Yu, H., Li, Y., Zhang, Z., Ren, J., Zhang, L., Xu, Z., et al. (2022). Silk Fibroin-Capped Metal-Organic Framework for Tumor-specific Redox Dyshomeostasis Treatment Synergized by Deoxygenation-Driven Chemotherapy. *Acta Biomater.* 138, 545–560. doi:10.1016/j.actbio.2021.11.009

Zhang, C., Chen, W., Zhang, T., Jiang, X., and Hu, Y. (2020). Hybrid Nanoparticle Composites Applied to Photodynamic Therapy: Strategies and Applications. *J. Mat. Chem. B* 8, 4726–4737. doi:10.1039/d0tb00093k

Zhang, C., Cheng, X., Chen, M., Sheng, J., Ren, J., Jiang, Z., et al. (2017). Fluorescence guided photothermal/photodynamic ablation of tumours using pH-responsive chlorin e6-conjugated gold nanorods. *Colloids Surfaces B Biointerfaces* 160, 345–354. doi:10.1016/j.colsurfb.2017.09.045

Zhang, C., Ren, J., He, J., Ding, Y., Huo, D., and Hu, Y. (2018). Long-term Monitoring of Tumor-Related Autophagy *In Vivo* by Fe3O4NO· Nanoparticles. *Biomaterials* 179, 186–198. doi:10.1016/j.biomaterials.2018.07.004

Zhang, C., Ren, J., Hua, J., Xia, L., He, J., Huo, D., et al. (2018). Multifunctional Bi2WO6 Nanoparticles for CT-Guided Photothermal and Oxygen-free Photodynamic Therapy. *ACS Appl. Mat. Interfaces* 10, 1132–1146. doi:10.1021/acsami.7b16000

Zhang, C., Ren, J., Yang, Y., Wang, D., He, J., Huo, D., et al. (2016). Ultra-sensitive Diagnosis of Orthotopic Patient Derived Hepatocellular Carcinoma by Fe@graphene Nanoparticles in MRI. *RSC Adv.* 6, 113919–113923. doi:10.1039/c6ra23511e

Zhang, C., Xia, D., Liu, J., Huo, D., Jiang, X., and Hu, Y. (2020). Bypassing the Immunosuppression of Myeloid-Derived Suppressor Cells by Reversing Tumor Hypoxia Using a Platelet-Inspired Platform. *Adv. Funct. Mat.* 30, 2000189. doi:10.1002/adfm.202000189

Zhang, X., Huang, Y., Song, H., Canup, B. S. B., Gou, S., She, Z., et al. (2020). Inhibition of Growth and Lung Metastasis of Breast Cancer by Tumor-Homing Triple-Bioresponsive Nanotherapeutics. *J. Control. Release* 328, 454–469. doi:10.1016/j.jconrel.2020.08.066

Zhao, L.-P., Zheng, R.-R., Chen, H.-Q., Liu, L.-S., Zhao, X.-Y., Liu, H.-H., et al. (2020). Self-Delivery Nanomedicine for O2-Economized Photodynamic Tumor Therapy. *Nano Lett.* 20, 2062–2071. doi:10.1021/acs.nanolett.0c00047

Zhao, P., Ren, S., Liu, Y., Huang, W., Zhang, C., and He, J. (2018). PL-W18O49-TPZ Nanoparticles for Simultaneous Hypoxia-Activated Chemotherapy and Photothermal Therapy. *ACS Appl. Mat. Interfaces* 10, 3405–3413. doi:10.1021/acsami.7b17323

Zhao, Z., Li, Y., and Xie, M.-B. (2015). Silk Fibroin-Based Nanoparticles for Drug Delivery. *Ijms* 16, 4880–4903. doi:10.3390/ijms16034880

Zuo, H., Tao, J., Shi, H., He, J., Zhou, Z., and Zhang, C. (2018). Platelet-mimicking Nanoparticles Co-loaded with W18O49 and Metformin Alleviate Tumor Hypoxia for Enhanced Photodynamic Therapy and Photothermal Therapy. *Acta Biomater.* 80, 296–307. doi:10.1016/j.actbio.2018.09.017

Conflict of Interest: The authors declare that the research was conducted in the absence of any commercial or financial relationships that could be construed as a potential conflict of interest.

Publisher's Note: All claims expressed in this article are solely those of the authors and do not necessarily represent those of their affiliated organizations, or those of the publisher, the editors and the reviewers. Any product that may be evaluated in this article, or claim that may be made by its manufacturer, is not guaranteed or endorsed by the publisher.

frontiers | Frontiers in Bioengineering and Biotechnology

TYPE Original Research
PUBLISHED 15 September 2022
DOI 10.3389/fbioe.2022.1006535

OPEN ACCESS

EDITED BY
Donglin Xia,
Nantong University, China

REVIEWED BY
Yao Luo,
Sichuan University, China
Li Ming,
Peking University People's Hospital, China

*CORRESPONDENCE
Yan Zhao,
zhaoyan@szbl.ac.cn
Lan Ma,
malan@sz.tsinghua.edu.cn

†These authors have contributed equally to this work

SPECIALTY SECTION
This article was submitted to Biomaterials, a section of the journal Frontiers in Bioengineering and Biotechnology

RECEIVED 29 July 2022
ACCEPTED 31 August 2022
PUBLISHED 15 September 2022

CITATION
Shi M, Du J, Shi J, Huang Y, Zhao Y and Ma L (2022), Ferroptosis-related gene ATG5 is a novel prognostic biomarker in nasopharyngeal carcinoma and head and neck squamous cell carcinoma. *Front. Bioeng. Biotechnol.* 10:1006535. doi: 10.3389/fbioe.2022.1006535

Ferroptosis-related gene ATG5 is a novel prognostic biomarker in nasopharyngeal carcinoma and head and neck squamous cell carcinoma

Ming Shi[1,2†], Jiangnan Du[1†], Jingjing Shi[1], Yunchuanxiang Huang[3], Yan Zhao[4]* and Lan Ma[1,3,4]*

[1]Institute of Biopharmaceutical and Health Engineering, Tsinghua Shenzhen International Graduate School, Tsinghua University, Shenzhen, China, [2]Dongguan Key Laboratory of Medical Bioactive Molecular Developmental and Translational Research, Guangdong Provincial Key Laboratory of Medical Molecular Diagnostics, Guangdong Medical University, Dongguan, China, [3]Tsinghua-Berkeley Shenzhen Institute, Tsinghua University, Shenzhen, China, [4]Shenzhen Bay Laboratory, Institute of Biomedical Health Technology and Engineering, Shenzhen, China

Nasopharyngeal carcinoma (NPC), a subtype of head and neck squamous cell carcinoma (HNSCC), is a malignant tumor that originates in the mucosal epithelium of the nasopharynx. Ferroptosis plays a key role in tumor suppression, while its prognostic value and critical factors in NPC have not been further explored. We select the Cancer Genome Atlas (TCGA) HNSCC dataset and the Gene Expression Omnibus (GEO) dataset of NPC samples, and find that ferroptosis-related factor ATG5 shows a high expression level with poor overall survival (OS) in HNSCC and NPC samples and is positively correlated with PD-L1/PD-L2 expression ($p < 0.05$). Furthermore, ATG5 high expression HNSCC patients show poor efficacy and short survival after receiving immune checkpoint blockade therapy treatment ($p < 0.05$). Moreover, ATG5 is significantly positively correlated with G2M checkpoint pathway ($\rho_{Spearman} = 0.41$, $p < 0.01$), and G2M checkpoint inhibitor drugs have lower IC_{50} in HNSCC patients with high expression of ATG5 ($p < 0.01$), indicating the potential value of G2M inhibitors in HNSCC/NPC treatment. In summary, our study shows that ferroptosis-related factors play a key role in immune infiltration in NPC and HNSCC, and ATG5, as a key immune invasion-related ferroptosis-related factor, has the potential to be a novel prognostic biomarker and a potential target in therapy for NPC and HNSCC.

KEYWORDS

ferroptosis-related genes, immune infiltration, nasopharyngeal carcinoma, head and neck squamous cell carcinoma, the Cancer Genome Atlas

Introduction

Nasopharyngeal carcinoma (NPC) is a type of head and neck squamous cell carcinoma (HNSCC) originating in the epithelial tissue of the nasopharynx (Lo and Huang 2002). Within addition, it is frequently an Epstein-Barr virus (EBV)-associated epithelial malignancy. Unlike other HNSCCs, the occurrence of NPC has a distinct ethnic and regional predisposition, mainly endemic in southern China, southeast Asia, north Africa, and the Arctic (Ma, Hui et al., 2017). NPC causes 50,000 deaths each year (Mahdavifar, Ghoncheh et al., 2016; Shivappa, Hebert et al., 2016), with the majority of new and fatal cases concentrated in China (Torre, Bray et al., 2015; Chen, Zheng et al., 2016). Early treatment efficacy rates for NPC are high, with a 10-year survival rate of more than 90% for stage I and more than 50% for stage II (Chua, Sham et al., 2003). However, most patients are already in advanced stage of NPCs when diagnosis, accounting for 60%–70% of total NPCs (Chen, L et al., 2012). At the same time, 10%–40% of patients with cured NPC show recurrence (Yu, Xia et al., 2016). Due to the late presentation of lesions, accompanied by some degree of cancer cell metastasis, the response of available therapies is poor, and the median survival in advanced patients is only 3 years (Al-Sarraf, LeBlanc et al., 1998). Studies have found that NPC was characterized highly infiltrated immune cells around and inside tumor lesions (Wang, Chen et al., 2018; Chen, Yin et al., 2020). Although immunotherapy has been introduced as treatment for NPC, there is still a need to improve the therapeutic effect (Hsu, Lee et al., 2017; Ma, Lim et al., 2018).

Ferroptosis is a cell death pathway that relies on iron ions to product reactive oxygen species (ROS), which causes the accumulation of lipid peroxide, and eventually damages the cell membrane structure, resulting in cell death (Stockwell, Friedmann Angeli et al., 2017). Cancer cells require and contain more iron ions than normal cells (Liang, Zhang et al., 2019). Through this differentiated property, iron ions can be induced to promote ferroptosis in cancer cells, achieving precise treatment of cancer (Hassannia, Vandenabeele et al., 2019). It was found that NPC cells could be killed by the induction of ferroptosis pathways, and they were most sensitive to ferroptosis inducers (Huang, Cao et al., 2021). According to the report, during cancer immunotherapy, ferroptosis can be activated by interferon gamma (IFNγ) released from $CD8^+$ T cells, and IFNγ down-regulates the expression of SLC3A2 and SLC7A11 to reduce the uptake of cystine in tumor cells, leading to ferroptosis in tumor cells (Wang, Green et al., 2019). Thus, ferroptosis may be a significant factor of NPC immunotherapy. However, the role of ferroptosis in NPC immunotherapy still needs more comprehensive studies.

In order to better understand the mechanisms of ferroptosis in NPC immunotherapy and explore more efficiency treatment for NPC, in this study, we selected the clinical data of HNSCC in the Cancer Genome Atlas (TCGA) to screen out the differential ferroptosis-related genes, and verified them by generating the expression data of NPC samples in the Gene Expression Omnibus (GEO). At the same time, aiming at the high association between NPC and immune microenvironment, we further studied NPC immune microenvironment through ferroptosis-related genes. Our data and studies have shown that the ferroptosis-related genes possessed high value in targeted drug development in NPC.

Materials and methods

Data acquisition

RNA-sequencing expression (level 3) profiles and corresponding clinical information for HNSCC were downloaded from TCGA dataset (https://portal.gdc.com). GSE12452 and GSE53819 microarray datasets were downloaded from the GEO database (https://www.ncbi.nlm.nih.gov/geo/). The extracted data were normalized by log2 transformation. The GEO microarray data were normalized by the normalize quantiles function of the "preprocessCore" package in R software (v3.4.1).

Bioinformatic analysis

The "limma" package in the R software (v4.0.3) was used to study the differentially expressed mRNA. "Adjusted $p < 0.05$ and Log2 (Fold Change) > 1 or Log2 (Fold Change) < −1" were defined as the threshold for the differential expression of mRNAs. Consistency analysis using "ConsensusClusterPlus" R package (v1.54.0) was performed; the maximum number of clusters was 6, 80% of the total sample was drawn 100 times, and "pheatmap" (v1.0.12) package was used for clustering heatmaps. The "immuneeconv" package was used to assess the results of immune score evaluation. Potential immune checkpoint blockade (ICB) response was predicted with the Tumor Immune Dysfunction and Exclusion (TIDE) algorithm using "ggplot2" (v3.3.3) and "ggpubr" (0.4.0) packages in the R software (v4.0.3). To evaluate the correlations between individual genes and pathway scores, "GSVA" package was used; Parameter was chosen as method = 'ssgsea' and scores were analyzed by Spearman correlation. The chemotherapeutic response for each sample was predicted based on the Genomics of Drug Sensitivity in Cancer (GDSC) (https://www.cancerrxgene.org/), used by "pRRophetic" package. All parameters were set as the default values. Using the batch effect of combat and tissue type of all tissues, the duplicate gene expression was summarized as a mean value.

Statistical analysis

Kaplan-Meier survival analysis of the different groups of samples from TCGA datasets was performed. Comparison

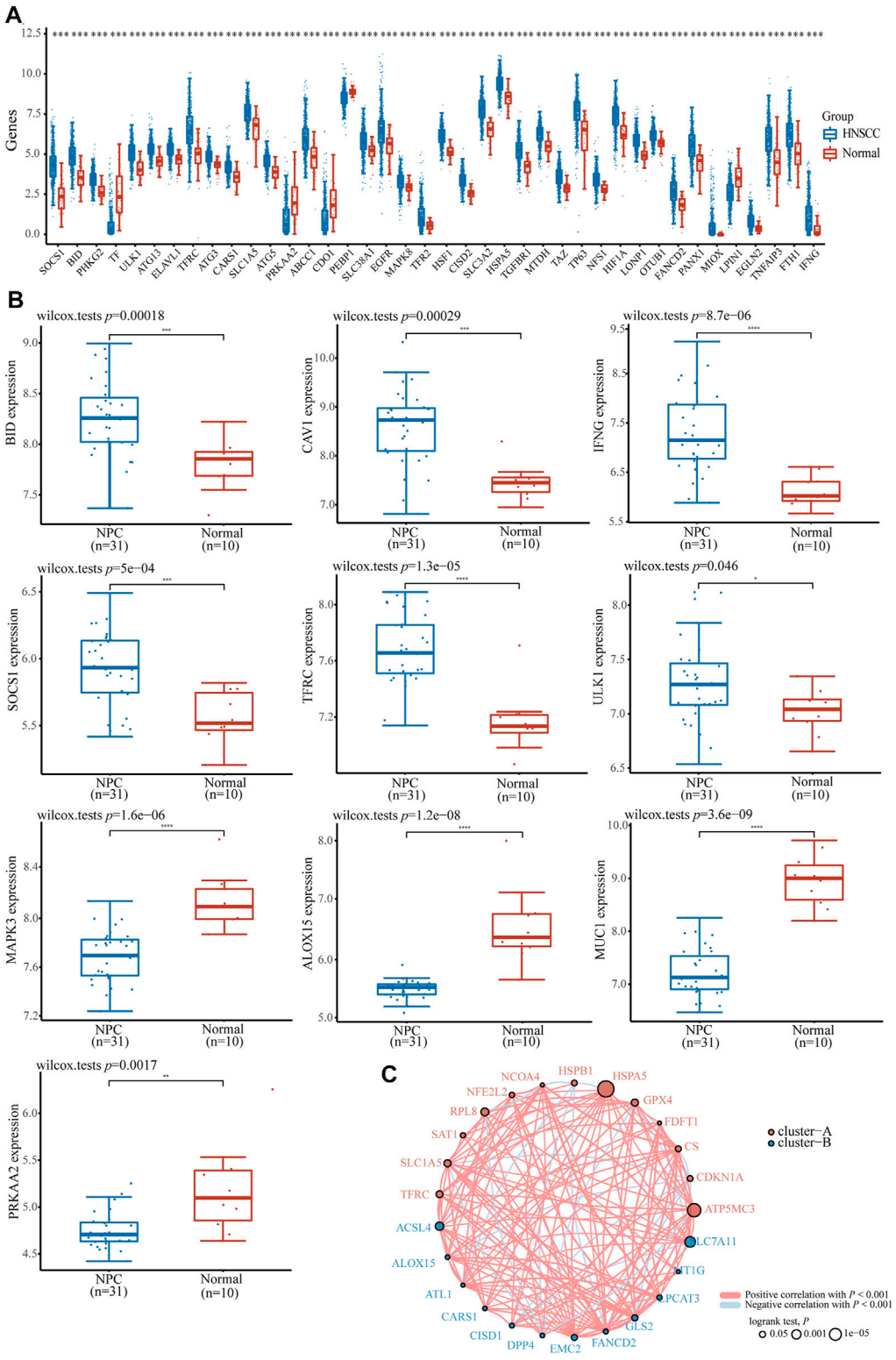

FIGURE 1
The expression distribution of ferroptosis-related gene in HNSCC and NPC patients. **(A)** ferroptosis-related gene in HNSCC and normal samples base on TCGA HNSCC dataset. **(B)** The expression distribution of ferroptosis-related gene in NPC and normal samples base on GSE12452 dataset. **(C)** The correlation of ferroptosis-related gene in HNSCC samples, circles represent the ferroptosis-related gene, red and blue represent positive and negative correlation between each gene, the size of the circle represent log rank *p*. **p* < 0.05, ***p* < 0.01, ****p* < 0.001.

among different groups was performed by log-rank test. The median survival time (LT50) for different groups was determined. For Kaplan-Meier curves, *p*-values and hazard ratio (HR) with 95% confidence interval (CI) were generated by log-rank tests and univariate Cox proportional hazards regression. The samples' half-maximal inhibitory concentration (IC_{50}) was estimated by ridge regression. All parameters were set as the default values. Using the batch effect of combat and tissue type of all tissues, the duplicate gene expression was summarized as a mean value. The statistical difference between two groups was compared through the Wilcox test, and significance differences between the three groups were assessed using the Kruskal–Wallis test.

Results

Differences in the expression of ferroptosis-related genes in NPC-affiliated HNSCC and normal tissues

To understand the role of ferroptosis-related genes in NPC, we investigated differences in the expression of ferroptosis-related genes between cancer tissues and normal tissues using TCGA HNSCC dataset and the GEO dataset of NPC samples. First, we downloaded and analyzed the expression profiles of 504 HNSCC and 44 normal cases and found that 69 genes, including *GPX4*, *BID*, *PHKG2*, *ULK1*, *ATG13*, *TFRC*, *ATG3*, *CARS1*, *SLC1A5*, *SOCS1*, *MAPK8*, *TFR2*, and others, were significantly highly expressed ($p < 0.05$); *TF*, *PRKAA2*, *CDO1*, *PEBP1*, *LPIN1*, and other 15 genes were significantly expressed at low levels ($p < 0.05$, Figure 1A); the expression of other ferroptosis-related genes were not significantly different between the tissues ($p > 0.05$, Supplementary Table S1); we found a similar trend in the GSE12452 dataset (Figure 1B). At the same time, most ferroptosis-related genes were positively correlated with HNSCC in prognosis analysis (Figure 1C). Taken together, these findings suggest that ferroptosis-related genes may play a key physiological role in the development of NPC and HNSCC.

Relationship between ferroptosis-related genes and immune cell infiltration in NPC-affiliated HNSCC

Considering NPC is highly infiltrated by immune cells and ferroptosis was activated by immunotherapy, we studied the relationship between ferroptosis-related genes and immune cell infiltration. Based on the expression level of ferroptosis-related genes, we first divided 504 patients with HNSCC into two groups, one with 475 patients and the other with 29 patients (Figure 2A) by R packet, and analyzed the gene expression profiles between the two groups (Figure 2B) by principal component analysis (PCA) method. The results showed that there were differences in gene expression between the two groups. Most ferroptosis-related genes were expressed at low levels in group 2 (Figure 2C), which had a better overall survival (OS) ($p < 0.05$, Figure 2D). Then we studied the expression of PD-L1 and PD-L2 in patients with HNSCC. It was shown that both PD-L1 and PD-L2 were overexpressed in HNSCC tissues and group 1 patients ($p < 0.01$, Figures 2E,F; Supplementary Figures S1A,B). Similar trends were found in two GSE datasets of NPCs (PD-L1, $p < 0.01$; PD-L2, $p < 0.05$, Figure 3A). Further analysis found that the expression of PD-L1 was positively correlated with the expression of 44 ferroptosis-related genes and negatively correlated with that of 24 genes in HNSCC tissues ($p < 0.05$, Figure 3B). Interestingly, PD-L2 expression was also positively correlated with that of 44 ferroptosis-related genes, although the specific genes are not same as PD-L1, 29 genes were negatively correlated with that of PD-L2 ($p < 0.05$, Supplementary Figure S1C). In the relationship between ferroptosis-related genes and HNSCC immune microenvironment, we found different ferroptosis-related gene expression level affect different immune cell types (Figure 3C). Naïve B cell, memory B cell, memory resting $CD4^+$ T cell, resting NK cell, gamma delta T cell, and macrophage M1 have higher activity ($p < 0.05$) in group 1 patients, while $CD8^+$ T cell, T cell follicular helper, and activated NK cell have high activity in group 2 patients, respectively ($p < 0.05$).

The ferroptosis-related gene ATG5 is overexpressed in NPC and can be used as a significant independent prognostic marker

To further explore the role of ferroptosis-related genes in NPC development and tumor immune infiltration, we screened ferroptosis-related genes with high-expression, low OS, and positive association with PD-L1/PD-L2 expression in HNSCC. A comparison of the two groups showed that ATG5 is the key ferroptosis-related gene, which was not only highly expressed and had worse OS in HNSCC, but also positively correlated with PD-L1 and PD-L2 expression ($p < 0.05$, Figure 4A). In addition, ATG5 was significantly highly expressed in the GSE dataset for NPC ($p < 0.05$, Figure 4B). We also observed high ATG5 expression in late-stage HNSCC patients, with a $p < 0.05$ (Figure 4C). High expression of ATG5 was found in HNSCC patients with a worse OS ($p < 0.05$, Figure 4D), similar result also can be found in the Kaplan-Meier analysis ($p < 0.05$, Figure 4E). Using Cox analysis, we found in univariate and multivariate analysis, age, TNM staging, and ATG5 expression were significantly correlated with HNSCC OS ($p < 0.01$, Figure 4F). Those results suggested that ferroptosis-related ATG5 plays an important role in tumor

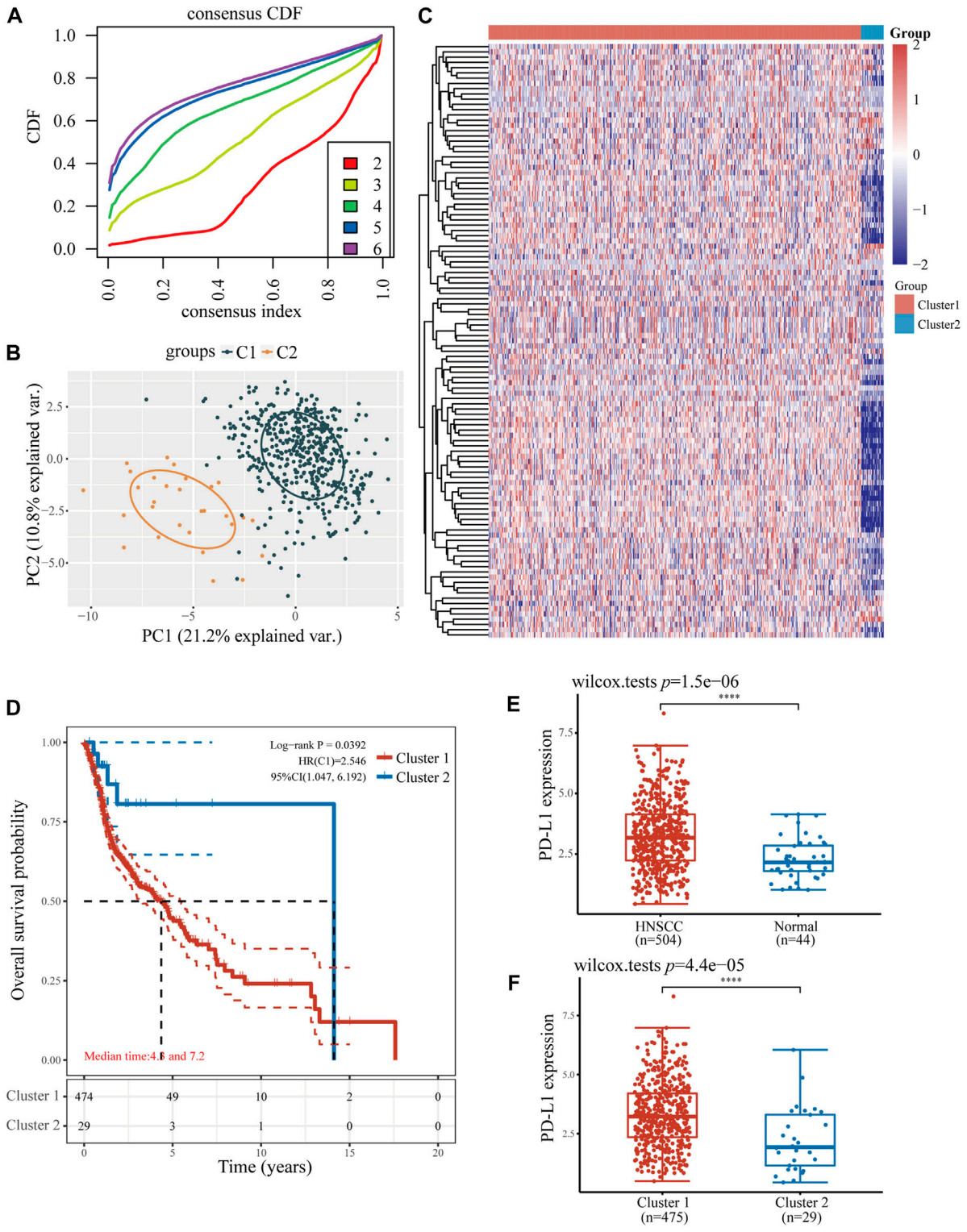

FIGURE 2
The relationship between ferroptosis-related genes and immune cell infiltration in two HNSCC subtypes. **(A)** The consensus clustering cumulative distribution function curves for k = 2–6. **(B)** The PCA of two HNSCC clusters. **(C)** The consistency of clustering results heatmap (k = 2), rows and columns represent samples, the different colors represent different types. **(D)** The Kaplan–Meier survival analysis of two clusters of samples from TCGA HNSCC dataset. **(E)** The expression level of PD-L1 in HNSCC and normal samples. **(F)** The expression level of PD-L1 in two clusters of HNSCC samples. *p < 0.05, **p < 0.01, ***p < 0.001.

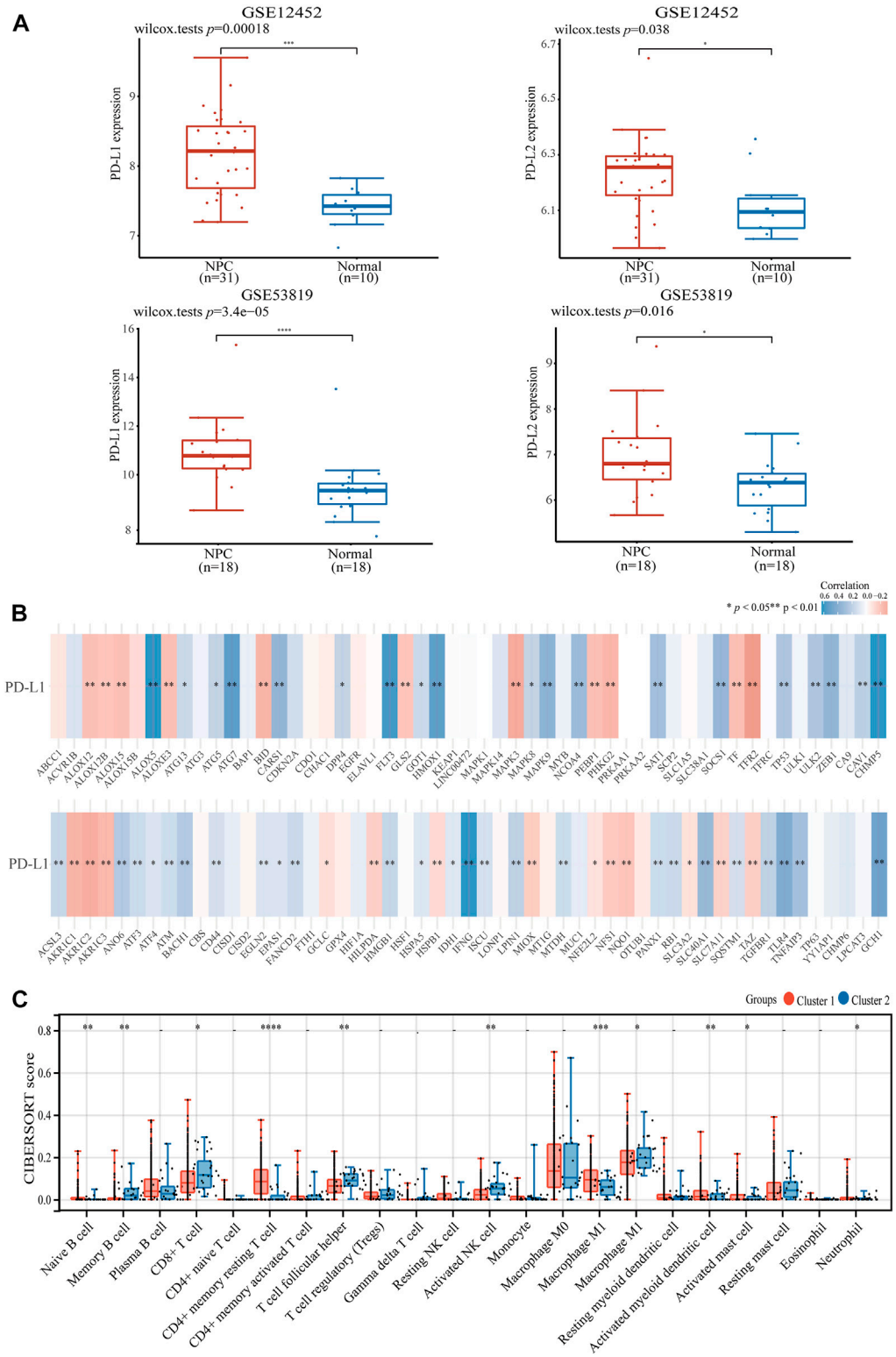

FIGURE 3
The expression of PD-L1 and PD-L2 in HNSCC and NPC patients. **(A)** The expression of PD-L1/PD-L2 in NPC and normal samples base on GSE12452 and GSE53819 dataset. **(B)** The correlation of PD-L1 with ferroptosis-related genes in TCGA HNSCC dataset. **(C)** The expression distribution of CIBERSORT immune score in two clusters of HNSCC samples. *$p < 0.05$, **$p < 0.01$, ***$p < 0.001$.

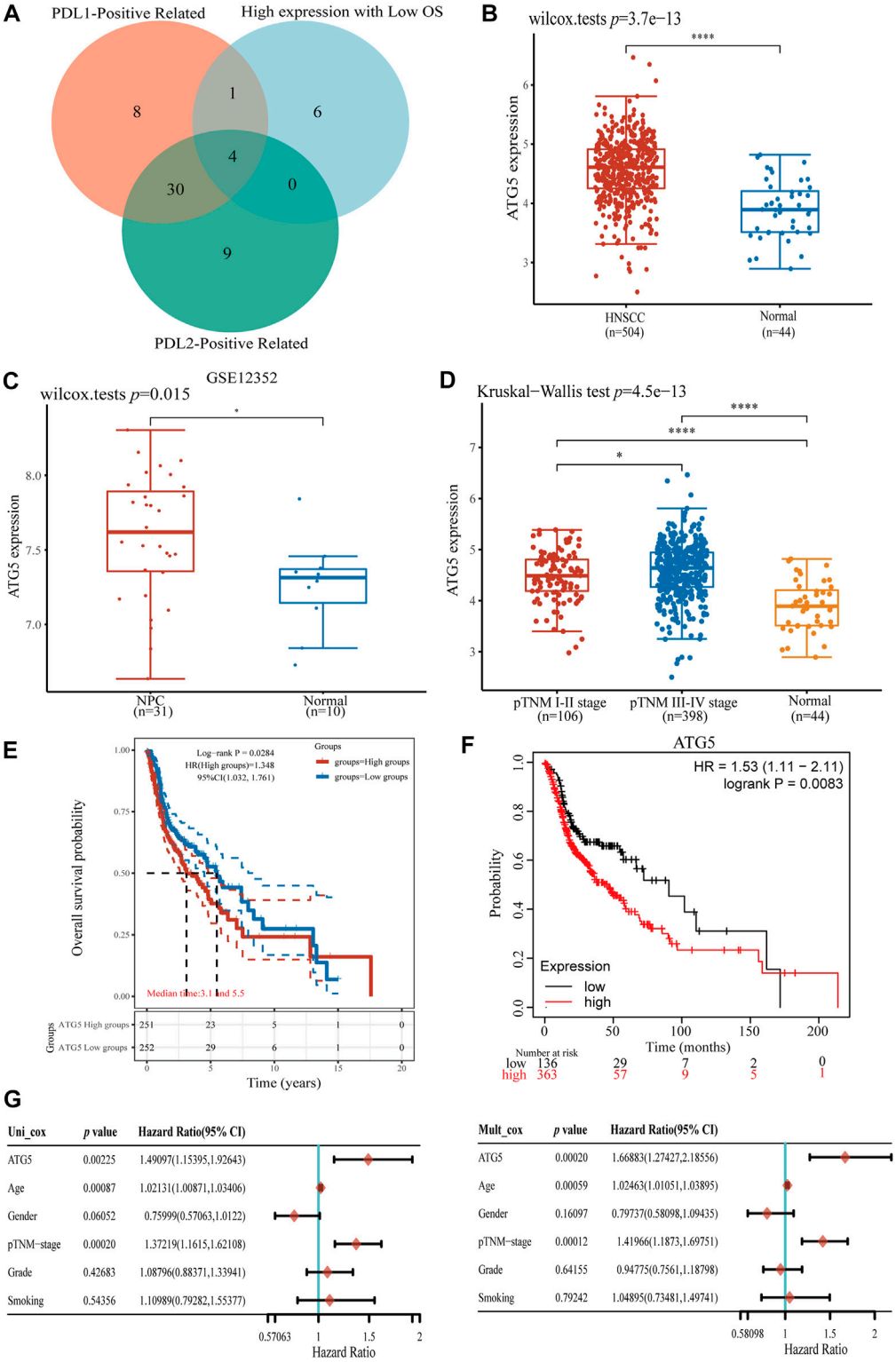

FIGURE 4
Analysis of ferroptosis-related gene ATG5 expression in HNSCC and NPC. **(A)** The Venn diagram of PD-L1/PD-L2 positive ferroptosis-related gene and high expression with OS in HNSCC samples, four ferroptosis-related genes were conformed. **(B)** ATG5 gene up-expression in HNSCC samples compared with normal samples. **(C)** ATG5 gene also highly expressed in NPC GSE12352 dataset **(D)** Boxplots of expression of ATG5 gene in different stage of HNSCC. **(E,F)** The Kaplan–Meier analysis of high and low ATG5 expression level in TCGA HNSCC dataset. **(G)** Forest plots of univariate and multivariate Cox regression of ATG5 expression and other clinicopathological factors. *$p < 0.05$, **$p < 0.01$, ***$p < 0.001$.

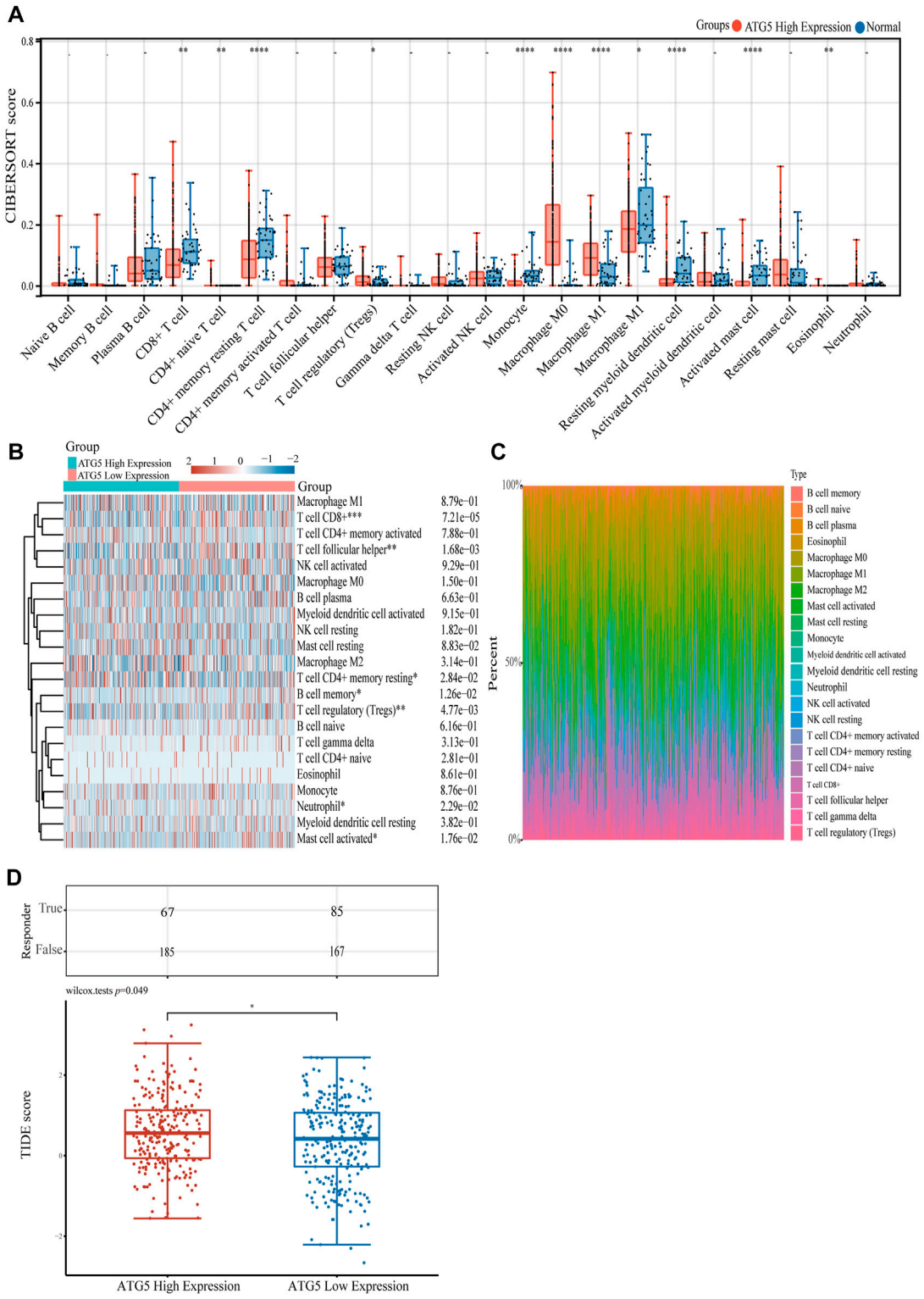

FIGURE 5
The relationship of ATG5 expression with immune cell infiltration. **(A)** The expression distribution of CIBERSORT immune score in ATG5 high expression HNSCC samples and normal samples. **(B)** Immune cell score heatmap of ATG5 high expression and ATG5 low expression in HNSCC samples. **(C)** The percentage abundance of tumor infiltrating immune cells between ATG5 high expression and ATG5 low expression HNSCC samples. **(D)** The distribution of immune response scores in ATG5 high expression and ATG5 low expression HNSCC samples in the prediction results. *$p < 0.05$, **$p < 0.01$, ***$p < 0.001$.

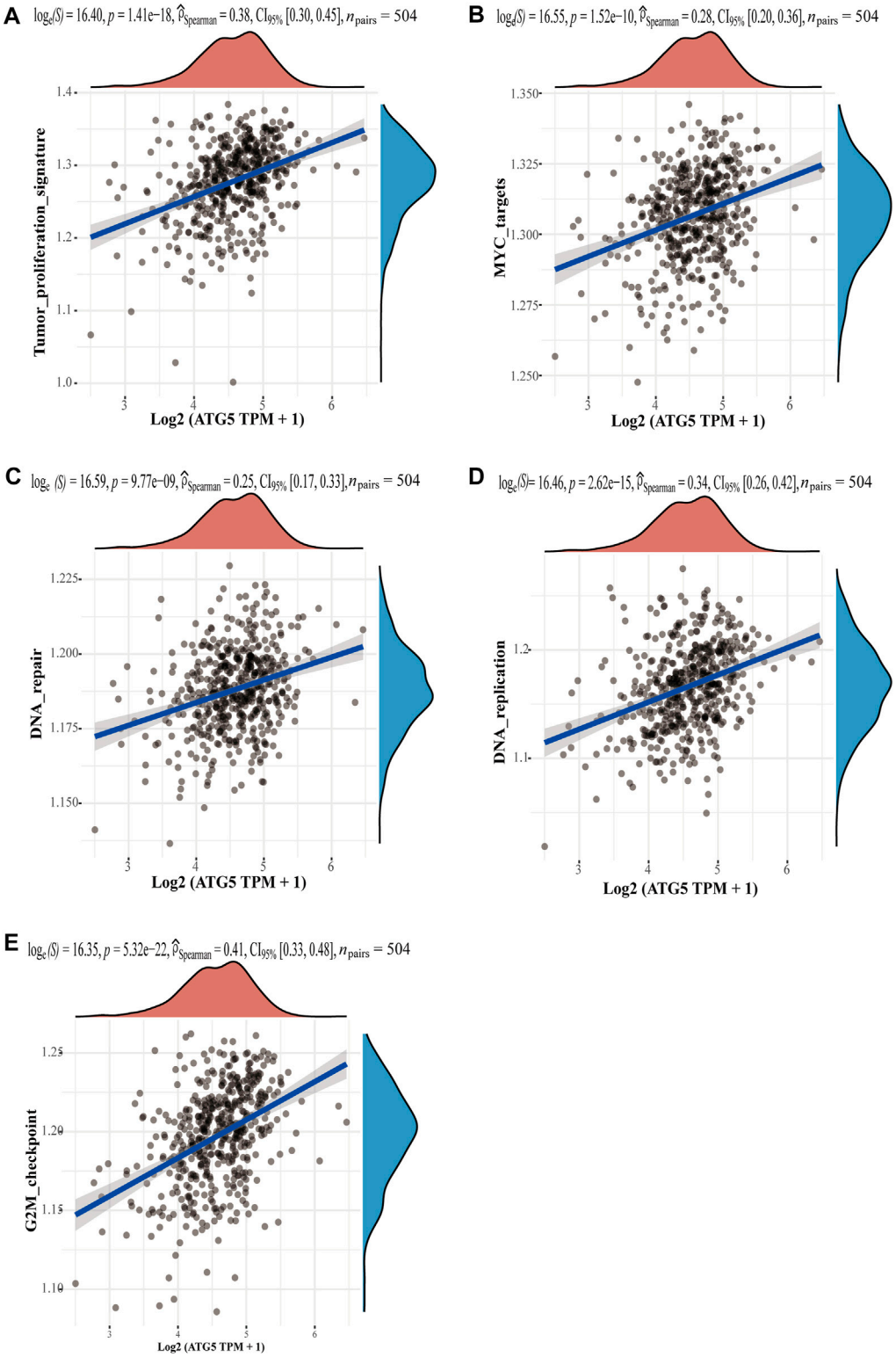

FIGURE 6
The correlations between ATG5 and pathways. **(A)** Tumor proliferation signatures, **(B)** MYC targets, **(C)** DNA repair, **(D)** DNA replication, and **(E)** G2M checkpoint. The abscissa represents the distribution of the gene expression, and the ordinate represents the distribution of the pathway score.

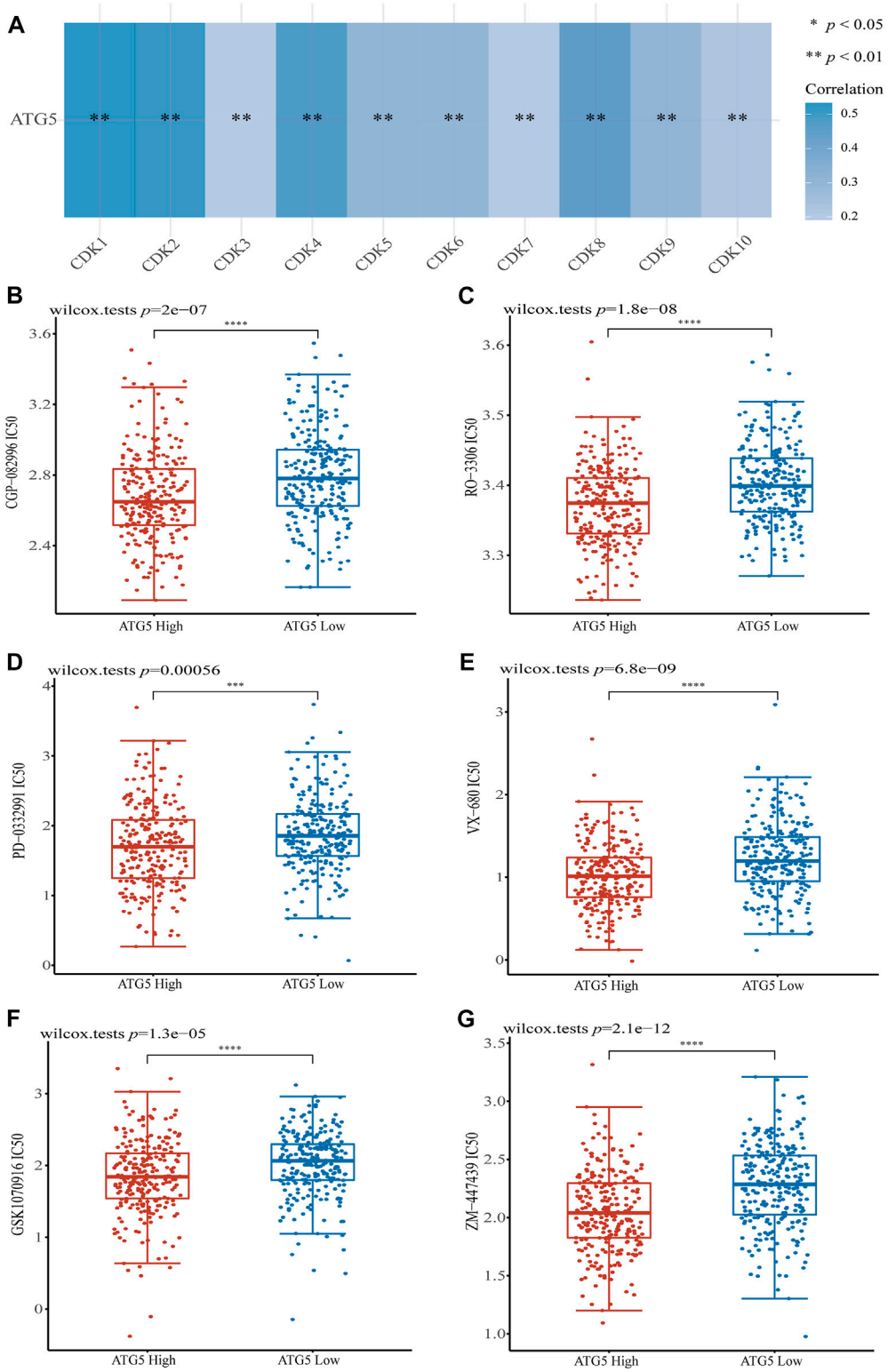

FIGURE 7
The correlations between ATG5 and G2M checkpoint. **(A)** The correlation of ATG5 and CDK family genes in TCGA HNSCC dataset. G2M checkpoint inhibitors **(B)** CGP-082996, **(C)** RO-3306, **(D)** PD-0332991, **(E)** VX-680, **(F)** GSK1070916 and **(G)** ZM-447439 had lower IC_{50} in ATG5 high expression HNSCC samples. *$p < 0.05$, **$p < 0.01$, ***$p < 0.001$.

development and immune infiltration in NPC and HNSCC, and thus, ATG5 could be used as an independent prognostic marker for NPC and HNSCC patients.

Relationship of ATG5 expression with ICB and immune cell infiltration

To gain a better understanding of the function of ATG5 in NPC immune cell infiltration, further studies showed that in HNSCC samples with high expression of ATG5, $CD8^+$ T cell, memory resting $CD4^+$ T cell, activated mast cell, monocyte, macrophage M2, and other immune cells were significantly reduced, and only T cell regulatory (Tregs) and macrophage M0 cells increased significantly, respectively ($p < 0.05$, Figure 5A). A heatmap showed trends and percentages of tumor-infiltrating immune cells in high and low ATG5 expression HNSCC samples (Figures 5B,C). To further understand the effect of ATG5 in HNSCC, based on expression profiling data, we used the TIDE algorithm to predict the responsiveness of high and low ATG5 expression groups in HNSCC to immune checkpoint inhibitors. The results showed that ATG5 high expression HNSCC patients had a higher TIDE score ($p < 0.05$, Figure 5D), predicted poor efficacy of ICB therapy, and poor survival after receiving ICB treatment.

ATG5 is significantly associated with the G2M checkpoint pathway in HNSCC

Given the important role of the ferroptosis-related gene ATG5 in NPC and HNSCC, we obtained the relationship between ATG5 and different pathways by single sample gene set enrichment analysis (ssGSEA) method, which calculated the correlation score between ATG5 gene and pathways in each HNSCC samples. The results demonstrated that ATG5 expression was significantly positively correlated with tumor proliferation signatures, MYC targets, DNA repair, DNA replication, and G2M checkpoint in HNSCC ($p < 0.05$, Figures 6A–E), and the Spearman coefficients were 0.38, 0.28, 0.25, 0.34, and 0.41, respectively. The CDK family genes are important regulators of G2M checkpoint, and ATG5 expression was also positively correlated with CDK1-10 expression in HNSCC ($p < 0.01$, Figure 7A). Based on this result, we performed drug therapy response prediction of high and low ATG5 expression in transcriptome of HNSCC samples, and found that the IC50 of G2M checkpoint inhibitors were lower in ATG5 high expression HNSCC samples ($p < 0.05$, Figures 7B–G), which showed a high sensitivity to G2M checkpoint inhibitors.

Discussion

Head and neck cancer refers to tumors and tumor-like conditions in anatomical areas of the head and neck. These anatomical areas include the oral cavity, paranasal sinuses, nasopharynx, larynx, pharynx, thyroid gland and its associated lymph nodes among others. Most head and neck cancers originate from the mucosal epithelium of the mouth, pharynx, and larynx and are collectively known as HNSCC (Johnson, Burtness et al., 2020), clinic information for HNSCC patients showed in Supplementary Table S2. NPC is the most aggressive epithelial tumor in HNSCC, with a high rate of aggressiveness and high incidence of metastasis (Cramer, Burtness et al., 2019; Jicman Stan et al., 2022). The incidence and development of NPC has a distinct regional pattern, with more than 70% of new cases concentrated in East and South-East Asia (Chen, Chan et al., 2019); researches on NPC in these regions are far less compared to other global high-prevalence cancers. Here, we used NPC-affiliated HNSCC database to study the role of ferroptosis-related genes in HNSCC and NPC, and found that it is possible ferroptosis-related genes affect the tumor immune microenvironment of NPC. Through screening, we found the ferroptosis-related gene ATG5 could serve as a significant independent prognostic marker. ATG5 is not only overexpressed with low OS, but also positive correlated with PD-L1/PD-L2 expression in HNSCC and NPC. Furthermore, ATG5 has a strong correlation with multiple pathways in HNSCC and affects the therapeutic efficacy of ICB therapy. In addition, the drug IC_{50} prediction showed ATG5 high expression HNSCC samples were more sensitive to G2M checkpoint inhibitors.

Ferroptosis is an iron-dependent regulatory process of cell death caused by excessive lipid peroxidation, and the occurrence and therapeutic effect of different types of tumors are related to ferroptosis (Chen, Kang et al., 2021). In this study, HNSCC patients were divided into two groups based on the characteristics of ferroptosis-related genes. Group two had a lower OS and higher correlation with $CD8^+$ T cells and activated NK cells by CIBERSORT analysis which is a method to characterize complex tissue cell composition from gene expression profiles (Newman, Liu et al., 2015). In addition, the low-expression of PD-L1/PD-L2 in group two was beneficial to recover T cell tumor response. The abundance of $CD8^+$ T cell is generally closely related to the prognosis of variety of tumor patients. $CD8^+$ T cells kill target cells by secreting perforin, or indirectly releasing cytokines such as tumor necrosis factor alpha (TNFα) (Zhang and Bevan 2011; Deng, Luo et al., 2019). The study found that $CD8^+$ T cells screen and eliminate invaders, and if $CD8^+$ T cell infiltration is less than 2.2% in tumor, the risk of developing disease progression after surgery will be 4-fold higher (Jansen, Prokhnevska et al., 2019). Activated natural killer (NK) cells also produce cytokines such as TNFα and IFNγ

and inhibit cancer angiogenesis and proliferation (Whiteside 2020; Wang, Chen et al., 2021).

The better OS and immune infiltration levels in group 2 suggested the important role of ferroptosis-related genes in HNSCC and NPC, therefore, we further screened poor prognosis of ferroptosis-related genes. Finally, ATG5 was found not only to be significantly highly expressed in HNSCC and NPC, but also showed a low prognosis and positively correlation with PD-L1/PD-L2 expression. ATG plays a central role in the process of autophagy, and is critical to the formation of autophagosomes (Xie, Kang et al., 2015), while ATG5-mediated autophagy contributes to ferroptosis (Dixon, Lemberg et al., 2012; Hou, Xie et al., 2016). Unrestricted lipid peroxidation during ferroptosis could lead to plasma membrane rupture, and in cancer, ferroptosis also occurs in an autophagy-dependent manner (Liu, Kuang et al., 2020). Knocking down autophagy-related proteins including ATG3, ATG5, ATG7 and ATG13 inhibits ferroptosis (Gao, Monian et al., 2016; Hou, Xie et al., 2016; Chen, Kang et al., 2021). ATG5 is necessary for the fusion of autophagosomes in both canonical and non-canonical autophagy (Ye, Zhou et al., 2018; Fraiberg and Elazar 2020), and immune-related diseases happened when ATG5 gene mutated (Martin, Gupta et al., 2012; Zhang, Cheng et al., 2015). Here we demonstrated the value of ATG5 with multiple approaches (Figures 4B–G). Furthermore, the abundance of $CD8^+$ T cells decreased in ATG5 high expression HNSCC patients, nevertheless the abundance of Tregs increased ($p < 0.05$, Figure 5A). High abundances of Tregs have been reported to be associated with adverse clinical outcomes (Sato, Olson et al., 2005; Beyer and Schultze 2006). Tregs create an immunosuppressive environment that impairs the activity of cytotoxic $CD8^+$ T cells (Serrels, Lund et al., 2015). We further assessed the effect of ATG5 in HNSCC through predictive effects of ICB therapy. ICB therapy helps immune system recognize and attack tumor cells to achieve cancer treatment (Mahoney, Rennert et al., 2015), but in most cancer types only one-third patients benefit from ICB therapy (Sharma, Hu-Lieskovan et al., 2017). Using TIDE, which is a bioinformatic method (Jiang, Gu et al., 2018), it was predicted that ATG5 high expression group had a higher TIDE score than ATG5 low expression group in HNSCC. It means dysfunction of tumor-infiltrating cytotoxic T lymphocytes (CTL) and rejection of CTL by immunosuppressors are stronger in ATG5 high expression HNSCC, and the ICB efficacy is worse. These results suggest that ATG5 is an effective prognostic biomarker and a predictive target for immunotherapy efficacy in HNSCC and NPC.

G2M checkpoint is an important regulatory mechanism in eukaryotic cells that regulates the normal operation of the cell cycle, ensuring the integrity of the number of chromosomes, and most tumor cells have a G1 checkpoint, thus, controlling the proliferation of tumor cells to the G2M stage is a feasible tumor treatment regimen (Chen T et al., 2012). Controlling tumor cells at the G2M phase through the G2M checkpoints not only inhibits the proliferation and growth of tumors, but also induces the apoptosis of tumor cells by DNA damage (Chen, Landen et al., 2013). Previous studies showed some autophagy genes contribute to cell cycle (Qu, Yu et al., 2003; Lee, Kawai et al., 2012; Maskey, Yousefi et al., 2013), and research found lack of ATG5, autophagy in proximal tubular epithelial cells significantly aggravated cell cycle arrest in the G2/M phase (Li, Peng et al., 2016). We found that ATG5 expression was significantly positively correlated with the G2M checkpoint signaling pathway in HNSCC (Spearman coefficient = 0.41). We used GDSC, the largest publicly available pharmacogenomics database, to predict the sensitivity of G2M checkpoint inhibitor drugs in high and low ATG5 expression HNSCC samples, which based on sample transcriptomes. The results showed ATG5 high expression samples were more sensitive to G2M checkpoint inhibitors. An unexpected finding that G2M checkpoint inhibitors may have a therapeutic effect on ATG5 high expression HNSCC and NPC, but more basic studies and clinical trials are still needed to validate the therapeutic effect.

In conclusion, in order to explore the role of ferroptosis in immunotherapy in HNSCC and NPC, this study analyzed the expression of ferroptosis-related genes in HNSCC and NPC. We found that ferroptosis-related genes were positively correlated with PD-L1 and PD-L2 expression, and the types of immune infiltrates were clearly different between two groups of HNSCC patients with different ferroptosis-related genes expression level. Ferroptosis-related gene ATG5 played a key role in HNSCC and NPC treatment, as ATG5 high expression HNSCC patients showed poor OS, and had poor response and survival after ICB therapy. Furthermore, ATG5 expression was significantly positively correlated with G2M checkpoints in HNSCC ($p < 0.001$, Spearman coefficient = 0.41) and ATG5 high expression HNSCC patients had lower IC_{50} of G2M checkpoint inhibitors by predicted. Therefore, ATG5 has potential as a significant independent prognostic marker in HNSCC and NPC, and ATG5 is an important target in HNSCC and NPC treatment of ferroptosis, immunotherapy and G2M checkpoint inhibitor.

Data availability statement

Publicly available datasets were analyzed in this study. This data can be found here: TCGA dataset (https://portal.gdc.com) GEO database (https://www.ncbi.nlm.nih.gov/geo/).

Author contributions

LM, YZ, and MS conceived and designed the project. MS and JD analyzed the data. MS and JS summarized literatures, MS, JD, and YH wrote the manuscript. All authors contributed to the article and approved the submitted version.

Funding

This work was supported by the National Key Research and Development Program of China (2020YFA0908900); Universities Stable Funding Key Projects (WDZC20200821104802001); GuangDong Basic and Applied Basic Research Foundation (2021A1515110819).

Acknowledgments

We would like to thank Shenzhen Bay Laboratory for the help of data analysis.

Conflict of interest

The authors declare that the research was conducted in the absence of any commercial or financial relationships that could be construed as a potential conflict of interest.

Publisher's note

Supplementary material

The Supplementary Material for this article can be found online at: https://www.frontiersin.org/articles/10.3389/fbioe.2022.1006535/full#supplementary-material

References

Al-Sarraf, M., LeBlanc, M., Giri, P. G., Fu, K. K., Cooper, J., Vuong, T., et al. (1998). Chemoradiotherapy versus radiotherapy in patients with advanced nasopharyngeal cancer: Phase III randomized intergroup study 0099. *J. Clin. Oncol.* 16, 1310–1317. doi:10.1200/JCO.1998.16.4.1310

Beyer, M., and Schultze, J. L. (2006). Regulatory T cells in cancer. *Blood* 108, 804–811. doi:10.1182/blood-2006-02-002774

Chen, H., Landen, C. N., Li, Y., Alvarez, R. D., and Tollefsbol, T. O. (2013). Enhancement of cisplatin-mediated apoptosis in ovarian cancer cells through potentiating G2/M arrest and p21 upregulation by combinatorial epigallocatechin gallate and sulforaphane. *J. Oncol.* 2013, 1–9. doi:10.1155/2013/872957

Chen, L., Hu, C. S., Chen, X. Z., Hu, G. Q., Cheng, Z. B., Sun, Y., et al. (2012). Concurrent chemoradiotherapy plus adjuvant chemotherapy versus concurrent chemoradiotherapy alone in patients with locoregionally advanced nasopharyngeal carcinoma: A phase 3 multicentre randomised controlled trial. *Lancet Oncol.* 13, 163–171. doi:10.1016/S1470-2045(11)70320-5

Chen, T., Stephens, P. A., Middleton, F. K., and Curtin, N. J. (2012). Targeting the S and G2 checkpoint to treat cancer. *Drug Discov. Today* 17, 194–202. doi:10.1016/j.drudis.2011.12.009

Chen, W., Zheng, R., Baade, P. D., Zhang, S., Zeng, H., Bray, F., et al. (2016). Cancer statistics in China, 2015. *CA A Cancer J. Clin.* 66, 115–132. doi:10.3322/caac.21338

Chen, X., Kang, R., Kroemer, G., and Tang, D. (2021). Broadening horizons: The role of ferroptosis in cancer. *Nat. Rev. Clin. Oncol.* 18, 280–296. doi:10.1038/s41571-020-00462-0

Chen, Y. P., Chan, A. T. C., Le, Q. T., Blanchard, P., Sun, Y., and Ma, J. (2019). Nasopharyngeal carcinoma. *Lancet* 394, 64–80. doi:10.1016/S0140-6736(19)30956-0

Chen, Y. P., Yin, J. H., Li, W. F., Li, H. J., Chen, D. P., Zhang, C. J., et al. (2020). Single-cell transcriptomics reveals regulators underlying immune cell diversity and immune subtypes associated with prognosis in nasopharyngeal carcinoma. *Cell. Res.* 30, 1024–1042. doi:10.1038/s41422-020-0374-x

Chua, D. T., Sham, J. S., Kwong, D. L., and Au, G. K. (2003). Treatment outcome after radiotherapy alone for patients with Stage I-II nasopharyngeal carcinoma. *Cancer* 98, 74–80. doi:10.1002/cncr.11485

Cramer, J. D., Burtness, B., Le, Q. T., and Ferris, R. L. (2019). The changing therapeutic landscape of head and neck cancer. *Nat. Rev. Clin. Oncol.* 16, 669–683. doi:10.1038/s41571-019-0227-z

Deng, Q., Luo, Y., Chang, C., Wu, H., Ding, Y., and Xiao, R. (2019). The emerging epigenetic role of CD8+T cells in autoimmune diseases: A systematic review. *Front. Immunol.* 10, 856. doi:10.3389/fimmu.2019.00856

Dixon, S. J., Lemberg, K. M., Lamprecht, M. R., Skouta, R., Zaitsev, E. M., Gleason, C. E., et al. (2012). Ferroptosis: An iron-dependent form of nonapoptotic cell death. *Cell.* 149, 1060–1072. doi:10.1016/j.cell.2012.03.042

Fraiberg, M., and Elazar, Z. (2020). Genetic defects of autophagy linked to disease. *Prog. Mol. Biol. Transl. Sci.* 172, 293–323. doi:10.1016/bs.pmbts.2020.04.001

Gao, M., Monian, P., Pan, Q., Zhang, W., Xiang, J., and Jiang, X. (2016). Ferroptosis is an autophagic cell death process. *Cell. Res.* 26, 1021–1032. doi:10.1038/cr.2016.95

Hassannia, B., Vandenabeele, P., and Vanden Berghe, T. (2019). Targeting ferroptosis to iron out cancer. *Cancer Cell.* 35, 830–849. doi:10.1016/j.ccell.2019.04.002

Hou, W., Xie, Y., Song, X., Sun, X., Lotze, M. T., Zeh, H. J., 3rd, et al. (2016). Autophagy promotes ferroptosis by degradation of ferritin. *Autophagy* 12, 1425–1428. doi:10.1080/15548627.2016.1187366

Hsu, C., Lee, S. H., Ejadi, S., Even, C., Cohen, R. B., Le Tourneau, C., et al. (2017). Safety and antitumor activity of pembrolizumab in patients with programmed death-ligand 1-positive nasopharyngeal carcinoma: Results of the KEYNOTE-028 study. *J. Clin. Oncol.* 35, 4050–4056. doi:10.1200/JCO.2017.73.3675

Huang, S., Cao, B., Zhang, J., Feng, Y., Wang, L., Chen, X., et al. (2021). Induction of ferroptosis in human nasopharyngeal cancer cells by cucurbitacin B: Molecular mechanism and therapeutic potential. *Cell. Death Dis.* 12, 237. doi:10.1038/s41419-021-03516-y

Jansen, C. S., Prokhnevska, N., Master, V. A., Sanda, M. G., Carlisle, J. W., Bilen, M. A., et al. (2019). An intra-tumoral niche maintains and differentiates stem-like CD8 T cells. *Nature* 576, 465–470. doi:10.1038/s41586-019-1836-5

Jiang, P., Gu, S., Pan, D., Fu, J., Sahu, A., Hu, X., et al. (2018). Signatures of T cell dysfunction and exclusion predict cancer immunotherapy response. *Nat. Med.* 24, 1550–1558. doi:10.1038/s41591-018-0136-1

Jicman Stan, D., Niculet, E., Lungu, M., Onisor, C., Rebegea, L., Vesa, D., et al. (2022). Nasopharyngeal carcinoma: A new synthesis of literature data (review). *Exp. Ther. Med.* 23, 136. doi:10.3892/etm.2021.11059

Johnson, D. E., Burtness, B., Leemans, C. R., Lui, V. W. Y., Bauman, J. E., and Grandis, J. R. (2020). Head and neck squamous cell carcinoma. *Nat. Rev. Dis. Prim.* 6, 92. doi:10.1038/s41572-020-00224-3

Lee, I. H., Kawai, Y., Fergusson, M. M., RoviraII, Bishop, A. J., Motoyama, N., et al. (2012). Atg7 modulates p53 activity to regulate cell cycle and survival during metabolic stress. *Science* 336, 225–228. doi:10.1126/science.1218395

Li, H., Peng, X., Wang, Y., Cao, S., Xiong, L., Fan, J., et al. (2016). Atg5-mediated autophagy deficiency in proximal tubules promotes cell cycle G2/M arrest and renal fibrosis. *Autophagy* 12, 1472–1486. doi:10.1080/15548627.2016.1190071

Liang, C., Zhang, X., Yang, M., and Dong, X. (2019). Recent progress in ferroptosis inducers for cancer therapy. *Adv. Mat.* 31, e1904197. doi:10.1002/adma.201904197

Liu, J., Kuang, F., Kroemer, G., Klionsky, D. J., Kang, R., and Tang, D. (2020). Autophagy-dependent ferroptosis: Machinery and regulation. *Cell. Chem. Biol.* 27, 420–435. doi:10.1016/j.chembiol.2020.02.005

Lo, K. W., and Huang, D. P. (2002). Genetic and epigenetic changes in nasopharyngeal carcinoma. *Semin. Cancer Biol.* 12, 451–462. doi:10.1016/s1044579x02000883

Ma, B. B. Y., Hui, E. P., and Chan, A. T. C. (2017). Investigational drugs for nasopharyngeal carcinoma. *Expert Opin. Investig. Drugs* 26, 677–685. doi:10.1080/13543784.2017.1324568

Ma, B. B. Y., Lim, W. T., Goh, B. C., Hui, E. P., Lo, K. W., Pettinger, A., et al. (2018). Antitumor activity of nivolumab in recurrent and metastatic nasopharyngeal carcinoma: An international, multicenter study of the mayo clinic phase 2 consortium (NCI-9742). *J. Clin. Oncol.* 36, 1412–1418. doi:10.1200/JCO.2017.77.0388

Mahdavifar, N., Ghoncheh, M., Mohammadian-Hafshejani, A., Khosravi, B., and Salehiniya, H. (2016). Epidemiology and inequality in the incidence and mortality of nasopharynx cancer in Asia. *Osong Public Health Res. Perspect.* 7, 360–372. doi:10.1016/j.phrp.2016.11.002

Mahoney, K. M., Rennert, P. D., and Freeman, G. J. (2015). Combination cancer immunotherapy and new immunomodulatory targets. *Nat. Rev. Drug Discov.* 14, 561–584. doi:10.1038/nrd4591

Martin, L. J., Gupta, J., Jyothula, S. S., Butsch Kovacic, M., Biagini Myers, J. M., Patterson, T. L., et al. (2012). Functional variant in the autophagy-related 5 gene promotor is associated with childhood asthma. *PLoS One* 7, e33454. doi:10.1371/journal.pone.0033454

Maskey, D., Yousefi, S., Schmid, I., Zlobec, I., Perren, A., Friis, R., et al. (2013). ATG5 is induced by DNA-damaging agents and promotes mitotic catastrophe independent of autophagy. *Nat. Commun.* 4, 2130. doi:10.1038/ncomms3130

Newman, A. M., Liu, C. L., Green, M. R., Gentles, A. J., Feng, W., Xu, Y., et al. (2015). Robust enumeration of cell subsets from tissue expression profiles. *Nat. Methods* 12, 453–457. doi:10.1038/nmeth.3337

Qu, X., Yu, J., Bhagat, G., Furuya, N., Hibshoosh, H., Troxel, A., et al. (2003). Promotion of tumorigenesis by heterozygous disruption of the beclin 1 autophagy gene. *J. Clin. Invest.* 112, 1809–1820. doi:10.1172/JCI20039

Sato, E., Olson, S. H., Ahn, J., Bundy, B., Nishikawa, H., Qian, F., et al. (2005). Intraepithelial CD8+ tumor-infiltrating lymphocytes and a high CD8+/regulatory T cell ratio are associated with favorable prognosis in ovarian cancer. *Proc. Natl. Acad. Sci. U. S. A.* 102, 18538–18543. doi:10.1073/pnas.0509182102

Serrels, A., Lund, T., Serrels, B., Byron, A., McPherson, R. C., von Kriegsheim, A., et al. (2015). Nuclear FAK controls chemokine transcription, Tregs, and evasion of anti-tumor immunity. *Cell.* 163, 160–173. doi:10.1016/j.cell.2015.09.001

Sharma, P., Hu-Lieskovan, S., Wargo, J. A., and Ribas, A. (2017). Primary, adaptive, and acquired resistance to cancer immunotherapy. *Cell.* 168, 707–723. doi:10.1016/j.cell.2017.01.017

Shivappa, N., Hebert, J. R., Zucchetto, A., Montella, M., Libra, M., Garavello, W., et al. (2016). Increased risk of nasopharyngeal carcinoma with increasing levels of diet-associated inflammation in an Italian case-control study. *Nutr. Cancer* 68, 1123–1130. doi:10.1080/01635581.2016.1216137

Stockwell, B. R., Friedmann Angeli, J. P., Bayir, H., Bush, A. I., Conrad, M., Dixon, S. J., et al. (2017). Ferroptosis: A regulated cell death nexus linking metabolism, redox biology, and disease. *Cell.* 171, 273–285. doi:10.1016/j.cell.2017.09.021

Torre, L. A., Bray, F., Siegel, R. L., Ferlay, J., Lortet-Tieulent, J., and Jemal, A. (2015). Global cancer statistics, 2012. *CA A Cancer J. Clin.* 65, 87–108. doi:10.3322/caac.21262

Wang, S., Chen, S., Ying, Y., Ma, X., Shen, H., Li, J., et al. (2021). Comprehensive analysis of ferroptosis regulators with regard to PD-L1 and immune infiltration in clear cell renal cell carcinoma. *Front. Cell. Dev. Biol.* 9, 676142. doi:10.3389/fcell.2021.676142

Wang, W., Green, M., Choi, J. E., Gijon, M., Kennedy, P. D., Johnson, J. K., et al. (2019). CD8(+) T cells regulate tumour ferroptosis during cancer immunotherapy. *Nature* 569, 270–274. doi:10.1038/s41586-019-1170-y

Wang, Y. Q., Chen, Y. P., Zhang, Y., Jiang, W., Liu, N., Yun, J. P., et al. (2018). Prognostic significance of tumor-infiltrating lymphocytes in nondisseminated nasopharyngeal carcinoma: A large-scale cohort study. *Int. J. Cancer* 142, 2558–2566. doi:10.1002/ijc.31279

Whiteside, T. L. (2020). NK cells in the tumor microenvironment and thioredoxin activity. *J. Clin. Invest.* 130, 5115–5117. doi:10.1172/JCI141460

Xie, Y., Kang, R., Sun, X., Zhong, M., Huang, J., Klionsky, D. J., et al. (2015). Posttranslational modification of autophagy-related proteins in macroautophagy. *Autophagy* 11, 28–45. doi:10.4161/15548627.2014.984267

Ye, X., Zhou, X. J., and Zhang, H. (2018). Exploring the role of autophagy-related gene 5 (ATG5) yields important insights into autophagy in autoimmune/autoinflammatory diseases. *Front. Immunol.* 9, 2334. doi:10.3389/fimmu.2018.02334

Yu, Y. H., Xia, W. X., Shi, J. L., Ma, W. J., Li, Y., Ye, Y. F., et al. (2016). A model to predict the risk of lethal nasopharyngeal necrosis after re-irradiation with intensity-modulated radiotherapy in nasopharyngeal carcinoma patients. *Chin. J. Cancer* 35, 59. doi:10.1186/s40880-016-0124-0

Zhang, N., and Bevan, M. J. (2011). CD8(+) T cells: Foot soldiers of the immune system. *Immunity* 35, 161–168. doi:10.1016/j.immuni.2011.07.010

Zhang, Y. M., Cheng, F. J., Zhou, X. J., Qi, Y. Y., Zhao, M. H., and Zhang, H. (2015). Rare variants of ATG5 are likely to Be associated with Chinese patients with systemic lupus erythematosus. *Med. Baltim.* 94, e939. doi:10.1097/MD.0000000000000939

frontiers | Frontiers in Bioengineering and Biotechnology

TYPE Original Research
PUBLISHED 29 September 2022
DOI 10.3389/fbioe.2022.996763

OPEN ACCESS

EDITED BY
Qun Wang,
Iowa State University, United States

REVIEWED BY
Antonino S. Fiorillo,
University Magna Graecia of Catanzaro, Italy
Ramón G Rubio,
Complutense University of Madrid, Spain
Kunyu Qiu,
Putnam Associates, United States

*CORRESPONDENCE
Donglin Xia,
xiadonglin@ntu.edu.cn

SPECIALTY SECTION
This article was submitted to Biomaterials, a section of the journal Frontiers in Bioengineering and Biotechnology

RECEIVED 18 July 2022
ACCEPTED 06 September 2022
PUBLISHED 29 September 2022

CITATION
Yang Y, Wang X, Yuan X, Zhu Q, Chen S and Xia D (2022), Glucose-activatable insulin delivery with charge-conversional polyelectrolyte multilayers for diabetes care.
Front. Bioeng. Biotechnol. 10:996763.
doi: 10.3389/fbioe.2022.996763

Glucose-activatable insulin delivery with charge-conversional polyelectrolyte multilayers for diabetes care

Yanguang Yang[1], Xiangqian Wang[1], Xiaopeng Yuan[1], Qiwei Zhu[1], Shusen Chen[1] and Donglin Xia[2]*

[1]Department of Radiotherapy, Nantong Tumor Hospital, Tumor Hospital Affiliated to Nantong University, Nantong, China, [2]School of Public Health, Nantong University, Nantong, China

One of the most effective treatments for diabetes is to design a glucose-regulated insulin (INS) delivery system that could adjust the INS release time and rate to reduce diabetes-related complications. Here, mixed multiple layer-by-layer (mmLbL)-INS microspheres were developed for glucose-mediated INS release and an enhanced hypoglycemic effect for diabetes care. To achieve ultrafast glucose-activated INS release, glucose oxidase (GOx) was assembled with a positively charged polymer and modified on INS LbL. The mmLbL-INS microspheres were constructed with one, two, and four layers of the polyelectrolyte LbL assembly at a ratio of 1:1:1. Under hyperglycemia, GOx converts a change in the hyperglycemic environment to a pH stimulus, thus providing sufficient hydrogen ion. The accumulated hydrogen ion starts LbL charge shifting, and anionic polymers are converted to cationic polymers through hydrolytic cleavage of amine-functionalized side chains. The results of *in vitro* INS release suggested that glucose can modulate the mmLbL-INS microspheres in a pulsatile profile. *In vivo* studies validated that this formulation enhanced the hypoglycemic effect in STZ-induced diabetic rats within 2 h of subcutaneous administration and facilitated stabilization of blood glucose levels for up to 2 days. This glucose-activatable LbL microsphere system could serve as a powerful tool for constructing a precisely controlled release system.

KEYWORDS

glucose-activity, diabetes, insulin, charge shifting, layer-by-layer

Introduction

In diabetes care, maintaining stable blood glucose levels (BGLs) in normoglycemia is a must because hyperglycemia would induce secondary complications, such as vascular, renal, or neural damage (Kang, 2018; Kaura Parbhakar et al., 2020; Shah and Wu, 2022). Most patients with type 2 diabetes need direct intravenous exogenous insulin (INS), and therefore, they are administered multiple injections of INS with careful dosing, which ultimately results

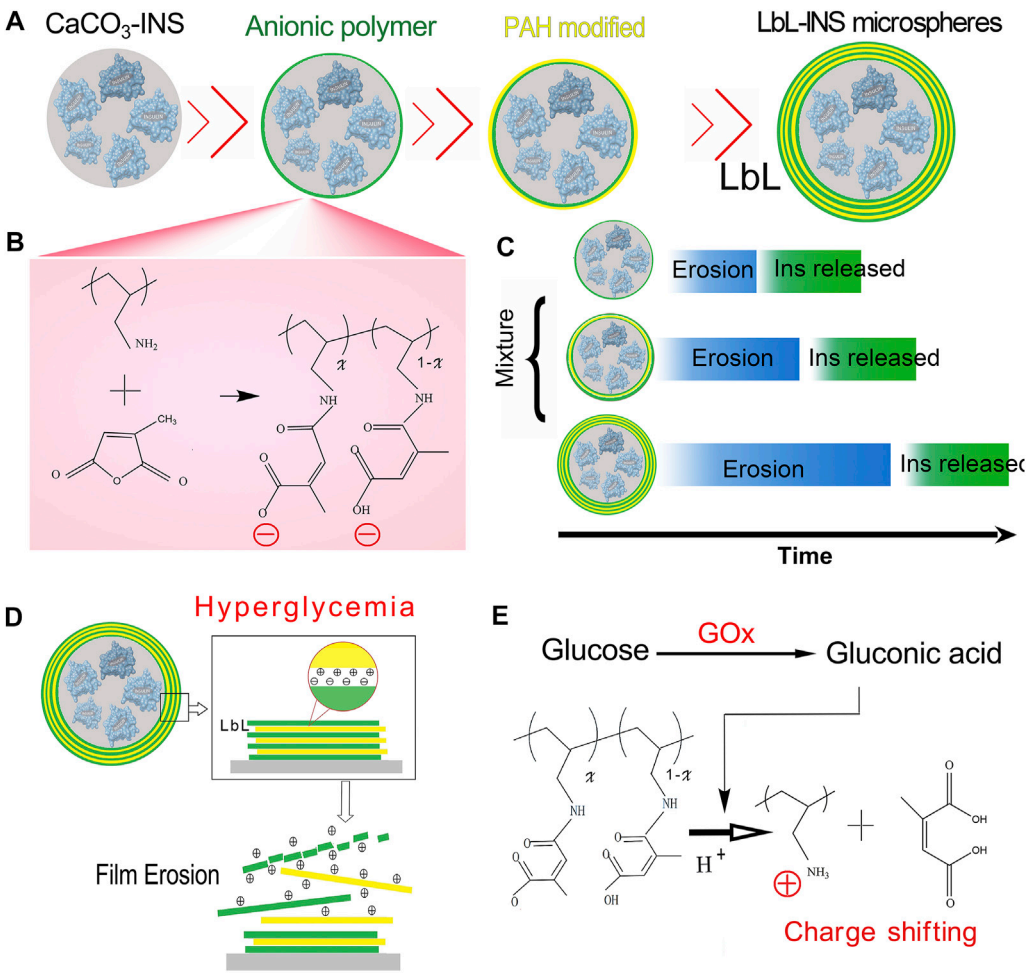

FIGURE 1
Scheme of the mixed multiple layer-by-layer insulin (mmLbL-INS) microcapsules. **(A)** Synthesis of the multiple LbL-INS microcapsules. The anionic polymer was regarded stable in physiologically relevant environments and hydrolysis of the charge-shifting anionic polymer under acidic conditions yields a cationic polymer. Based on the LbL assembly of multilayered polyelectrolyte films, with repeat assembly sequences polycation PAH and anionic polymer, we fabricated LbL-INS microspheres with different layers. **(B)** Synthesis of degradable anionic polymers. **(C)** Schematic of mmLbL-INS microcapsules controlling the INS release time. **(D)** In hyperglycemia, glucose-activated changes in the net charge of the polymer led to changes in the nature of ionic interactions in the multilayers and promoted film disruption. **(E)** Hydrolysis of the citraconic amide side chains of the charge-shifting anionic polymer under acidic conditions.

in poor compliance (Ling and Chen, 2013). Various INS delivery systems are sensitive to different external stimuli, such as pH (Akhmedov et al., 2010; Yoshida et al., 2012; Dmitriev et al., 2019), temperature (Huynh et al., 2008; Killeen et al., 2020), or light (Solimena and Speier, 2010; Sarode et al., 2016; Yu et al., 2022), were investigated. However, most INS delivery systems are associated with a lag time of more than 2 h in hypoglycemia. Thus, precise control of the amount and rate of INS released into the blood in order to maintain the BGL within the narrow concentration window required to avoid hyperglycemia and hypoglycemia is challenging.

The layer-by-layer (LbL) assembly method relies on solid exfoliation to produce colloids of sheets and can control drug release under particular external stimulus (Baba et al., 2010; Huang et al., 2013; Zheng et al., 2014; Jiang and Kobayashi, 2017; Zhang et al., 2021). LbL drug administration has showed some advantages in the precise control of size, or membrane thickness at the nanoscale level (Balabushevich et al., 2003; Xing et al., 2007). Although great success has been obtained with these LbL-modified INS therapies in controlled release, they exhibited a slow rate of INS release, which restricted timely BGL control, probably because of mass transport limitation (Ravaine et al., 2008). The rate of INS release needs to be improved to enhance the effects of glycemic control.

Blood glucose-activated drug release systems allow rapid and precisely controlled responses to changes in BGLs, thereby ensuring good glycemic control (Xia et al., 2018). In the past

few decades, many studies have focused on developing glucose-responsive systems capable of continuously delivering accurate levels of INS in response to the BGL because it is immediate and effective (Chen et al., 2011; Paez et al., 2013; Li et al., 2015; Llanos et al., 2015; Kompala and Neinstein, 2022). To achieve the desired glucose-activated INS release, glucose oxidase (GOx) and a positively charged polymer were assembled with INS to form multilayer films (Chen et al., 2012). These multilayer films showed a linear release and exhibited the desired on–off sensitivity in response to stepwise glucose challenge. Gu et al. also reported that a useful glucose-mediated INS delivery platform consisting of GOx exhibited good results (Gu et al., 2013). GOx plays a major role in the construction of glucose-activated controlled INS release devices (Chu et al., 2012).

An anionic polymer can rapidly convert back to a cationic polymer in acidic environments within seconds. In this study, mixed multiple layer-by-layer (mmLbL)-INS microspheres were developed for glucose-mediated INS release and an enhanced hypoglycemic effect for diabetes care (Figure 1). The mmLbL-INS microspheres were constructed with one, two, and four layers of the polyelectrolyte LbL assembly at a ratio of 1:1:1. We anticipate that the resulting mmLbL-INS microspheres can be used for glucose-regulated INS delivery to enhance the hypoglycemic effect and maintain blood glucose homeostasis to reduce complications in diabetic patients.

Materials and methods

Materials and animals

Poly (allylamine hydrochloride) (PAH, MW ≈ 60,000) was purchased from Alfa Aesar Organics (Ward Hill, MA). Recombinant cow INS (potency: 27 U/mg) was obtained from Bomei Biotechnology (Hefei, China). Citraconic anhydride and poly (styrene sulfonate) (PSS) were purchased from J&K Scientific (Beijing, China). GOx was obtained by Tokyo chemical industry (Tokyo, Japan). Streptozocin (STZ) was purchased from Sigma-Aldrich, (St. Louis, MO, United States). The dialysis bag (molecular cutoff, 3500 Da) was purchased from Sangon Biotech (Shanghai, China). All other reagents were used without further purification unless noted.

The Sprague–Dawley (SD) rats (275–300 g) were provided by the Experimental Animal Center of Nantong University. All animal experiments were performed in compliance with all relevant ethical regulations and institutional guidelines provided by the Division of Comparative Medicine at Nantong University.

Synthesis of charge-shifting anionic polymers

The synthetic route used for degradable anionic polymers is shown in Figure 1B, which was reported in a previous paper (Liu et al., 2008). Briefly, 100 mg PAH was dissolved in 1.0 M NaOH (4 ml) and stirred until completely dissolved. Then, 400 μL citraconic anhydride was added dropwise to PAH solution, and aqueous NaOH was added as necessary to maintain the pH above 8. Finally, the resulting reaction mixture was placed in dialysis bag (MWCO = 3500) and no reacting parts were removed by dialysis with water (pH > 7.4) for 24 h.

Preparation of premixed LbL-INS microcapsules

The cores of the microcapsules were fabricated according to early reported (Bosio et al., 2014). In brief, 0.35 g Na_2CO_3, 0.02 g PSS and certain amounts of INS was added to 10 ml distilled water, then 10 ml $CaCl_2$ solution (0.33 M) was added and vigorous stirred for 10 s. The obtained microparticles were washed for three times and were separated by centrifugation.

Multilayered films were fabricated on the INS microcapsules using an alternate dipping procedure according to the following general protocol: microcapsules are submerged in a solution of anionic polymers for 5 min, and washed with water (pH > 7.4), anionic polymers modified microcapsules were submerged in a solution with excess of PAH for 5 min, and washed. The following two, three and four bilayers were fabricated in the same way by alternating adsorptions of anionic polymers and PAH as shown in Figure 1A. The premixed LbL-INS microcapsules with 1, 2, four layers at the rate of 1:1:1 was used in this study.

Scanning electron microscopy and zeta potentials

To investigate morphological changes in mmLbL-INS microspheres after the LbL process, the morphologies of $CaCO_3$-INS and four-bilayered microspheres were selected for characterization. The surface morphology of mmLbL-INS microspheres corroded in different pHs was also investigated through scanning electron microscopy (SEM) (JSM-6700F, JEOL, Japan) on conductive adhesive tapes (Briones et al., 2010).

LBL deposition of anionic polymers/PAH on the particles and the charge conversion in different pH were qualitatively monitored by measuring the zeta potentials of the coated particles by using Zetasizer Nano ZS (Malvern, Worcestershire, United Kingdom).

Drug loading content

According to our previous study, a HPLC detection method was established to determine the INS concentration

(Xia et al., 2018). HPLC was performed using a LC-2030 series (Shimadzu Corporation, Japan).

Then, 1, 3, 5, and 10 mg of INS (WT) was dissolved in $CaCl_2$ solution in advance, followed by the preparation of the four-bilayered LbL-INS microspheres. INS was encapsulated in the LbL-INS microspheres using a hypotonic dialysis method. The LbL-INS microspheres (3 mg/ml) were dispersed in dilute hydrochloric acid, and a clear solution was used for measurement with HPLC. The loading content can be calculated as follows.

$$\text{Drug loading content (\%)} = \frac{\text{Total mass of INS in the microspheres}}{\text{Total mass of the microspheres}} \times 100\%$$

Release rate tests

After being suspended in 100 mg/dl (equivalent of 5.6 mM) D-glucose for 10 days, the mmLbL-INS microspheres were incubated in PBS with 400 mg/dl (equivalent of 22.2 mM) glucose *in vitro*. The INS released from the mmLbL-INS microspheres was collected at predetermined time intervals and detected through HPLC. Then, the release rates were calculated.

In vitro testing of release behavior of mmLbL-INS microspheres and fluorescence microscopy analysis

To verify the effect of "charge-conversional", LbL-INS microspheres were resuspended in PBS containing different glucose concentrations at 37°C to study the INS release behavior. At predetermined times, the amounts of INS released into the supernatant was determined through HPLC, and morphological changes were investigated through SEM.

INS-FITC (green) and rhodamine B (red)-modified GOx were packed in the LbL-INS microspheres and resuspended in PBS containing different glucose concentrations. Fluorescence microscopy was performed using a Leica DM 2500 microscope (Wetzlar, Germany) at the same laser power.

In vivo oral glucose tolerance test in STZ diabetic rats

STZ diabetic rats were prepared by treated with STZ (50 mg/kg) into male SD rats. The rats were considered diabetic if their plasma glucose levels were ≥10 mM (Shao et al., 2021).

The diabetic rats were separated into three groups (n = 8): Control group: 1 ml PBS was subcutaneously injected; $CaCO_3$-INS group: 1 ml of 0.035 mg/ml $CaCO_3$-INS microspheres (the diabetic rats treated with >0.035 mg/ml $CaCO_3$-INS microspheres died within 15 min because of hypoglycemia. So, in the following studies, 0.035 mg/ml of $CaCO_3$-INS microspheres were used in *in vivo* studies); and mmLbL-INS microspheres group: 1 ml of mmLbL-INS microspheres was subcutaneously injected. The oral glucose tolerance test (OGTT) was performed as described by Kim (Kim et al., 2016). In brief, diabetic rats were orally administered glucose (2.0 g/kg b.w), blood was collected from the tail vein to measure blood glucose and INS concentrations. The plasma glucose was measured using a hand-held glucometer at regular intervals (0, 15, 30, 60, 120 min). Blood was collected from the tail vein 0, 15, 30, 45, 60, 75, 90, 105 and 120 min after glucose administration. The blood INS was then quantified via HPLC as previous report (Xia et al., 2018).

Long-term effect of mmLbL-INS microspheres

The diabetic rats were subcutaneously injected with PBS (blank), $CaCO_3$-INS microspheres (0.035 mg/ml), and mmLbL-INS microspheres (1 mg/ml) into the back. Each diabetic rat was individually housed in metabolic cages and fed with maintenance diets (Xietong Engineering Co., Ltd, referring to the national standard GB 14924.1-2001) 3 times daily. 0.5 h after every feeding, leftover food was removed, and feed intakes were measured. After feeding for 2 h, BGLs were measured.

Hematological indices

Hematological parameters such as hematocrit (HCT), released hemoglobin (HGB), mean corpuscular volume (MCV), mean corpuscular hemoglobin (MCH), and mean corpuscular hemoglobin concentration (MCHC) were determined using an HEMAVET 950FS Hematology System analyzer after the administration of LbL-INS microspheres for 24 h.

Blood biochemistry index

After administering mmLbL-INS microspheres for 2 days, the levels of liver function markers, including alkaline phosphatase (ALP), alanine aminotransferase (ALT), and aspartate aminotransferase (AST), the kidney function marker urea nitrogen (BUN), as well as creatinine (Cr), were determined using an automated biochemical analyzer (Trilogy, France).

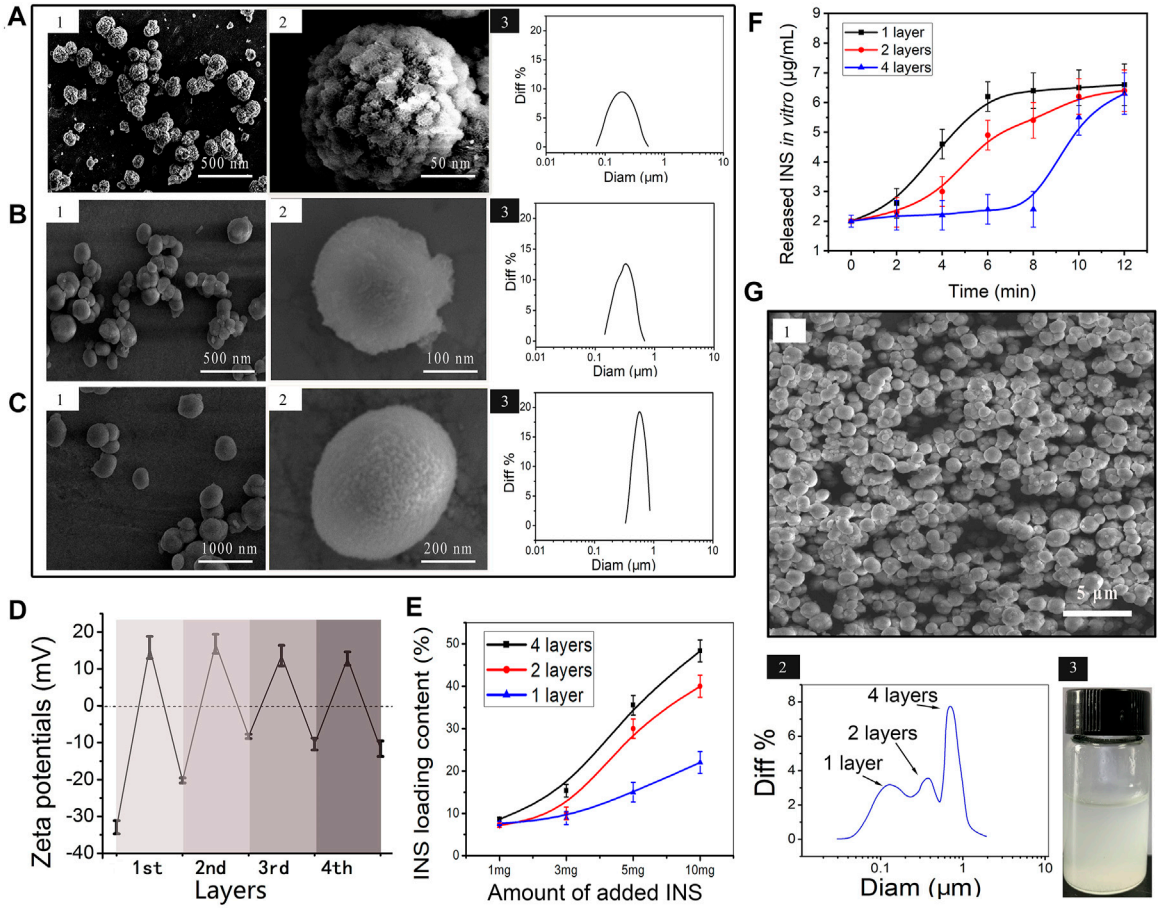

FIGURE 2
Characterization of the mmLbL-INS microcapsules. **(A–C)** SEM images and DLS results of LbL-INS microcapsules with **(A)** one layer, **(B)** two layers, and **(C)** four layers. (1) SEM images, (2) high-magnification SEM image, (3) dynamic light scattering (DLS) results. **(D)** Zeta potentials of multiple LbL-INS microcapsules with different layers. **(E)** Relationship between the initial INS concentration and INS loading content in the LbL-INS microcapsules. **(F)** INS release behavior of multiple LbL-INS microcapsules in pH 6.5 solution. **(G)** SEM images, DLS results, and the image of mmLbL-INS microcapsules.

Statistical analysis

All values were averaged and expressed as the mean ± standard error of the mean. Analysis of variance was performed, with dialysis time, initial INS concentration, and volume ratio as three independent variables. p values ≤0.05 were considered significant.

Results

Preparation of LbL-INS microspheres

In this study, the microspheres were prepared by the LBL assembly of multilayered polyelectrolyte films, with repeat assembly sequences polycation PAH and anionic polymer, as shown in Figure 1B. Morphological changes in the LbL-INS microcapsule with different polyelectrolyte films were monitored through SEM (Figures 2A–C). $CaCO_3$-INS microparticles with the one-layer polyelectrolyte film showed clearly visible wrinkles and inward depression on the surface (Figure 2A). The surface of the LbL-INS microspheres became smooth and glossy as the layers increased (Figures 2B, C). The average diameter of the LbL-INS microspheres, through dynamic light scattering (DLS), increased slightly with an increase in the number of layers (Supplementary Figure S1).

The LbL assembly process was also monitored through zeta-potential measurements (Figure 2D). The uncoated $CaCO_3$ microparticles produced a negative zeta-potential (−32 mV). The average zeta-potential value for the first layer increased to 14 mV, corresponding to the adsorption

of the polycation PAH, that for the second layer (−20 mV) corresponded to the adsorption of the anionic polymer, that for the third layer (15 mV) corresponded to another layer of PAH, and that for the fourth layer (−10 mV) corresponded to a new layer of anionic polymer. Alternating zeta-potentials were obtained with the subsequent deposition of PAH and polyanions, suggesting the gradual adsorption of the PAH/anionic polymer layers on the $CaCO_3$-INS microparticles.

Not unexpectedly, the loading content was significantly positively correlated with the initial INS concentration, not only in one-layer LbL-INS microspheres but also in two- and four-layer LbL-INS microspheres (Figure 2E). Increasing the layers of microspheres resulted in high INS loading content. Combining the results in Figures 1A–C, we speculated that the polycation PAH and anionic polymer modified on the $CaCO_3$-microparticles could prevent INS leakage, leading to an increase in INS loading content. In consideration of the loading efficiency and cost-savings, in the following experiment, an initial INS concentration of 5 mg/ml was adopted to achieve the acceptable encapsulation concentration in mmLbL-INS microspheres.

The hyperglycemia response time of LbL-INS microspheres with different bilayers was studied (Figure 2F). The one-layer LbL-INS microspheres took approximately 4.1 ± 0.4 min to transform to explosive release. Relatively, the multilayered polyelectrolyte films on the four-layer LbL-INS microspheres took as long as 9.3 min to remove and start INS release. The retention time of LbL-INS microspheres extended with an increase in the number of layers. The aforementioned results revealed that mmLbL-INS microspheres with different layers showed different glucose-activated response rates. According to the characteristics of INS clinical needs (Gracia-Ramos et al., 2016; Maiorino et al., 2017), premixed INS analogs (rapid-acting and long-acting analog ratio in varying proportions) represent an alternative treatment for type 2 diabetes. In this study, mmLbL-INS microspheres constructed with one, two, and four layers at a ratio of 1:1:1 and the INS concentration of 0.98 ± 0.13 mg/ml were used in the following studies. The SEM, dynamic light scattering, and images of the mixture of LbL-INS microspheres are presented in Figure 2G. The mmLbL-INS microspheres with different layers maintained their respective structure and size.

In vitro testing of glucose-activated release behavior

Next, we investigated the glucose-activated release behavior of mmLbL-INS microspheres in response to BGLs. To validate our design, mmLbL-INS microspheres were incubated in PBS (pH 7.4) at 37°C with 25–400 mg/dl glucose and INS release was monitored by HPLC. As shown in Figure 3A, increasing the glucose concentration to >100 mg/dl would greatly accelerate INS release.

In glycemia, GOx could convert glucose to glucose acid (Botezatu et al., 2021). As more and more lactic acid is produced, pH falls. Based on the principle, the mmLbL-INS microspheres were expected to show glucose-activated release behavior. To examine whether the glycemia control effect of the INS microspheres was due to sustained INS release or glucose-responsive INS release, the cumulative INS released from mmLbL-INS microspheres were determined in normal glycemia or hyperglycemia, respectively. As shown in Figures 3B,C, incubation of mmLbL-INS microspheres at the normal glucose level resulted in a slightly increased cumulative release of INS within 15 min. When the glucose concentration increased to the hyperglycemic level, >60% of INS was released by 15 min from the mmLbL-INS microspheres group. As expected, the cumulative release rate of $CaCO_3$-INS microspheres increased straightly not only in hypoglycemia but also in normoglycemia.

To further assess glucose-responsive INS release, FITC-INS was used to trace the INS release behavior of mmLbL-INS microspheres. When 2 ml of the mmLbL-INS microspheres were imaged in the presence of 50 and 100 mg/dl glucose (Figures 3D,E), slight green fluorescence was found, clearly indicating that almost no INS released. When these mmLbL-INS microspheres were in hyperglycemia (Figures 3F,G), the fluorescence intensity of the supernatant enhanced remarkably (Supplementary Figure S2). The results indicated that the sensitivity of mmLbL-INS microspheres to BGLs can enhance the INS release rate.

To examine the stability of the glucose activity effect of mmLbL-INS microspheres incubated in the normoglycemic solution (100 mg/dl of glucose). After immersion for 10 days, INS concentrations in the supernatant were stable (Figure 3H). Then, the glucose concentration was immediately adjusted to 400 mg/dl, the concentration of released INS rose quickly and reached 27 μg/ml within minutes. The INS concentration in the supernatant showed a steady rise with the long-term storage of mmLbL-INS microspheres in a high sugar solution (400 mg/dl) (Figure 3I).

Furthermore, the INS release profile of mmLbL-INS microspheres exhibited a pulsatile pattern (close-loop) when the glucose concentration was cyclically varied between the normal and hyperglycemic levels for several repetitions, as shown in Figure 3J. The mmLbL-INS microspheres responded to changes in glucose levels, and the INS release rate increased to over 25 μg/mL/h in hyperglycemic state.

As more and more lactic acid was produced in hyperglycemia, because GOx in the mmLbL-INS microspheres converted glucose to glucose acid, pH fell. The charge-shifting anionic polymers on the mmLbL-INS microspheres disrupted the ultrathin polyelectrolyte multilayers in acidic media and the INS released. Contrarily, in normal glycemia, the INS released behavior stopped in the mmLbL-INS microspheres as the pH value came to normal. These results also confirmed that GOx maintains its bioactivity even after 10 days, and thus makes the delivery system highly stable.

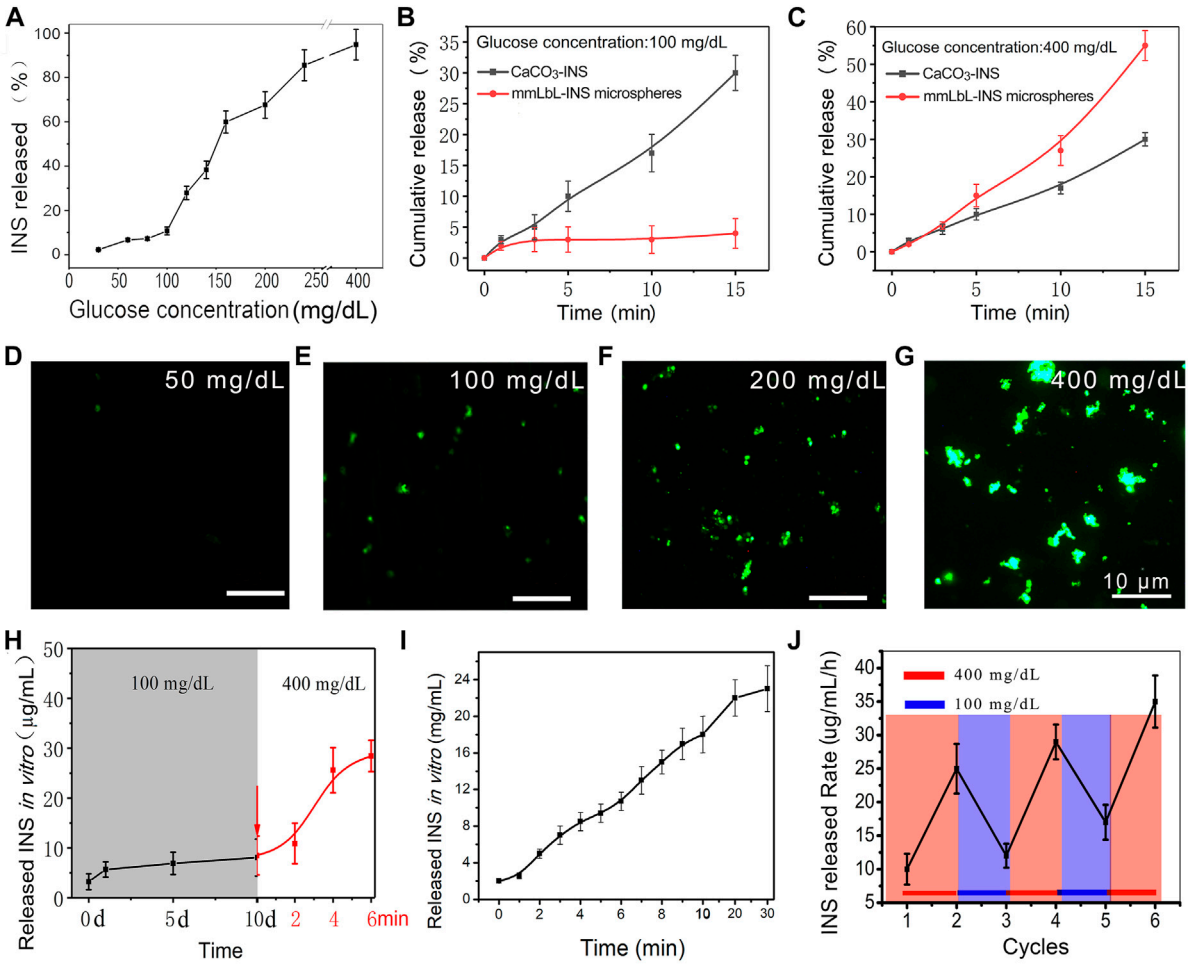

FIGURE 3
Glucose-activated INS release behavior of the mmLbL-INS microcapsules. **(A)** The INS release behavior at different glucose concentrations **(B and C)** Cumulative INS release behavior of mmLbL-INS microcapsules immersed in 100 and 400 mg/dl glucose solutions. **(D–G)** Fluorescence images of mmLbL-INS microcapsules that released INS into the medium after being immersed in different glucose concentrations (green fluorescence: FTIC-INS). **(H)** Stability analysis of the glucose activity effect. After being stored in 5 mmol/L glucose solution at 4°C for 10 days, the mmLbL-INS microcapsules released INS *in vitro* (read line) when immersed in 400 mg/dl glucose solution. **(I)** INS release behavior of the mmLbL-INS microcapsules changed over time in 400 mg/dl glucose solution. **(J)** INS release exhibited a pulsatile profile in response to different glucose concentrations. The mmLbL-INS microcapsules were immersed in normal (100 mg/dl) or hyperglycemic level (400 mg/dl) solution for several repetitions.

Release mechanism and charge-shifting effect

Polyelectrolyte films and GOx, modified on the surface of LbL-INS microspheres, were expected to realize the glucose-responsive INS releasing behavior. Then, FITC was used as a tracer of INS, and visible green fluorescence observed in the solution further confirmed the absence of INS in the LbL-$CaCO_3$-INS microspheres (Figure 4A). From the confocal images of LbL-INS microspheres, a red color (rhodamine B-modified GOx) could be found on the surface of the LbL-INS microspheres. In the overlay image, the green spheres were covered by red loops, which confirmed that poly-GOx was modified on the LbL-INS microspheres.

The pH of body (interstitial) fluids can be reduced by GOx, which can convert glucose to gluconic acid (Wu et al., 2011). The GOx, on the surface of LbL-INS microspheres, causing a local decrease in pH with an increase in glucose concentrations (Figure 4B). GOx catalyzes the conversion of glucose to gluconic acid as follows:

$$\text{glucose} + O_2 + H_2O \rightarrow \text{gluconic acid} + H_2O_2$$

The charge-shifting anionic polymers can disrupt the ultrathin polyelectrolyte multilayers in acidic media. Based on

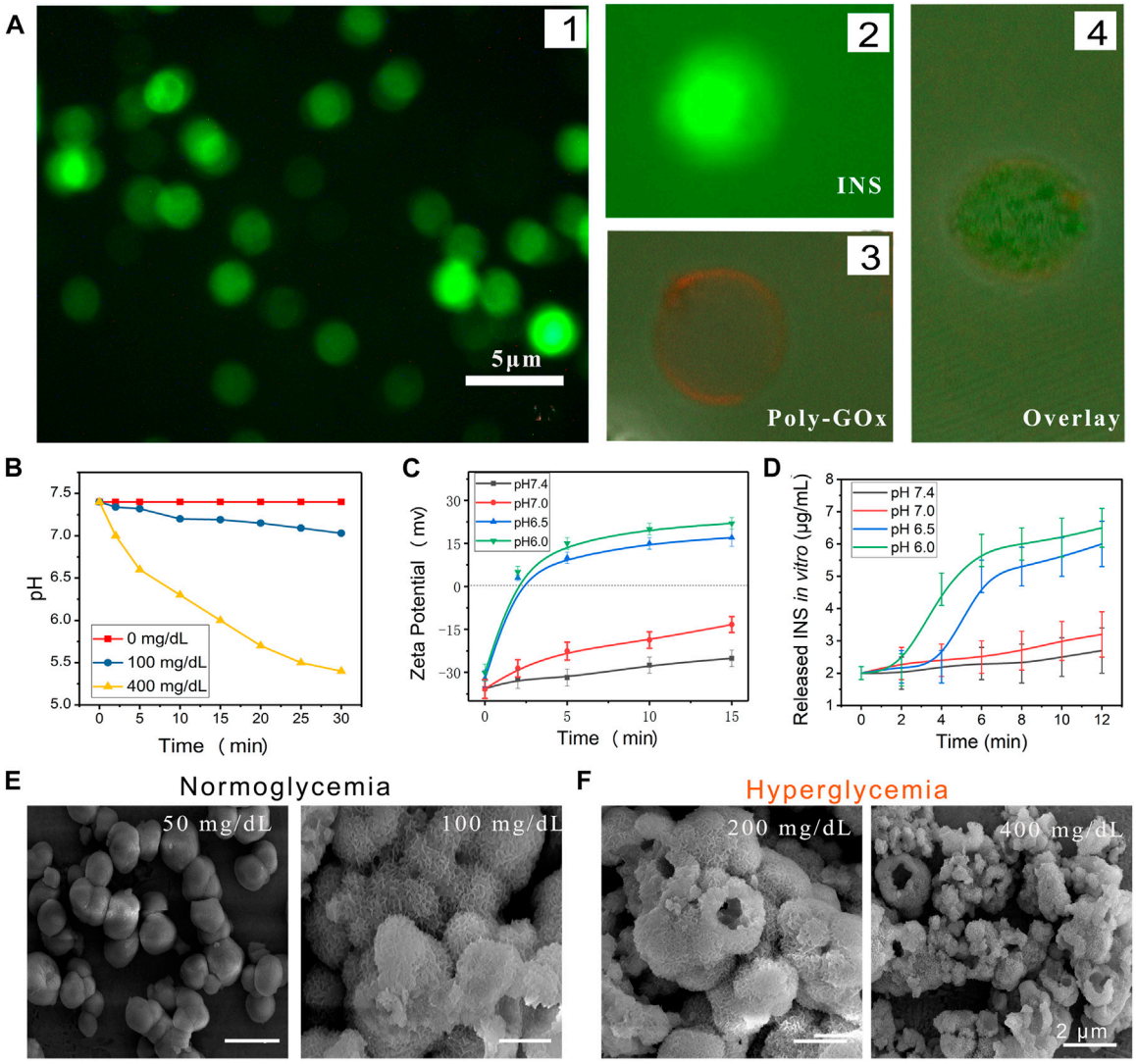

FIGURE 4
The mechanism of glucose-activated INS release behavior of mmLbL-INS microcapsules. **(A)** Fluorescence image of mmLbL-INS microcapsules. FITC-labeled INS (green) and rhodamine B (red)-modified biotin-GOx were used to fabricate mmLbL-INS microcapsules. **(B)** Relevant pH changes observed in different incubation solutions with mmLbL-INS microcapsules. **(C)** Charge conversion of anionic polymers at different pH. **(D)** INS release behavior of mmLbL-INS microcapsules in different pH solutions. **(E,F)** SEM of mmLbL-INS microcapsules immersed in different glucose concentrations.

this understanding, we designed a glucose-activated INS release system by using charge-shifting anionic polymers. As the normal blood sugar range is 70–100 mg/dl (Barkoudah and Weinrauch, 2015), the *in vitro* release of INS from the mmLbL-INS microspheres was evaluated in different concentrations of glucose within the solutions. To examine the glucose-responsive dissociation of mmLbL-INS microspheres, the microspheres were collected in micro-centrifuge tubes and incubated with PBS solutions with 100 (corresponding to the normal level) or 400 mg/dl (corresponding to the hyperglycemic level) glucose. In Figure 4B, the recorded pH values decreased from 7.4 to 5.4 within 30 min in 400 mg/dl glucose, confirming the enzymatic conversion of glucose to gluconic acid. By contrast, both control samples (no glucose and 100 mg/dl glucose) showed no observable changes in pH (pH > 7.0).

The polyelectrolyte multilayer was thus expected to show a charge conversion behavior in the acid environment (Figure 4C). Compared with incubation at pH 7.4 and 7.0, the zeta potential of the polyelectrolyte multilayer increased significantly when incubated at pH 6.5 and 6.0. The zeta

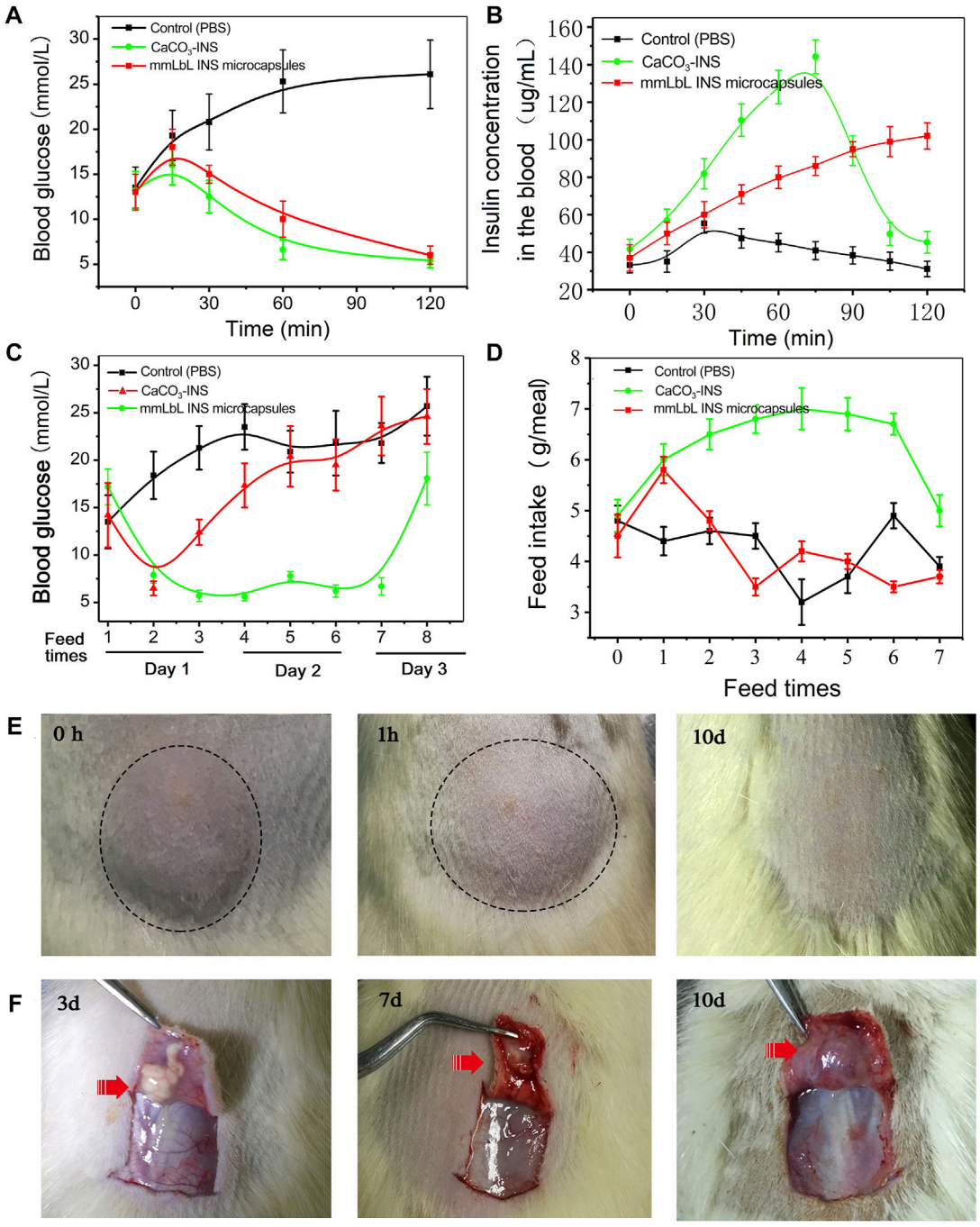

FIGURE 5
In vivo glycemic control tests results of mmLbL-INS microcapsules. **(A)** Change in glucose concentrations and **(B)** change in the INS concentration of the whole blood in the oral glucose tolerance test. **(C)** Long-term plasma blood glucose concentration. **(D)** Food intake in diabetic rats administered STZ. **(E)** Pictures of the injected set of mmLbL-INS microcapsules on different days. **(F)** The change of mmLbL-INS microcapsules in subcutaneous.

potential became positive within 2 min, despite the potential of the polyelectrolyte multilayer slowly increasing with incubation at pH 7.4 and 7.0.

Charge-shifting of the net charge of the polymer leads to changes in the nature of ionic interactions in the multilayers and promotes film disruption and the release of cationic film components (Figure 4D).

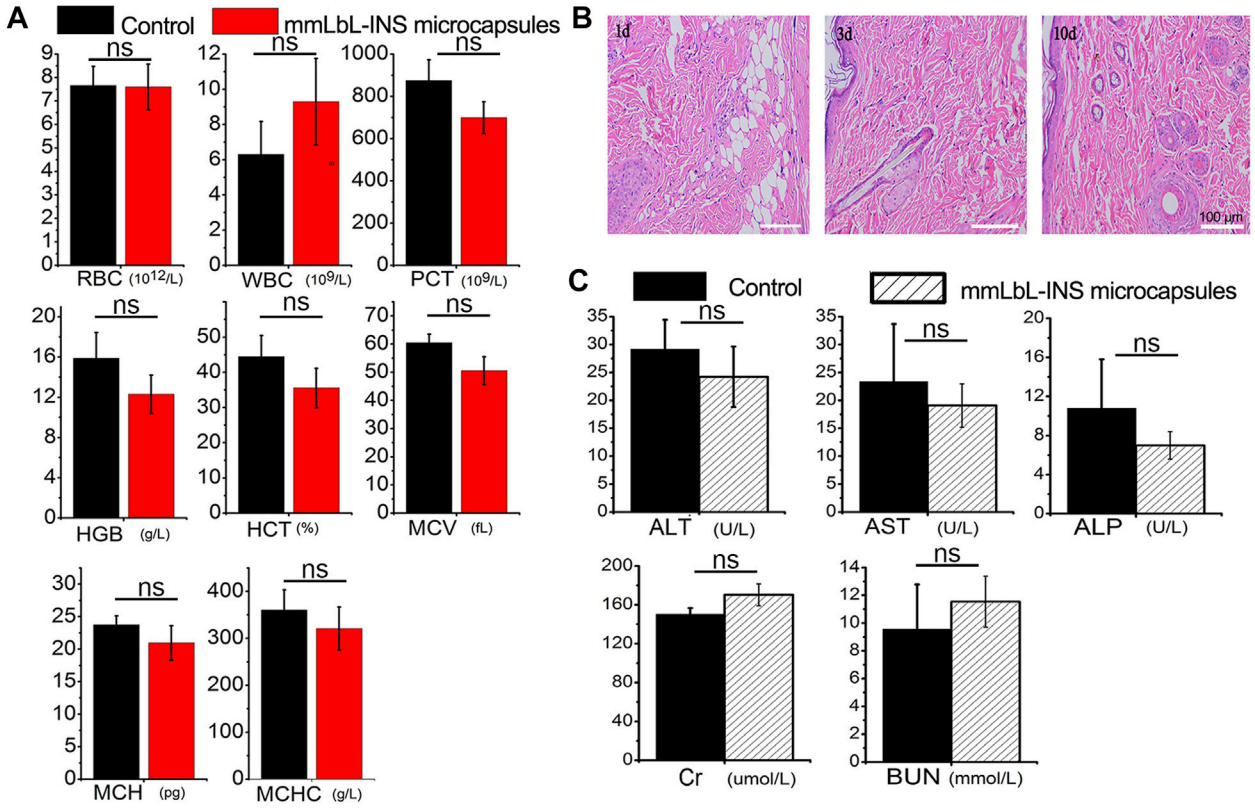

FIGURE 6
Biosafety of the mmLbL-INS microspheres. **(A)** Hematological parameters after administration of mmLbL-INS microcapsules for 3 days. Red blood cell (RBC), white blood cell (WBC), platelet count (PCT), hemoglobin (HGB), hematocrit (HCT), mean corpuscular volume (MCV), mean corpuscular hemoglobin (MCH), and mean corpuscular hemoglobin concentration (MCHC) were chosen. **(B)** H&E staining of the injected set. Bar = 100 μm. **(C)** Results of liver function markers, including alkaline phosphatase (ALP), alanine aminotransferase (ALT), and aspartate aminotransferase (AST), the kidney function marker urea nitrogen (BUN), and creatinine (Cr). Ns = not statistically different. (n = 8).

To offer a rapid glucose responsibility to these mmLbL-INS microspheres, GOx was conjugated with charge-conversional polyelectrolyte multilayers in the presence of N, N′-carbonyldiimidazole. When the BGL increased, GOx catalyzed the conversion of glucose to gluconic acid in the presence of oxygen, which provided enough hydrogen ion, leading to the low pH environment (Qiu et al., 2009). When exposed to low pH environments, hydrolysis of citraconic amide side chains of the charge-shifting anionic polymer yields a cationic polymer.

Morphological changes in the mmLbL-INS microspheres immersed during the course of glucose-activated INS release were also investigated through SEM (Figures 4E,F). The mmLbL-INS microspheres submerged in 50 mg/dl of glucose showed negligible INS release and remained intact. By contrast, the LbL-INS microspheres were found to corrode the polymer and rupture the $CaCO_3$ shell when exposed to a hyperglycemic environment. The $CaCO_3$-INS microparticles changed from smooth to inward depression on the surface. Their fluorescence intensity increased with the glucose concentration. Collectively, these results indicate the charge-shifting effect of the LbL-INS microspheres and the subsequent glucose-mediated and pH-dependent INS release.

In vivo OGTT result

The OGTT was used to determine the regulation of the BGL in STZ-induced diabetic rats after treatment with 1) PBS, (b) 0.035 mg/ml $CaCO_3$-INS microspheres, and (c) 1 mg/ml mmLbL-INS microspheres. Not surprisingly, the BGLs increased rapidly and were maintained over 25 mM (equivalent of 450 mg/dl) after 1 h of gastric perfusion of glucose in the PBS-treated control group (Figure 5A). As expected, the BGLs were well-controlled in the normal range of 3.9–6.1 mM within 2 h in the $CaCO_3$-INS and mmLbL-INS microspheres groups, like the normal rats (Supplementary Figure S3). The blood INS levels were also measured as shown in Figure 5B. More and more INS was found as time elapsed

when higher amounts of $CaCO_3$-INS microspheres were applied. A peak release behavior was observed in the mmLbL-INS microspheres group, and the INS release amount decreased as the glucose concentration returned to the normal blood glucose level (Supplementary Figure S4).

mmLbL-INS microspheres control hyperglycemia in diabetic rats

To examine the efficacy of mmLbL-INS microspheres in diabetes treatment, STZ-induced diabetic rats were subcutaneously injected with PBS solution, $CaCO_3$-INS (0.035 mg/ml INS), and mmLbL-INS microspheres (1 mg/ml INS). Figure 5C showed that the mmLbL-INS microspheres could maintain normoglycemia glucose levels in diabetic rats for more than seven feed times (approximately 3 days), after which the levels gradually increased, possibly due to the depletion of the reservoir INS with time. By contrast, the control group (PBS treated) demonstrated elevated BGLs between 230 and 450 mmol/L. As the $CaCO_3$-INS group released INS after dosing (could not release INS response to BGL), the BGL decreased to the normoglycemic level at first, and then increased directly with the depletion of the reservoir INS. Furthermore, the diabetic rats in the mmLbL-INS microspheres treatment group took more fodder, with no mortality (Figure 5D and Supplementary Figure S5). By contrast, diabetic rats in the control and $CaCO_3$-INS groups took less fodder because of diabetic ketoacidosis. Then, in order to maintain the BGL in normoglycemia as normal rats, the diabetes should administrate mmLbL-INS microspheres every 3 days.

To further investigate the *in vivo* biocompatibility and degradability of the mmLbL-INS microspheres, the sizes of skin protrusion caused by the subcutaneous injection were monitored over time (Figure 5E). The average lump size in the injection sites of rats treated with mmLbL-INS microspheres rapidly decreased in 1 h, as the tissue absorbed moisture into the mmLbL-INS microspheres. In the following days, the average lump size steadily decreased, suggesting that glucose-mediated degradation was substantially triggered (Supplementary Figure S6). No significant skin protrusion can be found after 10 days maybe due to the clearance of phagocytosis (Figure 5F).

Biosafety of mmLbL-INS microspheres

The mmLbL-INS microspheres showed satisfactory biocompatibility *in vitro* (Supplementary Figure S7). A complete blood analysis was performed after injection for 48 h, all parameters of the treated group were normal (Figure 6A). No inflammation was found around the injection site and no pathologic changes were noted through hematoxylin and eosin staining (Figure 6B). The liver function markers and the kidney function marker were normal (Figure 6C), suggesting no injury in rats after treatment with the mmLbL-INS microspheres.

Discussion

Due to the short half-life of INS *in vivo*, directly providing exogenous insulin may lead to multiple injections with careful dosing (Ling and Chen, 2013). Such widely applied treatment can not realize the on-demand release of insulin, leading to the poor patient compliance, and sometimes hypoglycemia, which probably results in the potential risk of brain damage or death (Alloubani et al., 2018; Kawada, 2018). Developing a "closed-loop" system capable of glucose-activated INS control release behavior was of great significance. In this study, the mmLbL-INS microspheres were stable in physiologically relevant environments. Once the blood sugar level increased, GOx converted a dramatic change in the environmental glucose level to a pH stimulus, and the outer anionic polymer was converted readily back to a cationic polymer through amide hydrolysis. The glucose-activated changes led to changes in the nature of ionic interactions in the multilayers and promoted film disruption. The INS release behavior was accomplished through premixed multiple LbL-INS microspheres with different retention times of INS release.

Various glucose-responsive controlled INS release strategies have been approved to maintain normoglycemia for diabetic patients (Chen et al., 2011; Paez et al., 2013; Li et al., 2015; Llanos et al., 2015; Abebe et al., 2022). An INS reservoir (GOx, CAT, and BSA) and could counter hyperglycemia in diabetic rats over a 1-week period (Chu et al., 2012). A glucose mediated INS delivery (consisting of GOx) presented a long-time diabetes management through an injectable nano-network was reported (Gu et al., 2013). A calcium carbonate templated INS microparticles also was reported for improving the efficiency of INS delivery by inhalation (Schmidt et al., 2014). PAH was chosen as the model polymer in preparation of mesoporous hybrid microcapsules, with high and tunable permeability, good stability and multiple functionalities (Jiafu et al., 2013). Although, great success has been obtained as these INS replacement therapies controlled blood glucose by close-loop release behavior, they showed a slow glucose-responsive rate as the mass transport limitation (Ravaine et al., 2008). There was a lag time of more than 2 h in hyperglycemia, which is not suitable for the practical application (Paez et al., 2013). One of the most critical challenges in diabetes treatment is to design self-regulated INS delivery systems, which could control INS release as soon as possible in response to the change of BGL, just like artificial pancreases. In this study, GOx was assembled with the anionic polymer to construct an ultra-fast glucose-activated anionic polymer. The anionic polymer was regarded stable in

physiologically relevant environments and hydrolysis of the charge-shifting anionic polymer under acidic conditions yields a cationic polymer. Based on the LbL assembly of multilayered polyelectrolyte films, with repeat assembly sequences polycation PAH and anionic polymer, we fabricated LbL-INS microspheres with different layers and mixed multiple LbL-INS (mmLbL-INS) microspheres proportionally to control the INS release rate in response to the BGL. The results of the mmLbL-INS microspheres showed that it was glucose-mediated INS release and an enhanced hypoglycemic effect for diabetes care. Once the blood sugar level increased, GOx converted a change in the environmental glucose level to a pH stimulus, and the outer anionic polymer was converted readily back to a cationic polymer through amide hydrolysis upon exposure to acidic environments. The results of *in vitro* INS release suggested that glucose can modulate the mmLbL-INS microspheres in an ultrafast glucose activated INS control release and pulsatile profile. *In vivo* studies also validated that this formulation enhanced the hypoglycemic effect in STZ-induced diabetic rats within 2 h of subcutaneous administration. Clinically, patients start on a total daily dose of about 0.5 U/day of INS per kg, and about 30 U of INS is needed daily (adult body weight ~60 kg). From the results in Figure 2, the INS concentration in mmLbL-INS microspheres could achieve (0.98 mg/ml, roughly corresponding to 28 U/mL). That is to say, a single injection of this mmLbL-INS microspheres into the diabetes patient can maintain the BGL in the normal range about 1 day. To improve the feasibility of clinical application, we could increase the INS content in mmLbL-INS microspheres or increase the injection volume.

In conclusion, this study presented a new glucose-activated mmLbL-INS microsphere INS delivery system as a promising therapeutic strategy in the sustained treatment of hyperglycemia. The LBL assembly of the polyelectrolyte could increase the stability of $CaCO_3$-INS, and glucose responsiveness was realized through the charge-shifting effort in aqueous environments by using GOx, which thus resulted in an increased INS release rate, without compromising the BGL response time. *In vivo* results showed that mmLbL-INS microspheres could overcome hyperglycemia within 2 h and maintain the baseline glucose level up to 2 days. This glucose-activatable LbL microspheres system can be a promising alternative in diabetes therapy and serve as a powerful tool for constructing a precisely controlled INS release system.

Data availability statement

The original contributions presented in the study are included in the article/Supplementary Material, further inquiries can be directed to the corresponding author.

Ethics statement

The animal study was reviewed and approved by The procedures used in our study were approved by the Committee of the Animal Research of Nantong University (20210631-033), and followed the guidelines the Use of Animals in Research of the International Association for the Study of Pain and the directive of the European Parliament (2010/63/EU).

Author contributions

DX and YY conceived the idea and designed the experiments. YY and XW, did the synthesis, characterization. YY and XY conducted the *in vitro* experiments, YY, QZ and SC did the *in vivo* analyses. YY, XW, XY, and DX analyzed all the data and wrote the manuscript. All the authors have proof-read this article and approved its publication.

Funding

This study was funded by the Science and Technology R&D Foundation of Nantong City (JC2020069, JC2020032), and the large instruments open foundation of Nantong university.

Conflict of interest

The authors declare that the research was conducted in the absence of any commercial or financial relationships that could be construed as a potential conflict of interest.

Publisher's note

Supplementary material

The Supplementary Material for this article can be found online at: https://www.frontiersin.org/articles/10.3389/fbioe.2022.996763/full#supplementary-material

References

Abebe, A., Wobie, Y., Kebede, B., Wale, A., Destaw, A., and Ambaye, A. S. (2022). Self-care practice and glycemic control among type 2 diabetes patients on follow up in a developing country: a prospective observational study. *J. Diabetes Metab. Disord.* 21 (1), 455–461. doi:10.1007/s40200-022-00995-4

Akhmedov, D., Braun, M., Mataki, C., Park, K. S., Pozzan, T., Schoonjans, K., et al. (2010). Mitochondrial matrix pH controls oxidative phosphorylation and metabolism-secretion coupling in INS-1E clonal beta cells. *FASEB J.* 24 (11), 4613–4626. doi:10.1096/fj.10-162222

Alloubani, A., Saleh, A., and Abdelhafiz, I. (2018). Hypertension and diabetes mellitus as a predictive risk factors for stroke. *Diabetes & Metabolic Syndrome Clin. Res. Rev.* 12, 577–584. doi:10.1016/j.dsx.2018.03.009

Baba, A., Taranekar, P., Ponnapati, R. R., Knoll, W., and Advincula, R. C. (2010). Electrochemical surface plasmon resonance and waveguide-enhanced glucose biosensing with N-alkylaminated polypyrrole/glucose oxidase multilayers. *ACS Appl. Mat. Interfaces* 2 (8), 2347–2354. doi:10.1021/am100373v

Balabushevich, N. G., Tiourina, O. P., Volodkin, D. V., Larionova, N. I., and Sukhorukov, G. B. (2003). Loading the multilayer dextran sulfate/protamine microsized capsules with peroxidase. *Biomacromolecules* 4 (5), 1191–1197. doi:10.1021/bm0340321

Barkoudah, E., and Weinrauch, L. A. (2015). Screening for type 2 diabetes mellitus. *Ann. Intern. Med.* 163 (9), 726. doi:10.7326/L15-5153

Bosio, V. E., Cacicedo, M. L., Calvignac, B., Leon, I., Beuvier, T., Boury, F., et al. (2014). Synthesis and characterization of CaCO3-biopolymer hybrid nanoporous microparticles for controlled release of doxorubicin. *Colloids Surfaces B Biointerfaces* 123, 158–169. doi:10.1016/j.colsurfb.2014.09.011

Botezatu, A., Elizondo, C., Bajec, M., and Miller, R. (2021). Enzymatic management of pH in white wines. *Molecules* 26 (9), 2730. doi:10.3390/molecules26092730

Briones, E., Colino, C. I., and Lanao, J. M. (2010). Study of the factors influencing the encapsulation of zidovudine in rat erythrocytes. *Int. J. Pharm. X.* 401 (1-2), 41–46. doi:10.1016/j.ijpharm.2010.09.006

Chen, X., Luo, J., Wu, W., Tan, H., Xu, F., and Li, J. (2012). The influence of arrangement sequence on the glucose-responsive controlled release profiles of insulin-incorporated LbL films. *Acta Biomater.* 8 (12), 4380–4388. doi:10.1016/j.actbio.2012.08.014

Chen, X., Wu, W., Guo, Z., Xin, J., and Li, J. (2011). Controlled insulin release from glucose-sensitive self-assembled multilayer films based on 21-arm star polymer. *Biomaterials* 32 (6), 1759–1766. doi:10.1016/j.biomaterials.2010.11.002

Chu, M. K., Chen, J., Gordijo, C. R., Chiang, S., Ivovic, A., Koulajian, K., et al. (2012). *In vitro* and *in vivo* testing of glucose-responsive insulin-delivery microdevices in diabetic rats. *Lab. Chip* 12 (14), 2533–2539. doi:10.1039/c2lc40139h

Dmitriev, A. V., Henderson, D., and Linsenmeier, R. A. (2019). Diabetes alters pH control in rat retina. *Invest. Ophthalmol. Vis. Sci.* 60 (2), 723–730. doi:10.1167/iovs.18-26073

Gracia-Ramos, A. E., Cruz-Dominguez, M. D., Madrigal-Santillan, E. O., Morales-Gonzalez, J. A., Madrigal-Bujaidar, E., and Aguilar-Faisal, J. L. (2016). Premixed insulin analogue compared with basal-plus regimen for inpatient glycemic control. *Diabetes Technol. Ther.* 18 (11), 705–712. doi:10.1089/dia.2016.0176

Gu, Z., Aimetti, A. A., Wang, Q., Dang, T. T., Zhang, Y., Veiseh, O., et al. (2013). Injectable nano-network for glucose-mediated insulin delivery. *ACS Nano* 7 (5), 4194–4201. doi:10.1021/nn400630x

Huang, X., Wang, X., Wang, S., Yang, J., Zhong, L., and Pan, J. (2013). UV and dark-triggered repetitive release and encapsulation of benzophenone-3 from biocompatible ZnO nanoparticles potential for skin protection. *Nanoscale* 5 (12), 5596–5601. doi:10.1039/c3nr00090g

Huynh, D. P., Nguyen, M. K., Pi, B. S., Kim, M. S., Chae, S. Y., Lee, K. C., et al. (2008). Functionalized injectable hydrogels for controlled insulin delivery. *Biomaterials* 29 (16), 2527–2534. doi:10.1016/j.biomaterials.2008.02.016

Jiafu, S, Wenyan, Z., Xiaoli, W., Jiang, Z., Zhang, S., Zhang, X., et al. (2013). Exploring the segregating and mineralization-inducing capacities of cationic hydrophilic polymers for preparation of robust, multifunctional mesoporous hybrid microcapsules. *ACS Appl. Mat. Interfaces* 5 (11), 5174–5185. doi:10.1021/am401017y

Jiang, H., and Kobayashi, T. (2017). Ultrasound stimulated release of gallic acid from chitin hydrogel matrix. *Mater. Sci. Eng. C* 75, 478–486. doi:10.1016/j.msec.2017.02.082

Kang, S. (2018). Personalized prediction of drug efficacy for diabetes treatment via patient-level sequential modeling with neural networks. *Artif. Intell. Med. (2017).* 85, 1–6. doi:10.1016/j.artmed.2018.02.004

Kaura Parbhakar, K., Rosella, L. C., Singhal, S., and Quiñonez, C. R. (2020). Acute and chronic diabetes complications associated with self-reported oral health: A retrospective cohort study. *BMC Oral Health* 20 (1), 66. doi:10.1186/s12903-020-1054-4

Kawada, T. (2018). Hyperuricaemia and type 2 diabetes mellitus. *Clin. Exp. Pharmacol. Physiol.* 45, 870. doi:10.1111/1440-1681.12937

Killeen, A. L., Brock, K. M., Dancho, J. F., and Walters, J. L. (2020). Remote temperature monitoring in patients with visual impairment due to diabetes mellitus: A proposed improvement to current standard of care for prevention of diabetic foot ulcers. *J. Diabetes Sci. Technol.* 14 (1), 37–45. doi:10.1177/1932296819848769

Kim, J. Y., Michaliszyn, S. F., Nasr, A., Lee, S., Tfayli, H., Hannon, T., et al. (2016). The shape of the glucose response curve during an oral glucose tolerance test heralds biomarkers of type 2 diabetes risk in obese youth. *Diabetes Care* 39 (8), 1431–1439. doi:10.2337/dc16-0352

Kompala, T., and Neinstein, A. B. (2022). Smart insulin pens: Advancing digital transformation and a connected diabetes care ecosystem. *J. Diabetes Sci. Technol.* 16 (3), 596–604. doi:10.1177/1932296820984490

Li, X., Wu, W., and Li, J. (2015). Glucose-responsive micelles for insulin release. *J. Control. Release* 213, 122–123. doi:10.1016/j.jconrel.2015.05.206

Ling, M. H., and Chen, M. C. (2013). Dissolving polymer microneedle patches for rapid and efficient transdermal delivery of insulin to diabetic rats. *Acta Biomater.* 9 (11), 8952–8961. doi:10.1016/j.actbio.2013.06.029

Liu, X., Zhang, J., and Lynn, D. M. (2008). Polyelectrolyte multilayers fabricated from 'charge-shifting' anionic polymers: A new approach to controlled film disruption and the release of cationic agents from surfaces. *Soft Matter* 4 (8), 1688–1695. doi:10.1039/b804953j

Llanos, P., Contreras-Ferrat, A., Barrientos, G., Valencia, M., Mears, D., and Hidalgo, C. (2015). Glucose-dependent insulin secretion in pancreatic beta-cell islets from male rats requires Ca2+ release via ROS-stimulated ryanodine receptors. *PLoS One* 10 (6), e0129238. doi:10.1371/journal.pone.0129238

Maiorino, M. I., Bellastella, G., Esposito, K., and Giugliano, D. (2017). Premixed insulin regimens in type 2 diabetes: pros. *Endocrine* 55 (1), 45–50. doi:10.1007/s12020-016-0917-6

Paez, J. L., Doiny, D., Estrada, A., Figueroa, J., Filgueiras-Rama, D., and Merino, J. L. (2013). Dronedarone: an option in the treatment of ventricular arrhythmias. *Rev. Espanola Cardiol.* 66 (8), 668–670. doi:10.1016/j.rec.2013.02.008

Qiu, J. D., Wang, R., Liang, R. P., and Xia, X. H. (2009). Electrochemically deposited nanocomposite film of CS-Fc/Au NPs/GOx for glucose biosensor application. *Biosens. Bioelectron. X.* 24 (9), 2920–2925. doi:10.1016/j.bios.2009.02.029

Ravaine, V., Ancla, C., and Catargi, B. (2008). Chemically controlled closed-loop insulin delivery. *J. Control. Release* 132 (1), 2–11. doi:10.1016/j.jconrel.2008.08.009

Sarode, B. R., Kover, K., Tong, P. Y., Zhang, C., and Friedman, S. H. (2016). Light control of insulin release and blood glucose using an injectable photoactivated depot. *Mol. Pharm.* 13 (11), 3835–3841. doi:10.1021/acs.molpharmaceut.6b00633

Schmidt, S., Uhlig, K., Duschl, C., and Volodkin, D. (2014). Stability and cell uptake of calcium carbonate templated insulin microparticles. *Acta Biomater.* 10 (3), 1423–1430. doi:10.1016/j.actbio.2013.11.011

Shah, A. R., and Wu, R. (2022). "Disparities in diabetes-related retinal disease and approaches to improve screening rates," in *A practical guide to*

diabetes-related eye care (Arlington (VA): American Diabetes Association), 16–19.

Shao, J., Feng, L., Zhao, Q., Chen, C., Li, J., Ma, Q., et al. (2021). Erythrocyte-mimicking subcutaneous platform with a laser-controlled treatment against diabetes. *J. Control. Release* 341, 261–271. doi:10.1016/j.jconrel.2021.11.021

Solimena, M., and Speier, S. (2010). Insulin release: shedding light on a complex matter. *Cell Metab.* 12 (1), 5–6. doi:10.1016/j.cmet.2010.06.002

Wu, Q., Wang, L., Yu, H., Wang, J., and Chen, Z. (2011). Organization of glucose-responsive systems and their properties. *Chem. Rev.* 111 (12), 7855–7875. doi:10.1021/cr200027j

Xia, D., He, H., Wang, Y., Wang, K., Zuo, H., Gu, H., et al. (2018). Ultrafast glucose-responsive, high loading capacity erythrocyte to self-regulate the release of insulin. *Acta Biomater.* 69, 301–312. doi:10.1016/j.actbio.2018.01.029

Xing, Q., Eadula, S. R., and Lvov, Y. M. (2007). Cellulose fiber-enzyme composites fabricated through layer-by-layer nanoassembly. *Biomacromolecules* 8 (6), 1987–1991. doi:10.1021/bm070125x

Yoshida, K., Hashide, R., Ishii, T., Takahashi, S., Sato, K., and Anzai, J. (2012). Layer-by-layer films composed of poly(allylamine) and insulin for pH-triggered release of insulin. *Colloids Surfaces B Biointerfaces* 91, 274–279. doi:10.1016/j.colsurfb.2011.11.017

Yu, G., Zhang, M., Gao, L., Zhou, Y., Qiao, L., Yin, J., et al. (2022). Far-red light-activated human islet-like designer cells enable sustained fine-tuned secretion of insulin for glucose control. *Mol. Ther.* 30 (1), 341–354. doi:10.1016/j.ymthe.2021.09.004

Zhang, Y., Xiong, G. M., Ali, Y., Boehm, B. O., Huang, Y. Y., and Venkatraman, S. (2021). Layer-by-layer coated nanoliposomes for oral delivery of insulin. *Nanoscale* 13 (2), 776–789. doi:10.1039/d0nr06104b

Zheng, C., Ding, Y., Liu, X., Wu, Y., and Ge, L. (2014). Highly magneto-responsive multilayer microcapsules for controlled release of insulin. *Int. J. Pharm. X.* 475 (1-2), 17–24. doi:10.1016/j.ijpharm.2014.08.042

frontiers | Frontiers in Bioengineering and Biotechnology

TYPE Review
PUBLISHED 05 October 2022
DOI 10.3389/fbioe.2022.1007960

OPEN ACCESS

EDITED BY
Donglin Xia,
Nantong University, China

REVIEWED BY
Li Wei,
Sichuan University, China
Shichao Ai,
Nanjing Drum Tower Hospital, China

*CORRESPONDENCE
Zhongwen Yang,
yangzhongwenyzw@126.com

SPECIALTY SECTION
This article was submitted to Biomaterials, a section of the journal Frontiers in Bioengineering and Biotechnology

RECEIVED 31 July 2022
ACCEPTED 20 September 2022
PUBLISHED 05 October 2022

CITATION
Yang Z, Shi C, Cheng D, Wang Y, Xing Y, Du F, Wu F, Jin Y, Dong Y and Li M (2022), Biomimetic nanomaterial-facilitated oxygen generation strategies for enhancing tumour treatment outcomes.
Front. Bioeng. Biotechnol. 10:1007960.
doi: 10.3389/fbioe.2022.1007960

Biomimetic nanomaterial-facilitated oxygen generation strategies for enhancing tumour treatment outcomes

Zhongwen Yang*, Changsong Shi, Dongliang Cheng, Yu Wang, Yan Xing, Fanfan Du, Fangfang Wu, Yao Jin, Yueli Dong and Mengli Li

Department of Pediatric, Henan Provincial People's Hospital, Zhengzhou, China

Hypoxia, as a typical hallmark of the tumour microenvironment (TME), has been verified to exist in most malignancies and greatly hinders the outcome of tumour treatments, including chemotherapy, photodynamic therapy, radiotherapy, and immunotherapy. Various approaches to alleviate tumour hypoxia have been reported. Among them, biomimetic nanomaterial-facilitated tumour oxygenation strategies, based on the engagement of human endogenous proteins, red blood cells, the cell membrane, and catalase, are the most impressive due to their excellent tumour active-targeting ability and superior tumour-selective capability, which, however, have not yet been systematically reviewed. Herein, we are ready to describe the current progress in biomimetic nanomaterial-facilitated tumour oxygenation strategies and corresponding improvements in tumour treatment outputs. In this review, the underlying mechanism behind the superior effect of these biomimetic nanomaterials, compared with other materials, on alleviating the hypoxic TME is highlighted. Additionally, the ongoing problems and potential solutions are also discussed.

KEYWORDS

tumour hypoxia, nanomaterials, biomimetics, tumour microenvironment, tumour treatment

Introduction

Tumour hypoxia, which is usually characterized mainly by insufficient oxygen supply and caused by the rapid proliferation of tumour cells and incomplete development of the vascular system, has been shown to exist in most solid tumors (Brahimi-Horn et al., 2007; Chu et al., 2017; Huo et al., 2020; Yang et al., 2022a). Moreover, tumour hypoxia, as a typical hallmark of the tumour microenvironment (TME), has been recently proven to be one of the main reasons for cancer treatment failure (Carlson et al., 2011; Bouleftour et al., 2021). The hypoxic TME seriously reduces the sensitivity of tumours to conventional chemotherapy, radiotherapy (RT),

and photodynamic therapy (PDT) (Baggiani et al., 2011; Baumann et al., 2016; Ayob and Ramasamy, 2021; Bouleftour et al., 2021; Carvalho et al., 2021). Meanwhile, the hypoxic TME also induces an immunosuppressive TME through four aspects: 1) initiating macrophage polarization from M1-phenotype (anti-tumour) to M2-phenotype (pro-tumour) (Delprat et al., 2020; Lee et al., 2020; Wu et al., 2020); 2) upregulating the expression of immune checkpoint blockades, such as programmed death ligand 1 (PD-L1) and programmed death 1 (PD-1) (Noman et al., 2014; Voron et al., 2015); 3) recruiting the immunosuppressive cells, (M2-phenotype macrophages, regulatory T cells, and myeloid-derived suppressor cells) (Huang et al., 2012; Lindau et al., 2013); and 4) preventing dendritic cells from maturing (Gabrilovich et al., 1996). The hypoxia-associated TME not only interferes with T lymphocyte activation and proliferation but also induces rapid tumour proliferation and metastasis. As such, reversing the hypoxic TME would be an effective strategy for enhancing tumour treatment outcomes.

Some approaches to alleviate tumour hypoxia, such as mitochondrial respiration inhibition, tumour vasculature, and oxygen (O_2) delivery, have been extensively reported. While these strategies indeed have the ability to alleviate tumour hypoxia to some extent, they also lead to inescapable side effects on normal tissues due to their nontargeting and nonselectivity toward tumour cells (Zhou et al., 2018; Song et al., 2020; Tang et al., 2020; Liu et al., 2021a; Yang et al., 2022b). Some small molecules were also reported that could effectively carry or generate oxygen *in vitro*. However, their short blood half-life and poor tumor accessibility greatly limit the tumor oxygenation efficiency *in vivo*. Recently, biomimetic nanomaterial-facilitated tumour oxygenation strategies have been reported to be capable of making up for the shortcomings of the abovementioned tumour oxygenation strategies (Chen et al., 2019; Feng et al., 2019; Dong et al., 2020; Fang et al., 2021; Chen et al., 2022). For example, when hypoxia regulators (*e.g.,* mitochondrial respiration inhibitors, tumour vasculature antagonists, and O_2 carriers) are encased by human endogenous proteins, erythrocytes, red blood membranes, platelet membranes, cancer cell membranes, or exosomes, their tumour accessibility and blood half-life can be greatly improved (Gao et al., 2018; Gao et al., 2020; Gong et al., 2021; Gong et al., 2022). Furthermore, natural catalase (CAT) and nanozymes with CAT-like properties can also overcome the hypoxic TME through the *in situ* catalytic decomposition of tumour-overexpressed hydrogen peroxide (H_2O_2) and the *in situ* generation of O_2 (Liang et al., 2017; Ai et al., 2018; Liang et al., 2018; Chang et al., 2019; Liu et al., 2019; Yu et al., 2019).

In this review, we summarize the present advances in biomimetic nanomaterial-empowered tumour oxygenation strategies. These biomimetic nanomaterials integrate multitudinous advantages, such as excellent biocompatibility, prolonged circulation time, immune evasion, and tumour-targeting and tumour-selecting efficacy, which explains the superior effect of these biomimetic nanomaterials on alleviating the hypoxic TME and improving tumour treatment outputs compared with other materials (Kuo et al., 2014; Jiang et al., 2019a; Li et al., 2020a; Li et al., 2021a). In the present review, not only are the merits highlighted, but the ongoing problems and the potential solutions are also discussed and concluded. We hope this review will help researchers better understand the field of tumour hypoxia, which will promote the development of cancer treatment.

Human endogenous protein-facilitated tumour oxygenation strategies

Human endogenous proteins, such as haemoglobin (Hb), albumin (HSA), glutathione S-transferase (GST), and bovine serum albumin (BSA), have long been employed to fabricate biomimetic nanomaterials through an eco-friendly biomimetic synthesis technology due to their wonderful biocompatibility, good flexibility, and green synthesis features (Zhang et al., 2012; Yang et al., 2016a; Yang et al., 2017; Zhang and Han, 2018). Recently, human endogenous protein-fabricated biomimetic nanomaterials have also been reported to alleviate tumour hypoxia and improve tumour treatment outcomes (Yang et al., 2016b; Zhao et al., 2017; Yang et al., 2018).

Haemoglobin -based biomimetic nanomaterials

Hb is a special protein that has an iron-containing haem group (Zhao et al., 2016). The iron state of Hb can be transformed from Fe^{2+} (ferrous) to Fe^{3+} (ferric) under high O_2 pressure (oxidative environment), allowing for efficient O_2 binding and transport (Zhu et al., 2019). However, under low O_2 pressure (reductive environment), the iron state returns to Fe^{2+}, which is responsible for the rapid O_2-unleashing capacity. By virtue of their superior O_2-carrying/release capability, Hb-based biomimetic nanomaterials have been applied to tumour oxygenation to boost antitumor therapy. Recently, Zhang's group designed Hb-mediated biomimetic nanomaterials (Gd@HbCe$_6$-PEG NPs) to overcome the hypoxic TME-limited efficacy of PDT (Figure 1A) (Shi et al., 2020). The paramagnetic O_2-evolving Gd@HbCe$_6$-PEG NPs were synthesized through an eco-friendly biomimetic synthesis technology based on Hb's biological template role. The loading of Ce_6 was mainly due to hydrophobic interactions, while the loading of Gd^{3+} metal ions occurred *via* the strong affinity of transition metals with the amino acid residues of Hb. PEGylation endowed biomimetic nanomaterials with better biocompatibility and stability. They next assessed the oxygen delivery capability of oxy-Gd@HbCe$_6$-PEG by measuring oxygenated haemoglobin (HbO_2) through PA imaging. HbO_2, as a positive indicator of tumour oxygenation,

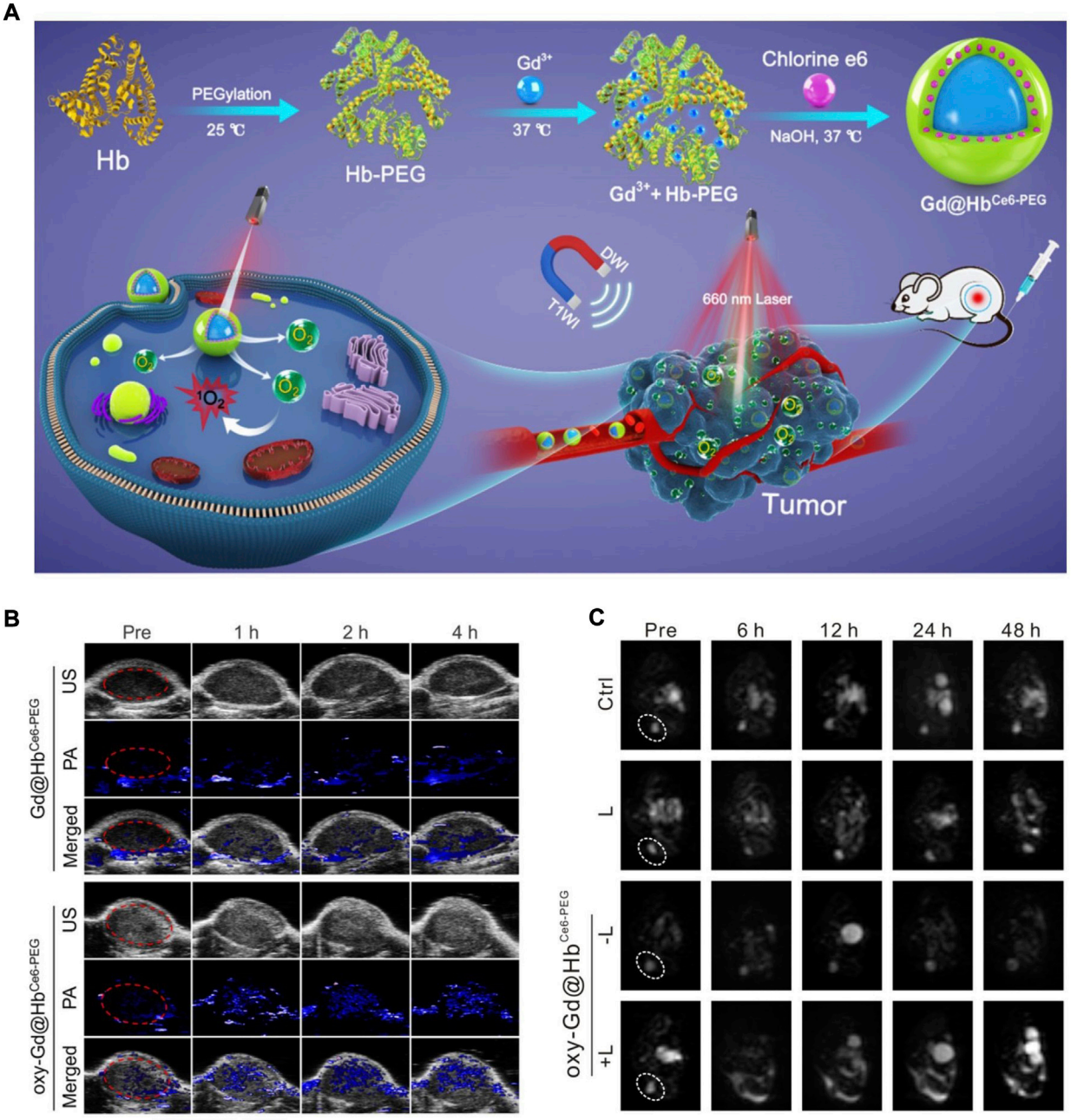

FIGURE 1
(A) A schematic diagram showing the Hb-mediated biomimetic nanomaterials (Gd@HbCe6-PEG NPs) for tumor oxygenation. **(B)** Representative PA images of the tumor sites after indicated treatments. **(C)** Representative DW images of the tumor sites after indicated treatments. Reprocessed with permission from ref 52. Copyright 2020, Ivyspring International Publisher.

displayed an increased signal intensity over time after the i.v. injection of oxy-Gd@HbCe$_6$-PEG NPs (Figure 1B), suggesting that Gd@HbCe$_6$-PEG is an applicable O_2 nanocarrier. Diffusion-weighted (DW) imaging *in vivo* is a powerful technology for measuring the direction and extent of the localized diffusion of water molecules. As a functional magnetic resonance (MR) imaging modality, DW imaging can reflect visible changes in tumour size and morphology. According to Figure 1C, the lowest intensity on the DW imaging map of the lesion areas was shown in the oxy-Gd@HbCe$_6$-PEG NP-rendered PDT group, indicating a noticeable treatment outcome.

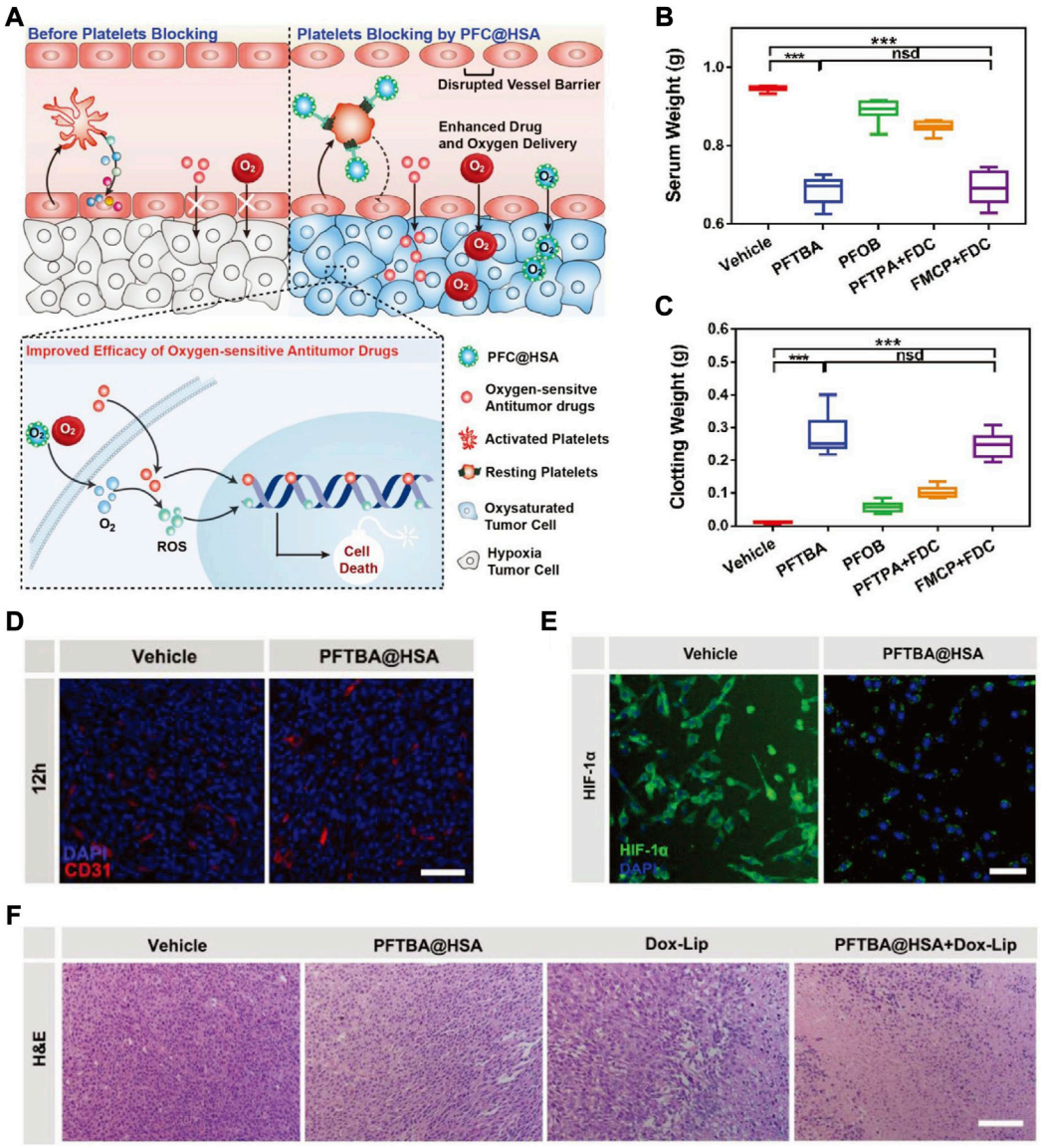

FIGURE 2
(A) The scheme showing PFTBA@HSA mediated platelet blocking for improved efficacy of oxygen-sensitive antitumor drugs. **(B,C)** Quantification of serum weight **(B)** and clotting weight **(C)**. **(D)** Representative immunofluorescence images of CD31 staining to depict tumor vessels (scale bar = 50 μm). **(E)** Representative immunofluorescence images of HIF-1α staining to track the degree of tumor hypoxia. **(F)** Representative images of H&E staining of the tumor tissues after indicated treatments (scale bar = 100 μm). Statistical significance was calculated by two-tail Student's t-test. *$p < 0.05$; **$p < 0.01$; ***$p < 0.001$. Reprocessed with permission from ref 53. Copyright 2018, WILEY-VCH Verlag GmbH & Co. KGaA, Weinheim.

HSA-based biomimetic nanomaterials

HSA is the protein in human plasma, accounting for approximately 60% of the total plasma protein. Recently, Wu's group selected HSA as the drug carrier to construct PFTBA@HSA nanoparticles (PFTBA@HSA NPs) (Zhou et al., 2018). The constructed HSA-mediated biomimetic nanomaterials could overcome the platelet-maintained tumour blood barrier and improve oxygen-sensitive antitumor efficacy (Figure 2A). A clot retraction experiment was performed to analyse the effects of PFTBA@HSA NPs on platelet functions. A shrinking amount of released serum that matched the inhibited shrinkage of blood clots was observed after treatment with PFTBA@HSA NPs (Figures 2B,C), suggesting the blocking platelet function of PFTBA@HSA NPs. After effective platelet inhibition by PFTBA@HSA NPs, the tumour vessel barriers were

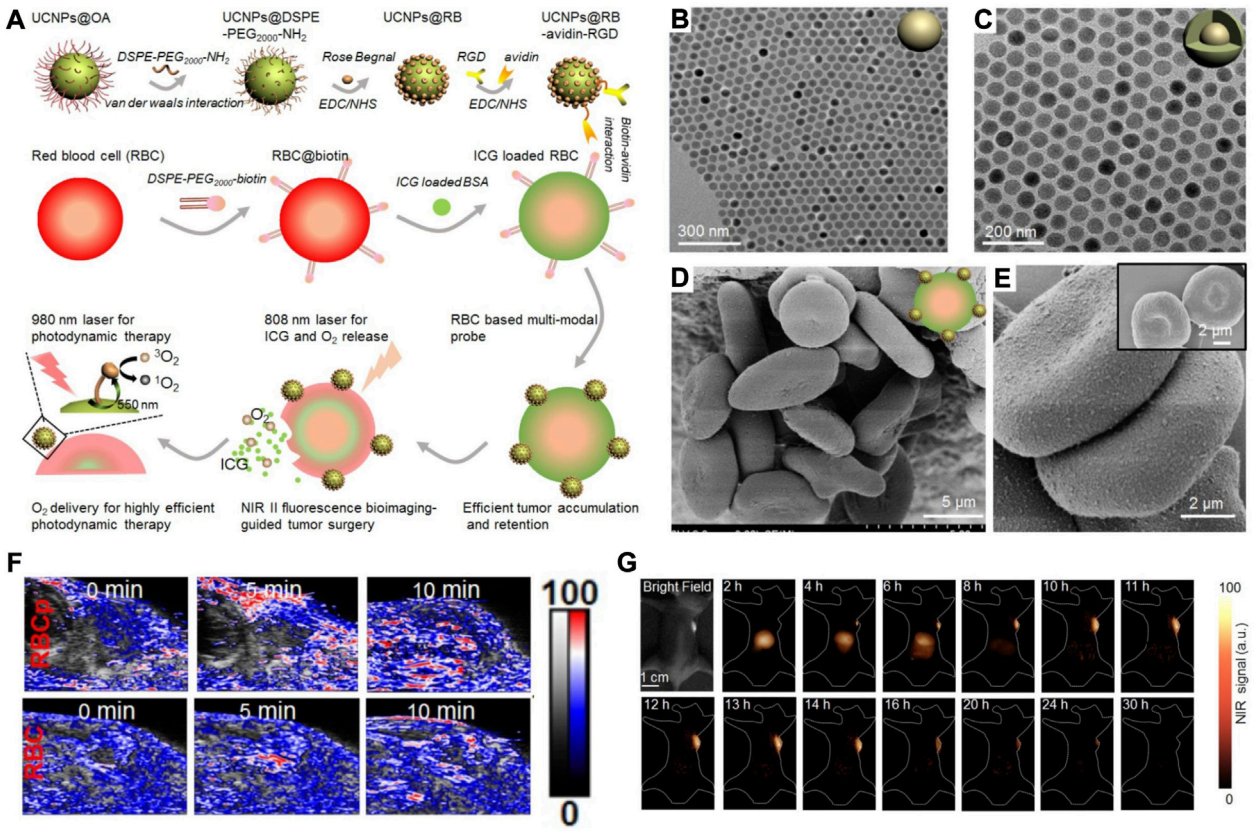

FIGURE 3
(A) The scheme showing the fabrication of RBCp and the application for NIR II fluorescence bioimaging-guided tumor surgery and PDT. **(B,C)** TEM images of NaGdF4:Yb, Er **(B)** and NaGdF4:Yb,Er@NaGdF4 **(C)**. **(D,E)** SEM images of RBC-based multimodal probes attached without UCNPs **(D)** and with UCNPs **(E)**. **(F)** Representative PA images of tumors after indicated treatments. **(G)** NIR II fluorescence bioimaging of the tumor-bearing mice after the *i.v.* injection of RBCp. Reprocessed with permission from ref 56. Copyright 2019, Ivyspring International Publisher.

successfully disrupted along with an enhanced tumour vessel permeability (Figure 2D) and a decreased degree of tumour hypoxia (Figure 2E). Eventually, the strong tumour oxygen perfusion assisted by PFTBA@HSA NP treatment amplified ROS production and cell death (Figure 2F).

Red blood cell-facilitated tumour oxygenation strategies

The principal function of red blood cells (RBCs) is delivering oxygen to all tissues in the body, including tumors (Beutler et al., 1977). Inspired by this, some RBC-based strategies to overcome hypoxia have been designed and release oxygen under hypoxic conditions (Tang et al., 2016).

As haemoglobin is bound to oxygen (oxyhemoglobin) and surrounded by the phospholipid bilayer of RBCs, bursting the RBS membranes can release oxygen to overcome hypoxia in the tumour. Due to its high spatial and temporal precision, laser light is a widely studied remote trigger in the drug release process. To achieve better controlled release outcomes, the Food and Drug Administration (FDA)-approved agent indocyanine green (ICG) was used. Based on this, an RBC-based biomimetic nanomaterial (UCNPs@RB@RGD@avidin crosslinked with RBC@ICG@biotin) was fabricated for near-infrared (NIR) II fluorescence bioimaging-guided tumour surgery and tumour oxygenation-boosted PDT (Figure 3A) (Wang et al., 2019). In this RBC-based biomimetic nanomaterial, UCNPs (lanthanide-doped $NaGdF_4$:Yb,Er@$NaGdF_4$ nanocrystals) were synthesized for translating 980 nm laser irradiation into 550 nm luminescence and demonstrated a core-shell nanostructure (Figures 3B,C). Additionally, the SEM and TEM results in Figures 3D,E show that lanthanide-doped $NaGdF_4$:Yb,Er@$NaGdF_4$ nanocrystals were successfully anchored onto the membranes of RBCs without any alteration of the RBC morphology. The *in vivo* results demonstrate that the RBCp structures could be completely destroyed, and O_2 was released immediately and activated by 808 nm laser irradiation for 10 min (Figure 3F). Moreover, the RBCps could also be used in NIR II

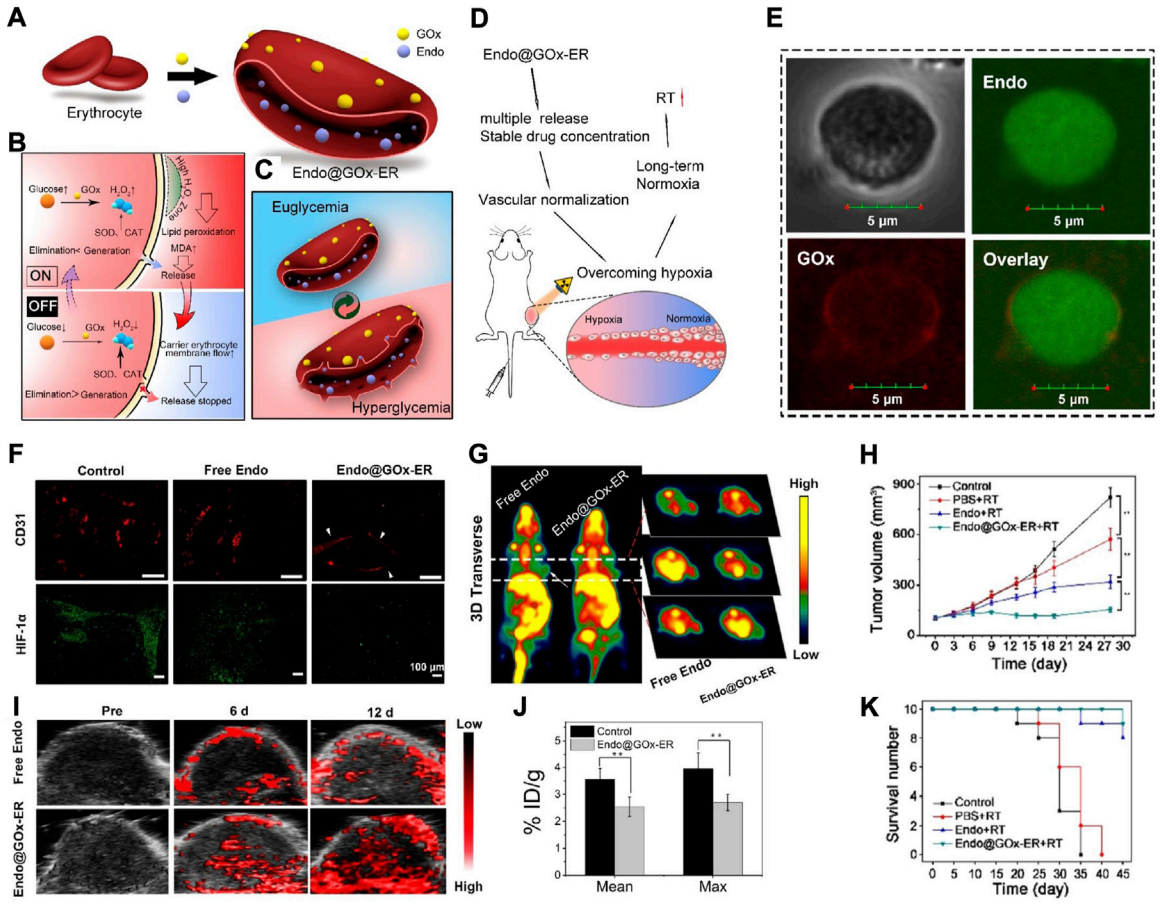

FIGURE 4
(A) The scheme showing the synthesis of Endo@GOx-ER. **(B,C)** The scheme displaying glucose-mediated release of Endo from Endo@GOx-ER. **(D)** The scheme representing the released Endo is capable of promoting tumor vascular normalization, reversing tumor hypoxia, and improving therapeutic outcomes of RT. **(E)** Confocal images demonstrating the encasement of Endo by biotin-GOx. The scale bar is 5 μm. **(F)** Immunofluorescence analysis of tumor sections stained with CD31 and HIF-1α. The scale bar is 100 μm. **(G)** Representative PA images showing the ratio of oxygenated hemoglobin to deoxygenated hemoglobin in tumors after indicated treatments. **(H)** Representative micro-PET scan images showing the absorption of ^{18}F-MISO in tumors after indicated treatments. **(I)** % ID/g of ^{18}F-MISO after indicated treatments. **(J,K)** Tumor volume **(J)** and survival number **(K)** of mice after indicated treatments. Reprocessed with permission from ref 59. Copyright 2020, American Chemical Society.

fluorescence bioimaging-guided liver tumour surgery, as NIR II fluorescence signals can be observed within the liver tumour for 4 h (Figure 3G). The results showed that the modified RBCs could absorb heat and swell, resulting in the burst release of ICG and O_2, which could overcome hypoxia in tumours and amplify PDT output.

Antiangiogenic drugs (such as Endo) have been demonstrated to be able to alter the oxygenation status of a tumour, but most of them fail to acquire satisfactory clinical therapeutic effects, mainly due to their unstoppable degradation and unstable features *in vivo* (Ding et al., 2014; Li et al., 2018). To solve this problem, Xia et al. recently reported a RBC-based biomimetic nanomaterial (Endo@GOx-ER), in which GOx served as a glucose-activated switch for responding to glucose and releasing Endo (Figure 4A) (Huang et al., 2020). Under hyperglycaemia, the accumulation of H_2O_2 (the product of GOx-catalysed glucose oxidation) would promote pore formation on RBCms. In normoglycaemia, the Endo release would be suppressed as the pore closed, thus contributing to a pulsatile release manner and sustained high plasma levels (Figures 4B–E). According to the immunofluorescence analysis of tumour sections stained with CD31 and HIF-1α as well as the representative PA images and micro-PET scanning images, it was obvious that Endo@GOx-ER treatment resulted in vascular normalization and accomplished long-term tumour hypoxia relief (Figures 4F–I). When Endo@GOx-ER treatment was combined with RT, persistent tumour regression and higher survival were obtained (Figures 4J,K), suggesting that this RBC-based biomimetic nanomaterial has clinical potential in overcoming tumour hypoxia-limited RT.

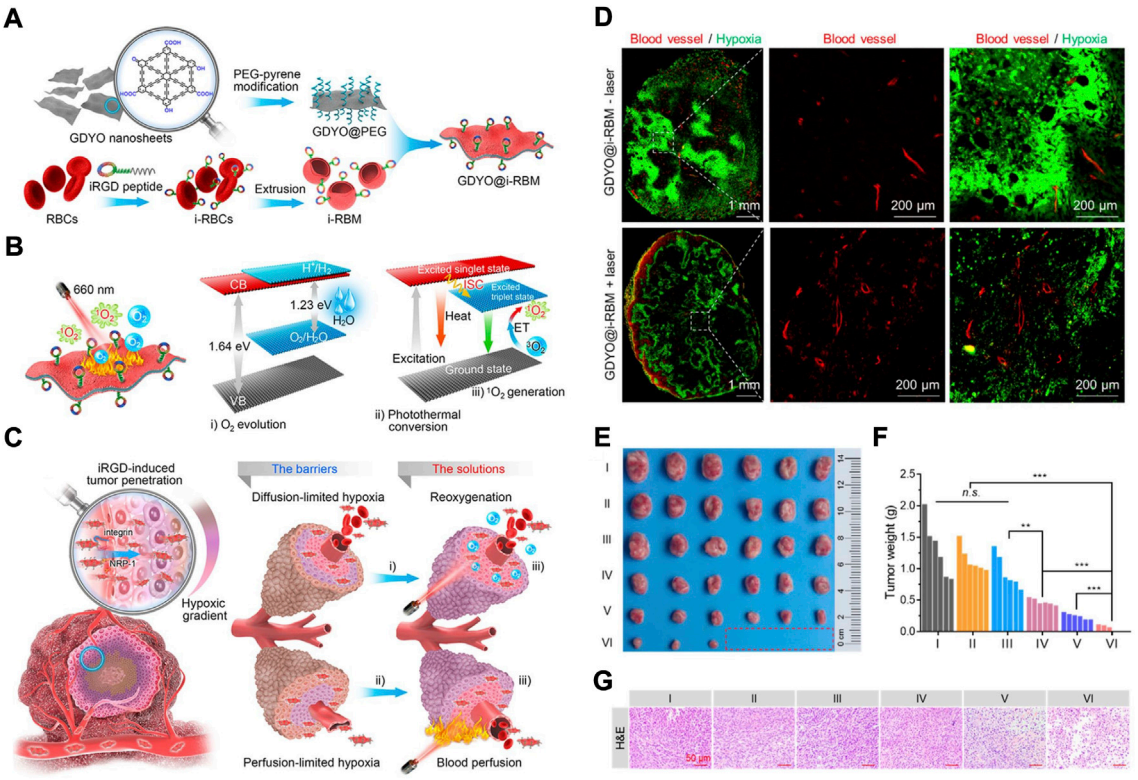

FIGURE 5
(A) The Scheme showing the synthetic process of GDYO@i-RBM. **(B)** The Scheme showing the working principles of GDYO@i-RBM: **(C)** The Scheme showing the reoxygenation process. **(D)** Immunofluorescence analysis of tumor sections stained with anti-CD31 antibody and anti-pimonidazole antibody after indicated treatments. **(E–G)** Photos **(E)**; tumor weight **(F)** and representative images of H&E staining **(G)** of the tumor tissues after I–**VI** treatments (I: PBS-laser; II: PBS + laser; III: GDYO@i-RBM-laser; IV: GDYO@PEG + laser; V: GDYO@RBM + laser; VI: GDYO@i-RBM + laser). Statistical significance was calculated by two-tail Student's t-test. *$p < 0.05$; **$p < 0.01$; ***$p < 0.001$. Reprocessed with permission from ref 64. Copyright, 2019 American Chemical Society.

Cell membrane-facilitated tumour oxygenation strategies

To achieve controlled drug release and overcome tumour hypoxia, bionic functional membranes derived from RBC membranes, platelet membranes, tumour cell membranes, etc., are valid choices (Zhang et al., 2018; Zhang et al., 2019a; Feng et al., 2019; Li et al., 2020a; Lyu et al., 2021).

Red blood cell membrane-based biomimetic nanomaterials

The possibility of using RBC membranes, termed RBCms, as drug carriers has become popular (Meng et al., 2021). Considering the potential clinical usefulness, RBCms are readily available, cost-effective, and allow scaled up preparation. Their long half-life (approximately 28 days) and low immunogenicity in circulation make them particularly well-suited to serve as a popular coating for chemotherapy drugs (Li et al., 2020a).

As we know RBCs coursing through veins primarily transport oxygen throughout the body, including the tumour. This has inspired the utilization of RBCms as oxygen carriers to overcome both diffusion-limited and perfusion-limited hypoxia (Figure 5) (Jiang et al., 2019b). In detail, a functional iRGD peptide was modified on the RBCms to enhance extravascular and hypoxic region penetration. The graphdiyne oxide (GDYO) nanosheets were loaded into iRGD-RBCm and denoted GDYO@i-RBM (Figure 5A). GDYO@i-RBM showed prolonged blood circulation and enlarged extravascular and hypoxic region penetration because of the functional iRGD peptide. When exposed to irradiation with a 660 nm laser, GDYO nanosheets can evolve sufficient O_2 to relieve perfusion-limited hypoxia; at the same time, the hyperthermia effect of GDYO overcomes perfusion-limited hypoxia because of the dilation of vessels and blood perfusion (Figure 5B). After i.v. injection, GDYO@i-RBM synchronously alleviated diffusion- and perfusion-limited hypoxia (Figure 5C) and further enhanced PDT, resulting from the changes in tumour volume and weight and pathological changes (Figures 5E–G). This work sheds new light on RBCm-based biomimetic nanomaterials for overcoming hypoxia.

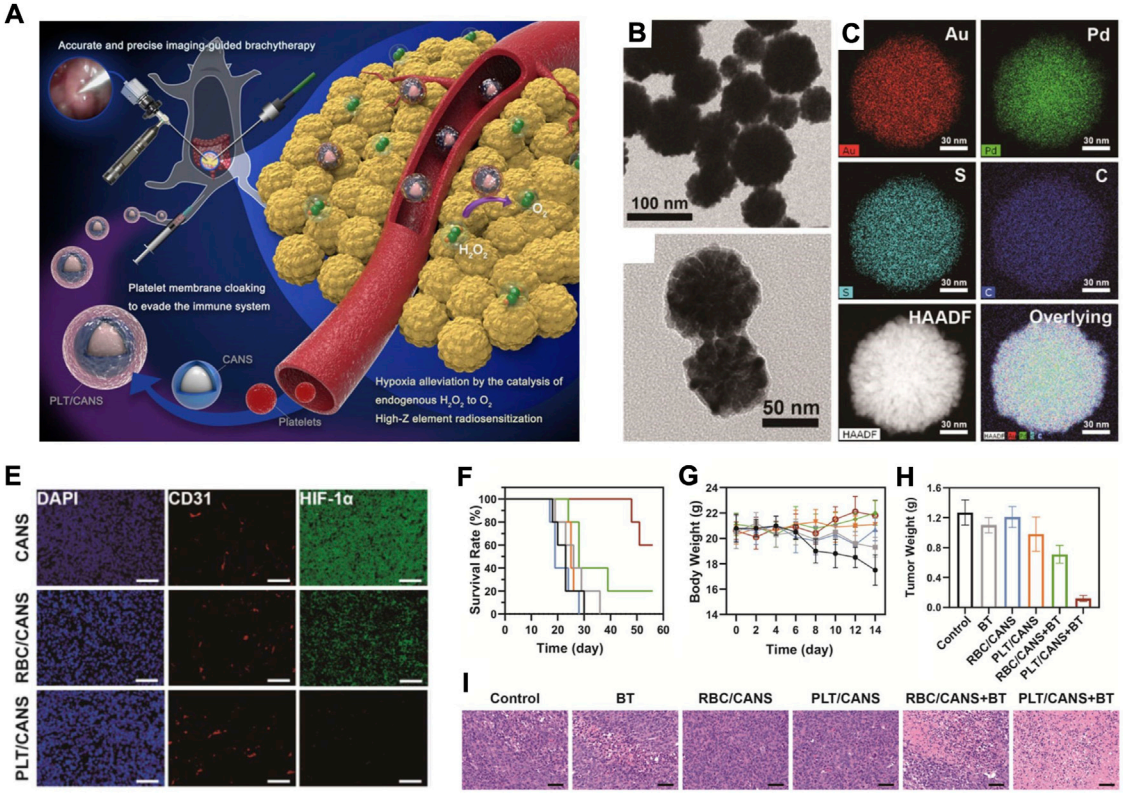

FIGURE 6
(A) The scheme showing the preparation of PLT/CANS and its application in alleviating tumor hypoxia. **(B)** TEM image of CANS. **(C,D)** TEM image **(C)** and **(D)** element mapping image of PLT/CANS. **(E)** Immunofluorescence analysis of tumor sections stained with TUNEL and HIF-1α after indicated treatments (scale bars: 50 μm). **(F–H)** Survival rates **(F)**; body weights **(G)** and tumor masses **(H)** of mice after indicated treatments. **(I)** H&E staining of tumor slices collected from different groups of mice (scale bars: 50 μm). Reprocessed with permission from ref 62. Copyright 2021, Ivyspring International Publisher.

Platelet membrane-based biomimetic nanomaterials

In addition to RBC membranes, platelet membranes have also been utilized to design biomimetic nanomaterials (Hu et al., 2015a; Hu et al., 2015b). These biomimetic nanomaterials retained the surface glycoproteins of platelets as well as the tumour active targeting function (Sarkar et al., 2013; Zhang et al., 2020). In addition, these biomimetic nanomaterials could be activated by tumour cells, leading to size tuning, deep tumour penetration, and better antitumor output (Zuo et al., 2018). In a recent study, Bao and his coworkers fabricated a platelet membrane-based biomimetic nanomaterial by coating core-shell Au@AuPd nanospheres with a platelet membrane (PLT/CANS) for enhanced interstitial brachytherapy (BT) (Figure 6A) (Lyu et al., 2021). TEM and element mapping results showed that the as-prepared CANS had a core-shell spherical structure (Figures 6B–D). Compared to RBC membrane-coated nanoplatforms, PLT-derived membranes not only can effectively evade blood clearance but also have a special tumour targeting ability. From the immunofluorescence analysis of tumour sections stained with TUNEL and HIF-1α, one can see that PLT/CANS treatment could conquer tumour hypoxia (Figure 6E). After the combinational treatment of PLT/CANS and BT, the tumour-bearing mice showed longer survival, stable bodyweight growth, and lower tumour mass (Figures 6F–H). Histological analysis further showed that the combinational treatment of PLT/CANS and BT most effectively induced cellular apoptosis (Figure 6I). Overall, this work showed that platelet membrane-based biomimetic nanomaterials could be a robust and efficient strategy for tumour treatment.

Cancer cell membrane-based biomimetic nanomaterials

As the study develops in depth, it has been found that the tumour cell membrane has a selective targeting homing ability due to the self-recognition to oncogenic cell lines. As a cancer cell membrane with a negative charge, the positive nanoparticles are easily bound to the tumour cell membrane, resulting in preferential

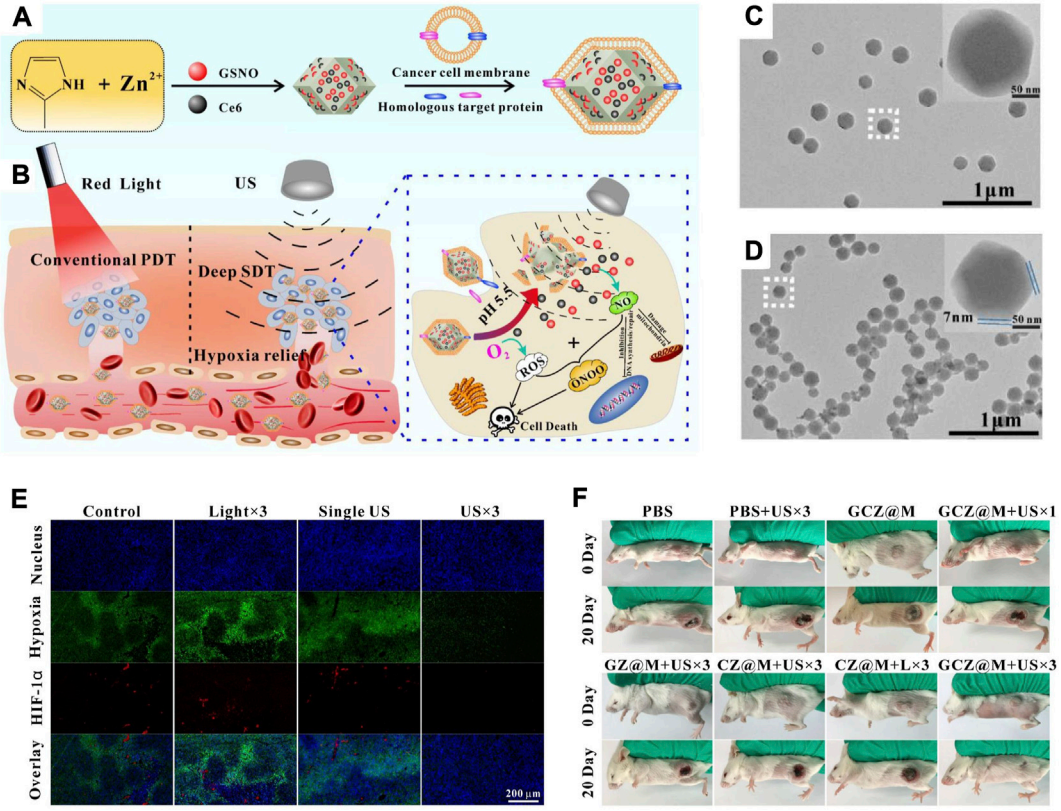

FIGURE 7
(A) Schematic illustration of the synthesis process of GCZ@M. **(B)** Schematic illustration of the tumor therapy principle. **(C,D)** TEM and magnification images (inset) of GCZ **(C)** and GCZ@M **(D)**. **(E)** Immunofluorescence analysis of tumor sections after indicated treatments. **(F)** Photos of tumor-bearing mice after indicated treatments. Reprocessed with permission from ref 71. Copyright 2019, Elsevier Ltd. All rights reserved.

uptake in tumors (Zhang et al., 2019b; Fang et al., 2021). Zhao et al. developed a biomimetic nanoplatform based on homologous tumour cell membranes with homologous targeting and low phototoxicity (Figure 7A) (An et al., 2020). Cancer cell membrane-based biomimetic nanomaterials (GCZ@M) were formed by the encapsulation of GSNO/Ce_6@ZIF-8 by the cancer cell membrane. The *in vivo* results revealed that GCZ@M could accumulate in tumours with the help of the homologous tumour cell membrane. The encapsulated drug that accumulates in tumours could be sustainably released, triggered by pH and ultrasound. Then, the therapeutic effect of sonodynamic therapy could be improved by the effect of overcoming hypoxia in tumours through the use of ultrasound and the therapeutic properties of GCZ (Figure 7B). As tumours have a dense stroma, GCZ@M showed a uniform size and good dispersion, while the cancer cell membrane was a thin film, which did not reduce the inherent size advantage of the nanoparticles (Figures 7C,D). Immunofluorescence analysis of tumour sections after GCZ@M treatment revealed that the NO and ROS produced by US could relieve tumour hypoxia, while the photographs of tumour-bearing mice after GCZ@M treatment exhibited an excellent therapeutic outcome (Figures 7E,F).

Catalase-facilitated tumour oxygenation strategies

Hydrogen peroxide (H_2O_2) is overexpressed in the TME (Han et al., 2019; Li et al., 2020b). The overexpressed H_2O_2 can be catalysed into O_2 by the natural catalase (CAT) or CAT-like nanozymes (Wang et al., 2020). The *in situ* generated O_2 in tumour sites can be taken advantage of to overcome hypoxia-confined poor tumour treatment outcomes.

Catalase -based biomimetic nanomaterials

As a natural antioxidant enzyme, CAT suffers from limited retention in tumour sites, leading to the limited generation of O_2 in deep hypoxic areas (Ansar et al., 2020; Li et al., 2020c). To address this problem, a series of CAT-based biomimetic nanomaterials was developed (Yen et al., 2019). Meng *et al* reported Ce_6-CAT/RPNPs/PEGDA biomimetic nanomaterials (Meng et al., 2019). As a light-induced *in situ* hybrid hydrogel system, Ce_6-CAT/RPNPs/PEGDA

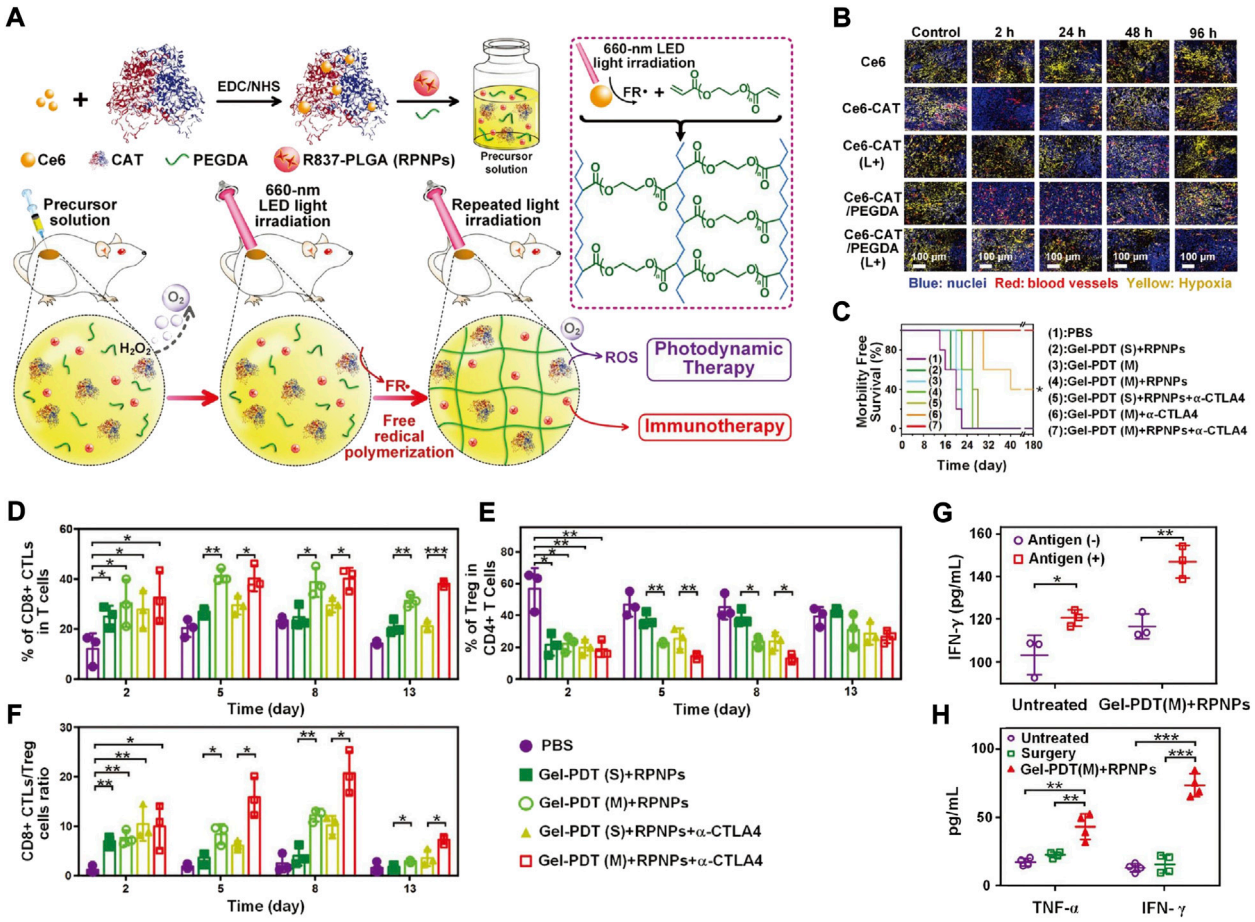

FIGURE 8
(A) Schematic illustration of the light-triggered fabrication of Ce6-CAT/PEGDA hydrogel in tumor sites. **(B)** Immunofluorescence analysis of tumor sections stained with anti-pimonidazole antibody (yellow) and anti-CD31 antibody (red). TUNEL **(C)** Morbidity free survival of the tumor-bearing mice after indicated treatments ($n = 7$). **(D–F)** Proportions of tumor-infiltrating $CD8^+$ CTLs **(D)**; Treg cells **(E)** and $CD8^+$ CTLs/Treg cells **(F)** after indicated treatments ($n = 3$). **(G)** The secretion of IFN-γ from restimulated splenocytes by the addition of the dead cell (antigen) *in vitro* ($n = 3$). **(H)** Serous cytokine (TNF-α, IFN-γ) levels after indicated treatments ($n = 4$). Statistical analysis was performed *via* one-way ANOVA using the Tukey post-test. $p < 0.05$; **, $p < 0.01$; ***, $p < 0.001$. Reprocessed with permission from ref 78. Copyright 2019 WILEY-VCH Verlag GmbH & Co. KGaA, Weinheim.

realized sustained tumour hypoxia modulation to facilitate both PDT and immunotherapy (Figure 8A). Immunofluorescence staining with pimonidazole as the hypoxyprobe was conducted to track the tumour hypoxia states. While the decomposition of H_2O_2 by CAT could generate O_2 in the TME, the poor retention ability of Ce_6-CAT alleviated the tumour hypoxia status at the initial state, but it was recovered within 48 h after PDT treatment. In contrast, after light irradiation, the Ce_6-CAT/PEGDA group showed a striking reduction in the degree of hypoxia over a period of 96 h, indicating that the retention of CAT could realize persistent tumour hypoxia relief (Figure 8B). With the sustained modulation of the hypoxic TME as well as the additional engagement of α-CTLA4 checkpoint blockade, the survival time was significantly prolonged (Figure 8C). Additionally, after combinational treatment with Ce_6-CAT/RPNPs/PEGDA and α-CTLA4 checkpoint blockade, the antitumor immunotherapeutic responses were also strengthened (Figures 8D–F), as reflected by the increased populations of $CD8^+$ CTLs (cytotoxic T lymphocytes) and the decreased populations of Treg cells (a kind of immunosuppressive cell). TNF-α and IFN-γ, two major indicators related to antitumor immune responses, were also detected in sera after different treatments. The TNF-α and IFN-γ concentrations were both significantly increased in the RPNPs/Ce_6-CAT/PEGDA group, which is useful for effectively preventing tumour recurrence (Figures 8G,H).

Catalase -like nanozyme-based biomimetic nanomaterials

CAT-like nanozymes are nanomaterials that possess CAT-like catalytic activity and enable the decomposition of H_2O_2 into O_2 (Gordijo et al., 2015; Lin et al., 2018). Recently, Qin and coworkers

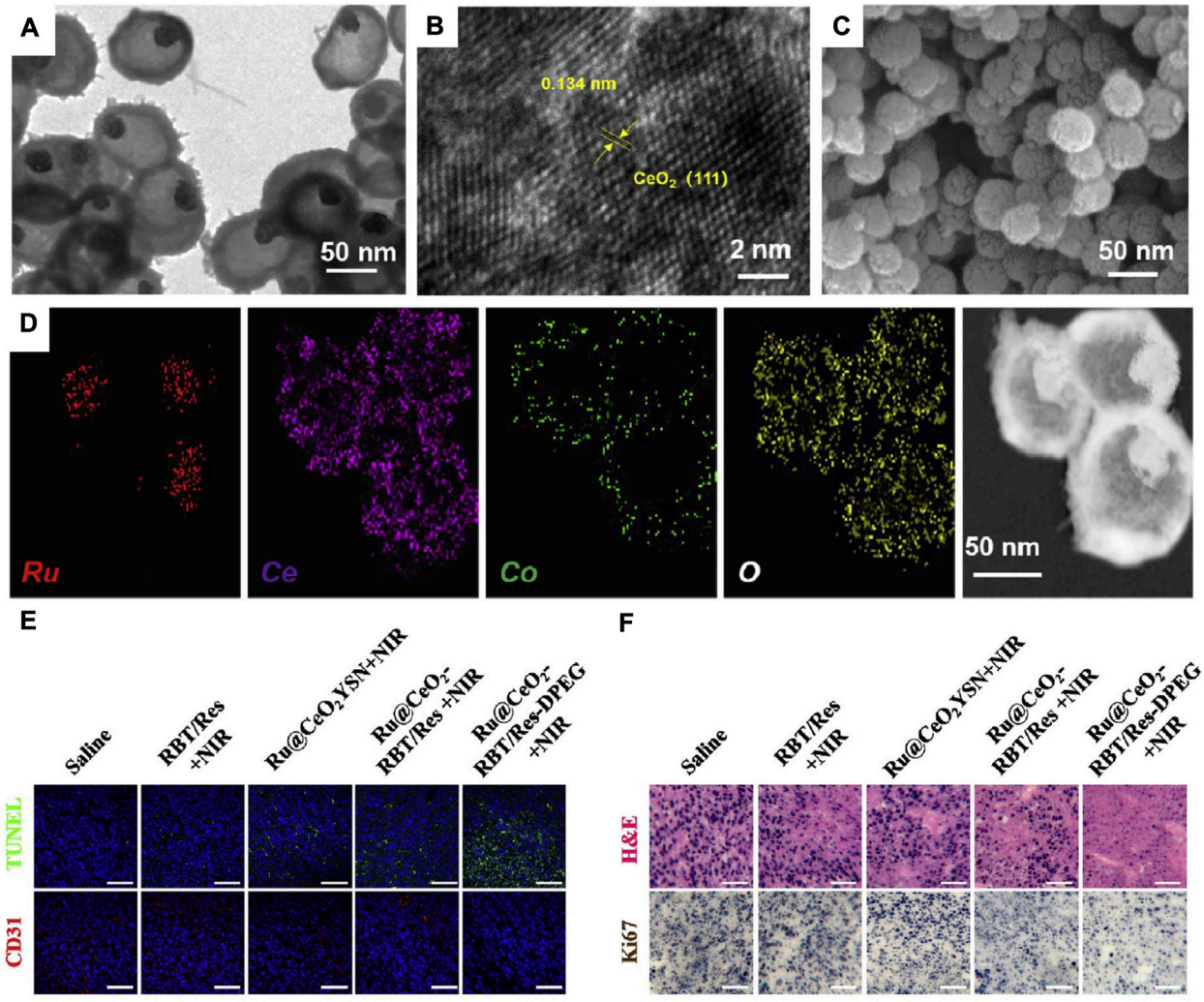

FIGURE 9
(A–D) TEM images **(A)**; HTEM images **(B)**; SEM images **(C)** and STEM-EDX elemental mapping images of Ru@CeO_2 YSNs. **(E)** Immunofluorescence analysis of tumor sections stained with TUNEL and CD31. **(F)** H&E and Ki-67co-staining of tumor slices collected from different groups of mice. Reprocessed with permission from ref 81. Copyright 2020 Elsevier Ltd. All rights reserved.

tailor made hollow Ru@CeO_2 (a type of CAT-like nanozyme)-based biomimetic nanomaterial (Ru@CeO_2-RBT/Res-DPEG) to alleviate tumour hypoxia and inhibit tumour metastasis and recurrence (Zhu et al., 2020). TEM images showed that the as-obtained Ru@CeO_2 has a uniform spherical core-shell structure with an average size of ~70 nm (Figure 9A). Meanwhile, the high-resolution TEM images showed that the lattice fringes with a spacing of 0.314 nm perfectly matched the (111) plane of CeO_2, indicating that the 3-6 nm interpenetrating CeO_2 nanocrystals composed the mesoporous shell of Ru@CeO_2 (Figure 9B). In addition, SEM images showed that Ru@CeO_2 had a roughly spherical morphology (Figure 9C), and STEM-EDX elemental mapping confirmed that Ru (red) was the core component of Ru@CeO_2, while Ce (purple) and O (yellow) were the shell components of Ru@CeO_2 (Figure 9D). Subsequently, Ru@CeO_2 was coated with RBT/Res-DPEG to improve the biocompatibility, reduce protein adsorption, and prolong the blood circulation time. Since Ru@CeO_2-RBT/Res-DPEG has the ability to effectively deplete H_2O_2 in the TME to generate O_2 and alleviate tumour hypoxia, Ru@CeO_2-RBT/Res-DPEG exerted a dramatic antitumor effect, as verified by more than half area of cell apoptosis (Figure 9E), serious cell necrosis and inhibited cell proliferative activity (Figure 9F).

Conclusion and outlook

Herein, we have summarized the latest progress in biomimetic nanomaterial-driven tumour oxygenation

strategies. We depicted in detail the multiple merits of these biomimetic nanomaterials, including immune evasion, prolongation of the circulation time, enhanced biocompatibility, and wonderful tumour-targeting and tumour-selecting efficacy. In light of these multiple merits, the biomimetic nanomaterials exerted superior effects on alleviating the hypoxic TME and improving tumour treatment outputs relative to other materials (Li et al., 2021b; Gowda et al., 2022; Li et al., 2022).

Although the current biomimetic nanomaterial-driven tumour oxygenation strategies have remarkably surmounted hypoxia-associated resistance in tumour treatment, there are still some ongoing challenges that should be solved before these strategies can be applied to clinical cancer treatment.

(1) In human endogenous protein-facilitated tumour oxygenation strategies, the protein structure may be altered due to covalent or noncovalent modifications and the application of organic solvents. Additionally, the release of the delivery systems from the human endogenous protein is also a challenge (Yang et al., 2020).
(2) In red blood cell-facilitated tumour oxygenation strategies, the limited proliferative ability of red blood cells extremely confines the mass production of red blood cell-based biomimetic nanomaterials and thus cannot meet clinical needs (Tang et al., 2016).
(3) In cell membrane-facilitated tumour oxygenation strategies, the cell membrane has difficulty completely covering the surface of nanomaterials and is easily detached from the surface of nanomaterials due to the lack of covalent bond constraints, thus limiting clinical applications (Liu et al., 2021b).
(4) In catalase-facilitated tumour oxygenation strategies, the intratumourally endogenous H_2O_2 amount is limited, which greatly restricts the ability of biomimetic nanomaterials to generate sufficient *in situ* O_2 (Song et al., 2018).

We envision that the ongoing challenges will be solved in the future and that biomimetic nanomaterial-empowered tumour oxygenation strategies will promote the development of cancer treatment in the clinic.

Author contributions

ZY conceived and supervised this review. ZY, YW, YX, FD, FW, YJ, YD, and ML retrieved and reviewed the literatures. ZY wrote the manuscript. CS and DC helped to write and revise the manuscript. All authors contributed to the article and approved the submitted version.

Conflict of interest

The authors declare that the research was conducted in the absence of any commercial or financial relationships that could be construed as a potential conflict of interest.

Publisher's note

All claims expressed in this article are solely those of the authors and do not necessarily represent those of their affiliated organizations, or those of the publisher, the editors and the reviewers. Any product that may be evaluated in this article, or claim that may be made by its manufacturer, is not guaranteed or endorsed by the publisher.

References

Ai, X. Z., Hu, M., Wang, Z. M., Lyu, L. N., Zhang, W. M., Li, J., et al. (2018). Enhanced cellular ablation by attenuating hypoxia status and reprogramming tumor-associated macrophages via NIR light-responsive upconversion nanocrystals. *Bioconjug. Chem.* 29 (4), 928–938. doi:10.1021/acs.bioconjchem.8b00068

An, J., Hu, Y. G., Li, C., Hou, X. L., Cheng, K., Zhang, B., et al. (2020). A pH/Ultrasound dual-response biomimetic nanoplatform for nitric oxide gas-sonodynamic combined therapy and repeated ultrasound for relieving hypoxia. *Biomaterials* 230, 119636. doi:10.1016/j.biomaterials.2019.119636

Ansar, M., Ivanciuc, T., Garofalo, R. P., and Casola, A. (2020). Increased lung catalase activity confers protection against experimental RSV infection. *Sci. Rep.* 10 (1), 3653. doi:10.1038/s41598-020-60443-2

Ayob, A. Z., and Ramasamy, T. S. (2021). Prolonged hypoxia switched on cancer stem cell-like plasticity in HepG2 tumourspheres cultured in serum-free media. *Vitro Cell. Dev. Biol. -Animal.* 57 (9), 896–911. doi:10.1007/s11626-021-00625-y

Baggiani, A., Ierardi, A., Caspani, B., Motta, F., Toniolo, D., Belloni, P., et al. (2011). Hypoxic liver perfusion with mitomycin-C for treating multifocal metastases and unresectable primary tumours: A single-centre series of 42 patients. *Radiol. Med.* 116 (8), 1239–1249. doi:10.1007/s11547-011-0724-3

Baumann, R., Depping, R., Delaperriere, M., and Dunst, J. (2016). Targeting hypoxia to overcome radiation resistance in head & neck cancers: Real challenge or clinical fairytale? *Expert Rev. Anticancer Ther.* 16 (7), 751–758. doi:10.1080/14737140.2016.1192467

Beutler, E., Dale, G. L., Guinto, D. E., and Kuhl, W. (1977). Enzyme replacement therapy in gaucher's disease: Preliminary clinical trial of a new enzyme preparation. *Proc. Natl. Acad. Sci. U. S. A.* 74 (10), 4620–4623. doi:10.1073/pnas.74.10.4620

Bouleftour, W., Rowinski, E., Louati, S., Sotton, S., Wozny, A. S., Moreno-Acosta, P., et al. (2021). A review of the role of hypoxia in radioresistance in cancer therapy. *Med. Sci. Monit.* 27, e934116. doi:10.12659/msm.934116

Brahimi-Horn, M. C., Chiche, J., and Pouyssegur, J. (2007). Hypoxia and cancer. *J. Mol. Med.* 85 (12), 1301–1307. doi:10.1007/s00109-007-0281-3

Carlson, D. J., Keall, P. J., Loo, B. W., Chen, Z. J., and Brown, J. M. (2011). Hypofractionation results in reduced tumor cell kill compared to conventional fractionation for tumors with regions of hypoxia. *Int. J. Radiat. Oncology*Biology*Physics* 79 (4), 1188–1195. doi:10.1016/j.ijrobp.2010.10.007

Carvalho, T. M. A., Di Molfetta, D., Greco, M. R., Koltai, T., Alfarouk, K. O., Reshkin, S. J., et al. (2021). Tumor microenvironment features and chemoresistance in pancreatic ductal adenocarcinoma: Insights into targeting physicochemical barriers and metabolism as therapeutic approaches. *Cancers* 13 (23), 6135. doi:10.3390/cancers13236135

Chang, M. Y., Wang, M., Wang, M. F., Shu, M. M., Ding, B. B., Li, C. X., et al. (2019). A multifunctional cascade bioreactor based on hollow-structured Cu2MoS4 for synergetic cancer chemo-dynamic therapy/starvation therapy/phototherapy/immunotherapy with remarkably enhanced efficacy. *Adv. Mater* 31 (51), 1905271. doi:10.1002/adma.201905271

Chen, K., Li, H., Xu, Y., Ge, H., and Ning, X. (2022). Photoactive "bionic virus" robustly elicits the synergy anticancer activity of immunophotodynamic therapy. *ACS Appl. Mat. Interfaces* 14 (3), 4456–4468. doi:10.1021/acsami.1c23983

Chen, Z., Wang, Z., and Gu, Z. (2019). Bioinspired and biomimetic nanomedicines. *Acc. Chem. Res.* 52 (5), 1255–1264. doi:10.1021/acs.accounts.9b00079

Chu, C. C., Lin, H. R., Liu, H., Wang, X. Y., Wang, J. Q., Zhang, P. F., et al. (2017). Tumor microenvironment-triggered supramolecular system as an *in situ* nanotheranostic generator for cancer phototherapy. *Adv. Mat.* 29 (23). doi:10.1002/adma.201605928

Delprat, V., Tellier, C., Demazy, C., Raes, M., Feron, O., and Michiels, C. (2020). Cycling hypoxia promotes a pro-inflammatory phenotype in macrophages via JNK/p65 signaling pathway. *Sci. Rep.* 10 (1), 882. doi:10.1038/s41598-020-57677-5

Ding, Y., Wang, Y., Zhou, J., Gu, X., Wang, W., Liu, C., et al. (2014). Direct cytosolic siRNA delivery by reconstituted high density lipoprotein for target-specific therapy of tumor angiogenesis. *Biomaterials* 35 (25), 7214–7227. doi:10.1016/j.biomaterials.2014.05.009

Dong, S., Dong, Y., Jia, T., Liu, S., Liu, J., Yang, D., et al. (2020). GSH-depleted nanozymes with hyperthermia-enhanced dual enzyme-mimic activities for tumor nanocatalytic therapy. *Adv. Mat.* 32 (42), e2002439. doi:10.1002/adma.202002439

Fang, H., Gai, Y., Wang, S., Liu, Q., Zhang, X., Ye, M., et al. (2021). Biomimetic oxygen delivery nanoparticles for enhancing photodynamic therapy in triple-negative breast cancer. *J. Nanobiotechnology* 19 (1), 81. doi:10.1186/s12951-021-00827-2

Feng, Q., Yang, X., Hao, Y., Wang, N., Feng, X., Hou, L., et al. (2019). Cancer cell membrane-biomimetic nanoplatform for enhanced sonodynamic therapy on breast cancer via autophagy regulation strategy. *ACS Appl. Mat. Interfaces* 11 (36), 32729. doi:10.1021/acsami.9b10948

Gabrilovich, D. I., Chen, H. L., Girgis, K. R., Cunningham, H. T., Meny, G. M., Nadaf, S., et al. (1996). Production of vascular endothelial growth factor by human tumors inhibits the functional maturation of dendritic cells. *Nat. Med.* 2 (10), 1096–1103. doi:10.1038/nm1096-1096

Gao, S., Zheng, P., Li, Z., Feng, X., Yan, W., Chen, S., et al. (2018). Biomimetic O2-Evolving metal-organic framework nanoplatform for highly efficient photodynamic therapy against hypoxic tumor. *Biomaterials* 178, 83–94. doi:10.1016/j.biomaterials.2018.06.007

Gao, Z., Li, Y., Zhang, Y., Cheng, K., An, P., Chen, F., et al. (2020). Biomimetic platinum nanozyme immobilized on 2D metal-organic frameworks for mitochondrion-targeting and oxygen self-supply photodynamic therapy. *ACS Appl. Mat. Interfaces* 12 (2), 1963–1972. doi:10.1021/acsami.9b14958

Gong, C., Yu, X., Zhang, W., Han, L., Wang, R., Wang, Y., et al. (2021). Regulating the immunosuppressive tumor microenvironment to enhance breast cancer immunotherapy using pH-responsive hybrid membrane-coated nanoparticles. *J. Nanobiotechnology* 19 (1), 58. doi:10.1186/s12951-021-00805-8

Gong, L., Zhang, Y., Zhao, J., Zhang, Y., Tu, K., Jiao, L., et al. (2022). All-in-one biomimetic nanoplatform based on hollow polydopamine nanoparticles for synergistically enhanced radiotherapy of colon cancer. *Small* 18 (14), e2107656. doi:10.1002/smll.202107656

Gordijo, C. R., Abbasi, A. Z., Amini, M. A., Lip, H. Y., Maeda, A., Cai, P., et al. (2015). Design of hybrid MnO2-polymer-lipid nanoparticles with tunable oxygen generation rates and tumor accumulation for cancer treatment. *Adv. Funct. Mater* 25 (12), 1858–1872. doi:10.1002/adfm.201404511

Gowda, V. K., Rosén, T., Roth, S. V., Söderberg, L. D., and Lundell, F. (2022). Nanofibril alignment during assembly revealed by an X-ray scattering-based digital twin. *ACS Nano* 16 (2), 2120–2132. doi:10.1021/acsnano.1c07769

Han, Y. K., Park, G. Y., Bae, M. J., Kim, J. S., Jo, W. S., and Lee, C. G. (2019). Hypoxia induces immunogenic cell death of cancer cells by enhancing the exposure of cell surface calreticulin in an endoplasmic reticulum stress-dependent manner. *Oncol. Lett.* 18 (6), 6269–6274. doi:10.3892/ol.2019.10986

Hu, C. M., Fang, R. H., Wang, K. C., Luk, B. T., Thamphiwatana, S., Dehaini, D., et al. (2015). Nanoparticle biointerfacing by platelet membrane cloaking. *Nature* 526 (7571), 118–121. doi:10.1038/nature15373

Hu, Q., Sun, W., Qian, C., Wang, C., Bomba, H. N., and Gu, Z. (2015). Anticancer platelet-mimicking nanovehicles. *Adv. Mater* 27 (44), 7043–7050. doi:10.1002/adma.201503323

Huang, H., Zhang, C., Wang, X. L., Shao, J. S., Chen, C., Li, H. M., et al. (2020). Overcoming hypoxia-restrained radiotherapy using an erythrocyte-inspired and glucose-activatable platform. *Nano Lett.* 20 (6), 4211–4219. doi:10.1021/acs.nanolett.0c00650

Huang, Y., Yuan, J., Righi, E., Kamoun, W. S., Ancukiewicz, M., Nezivar, J., et al. (2012). Vascular normalizing doses of antiangiogenic treatment reprogram the immunosuppressive tumor microenvironment and enhance immunotherapy. *Proc. Natl. Acad. Sci. U. S. A.* 109 (43), 17561. doi:10.1073/pnas.1215397109

Huo, D., Jiang, X. Q., and Hu, Y. (2020). Recent advances in nanostrategies capable of overcoming biological barriers for tumor management. *Adv. Mat.* 32 (27), 1904337. doi:10.1002/adma.201904337

Jiang, T., Heng, S., Huang, X., Zheng, L., Kai, D., Loh, X. J., et al. (2019). Biomimetic poly(poly(ε-caprolactone)-polytetrahydrofuran urethane) based nanofibers enhanced chondrogenic differentiation and cartilage regeneration. *J. Biomed. Nanotechnol.* 15 (5), 1005–1017. doi:10.1166/jbn.2019.2748

Jiang, W., Zhang, Z., Wang, Q., Dou, J. X., Zhao, Y. Y., Ma, Y. C., et al. (2019). Tumor reoxygenation and blood perfusion enhanced photodynamic therapy using ultrathin graphdiyne oxide nanosheets. *Nano Lett.* 19 (6), 4060–4067. doi:10.1021/acs.nanolett.9b01458

Kuo, C. T., Chiang, C. L., Chang, C. H., Liu, H. K., Huang, G. S., Huang, R. Y., et al. (2014). Modeling of cancer metastasis and drug resistance via biomimetic nano-cilia and microfluidics. *Biomaterials* 35 (5), 1562–1571. doi:10.1016/j.biomaterials.2013.11.008

Lee, J. B., Kim, D. H., Yoon, J. K., Park, D. B., Kim, H. S., Shin, Y. M., et al. (2020). Microchannel network hydrogel induced ischemic blood perfusion connection. *Nat. Commun.* 11 (1), 615. doi:10.1038/s41467-020-14480-0

Li, C., Yang, X. Q., An, J., Cheng, K., Hou, X. L., Zhang, X. S., et al. (2020). Red blood cell membrane-enveloped O2 self-supplementing biomimetic nanoparticles for tumor imaging-guided enhanced sonodynamic therapy. *Theranostics* 10 (2), 867–879. doi:10.7150/thno.37930

Li, L. H., Shih, Y. L., Huang, J. Y., Wu, C. J., Huang, Y. W., Huang, H. H., et al. (2020). Protection from hydrogen peroxide stress relies mainly on AhpCF and KatA2 in Stenotrophomonas maltophilia. *J. Biomed. Sci.* 27 (1), 37. doi:10.1186/s12929-020-00631-4

Li, M., Yin, F., Song, L., Mao, X., Li, F., Fan, C., et al. (2021). Nucleic acid tests for clinical translation. *Chem. Rev.* 121 (17), 10469. doi:10.1021/acs.chemrev.1c00241

Li, Q., Lin, B., Li, Y., and Lu, N. (2021). Erythrocyte-camouflaged mesoporous titanium dioxide nanoplatform for an ultrasound-mediated sequential therapies of breast cancer. *Int. J. Nanomedicine* 16, 3875–3887. doi:10.2147/ijn.s301855

Li, W., Wang, C., Wang, Z., Gou, L., Zhou, Y., Peng, G., et al. (2022). Physically cross-linked DNA hydrogel-based sustained cytokine delivery for *in situ* diabetic alveolar bone rebuilding. *ACS Appl. Mat. Interfaces* 14 (22), 25173–25182. doi:10.1021/acsami.2c04769

Li, X., Feng, X. Q., Sun, C. S., Liu, Y. X., Zhao, Q. F., and Wang, S. L. (2020). Mesoporous carbon-manganese nanocomposite for multiple imaging guided oxygen-elevated synergetic therapy. *J. Control. Release* 319, 104–118. doi:10.1016/j.jconrel.2019.12.042

Li, X., Gu, G., Soliman, F., Sanders, A. J., Wang, X., and Liu, C. (2018). The evaluation of durative transfusion of endostar combined with chemotherapy in patients with advanced non-small cell lung cancer. *Chemotherapy* 63 (4), 214–219. doi:10.1159/000493098

Liang, H., Wu, Y., Ou, X. Y., Li, J. Y., and Li, J. (2017). Au@Pt nanoparticles as catalase mimics to attenuate tumor hypoxia and enhance immune cell-mediated cytotoxicity. *Nanotechnology* 28 (46), 465702. doi:10.1088/1361-6528/aa8d9c

Liang, R. J., Liu, L. L., He, H. M., Chen, Z. K., Han, Z. Q., Luo, Z. Y., et al. (2018). Oxygen-boosted immunogenic photodynamic therapy with gold nanocages@manganese dioxide to inhibit tumor growth and metastases. *Biomaterials* 177, 149–160. doi:10.1016/j.biomaterials.2018.05.051

Lin, T., Zhao, X., Zhao, S., Yu, H., Cao, W., Chen, W., et al. (2018). O2-generating MnO2 nanoparticles for enhanced photodynamic therapy of bladder cancer by ameliorating hypoxia. *Theranostics* 8 (4), 990–1004. doi:10.7150/thno.22465

Lindau, D., Gielen, P., Kroesen, M., Wesseling, P., and Adema, G. J. (2013). The immunosuppressive tumour network: Myeloid-derived suppressor cells, regulatory T cells and natural killer T cells. *Immunology* 138 (2), 105–115. doi:10.1111/imm.12036

Liu, C. Z., Chen, Y. X., Zhao, J., Wang, Y., Shao, Y. L., Gu, Z. N., et al. (2021). Self-assembly of copper-DNAzyme nanohybrids for dual-catalytic tumor therapy. *Angew. Chem. Int. Ed. Engl.* 60 (26), 14445. doi:10.1002/ange.202101744

Liu, J., Cabral, H., Song, B., Aoki, I., Chen, Z. Y., Nishiyama, N., et al. (2021). Nanoprobe-based magnetic resonance imaging of hypoxia predicts responses to radiotherapy, immunotherapy, and sensitizing treatments in pancreatic tumors. *ACS Nano* 15 (8), 13526. doi:10.1021/acsnano.1c04263

Liu, Y. L., Pan, Y. X., Cao, W., Xia, F. F., Liu, B., Niu, J. Q., et al. (2019). A tumor microenvironment responsive biodegradable CaCO3/MnO2- based nanoplatform

for the enhanced photodynamic therapy and improved PD-L1 immunotherapy. *Theranostics* 9 (23), 6867–6884. doi:10.7150/thno.37586

Lyu, M., Chen, M., Liu, L., Zhu, D., Wu, X., Li, Y., et al. (2021). A platelet-mimicking theranostic platform for cancer interstitial brachytherapy. *Theranostics* 11 (15), 7589–7599. doi:10.7150/thno.61259

Meng, L., Wang, C., Lu, Y., Sheng, G., Yang, L., Wu, Z., et al. (2021). Targeted regulation of blood-brain barrier for enhanced therapeutic efficiency of hypoxia-modifier nanoparticles and immune checkpoint blockade antibodies for glioblastoma. *ACS Appl. Mat. Interfaces* 13 (10), 11657. doi:10.1021/acsami.1c00347

Meng, Z. Q., Zhou, X. F., Xu, J., Han, X., Dong, Z. L., Wang, H. R., et al. (2019). Light-triggered *in situ* gelation to enable robust photodynamic-immunotherapy by repeated stimulations. *Adv. Mater* 31 (24), 1900927. doi:10.1002/adma.201900927

Noman, M. Z., Desantis, G., Janji, B., Hasmim, M., Karray, S., Dessen, P., et al. (2014). PD-L1 is a novel direct target of HIF-1α, and its blockade under hypoxia enhanced MDSC-mediated T cell activation. *J. Exp. Med.* 211 (5), 781–790. doi:10.1084/jem.20131916

Sarkar, S., Alam, M. A., Shaw, J., and Dasgupta, A. K. (2013). Drug delivery using platelet cancer cell interaction. *Pharm. Res.* 30 (11), 2785–2794. doi:10.1007/s11095-013-1097-1

Shi, X., Yang, W., Ma, Q., Lu, Y., Xu, Y., Bian, K., et al. (2020). Hemoglobin-mediated biomimetic synthesis of paramagnetic O2-evolving theranostic nanoprobes for MR imaging-guided enhanced photodynamic therapy of tumor. *Theranostics* 10 (25), 11607. doi:10.7150/thno.46228

Song, C. H., Tang, C. C., Xu, W. G., Ran, J. C., Wei, Z., Wang, Y. F., et al. (2020). Hypoxia-targeting multifunctional nanoparticles for sensitized chemotherapy and phototherapy in head and neck squamous cell carcinoma. *Int. J. Nanomedicine* 15, 347–361. doi:10.2147/ijn.s233294

Song, X. J., Xu, J., Liang, C., Chao, Y., Jin, Q. T., Wang, C., et al. (2018). Self-supplied tumor oxygenation through separated liposomal delivery of H2O2 and catalase for enhanced radio-immunotherapy of cancer. *Nano Lett.* 18 (10), 6360–6368. doi:10.1021/acs.nanolett.8b02720

Tang, W., Zhen, Z., Wang, M., Wang, H., Chuang, Y. J., Zhang, W., et al. (2016). Red blood cell-facilitated photodynamic therapy for cancer treatment. *Adv. Funct. Mat.* 26 (11), 1757–1768. doi:10.1002/adfm.201504803

Tang, Y. Q., Chen, T. F., Zhang, Y., Zhao, X. C., Zhang, Y. Z., Wang, G. Q., et al. (2020). The tumor immune microenvironment transcriptomic subtypes of colorectal cancer for prognosis and development of precise immunotherapy. *Gastroenterol. Rep. (Oxf)* 8 (5), 381–389. doi:10.1093/gastro/goaa045

Voron, T., Colussi, O., Marcheteau, E., Pernot, S., Nizard, M., Pointet, A. L., et al. (2015). VEGF-A modulates expression of inhibitory checkpoints on CD8+ T cells in tumors. *J. Exp. Med.* 212 (2), 139–148. doi:10.1084/jem.20140559

Wang, D., Wu, H., Phua, S. Z. F., Yang, G., Qi Lim, W., Gu, L., et al. (2020). Self-assembled single-atom nanozyme for enhanced photodynamic therapy treatment of tumor. *Nat. Commun.* 11 (1), 357. doi:10.1038/s41467-019-14199-7

Wang, P., Wang, X., Luo, Q., Li, Y., Lin, X., Fan, L., et al. (2019). Fabrication of red blood cell-based multimodal theranostic probes for second near-infrared window fluorescence imaging-guided tumor surgery and photodynamic therapy. *Theranostics* 9 (2), 369–380. doi:10.7150/thno.29817

Wu, J. Y., Huang, T. W., Hsieh, Y. T., Wang, Y. F., Yen, C. C., Lee, G. L., et al. (2020). Cancer-derived succinate promotes macrophage polarization and cancer metastasis via succinate receptor. *Mol. Cell* 77 (2), 213–227.e5. doi:10.1016/j.molcel.2019.10.023

Yang, T., Wang, Y., Ke, H. T., Wang, Q. L., Lv, X. Y., Wu, H., et al. (2016). Protein-nanoreactor-assisted synthesis of semiconductor nanocrystals for efficient cancer theranostics. *Adv. Mater* 28 (28), 5923–5930. doi:10.1002/adma.201506119

Yang, W. T., Guo, W. S., Chang, J., and Zhang, B. B. (2017). Protein/peptide-templated biomimetic synthesis of inorganic nanoparticles for biomedical applications. *J. Mat. Chem. B* 5 (3), 401–417. doi:10.1039/c6tb02308h

Yang, W. T., Guo, W. S., Le, W. J., Lv, G. X., Zhang, F. H., Shi, L., et al. (2016). Albumin-bioinspired Gd:CuS nanotheranostic agent for *in vivo* photoacoustic/magnetic resonance imaging-guided tumor-targeted photothermal therapy. *ACS Nano* 10 (11), 10245. doi:10.1021/acsnano.6b05760

Yang, W. T., Wu, X. L., Dou, Y., Chang, J., Xiang, C. Y., Yu, J. N., et al. (2018). A human endogenous protein exerts multi-role biomimetic chemistry in synthesis of paramagnetic gold nanostructures for tumor bimodal imaging. *Biomaterials* 161, 256–269. doi:10.1016/j.biomaterials.2018.01.050

Yang, Z., Chen, H., Yang, P., Shen, X., Hu, Y., Cheng, Y., et al. (2022). Nano-oxygenated hydrogels for locally and permeably hypoxia relieving to heal chronic wounds. *Biomaterials* 282, 121401. doi:10.1016/j.biomaterials.2022.121401

Yang, Z., Deng, W., Zhang, X., An, Y., Liu, Y., Yao, H., et al. (2022). Opportunities and challenges of nanoparticles in digestive tumours as anti-angiogenic therapies. *Front. Oncol.* 11, 789330. doi:10.3389/fonc.2021.789330

Yang, Z., Du, Y., Sun, Q., Peng, Y., Wang, R., Zhou, Y., et al. (2020). Albumin-based nanotheranostic probe with hypoxia alleviating potentiates synchronous multimodal imaging and phototherapy for glioma. *ACS Nano* 14 (5), 6191–6212. doi:10.1021/acsnano.0c02249

Yen, T. Y., Stephen, Z. R., Lin, G. Y., Mu, Q. X., Jeon, M., Untoro, S., et al. (2019). Catalase-functionalized iron oxide nanoparticles reverse hypoxia-induced chemotherapeutic resistance. *Adv. Healthc. Mater* 8 (20), 1900826. doi:10.1002/adhm.201900826

Yu, M., Duan, X. H., Cai, Y. J., Zhang, F., Jiang, S. Q., Han, S. S., et al. (2019). Multifunctional nanoregulator reshapes immune microenvironment and enhances immune memory for tumor immunotherapy. *Adv. Sci. (Weinh)* 6 (16), 1900037. doi:10.1002/advs.201900037

Zhang, B. B., Jin, H. T., Li, Y., Chen, B. D., Liu, S. Y., and Shi, D. L. (2012). Bioinspired synthesis of gadolinium-based hybrid nanoparticles as MRI blood pool contrast agents with high relaxivity. *J. Mat. Chem.* 22 (29), 14494. doi:10.1039/c2jm30629h

Zhang, C., Xia, D. L., Liu, J. H., Huo, D., Jiang, X. Q., and Hu, Y. (2020). Bypassing the immunosuppression of myeloid-derived suppressor cells by reversing tumor hypoxia using a platelet-inspired platform. *Adv. Funct. Mater* 30 (22), 2000189. doi:10.1002/adfm.202000189

Zhang, L., Wang, Z., Zhang, Y., Cao, F., Dong, K., Ren, J., et al. (2018). Erythrocyte membrane cloaked metal-organic framework nanoparticle as biomimetic nanoreactor for starvation-activated colon cancer therapy. *ACS Nano* 12 (10), 10201. doi:10.1021/acsnano.8b05200

Zhang, L. Y., and Han, F. (2018). Protein coated gold nanoparticles as template for the directed synthesis of highly fluorescent gold nanoclusters. *Nanotechnology* 29 (16), 165702. doi:10.1088/1361-6528/aaae47

Zhang, M. K., Ye, J. J., Li, C. X., Xia, Y., Wang, Z. Y., Feng, J., et al. (2019). Cytomembrane-mediated transport of metal ions with biological specificity. *Adv. Sci. (Weinh)* 6 (17), 1900835. doi:10.1002/advs.201900835

Zhang, M., Ye, J. J., Xia, Y., Wang, Z. Y., Li, C. X., Wang, X. S., et al. (2019). Platelet-Mimicking biotaxis targeting vasculature-disrupted tumors for cascade amplification of hypoxia-sensitive therapy. *ACS Nano* 13 (12), 14230–14240. doi:10.1021/acsnano.9b07330

Zhao, P. F., Zheng, M. B., Luo, Z. Y., Fan, X. J., Sheng, Z. H., Gong, P., et al. (2016). Oxygen nanocarrier for combined cancer therapy: Oxygen-boosted ATP-responsive chemotherapy with amplified ROS lethality. *Adv. Healthc. Mat.* 5 (17), 2161–2167. doi:10.1002/adhm.201600121

Zhao, Y., Peng, J., Li, J. J., Huang, L., Yang, J. Y., Huang, K., et al. (2017). Tumor-targeted and clearable human protein-based MRI nanoprobes. *Nano Lett.* 17 (7), 4096–4100. doi:10.1021/acs.nanolett.7b00828

Zhou, Z. G., Zhang, B. L., Wang, S. S., Zai, W. J., Yuan, A., Hu, Y. Q., et al. (2018). Perfluorocarbon nanoparticles mediated platelet blocking disrupt vascular barriers to improve the efficacy of oxygen-sensitive antitumor drugs. *Small* 14 (45), 1801694. doi:10.1002/smll.201801694

Zhu, C. Q., Guo, X. M., Luo, L. H., Wu, Z., Luo, Z. Y., Jiang, M., et al. (2019). Extremely effective chemoradiotherapy by inducing immunogenic cell death and radio-triggered drug release under hypoxia alleviation. *ACS Appl. Mat. Interfaces* 11 (50), 46536. doi:10.1021/acsami.9b16837

Zhu, X. F., Gong, Y. C., Liu, Y. A., Yang, C. H., Wu, S. J., Yuan, G. L., et al. (2020). Ru@CeO2 yolk shell nanozymes: Oxygen supply *in situ* enhanced dual chemotherapy combined with photothermal therapy for orthotopic/subcutaneous colorectal cancer. *Biomaterials* 242, 119923. doi:10.1016/j.biomaterials.2020.119923

Zuo, H., Tao, J., Shi, H., He, J., Zhou, Z., and Zhang, C. (2018). Platelet-mimicking nanoparticles co-loaded with W18O49 and metformin alleviate tumor hypoxia for enhanced photodynamic therapy and photothermal therapy. *Acta Biomater.* 80, 296–307. doi:10.1016/j.actbio.2018.09.017

frontiers | Frontiers in Bioengineering and Biotechnology

TYPE Original Research
PUBLISHED 05 October 2022
DOI 10.3389/fbioe.2022.1007430

OPEN ACCESS

EDITED BY
Jingwei Xie,
University of Nebraska Medical Center, United States

REVIEWED BY
Xiaoran Li,
Donghua University, China
Jiajia Xue,
Beijing University of Chemical Technology, China

*CORRESPONDENCE
Shue Wang,
swang@newhaven.edu

SPECIALTY SECTION
This article was submitted to Tissue Engineering and Regenerative Medicine, a section of the journal Frontiers in Bioengineering and Biotechnology

RECEIVED 30 July 2022
ACCEPTED 16 September 2022
PUBLISHED 05 October 2022

CITATION
Zhao Y, Richardson K, Yang R, Bousraou Z, Lee YK, Fasciano S and Wang S (2022), Notch signaling and fluid shear stress in regulating osteogenic differentiation. *Front. Bioeng. Biotechnol.* 10:1007430. doi: 10.3389/fbioe.2022.1007430

Notch signaling and fluid shear stress in regulating osteogenic differentiation

Yuwen Zhao[1,2], Kiarra Richardson[1,3], Rui Yang[1,4], Zoe Bousraou[1], Yoo Kyoung Lee[1], Samantha Fasciano[5] and Shue Wang[1]*

[1]Department of Chemistry, Chemical and Biomedical Engineering, University of New Haven, West Haven, CT, United States, [2]Department of Bioengineering, Lehigh University, Bethlehem, PA, United States, [3]Department of Biomedical Engineering, Duke University, Durham, NC, United States, [4]Department of Biomedical Engineering, University of Connecticut, Storrs, CT, United States, [5]Department of Cellular and Molecular Biology, University of New Haven, West Haven, CT, United States

Osteoporosis is a common bone and metabolic disease that is characterized by bone density loss and microstructural degeneration. Human bone marrow-derived mesenchymal stem cells (hMSCs) are multipotent progenitor cells with the potential to differentiate into various cell types, including osteoblasts, chondrocytes, and adipocytes, which have been utilized extensively in the field of bone tissue engineering and cell-based therapy. Although fluid shear stress plays an important role in bone osteogenic differentiation, the cellular and molecular mechanisms underlying this effect remain poorly understood. Here, a locked nucleic acid (LNA)/DNA nanobiosensor was exploited to monitor mRNA gene expression of hMSCs that were exposed to physiologically relevant fluid shear stress to examine the regulatory role of Notch signaling during osteogenic differentiation. First, the effects of fluid shear stress on cell viability, proliferation, morphology, and osteogenic differentiation were investigated and compared. Our results showed shear stress modulates hMSCs morphology and osteogenic differentiation depending on the applied shear and duration. By incorporating this LNA/DNA nanobiosensor and alkaline phosphatase (ALP) staining, we further investigated the role of Notch signaling in regulating osteogenic differentiation. Pharmacological treatment is applied to disrupt Notch signaling to investigate the mechanisms that govern shear stress induced osteogenic differentiation. Our experimental results provide convincing evidence supporting that physiologically relevant shear stress regulates osteogenic differentiation through Notch signaling. Inhibition of Notch signaling mediates the effects of shear stress on osteogenic differentiation, with reduced ALP enzyme activity and decreased Dll4 mRNA expression. In conclusion, our results will add new information concerning osteogenic differentiation of hMSCs under shear stress and the regulatory role of Notch signaling. Further studies may elucidate the mechanisms underlying the mechanosensitive role of Notch signaling in stem cell differentiation.

KEYWORDS

osteogenic differentiation, mesenchymal stem cells, notch signaling, shear stress, LNA/DNA nanobiosensor, single cell gene expression, Dll4 mRNA expression

Introduction

Osteoporosis is a systemic metabolic bone disease characterized by reduced bone formation in the bone marrow space, which leads to bone mass loss and microstructural degeneration (Raisz, 2005). In the United States, it is estimated that ~ 10 million people have osteoporosis and more than 34 million are at risk (Weycker et al., 2016). It is also estimated that osteoporosis causes more than 9 million fractures annually worldwide. In recent years, the cost of treating osteoporosis is increasing due to the increased aged population and space travel, causing challenges to public health care. In space, the reason for developing osteoporosis is mainly related to low (micro-to zero-) gravity conditions, with possible contributions of cosmic ray radiation (Gambacurta et al., 2019). For example, bone density loss occurs in the weightless environment of space due to the lack of gravity force. Thus, the bone no longer needs to support the body against gravity. Astronauts lose about 1%–2% of their bone mineral density every month during space travel. Osteoporosis is one of the major consequences of long-duration spaceflights in astronauts, seriously undermining their health (Cappellesso et al., 2015). Currently, the autologous bone graft is the "gold standard" approach to restoring large bone defects with bone loss, where a piece of bone is taken from another body site, and transplanted into the defect (Pape et al., 2010). However, the availability of donated bone and the necessity of an invasive and expensive surgery limited its application. Another approach to treat osteoporosis is to stimulate osteogenesis or inhibit bone resorption through drug-based agents, i.e., bisphosphonates (Jiang et al., 2021). However, drug-based agents are limited due to their side effects and lack of capability of regaining the lost bone density. Thus, there is an urgent need for alternative therapeutic approaches for osteoporosis, especially therapies that are able to counteract bone mass loss, which is crucial for aged populations and astronauts that are needed for prolonged space missions.

Human bone marrow-derived mesenchymal stem cells (hMSCs) are ideal candidates for cell-based therapies for bone tissue engineering and regenerative medicine due to their multipotency. Under mechanical or chemical stimulation, hMSCs can be induced to differentiate into various lineages, including osteoblasts (bone), neuroblasts (neural tissue), adipoblasts (fat), myoblasts (muscle), and chondroblasts (cartilage) (Han et al., 2019). Moreover, the fate commitment and differentiation of hMSCs is closely controlled by the local mechanical and chemical environment that maintains a balance between osteogenic differentiation and adipogenic differentiation. Reduced osteogenic differentiation and increased adipogenic differentiation might lead to osteoporosis. Although the differentiation capacity of hMSCs has been demonstrated, the mechanisms that control their plasticity remain poorly understood, especially how hMSCs can be differentiated into osteoblasts and make bones. It is believed that mechanical stimulation impacts hMSCs osteogenic differentiation. Over the last few decades, unremitting efforts have been devoted to understanding biochemical signals that regulate hMSCs commitment. Based on these efforts, a number of chemical stimuli (e.g., small bioactive molecules, growth factors, and genetic regulators) have been identified in regulating hMSCs lineage commitment, including bone morphogenetic protein (BMP), Wnt, and Notch signaling (Guilak et al., 2009; Wang Y.-K. et al., 2012; Heo et al., 2016). Since the last decade, the effects of physical/mechanical cues of the microenvironment on hMSCs fate determination have been investigated extensively. For instance, several studies provide evidence that mechanical cues, including shear, stiffness and topography, and electrical stimulation, and acoustic tweezing cytometry (ATC) (Xue et al., 2016; Xue et al., 2017), both direct and indirect, play important roles in regulating stem cell fate. Moreover, it had been shown that extracellular matrix (ECM) and topography enhance hMSCs osteogenic differentiation by cellular tension and mechanotransduction of Yes-associated protein (YAP) activity (Assunção et al., 2020; Yang et al., 2020; Kashani et al., 2021; Saghati et al., 2021). Although these studies have made significant progress in understanding the stimuli that regulates hMSCs differentiation, the fundamental mechanism of osteogenic differentiation remains uncharacterized. Particularly, the interaction of biophysical factors and biochemical signals is obscure. Thus, understanding the interaction of biophysical and chemical signals in osteogenic differentiation may provide new insights to improve our techniques in cell-based therapies and organ repair.

Osteogenic differentiation is a dynamic process and involves several significant signaling pathways, including YAP/TAZ (transcriptional coactivator with PDZ-binding motif), Notch, and RhoA signaling (Karystinou et al., 2015; Lorthongpanich et al., 2019). It has been shown that fluid shear force, including that encountered in microgravity models, regulates *in vitro* osteogenic differentiation of mesenchymal stem cells (MSCs) (Navran, 2008; Weber et al., 2012; Kim et al., 2014; Qin et al., 2019). For example, it has been shown that physiologically relevant fluid-induced shear stress of 3–9 dynes/cm^2 could be conducive to cell conditioning, and assist in promoting genes (Sacks and Yoganathan, 2008; Williams et al., 2017; Gonzalez et al., 2020). It is also reported that hMSCs were able to differentiate into endothelial cells and activate interstitial cells deeper when exposed to physiologically relevant steady fluid-induced shear stress (4–5 dynes/cm^2) (Rath et al., 2015). Although current studies revealed shear stress could enhance osteogenic differentiation, the involvement of Notch signaling in shear stress induced osteogenesis is not clear due to a lack of effective tools to detect and monitor the gene expression in live cells. Current approaches for gene detection are limited due to the requirements of physical isolation of cells or fixation, where

the spatial and temporal gene expression information is missing. For example, RNA *in situ* hybridization and single cell transcriptomics are limited to fixed cells (Wang F. et al., 2012). Although fluorescent protein tagging techniques are able to track dynamic gene expression in live cells, it is limited by transfection efficiency and the requirements of genetic modification to express engineered transcripts (Yu et al., 2006). Thus, dynamic monitoring of gene expression in live cells at the single cell level will reveal the fundamental regulatory mechanism of cells during dynamic biological processes, which will eventually open opportunities to develop novel approaches for tissue engineering and regenerative medicine.

Here, we exploited a double-stranded locked nucleic acid/DNA (LNA/DNA) nanobiosensor to elucidate the regulatory role of Notch signaling during osteogenic differentiation of hMSCs that were exposed to physiologically relevant shear stress (3–7 dynes/cm^2). The effects of fluid shear stress on hMSCs proliferation and osteogenic differentiation were first investigated and compared under different levels of fluid shear stress. The phenotypic behaviors, including cell morphology, proliferation, and differentiation, were compared and characterized. We further detected Notch 1 ligand Delta-like 4 (Dll4) gene expression by incorporating this LNA/DNA nanobiosensor with hMSCs imaging during osteogenic differentiation. Finally, we examined the role of Notch signaling in regulating osteogenic differentiation of hMSCs that are under shear stress. Pharmacological administration is applied to disrupt Notch signaling to investigate the cellular and molecular mechanisms that govern osteogenic differentiation. Our experimental results provide convincing evidence supporting that physiologically relevant shear stress regulates osteogenic differentiation through Notch signaling. Inhibition of Notch signaling will mediate the effects of shear stress on osteogenic differentiation, with reduced alkaline phosphatase (ALP) enzyme activity and decreased Dll4 mRNA expression. In conclusion, our results will add new information concerning osteogenic differentiation of hMSCs under shear stress and the involvement of Notch signaling. Further studies may elucidate the mechanisms underlying the mechanosensitive role of Notch signaling in stem cell differentiation.

Materials and methods

Cell culture and reagents

hMSCs were acquired from Lonza, which were isolated from normal (non-diabetic) adult human bone marrow withdrawn from bilateral punctures of the posterior iliac crests of normal volunteers. hMSCs were cultured in mesenchymal stem cell basal medium MSCBM (Catalog #: PT-3238, Lonza) with GA-1000, L-glutamine, and mesenchymal cell growth factors (Catalog #: PT-4105, Lonza). Cells were cultured in a tissue culture dish at 37°C and 5% CO_2 in a humidified incubator. Cells were maintained regularly with medium change every 3 days and passaged using 0.25% EDTA-Trypsin (Invitrogen). hMSCs from passage 2-7 were used in the experiments. For osteogenic induction studies, hMSCs were seeded at a concentration of 400 cells/mm^2 with a volume of 500 μL basal medium in 24 well-plates. Once the cells reach 80% confluency, for the control group, cells were maintained in basal medium. For induction group, the basal medium was replaced with osteogenic differentiation medium (Catalog #: PT-3002, Lonza). Osteogenic differentiation medium was changed every 2 days. For studying Notch signaling, hMSCs were treated with 20 μM γ-secretase inhibitor DAPT (Sigma Aldrich) after osteogenic induction. It is noted that DAPT treatment was performed daily. Images were taken after 3 and 5 days of osteogenic induction, respectively.

Design of LNA probe

An LNA detecting probe is a 20-base pair nucleotide sequence with alternating LNA/DNA monomers that is complementary to target mRNA sequence with a 100% match. For target mRNA detection, a fluorophore (6-FAM) was labeled at the 5′ end of the LNA probe for fluorescence detection. The design process of the LNA probe for mRNA detection was reported previously. (Wang et al., 2015; Wang et al., 2018b; Wang et al., 2019; Zhao et al., 2022) Briefly, the target mRNA sequence was first acquired from GeneBank. A 20-base pair nucleotide sequence was selected and optimized using mFold server and NCBI Basic Local Alignment Search Tool (BLAST) database. A quencher probe is a 10-base pair nucleotide sequence with LNA/DNA monomers that is complementary to the 5′ end of the LNA detecting probe. An Iowa Black RQ fluorophore was labeled at the 3′ end of the quencher probe. The Dll4 LNA detecting probe was designed based on target mRNA sequences (5′-3′: +AA +GG +GC +AG +TT +GG +AG +AG +GG +TT). The LNA detecting probe and quencher sequence were synthesized by Integrated DNA Technologies Inc. (IDT).

Preparation of double-stranded LNA probe

To prepare the LNA/DNA nanobiosensor, the LNA detecting probe and quencher probe were initially prepared in 1x Tris EDTA buffer (pH = 8.0) at a concentration of 100 nM. The LNA probe and quencher were mixed at the ratio of 1:2 and incubated at 95°C in a dry water bath for 5 min and cooled down to room temperature over the course of 2 h. Once cooled down, the prepared LNA probe and quencher mixer can be stored in a refrigerator for up to 7 days. For mRNA detection, the prepared double-stranded LNA/DNA probe was then transfected into

hMSCs using Lipofectamine 2000 following manufacturers' instructions. mRNA gene expression can thus be evaluated by measuring the fluorescence intensity of hMSCs transfected with LNA/DNA probes.

Simulation of orbital shear stress

hMSCs were exposed to 30/60 RPM orbital shear stress using a low-speed orbital shaker (Corning LSE, 6780-FP, orbit, 1.9 cm, speed range, 3–60 rpm). The orbital shear was applied to hMSCs after osteogenic induction for 6 h per day or continuously for a total of 3 and 5 days. The orbital shaker was placed inside the incubator to maintain cell environment. The orbital shear stress was calculated using the following equation:

$$\tau_{max} = a \times \sqrt{\rho \cdot \eta \cdot \omega^3}$$

Where τ_{max} is near-maximal shear stress, a is the orbital radius of rotation, ρ is the density of cell culture medium, η is the dynamic viscosity of the medium, ω is the angular velocity and $\omega = 2\pi f$. f is the frequency of rotation (revolution per second).

Cell proliferation and viability

To evaluate the effects of applied orbital shear stress on hMSCs proliferation and viability, a cell proliferation and viability reagent (Cell Counting kit-8, cck-8 assay, Sigma Aldrich) was utilized following the manufacturers' instructions. First, hMSCs were seeded in three flat-bottom 96-well tissue culture well plates with the density of 2000 cells/well with the volume of 100 µl basal culture medium. After 24 h of incubation to allow cell attachment, two 96-well plates were placed on orbital shaker. Out of these two well-plates, one well plate was kept on the orbital shaker to experience continuous orbital shear stress for 3 or 5 days, the other well plates was kept on the orbital shaker for 6 h per day for a duration of 3 or 5 days. The third 96-well plate was kept in static condition in the incubator for comparison. Cell viability was evaluated after 3 or 5 days of applying shear stress. After applying shear, CCK-8 reagents were added to each well and incubated for 4 h. The absorbance of each sample was measured at 450 nm and compared using a fluorescence microplate reader (BioTek, Synergy 2).

Live/dead viability staining

The hMSCs viability after orbital shear was evaluated using live/dead viability assay (ThermoFisher). hMSCs were stained using propidium iodide (PI, 10 µg/ml), a fluorescent agent that binds to DNA by intercalating between the bases with little or no sequence preference. The cell nucleus was stained using Hoechst 33342 for 30 min at the concentration of 20 µM. After staining, hMSCs were washed three times with 1x PBS to remove extra dye. hMSCs were then imaged using Texas Red (535/617 nm) and DAPI (360/460 nm) filters on the ZOE image station.

Staining

To quantify hMSCs osteogenic differentiation, alkaline phosphatase enzyme activities were evaluated and measured by using two ALP staining assays, AP live staining (ThermoFisher) and ALP staining kit (for fixed cells, Sigma-Aldrich). For fixed cells, the staining solution was first prepared by mixing Fast Red Violet solution, Naphthol AS-BI phosphate solution and water at a ratio of 2:1:1. Next, hMSCs were fixed using 4% cold-Paraformaldehyde (PFA) for 2 min which enable the maintenance of the ALP activation. After fixation, the PFA was aspirated without wash. The staining solution was then added to the fixed cells for 15 min under room temperature and protected from light. The cells were then washed three times with 1x PBS, 15 min each time, before taking images. For AP live staining, hMSCs were stained using AP live stain at the concentration of 10X stock solution for 30 min according to manufacturers' instructions. After staining, hMSCs were washed twice using basal medium. Images were captured after 30 min of staining. For F-actin staining, hMSCs were first fixed with 4% PFA solution for 10 min before being permeabilized and blocked with the PBST solution (PBS + 0.5% Triton + 1% BSA) for 1 h. After wash with 1x PBS three times, hMSCs were incubated with phalloidin (1:30) for 1 h at room temperature. The cells were then washed three times using 1x PBS, before imaging.

Imaging and statistical analysis

Images were captures using ZOE Fluorescent Cell Imager with an integrated digital camera (BIO-RAD) or Nikon TE 2000 with a Retiga R1 monochrome CCD Camera. For comparison, all the images were taken with the same setting, including exposure time and gain. Data collection and imaging analysis were performed using NIH ImageJ software. To quantify Dll4 mRNA and ALP enzyme activity, the mean fluorescence intensity of each cell was measured. The background noise was then subtracted. All the cells were quantified in the same field of view and at least five images for each condition were quantified. All experiments were repeated at least three times and over 100 cells were quantified for each group. Results were analyzed using independent, two-tailed Student *t*-test in Excel (Microsoft). $p < 0.05$ was considered statistically significant.

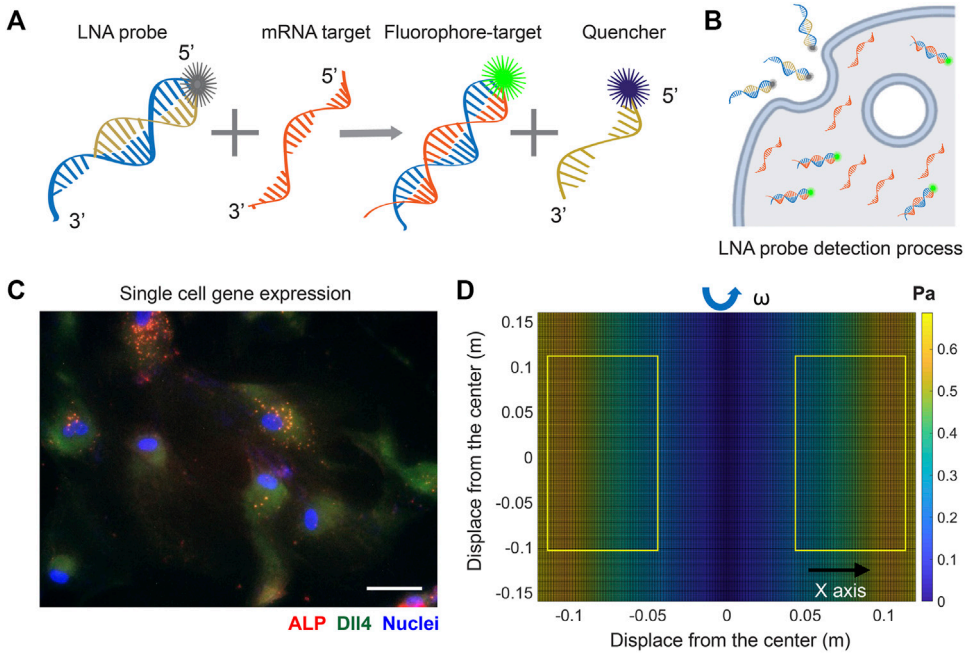

FIGURE 1
LNA/DNA nanobiosensor for single cell gene expression analysis in living cells. **(A)** Schematic illustration of LNA/DNA nanobiosensor for mRNA detection. Briefly, the LNA/DNA nanobiosensor is a complex of LNA donor and quencher probe. The fluorophore at the 5′ of LNA donor probe is quenched due to close proximity. In the presence of target mRNA sequence, the LNA donor sequence is displaced from the quencher to bind to the target sequence, allowing the fluorophore to fluorescence. **(B)** Schematic illustration of cellular endocytic uptake of LNA/DNA nanobiosensor by cells for intracellular gene detection. **(C)** Representative fluorescence image of Dll4 mRNA expression, ALP expression in hMSCs using LNA/DNA nanobiosensor. Green: Dll4 mRNA; red: ALP; blue: Nuclei. Scale bar: 100 μm. **(D)** Simulated distribution of orbital shear stress. Yellow labeled rectangles indicate the location of well-plates. The estimated shear stress were in the range of 0.3–0.6 Pa.

Results

Design LNA/DNA nanobiosensor for mRNA detection

To investigate the involvement of Notch signaling in osteogenic differentiation of hMSCs that were exposed to shear stress, we utilized an LNA/DNA nanobiosensor for mRNA gene expression analysis. The LNA/DNA nanobiosensor is a complex of an LNA detecting probe and a quencher, Figure 1A. The LNA detecting probe is a 20-base pair single stranded oligonucleotide sequence with alternating LNA/DNA monomers, which are designed to be complementary to the target mRNA sequence. The LNA nucleotides are modified DNA nucleotides with higher thermal stability and specificity. A fluorophore (6-FAM (fluorescein)) was labeled at the 5′ end of the LNA detecting probe for mRNA detection. Design, characterization, and optimization of LNA/DNA nanobiosensor have been reported previously (Wang et al., 2015; Zheng et al., 2017; Wang et al., 2018a; Zhao et al., 2022). Briefly, the LNA probe will bind to the quencher spontaneously to form a LNA - quencher complex. Due to their close physical proximity, the fluorophore at the 5′ end of the LNA probe is quenched by quencher due to its quenching ability (Moreira et al., 2005). After it is internalized by cells and in the presence of the target mRNA sequence in the cytoplasm, the LNA probe is thermodynamically displaced from the quencher and binds to specific target mRNA sequences, which permits the fluorophore to reacquire fluorescence signal, Figure 1B. This displacement is due to the larger difference in binding free energy between LNA probe to target mRNA *versus* LNA probe to quencher. Thus, the fluorescence intensity of individual cells containing LNA/DNA nanobiosensor can serve as a quantitative measurement of the amount of target mRNA in each cell. In this study, hMSCs were transfected with the LNA/DNA nanobiosensor prior to osteogenic induction. The mRNA expression at the single cell level was clearly evident, Figure 1C.

Simulation of orbital shear stress and analysis

To evaluate the effects of physiologically relevant shear stress on osteogenic differentiation, the shear stress was estimated using Strokes' second problem, which concerns a plate oscillating along one axis in the plane of the plate, with a

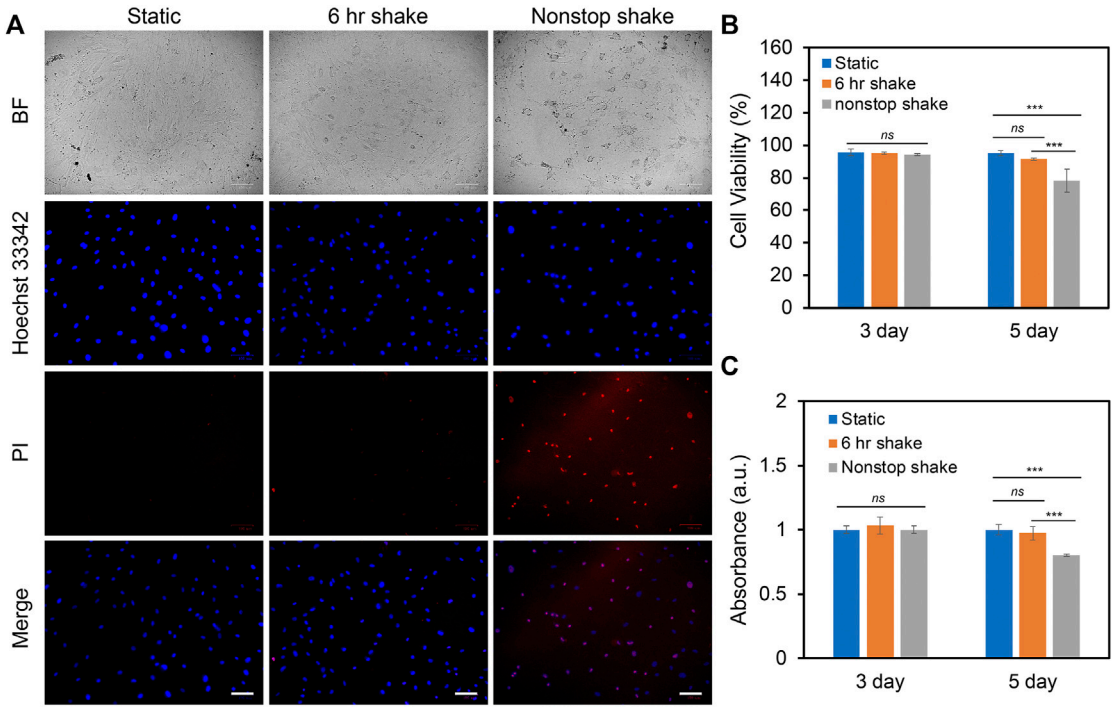

FIGURE 2
Effects of shear stress on cell viability and proliferation. **(A)** Representative bright field and fluorescence images of hMSCs after 5 days of culture with the speed of 20 RPM under static, 6 h shake, and nonstop shake conditions, respectively. Static: cells were placed in a CO_2 incubator without shear; 6 h shake: cells were placed on the orbital shaker for 6 h per day; nonstop shake: cells were placed on the orbital shaker without stop. Samples were stained with propidium iodide (PI, red), and hoechst 33342 (blue), respectively. Scale bar: 100 μm. **(B)** Comparison of cell viability of hMSCs after 3 and 5 days of culture under three different conditions, respectively. Cell viability was calculated as: # of live cells per field/total # of cells per field x 100%. Data represents over 500 cells in each group and expressed as mean± s.e.m. (n = 4, *ns*, not significant, ***, $p < 0.001$, **, $p < 0.01$). **(C)** Comparison of the proliferation of hMSCs cultured in different conditions. Data were acquired using a cck-8 assay and the absorbance at 450 nm was compared. Data are expressed as mean± s.e.m. (n = 4, *ns*, not significant, ***, $p < 0.001$, **, $p < 0.01$).

liquid above it. Although the orbital shaker does not produce uniform laminar shear stress on seeded cells, most of the cells were exposed to near-maximum shear that is calculated as: $\tau_{max} = a \times \sqrt{\rho \cdot \eta \cdot (2\pi f)^3}$, where a is the orbital radius of rotation. The density of hMSCs culture medium is ~1.015 × 10^3 kg/m^3, the dynamic viscosity is 0.958 × 10^{-4} kg/m.s (Poon, 2022). Since the cells in different wells were placed at different locations on the shaker, the shear stress is slightly different. Thus, we simulated the distribution of the shear stress over the shaker platform. Since the orbital shaker shakes along one axis (y), the shear stress along the y axis is the same. The orbital shear stress was simulated at 30 RPM. The maximum shear stress is approximately 0.7 Pascal (7.1 dyne/cm^2), which is on the edge of the shaker. At the center of the shaker, the shear stress is zero. The well-plates with the dimensions of 120 mm × 85 mm were placed on the shaker, labeled in Figure 1D. Thus, the applied shear stress to different wells ranges from 3 dyne/cm^2 to 7 dyne/cm^2, which are similar to the values reported by others (Dardik et al., 2005; Lim et al., 2014; Iovene et al., 2021) .

Fluid shear stress modulates human bone marrow-derived mesenchymal stem cells proliferation and viability

In order to study the effects of different levels of shear stress on cell proliferation and viability, three groups of experiments were designed and compared: static condition, 6 h shake, and nonstop shake. For static condition, cells were placed in the humidified CO_2 incubator without applying shear; for the 6 h shake, cells were applied shear stress for 6 h per day for a total duration of 3 and 5 days; for the nonstop shake group, cells were applied orbital shear stress without a stop for a total of 3 and 5 days. Two different levels of shear stress were investigated: low fluid shear stress and high fluid shear stress. The low fluid shear stress were defined as the shear stress that is physiologically relevant with a range of 1–9 dynes/cm^2; while high fluid shear stress is double the magnitude of low fluid shear stress (9–20 dynes/cm^2). The cell viability and proliferation were evaluated using live/dead cell assay and cell counting kit (cck-8) assay after 3 and 5 days, respectively. Under low fluid shear

stress, the cell viability and proliferation were evaluated and compared. Figure 2A shows the bright field and fluorescent images of hMSCs after 5 days of shear stress under different groups. It is evident that the number of dead cells increased when hMSCs were exposed to continuous shear for 5 days. We further quantified the effects of shear stress on cell viability and proliferation. The cell viability was calculated as: # of live cells per field/# of total cells per field x 100%. After applying shear for 3 days, the cell viability and proliferation of hMSCs under shear stress did not show a significant difference compared to hMSCs in the static condition, left panel of Figures 2B,C. After 5 days, hMSCs under continuous shear stress showed significantly reduced cell viability and proliferation, with a 21.5% decrease in cell viability and a 19.8% decrease in proliferation compared to the cells in the static condition, right panel of Figures 2B,C. It is noted that after applying shear stress for 5 days with 6 h per day, the cell viability and proliferation of hMSCs did not show a significant difference compared to the hMSCs that were in the static condition. Furthermore, we studied the effects of high fluid shear stress (9–20 dynes/cm^2) on hMSCs viability and proliferation, Supplementary Figure S1. For the hMSCs that were exposed to high shear stress for 3 days, the cell viability was decreased by 55% for the nonstop shake group. After 5 days of applying shear stress, the number of dead cells in both the 6 h shake and nonstop shake groups increased significantly, Supplementary Figure S1A. Moreover, compared to hMSCs in the static condition, the cell viability was decreased by 14.8% and 19.2%, respectively, Supplementary Figure S1B. The effect of high fluid shear stress on cell proliferation has similar effects, Supplementary Figure S1C. After 5 days of applying shear stress, the absorbance of hMSCs under 6 h shear and continuous shear were significantly decreased by 23.8% and 28.3%, respectively. These results revealed that shear stress modulate cell proliferation and viability is time- and speed-dependent. With high fluid shear stress, the cell viability and proliferation were decreased. With low fluid shear stress, the viability and proliferation was not affected when cells were exposed to periodic shear (6 h shear/day) instead of continuous shear (nonstop shear). In summary, for hMSCs under low fluid shear stress with 6 h per day for 5 days, there is no significant difference in cell viability and proliferation compared to the static condition. Thus, we chose this condition (3–7 dynes/cm^2) to avoid the effects of shear stress on cell viability and proliferation for the rest of our studies.

Low fluid shear stress modulates human bone marrow-derived mesenchymal stem cells morphology

To investigate the impacts of low fluid shear stress on hMSCs morphology, we quantified and compared cell phenotypic behaviors, including cell area, cell length, cell aspect ratio, and cell perimeter with and without shear stress for 3 and 5 days, respectively. Cells subjected to shear stress (6 h per day) were compared to cells that were simply plated into tissue culture plates without shear (Control group). The control group provides a benchmark to account for any effects of exposing the cells to shear stress. For dynamic culture, hMSCs were exposed to shear stress (~3–7 dyne/cm^2) for 3 days or 5 days with 6 h per day. After 3 days or 5 days of static or dynamic incubation, hMSCs were fixed, stained, and analyzed. Figures 3A,B showed the representative bright field and fluorescence images of hMSCs under static conditions (Figure 3A) and hMSCs that were exposed to shear stress (Figure 3B), respectively. We further quantified and compared the cell area, aspect ratio, cell perimeter, and cell length, Figures 3C,D and Supplementary Figures S2A–2B. After 3 days of culture, the cell area, aspect ratio, perimeter, and cell length of hMSCs cultured under shear stress showed a slight increase (a 16.3% increase in cell area, a 14.9% increase in cell aspect ratio, a 18% increase in perimeter, and a 12% increase in cell length) compared to hMSCs cultured in the static condition. However, hMSCs exposed to low fluid shear stress for 5 days showed a 55% increase in cell area, a 72% increase in cell length, a 16% increase in cell aspect ratio, and a 30% increase in cell perimeter, respectively, compared to hMSCs cultured under static conditions, Figures 3C,D and Supplementary Figures S2A–2B. These results indicate that hMSCs are sensitive to low fluid shear stress with significant morphology changes. This finding is consistent with previously reported studies (Asada et al., 2005; Dardik et al., 2005).

Low fluid shear stress promotes osteogenic differentiation

We further elucidated the effects of low fluid shear stress on osteogenic differentiation by applying shear with the estimated shear stress of 3–7 dyne/cm^2. Briefly, hMSCs were initially seeded in two well plates and cultured in the basal medium under static condition. Once the cells reached 70–80% confluency, osteogenic induction was performed and one well plate was placed on top of the orbital shaker, while the other plate was placed in the static condition without exposure to shear. After 5 days of osteogenic induction and shaking, osteogenic differentiation was evaluated and compared by measuring ALP enzyme activity, a reliable biochemical marker for early osteogenic differentiation (Reible et al., 2017). The ALP enzyme activities of hMSCs were imaged, quantified, and compared after 5 days of osteogenic induction for both groups. F-actin and nucleus were also stained for better identification of each cell. Figures 4A,B showed representative bright field and fluorescence images of hMSCs under static condition and shear stress, respectively. It is also noted that actin cytoskeleton is under remodeling when hMSCs are cultured in osteogenic induction medium. Undifferentiated hMSCs showed parallel actin filaments traversing the entire length of

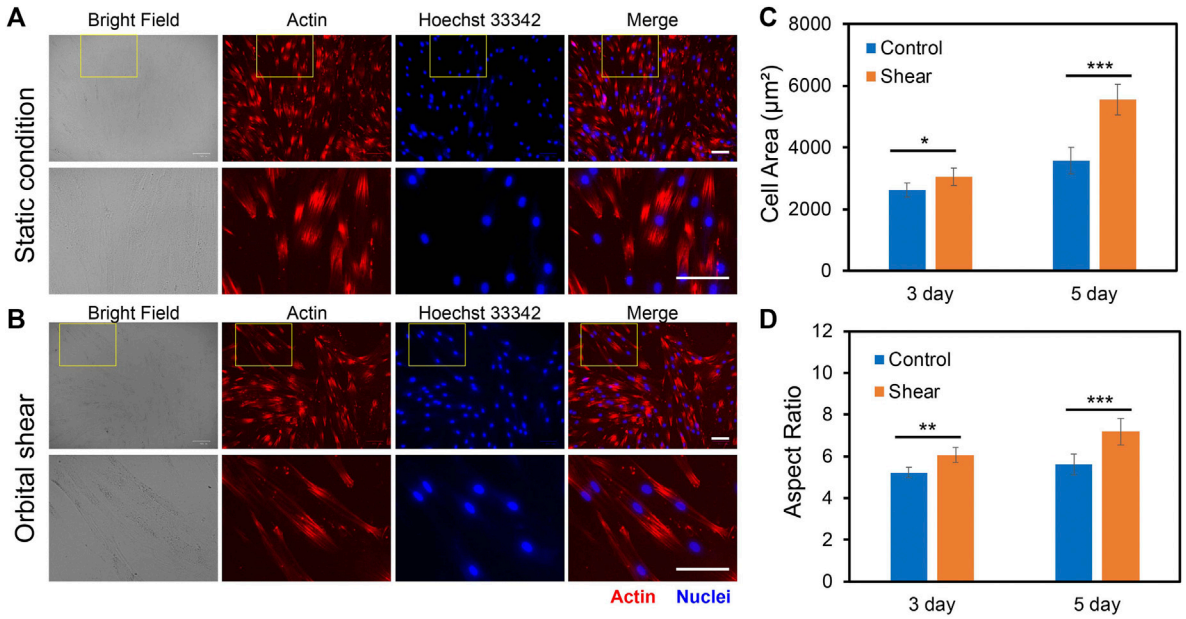

FIGURE 3
Effects of orbital shear stress on hMSCs morphology change. Representative bright field and fluorescence images of hMSCs under static condition **(A)** and exposed to shear stress **(B)**. The bottom panel showed the enlarged area of a yellow rectangle in the upper panel. hMSCs were exposed to orbital shear for 6 h per day for 5 days. Samples were stained with F-actin (red; by phalloidin), and nuclei (blue; by hoechst 33342), respectively. Scale bar: 100 μm. Quantification of observed cell area **(C)** and cell aspect ratio **(D)** of hMSCs after 3 and 5 days of exposure to orbital shear with 6 h per day. Data represent over 100 cells in each group and are expressed as mean± s.e.m. (n = 5, ***, $p < 0.001$, **, $p < 0.01$, *, $p < 0.05$).

the spindle shaped cells and remained unaltered, as seen in Supplementary Figures S3A–3B. However, under osteogenic induction, hMSCs underwent significant actin cytoskeleton remodeling accompanied by the formation of actin bundles framing the angular cell body with abundant stress fibers and increased actin polymerization. Under shear stress, actin cytoskeleton showed significant modification when hMSCs were induced for osteogenic differentiation, Supplementary Figures S3C–3D. The results showed that without osteogenic induction, there is a minimum green fluorescence signal, which indicates minimum ALP enzyme activity. With osteogenic induction, ALP enzyme activity was significantly increased in hMSCs under static condition and shear stress. We further quantified and compared ALP activity by measuring the mean green fluorescence intensity of ALP stained hMSCs. The fluorescence intensity was normalized for better comparison. Under the static condition, the ALP activity of hMSCs cultured in osteogenic induction medium increased by 1.8 folds compared to hMSCs cultured in basal medium. Under low fluid shear stress, the ALP activity was increased by 2.1 folds. Moreover, compared to the static condition, hMSCs exposed to shear stress showed a 15% increase ((ALP intensity of hMSCs with shear–ALP intensity of hMSCs without shear)/ALP intensity of hMSCs without shear) of ALP activity after osteogenic induction, Figure 4C. We further quantified the differentiation percentage of hMSCs with and without fluid shear stress, which was calculated by the number of ALP labeled cells per field/total number of cells per field. With low fluid shear stress, the hMSCs differentiation percentage increased to 45.51%, compared to 38.02% for hMSCs under the static condition. These results indicate that low fluid shear stress significantly enhanced osteogenic differentiation with increased ALP enzyme activity and osteogenic differentiation rate.

Notch signaling is involved in shear stress induced osteogenic differentiation

The previous study has shown that Notch signaling is involved during hMSCs osteogenic differentiation, disruption of Notch signaling mediated ALP activity, and osteogenic differentiation efficiency. Our group also recently showed that Dll4 mRNA is a molecular biomarker of osteogenic differentiated hMSCs (Zhao et al., 2022). Inhibition of Notch signaling reduces osteogenic differentiation with decreased ALP enzyme activity. However, it is obscure whether low fluid shear stress regulates osteogenic differentiation of hMSCs through Notch signaling. To better understand the involvement of Notch signaling during osteogenic differentiation, we utilized a pharmacological drug, DAPT,

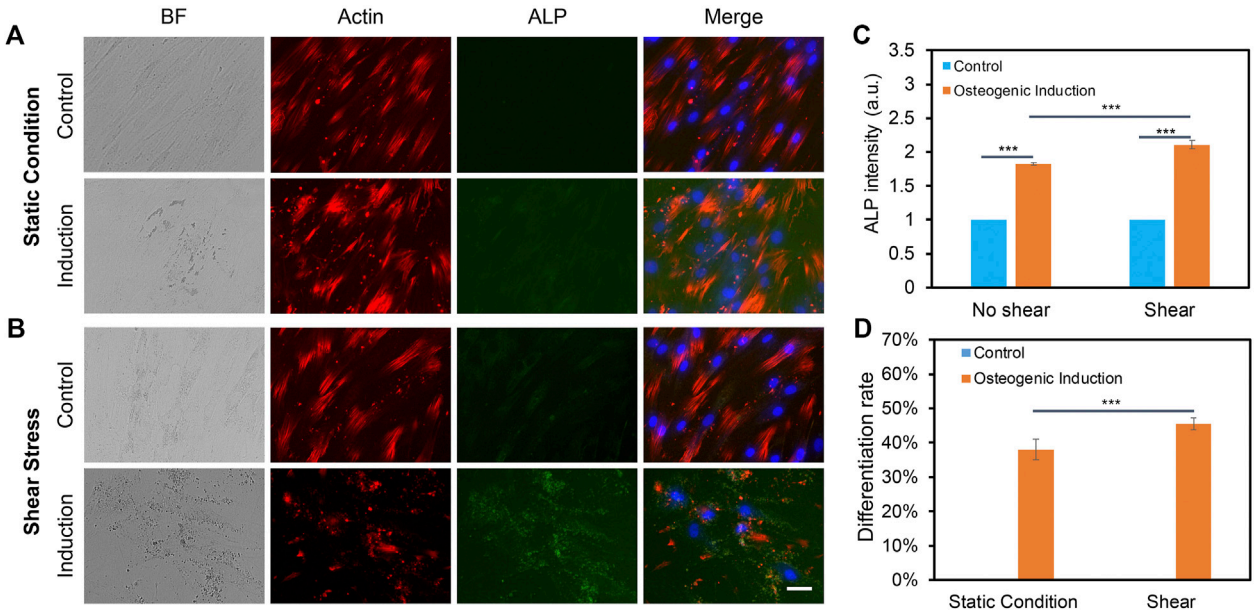

FIGURE 4
Orbital shear stress enhanced hMSCs osteogenic differentiation. Representative bright field and fluorescence images of hMSCs cultured with basal culture medium and osteogenic induction medium for 5 days under static condition **(A)**, and exposed to shear stress **(B)**, respectively. hMSCs that were exposed to orbital shear stress for 5 days with 6 h per day. Samples were stained with ALP (green; by ALP live stain), F-actin (red; by phalloidin), and nuclei (blue; by hoechst 33342), respectively. Scale bar: 100 μm. **(C)** Fluorescence intensity of ALP activity of hMSCs with and without shear stress after 5 days of osteogenic induction compared to control group. **(D)** Osteogenic differentiation percentage with and without shear stress. Data represent over 100 cells in each group and are expressed as mean± s.e.m. (n = 6, ***, $p < 0.001$, **, $p < 0.01$).

to perturb Notch signaling. DAPT is a γ-secretase inhibitor that blocks Notch endoproteolysis and thus serves as a Notch signaling inhibitor (Hellström et al., 2007). hMSCs were treated with DAPT at a concentration of 20 μM during osteogenic differentiation with or without shear stress to observe potential related effects. A control group was designed without osteogenic induction. The osteogenic differentiation under different treatments was evaluated and compared by measuring the mean red fluorescence intensity to examine osteogenic differentiation efficiency. Figures 5A,B and Supplementary Figures S4A–4B show representative images of hMSCs under static condition and shear stress that were cultures in basal medium, induction medium, and induction medium with the treatment of DAPT, respectively. These results indicate that inhibition of Notch signaling using γ-secretase inhibitor DAPT mediated osteogenic differentiation in both static condition and shear stress. Particularly, under static condition, with the treatment of DAPT, ALP enzyme activity after 5 days of osteogenic induction was decreased by 28.8% (Fluorescent intensity with induction - Fluorescent intensity with DAPT)/Fluorescent intensity with induction). Meanwhile, for the hMSCs exposed to low fluid shear stress, ALP enzyme activity after 5 days of induction was decreased by 18.2% with the treatment of DAPT. Interestingly, DAPT treatment for the hMSCs under shear stress has fewer effects on osteogenic differentiation, indicating low fluid shear stress rescued the inhibition effects of Notch signaling due to pharmaceutical treatment.

To further investigate the mechanisms of Notch signaling during osteogenic differentiation that were exposed to low fluid shear stress, we examined Notch 1 ligand, Dll4 mRNA expression under static condition and shear stress with basal culture medium, induction medium, and induction medium with DAPT treatment using an LNA/DNA nanobiosensor. Figures 5A,B, Supplementary Figures S5A–S5B, and Supplementary Figure S6 showed representative images of hMSCs under static condition and shear stress with different treatments. Dll4 mRNA expression were quantified and compared by measuring the mean green fluorescent intensity. Under the static condition, hMSCs cultured with osteogenic induction medium show a significant increase in the expression of Dll4 mRNA (~ 2.26 folds increase). Meanwhile, with the treatment of γ-secretase inhibitor DAPT, a significant decrease of Dll4 mRNA (~45.6%) was observed compared to the osteogenic induction group, Figure 5D. When exposed to low fluid shear stress, Dll4 mRNA expression of hMSCs under osteogenic induction group was increased 2.72 folds compared to hMSCs that were cultured in basal medium. The treatment of DAPT inhibited osteogenic differentiation by ~ 50%, Figure 5D. Compared to static condition, Dll4 mRNA expression was

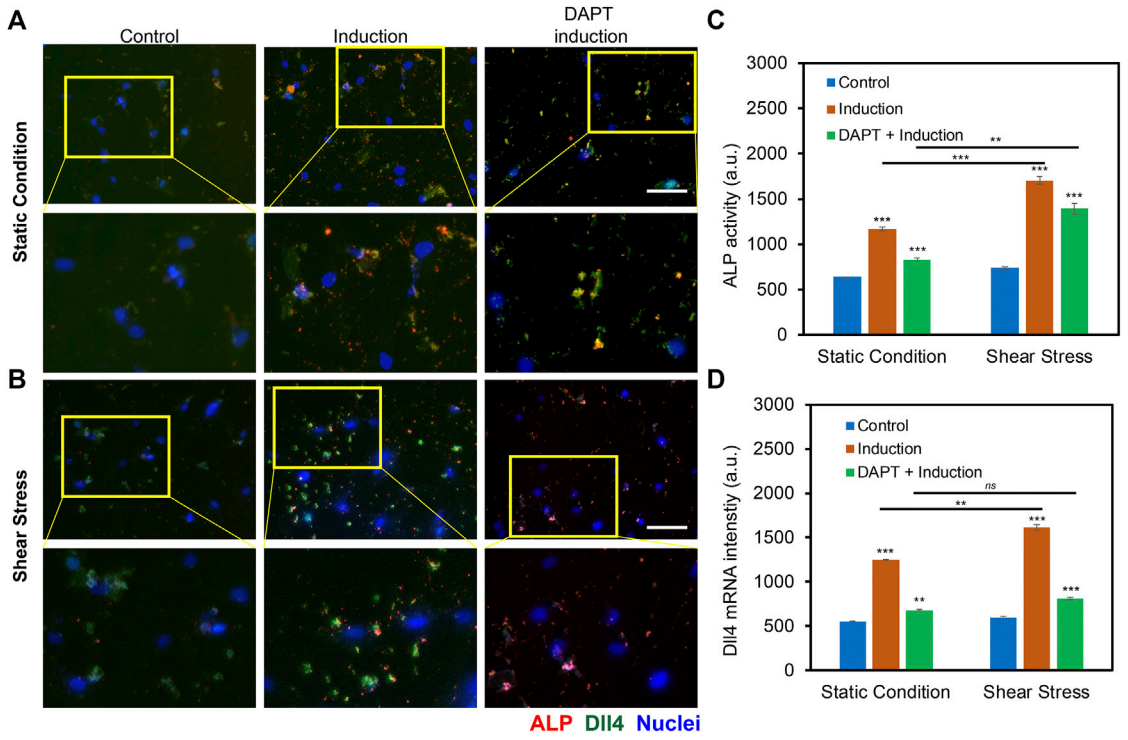

FIGURE 5
Notch signaling in regulating osteogenic differentiation of hMSCs with and without orbital shear stress. **(A)** Representative images of hMSCs in control, induction, and DAPT treatment groups without **(A)** and with **(B)** shear stress. Control: cells were cultured in the basal medium; induction: cells were cultured in osteogenic induction medium after cell seeding; DAPT: cells were treated with DAPT (20 μM) daily after osteogenic induction. Images were taken after 5 days of induction. The bottom images are enlarged areas of hMSCs in the labeled yellow rectangle. Green: Dll4 mRNA expression; red: ALP activity; blue: nucleus. Scale bar: 100 μm. **(C)** Comparison of ALP activity of hMSCs with and without shear stress under different conditions. **(D)** Mean fluorescent intensity of Dll4 mRNA expression of hMSCs after 5 days of osteogenic induction under different conditions as indicated. Error bars, s.e.m, with $n = 100–150$ cells. p-Values were calculated using a two-sample t-test with respect to control. *ns*, not significant, *, $p < 0.05$; **, $p < 0.01$; ***, $p < 0.005$.

increased by 22.8% when hMSCs were cultured in osteogenic induction medium. DAPT treatment mediated the effects of shear stress on osteogenic differentiation, with only ~16% increase of Dll4 mRNA expression. These results provide evidence that Notch signaling is involved and regulates osteogenic differentiation of hMSCs under low fluid shear stress. Low fluid shear stress upregulates Dll4 mRNA expression of hMSCs that were under osteogenic induction, indicating the involvement of Notch signaling in mechanoregulated osteogenic differentiation. Inhibition of Notch signaling mediated the effects of shear stress induced osteogenic differentiation, with reduced ALP enzyme activity and decreased Dll4 mRNA expression.

Discussions

In this study, we investigated the role of Notch signaling in regulating osteogenic differentiation of hMSCs induced by physiologically relevant shear stress using an LNA/DNA nanobiosensor. This LNA/DNA nanobiosensor can be designed in a short sequence (20–25 nts) to monitor gene expression activities, including mRNA, microRNA, and protein, in live cells at the single cell level. Unlike traditional techniques for mRNA detection, this technique is capable of detecting gene expression dynamics in live cells without lysis or fixation. This LNA/DNA nanobiosensor has been utilized to study spatiotemporal mRNA expression dynamics in collective cell migration (Riahi et al., 2015), mice lung cancer (Tao et al., 2014), wounded corneal tissue repair (Wang et al., 2015), and liver tissue (Riahi et al., 2014). Recently, our group utilized this nanobiosensor to monitor Dll4 mRNA expression dynamics in hMSCs during osteogenic differentiation (Zhao et al., 2022). This nanobiosensor has high thermal stability and specificity. Our previous studies showed the fluorescence intensity did not have a significant change as the incubation time increased up to 14 days (Zhao et al., 2022). The specificity of this nanobiosensor was also previously characterized and compared (Zhao et al., 2022). Overall, this nanobiosensor is sensitive, specific, and stable to track Dll4 mRNA expression dynamics during osteogenic differentiation. Furthermore, it is noted that this LNA/DNA

nanobiosensor is suitable for other different cell types and tissue environments. Previous studies have showed this nanobiosensor can detect microRNA expression dynamics during 3D collective cancer invasion (Dean et al., 2016). In addition, this nanobiosensor can be applied to track gene expression dynamics during osteogenic differentiation of hMSCs that were exposed to physiologically relevant microenvironment when cells are co-cultured with bone tissue scaffolds. The capability of monitoring gene expression dynamics in 3D physiological relevant microenvironments will open the opportunities to uncover unrecognized features and mechanisms of cell-cell interactions and cell-matrix interactions, which will eventually open opportunities to develop novel tools for tissue engineering and regenerative medicine.

Notch signaling is an evolutionary well-conserved pathway that regulates cell proliferation, cell fate determination, and stem cell differentiation in both embryonic and adult organs (Artavanis-Tsakonas et al., 1999; Mizutani et al., 2007; Nelson et al., 2007; Bjornson et al., 2012). There are four Notch receptors (Notch1-4) and five different Notch ligands (Dll1, Dll3, Dll4, Jag1, and Jag2). In recent years, the role of Notch signaling in osteogenic differentiation has attracted researchers' interest. Several studies showed that Notch signaling is active during osteogenic differentiation (Bagheri et al., 2018; Wagley et al., 2020). Notch signaling has also been reported to control tip cell formation during angiogenesis and leader cell formation during collective cell migration (Hellström et al., 2007; Riahi et al., 2015). Recently, Xu C *et. al.* reported that Notch ligand, Dll4, could induce bone formation in male mice without causing adverse effects in other organs (Xu et al., 2022). Notch signaling also plays an important role in controlling osteoblast and osteoclast differentiation and function, and regulates skeletal homeostasis (Yu and Canalis, 2020). Cao *et al.* reported that Notch receptor Notch1 and Notch ligand Dll1 are involved in osteogenic differentiation (Cao et al., 2017). They observed that Notch1 inhibition reduced ALP activity during BMP-induced osteogenic differentiation of hMSCs *in vitro*. In contrast, it has been reported that inhibition of Notch signaling promotes adipogenic differentiation of MSCs (Song et al., 2015), indicating that Notch involvement is lineage-dependent during MSCs differentiation. Although numerous studies have demonstrated the involvement of Notch signaling during osteogenic differentiation, it is unclear whether Notch signaling regulates osteogenic differentiation of hMSCs when exposed to physiologically relevant fluid shear stress. Here, we demonstrated that Notch signaling regulates osteogenic differentiation of hMSCs that were exposed to low fluid shear stress. We first examined the effects of shear stress on cell viability and proliferation. Our results showed shear stress regulates hMSCc viability and proliferation is time- and speed-dependent. There were minimum effects when hMSCs were exposed to low fluid shear stress (3–7 dye/cm^2) for 6 h per day with a duration of 5 days. We next studied the effects of shear stress on hMSCs morphology and osteogenic differentiation. The results indicate that low fluid shear stress modulates hMSCs morphology and enhances osteogenic differentiation with increased ALP enzyme activity. To elucidate the mechanisms of Notch signaling during osteogenic differentiation, we investigated Dll4 mRNA expression after 5 days of induction. Without shear stress, disruption of Notch signaling using γ-secretase inhibitor DAPT reduced ALP activity and decreased Dll4 mRNA expression. When exposed to shear stress, the effects of Notch inhibition on osteogenic differentiation were partially recovered with enhanced ALP activity and increased Dll4 mRNA expression. Overall, our results suggested that Notch signaling is involved in osteogenic differentiation and Dll4 mRNA expression was increased when hMSCs were exposed to shear stress, indicating the mechanosensitive role of Notch signaling. It is also noted that Notch signaling has been reported mechanosensitive and can be activated through laser tweezer and intercellular tension (Wang et al., 2017). Recently, *Jiao et. al.* reported that fluid shear stress facilitated osteogenic differentiation of MSCs with enhanced ALP, osteocalcin, and collagen I expression. In addition, nuclear transfer of YAP protein was enhanced after being exposed to fluid shear stress (Jiao et al., 2022). *Hu et. al.* reported that mechanosensitive ion channel TRPV4 is involved in shear stress induced early osteogenic differentiation of MSCs, inhibition of TRPV4 mitigated shear stress induced early osteogenic differentiation (Hu et al., 2017). *Liu et. al.* reported that fluid shear stress regulates osteogenic differentiation of MSCs through Transient receptor potential melastatin 7 (TRPM7)-Osterix axis, which is mechanosensitive to shear force of 1.2 Pa (Liu et al., 2015). Furthermore, several studies have shown that MAP kinase and intracellular signaling cascades could be activated by shear stress and induce osteogenic differentiation (Liu et al., 2010; Yourek et al., 2010). Thus, further mechanistic studies, using 2D and 3D models, are required to elucidate the molecular and cellular processes that regulate osteogenic differentiation. Specifically, the fundamental regulatory mechanisms of mechanosensitive role of Notch signaling and its upstream and downstream signaling pathways should be further investigated using loss- and gain-of function experiments. Moreover, upstream mechanical sensor and biochemical stimuli, may orchestrate other signals and transduce into intracellular activation of various pathways that regulate osteogenic differentiation. Thus, the mechanosensitive role of Notch signaling and its crosstalk with biophysical factors during osteogenesis at the molecular, cell, and tissue level should be further elucidated using 2D and 3D models. Understanding the fundamental mechanisms of the osteogenic differentiation of hMSCs induced by fluid shear stress will provide valuable information that can be used for bone tissue engineering. In addition, the elucidation of mechanotransduction of fluid shear stress during osteogenic differentiation of MSCs will open opportunities to uncover unrecognized mechanosensitive genes.

Conclusion

In this study, an LNA/DNA nanobiosensor was exploited to detect the Dll4 mRNA gene expression profile during

osteogenic differentiation of hMSCs that were exposed to physiologically relevant low fluid shear stress. We first investigated the effects of shear stress on hMSCs phenotypic behaviors including cell morphology, cell proliferation, and viability. Our results showed that high fluid shear will result in decreased cell viability and proliferation, while low fluid shear stress has minimal impacts on cell viability and proliferation. Next, we utilized an LNA/DNA nanobiosensor to monitor Dll4 mRNA expression of hMSCs during osteogenic differentiation, which enables us to identify the regulatory role of Notch signaling. Our results showed that Notch signaling regulates hMSCs osteogenic differentiation. Inhibition of Notch signaling mediates osteogenic differentiation with reduced ALP enzyme activity and Dll4 expression. We further revealed that Notch signaling is involved in shear stress induced osteogenic differentiation. During osteogenic differentiation, Dll4 mRNA expression was increased when hMSCs were exposed to low fluid shear stress, indicating the involvement of Notch signaling in mechanoregulated osteogenic differentiation. Inhibition of Notch signaling mediated the effects of shear stress induced osteogenic differentiation, with reduced ALP enzyme activity and decreased Dll4 mRNA expression. In conclusion, our results provide convincing evidence that Notch signaling regulates shear stress induced osteogenic differentiation, indicating the mechanosensitive role of Notch signaling in osteogenic differentiation. Further studies may elucidate the mechanisms underlying the mechanosensitive role of Notch signaling in regulating stem cell differentiation.

Data availability statement

The original contributions presented in the study are included in the article/Supplementary Material, further inquiries can be directed to the corresponding author.

Author contributions

YZ and SW conceived the initial idea of the study. YZ, RY, ZB, KR, YL, and SF performed the experiments. YZ and SW contributed to the experimental design and data analysis. YZ and SW wrote the manuscript with feedback from all authors.

Funding

This work is supported by NSF CAREER (CMMI: 2143151) and NASA CT Space Grant Consortium Faculty Research Grant (Award Number: P-1558). YZ is supported by the Provost Graduate Fellowship. KR is supported by NASA CT Student Research Grant.

Conflict of interest

The authors declare that the research was conducted in the absence of any commercial or financial relationships that could be construed as a potential conflict of interest.

Publisher's note

Supplementary material

The Supplementary Material for this article can be found online at: https://www.frontiersin.org/articles/10.3389/fbioe.2022.1007430/full#supplementary-material

References

Artavanis-Tsakonas, S., Rand, M. D., and Lake, R. J. (1999). Notch signaling: cell fate control and signal integration in development. *Science* 284 (5415), 770–776. doi:10.1126/science.284.5415.770

Asada, H., Paszkowiak, J., Teso, D., Alvi, K., Thorisson, A., Frattini, J. C., et al. (2005). Sustained orbital shear stress stimulates smooth muscle cell proliferation via the extracellular signal-regulated protein kinase 1/2 pathway. *J. Vasc. Surg.* 42 (4), 772–780. doi:10.1016/j.jvs.2005.05.046

Assunção, M., Dehghan-Baniani, D., Yiu, C. H. K., Später, T., Beyer, S., and Blocki, A. (2020). Cell-derived extracellular matrix for tissue engineering and regenerative medicine. *Front. Bioeng. Biotechnol.* 8, 602009. doi:10.3389/fbioe.2020.602009

Bagheri, L., Pellati, A., Rizzo, P., Aquila, G., Massari, L., De Mattei, M., et al. (2018). Notch pathway is active during osteogenic differentiation of human bone marrow mesenchymal stem cells induced by pulsed electromagnetic fields. *J. Tissue Eng. Regen. Med.* 12 (2), 304–315. doi:10.1002/term.2455

Bjornson, C. R., Cheung, T. H., Liu, L., Tripathi, P. V., Steeper, K. M., and Rando, T. A. (2012). Notch signaling is necessary to maintain quiescence in adult muscle stem cells. *Stem cells* 30 (2), 232–242. doi:10.1002/stem.773

Cao, J., Wei, Y., Lian, J., Yang, L., Zhang, X., Xie, J., et al. (2017). Notch signaling pathway promotes osteogenic differentiation of mesenchymal stem cells by enhancing BMP9/Smad signaling. *Int. J. Mol. Med.* 40 (2), 378–388. doi:10.3892/ijmm.2017.3037

Cappellesso, R., Nicole, L., Guido, A., and Pizzol, D. (2015). Spaceflight osteoporosis: current state and future perspective. *Endocr. Regul.* 49 (4), 231–239. doi:10.4149/endo_2015_04_231

Dardik, A., Chen, L., Frattini, J., Asada, H., Aziz, F., Kudo, F. A., et al. (2005). Differential effects of orbital and laminar shear stress on endothelial cells. *J. Vasc. Surg.* 41 (5), 869–880. doi:10.1016/j.jvs.2005.01.020

Dean, Z. S., Elias, P., Jamilpour, N., Utzinger, U., and Wong, P. K. (2016). Probing 3D collective cancer invasion using double-stranded locked nucleic acid biosensors. *Anal. Chem.* 88 (17), 8902–8907. doi:10.1021/acs.analchem.6b02608

Gambacurta, A., Merlini, G., Ruggiero, C., Diedenhofen, G., Battista, N., Bari, M., et al. (2019). Human osteogenic differentiation in space: Proteomic and epigenetic clues to better understand osteoporosis. *Sci. Rep.* 9 (1), 8343–8410. doi:10.1038/s41598-019-44593-6

Gonzalez, B. A., Perez-Nevarez, M., Mirza, A., Perez, M. G., Lin, Y.-M., Hsu, C.-P. D., et al. (2020). Physiologically relevant fluid-induced oscillatory shear stress stimulation of mesenchymal stem cells enhances the engineered valve matrix phenotype. *Front. Cardiovasc. Med.* 7, 69. doi:10.3389/fcvm.2020.00069

Guilak, F., Cohen, D. M., Estes, B. T., Gimble, J. M., Liedtke, W., and Chen, C. S. (2009). Control of stem cell fate by physical interactions with the extracellular matrix. *Cell stem Cell* 5 (1), 17–26. doi:10.1016/j.stem.2009.06.016

Han, Y., Li, X., Zhang, Y., Han, Y., Chang, F., and Ding, J. (2019). Mesenchymal stem cells for regenerative medicine. *Cells* 8 (8), 886. doi:10.3390/cells8080886

Hellström, M., Phng, L.-K., Hofmann, J. J., Wallgard, E., Coultas, L., Lindblom, P., et al. (2007). Dll4 signalling through Notch1 regulates formation of tip cells during angiogenesis. *Nature* 445 (7129), 776–780. doi:10.1038/nature05571

Heo, S.-J., Driscoll, T. P., Thorpe, S. D., Nerurkar, N. L., Baker, B. M., Yang, M. T., et al. (2016). Differentiation alters stem cell nuclear architecture, mechanics, and mechano-sensitivity. *Elife* 5, e18207. doi:10.7554/elife.18207

Hu, K., Sun, H., Gui, B., and Sui, C. (2017). TRPV4 functions in flow shear stress induced early osteogenic differentiation of human bone marrow mesenchymal stem cells. *Biomed. Pharmacother.* 91, 841–848. doi:10.1016/j.biopha.2017.04.094

Iovene, A., Zhao, Y., Wang, S., and Amoako, K. (2021). Bioactive polymeric materials for the advancement of regenerative medicine. *J. Funct. Biomater.* 12 (1), 14. doi:10.3390/jfb12010014

Jiang, Y., Zhang, P., Zhang, X., Lv, L., and Zhou, Y. (2021). Advances in mesenchymal stem cell transplantation for the treatment of osteoporosis. *Cell Prolif.* 54 (1), e12956. doi:10.1111/cpr.12956

Jiao, F., Xu, J., Zhao, Y., Ye, C., Sun, Q., Liu, C., et al. (2022). Synergistic effects of fluid shear stress and adhesion morphology on the apoptosis and osteogenesis of mesenchymal stem cells. *J. Biomed. Mater. Res. A* 110, 1636–1644. doi:10.1002/jbm.a.37413

Karystinou, A., Roelofs, A. J., Neve, A., Cantatore, F. P., Wackerhage, H., and De Bari, C. (2015). Yes-associated protein (YAP) is a negative regulator of chondrogenesis in mesenchymal stem cells. *Arthritis Res. Ther.* 17 (1), 147. doi:10.1186/s13075-015-0639-9

Kashani, S. Y., Moraveji, M. K., Taghipoor, M., Kowsari-Esfahan, R., Hosseini, A. A., Montazeri, L., et al. (2021). An integrated microfluidic device for stem cell differentiation based on cell-imprinted substrate designed for cartilage regeneration in a rabbit model. *Mater. Sci. Eng. C* 121, 111794. doi:10.1016/j.msec.2020.111794

Kim, K. M., Choi, Y. J., Hwang, J.-H., Kim, A. R., Cho, H. J., Hwang, E. S., et al. (2014). Shear stress induced by an interstitial level of slow flow increases the osteogenic differentiation of mesenchymal stem cells through TAZ activation. *PloS one* 9 (3), e92427. doi:10.1371/journal.pone.0092427

Lim, K. T., Hexiu, J., Kim, J., Seonwoo, H., Choung, P.-H., and Chung, J. H. (2014). Synergistic effects of orbital shear stress on *in vitro* growth and osteogenic differentiation of human alveolar bone-derived mesenchymal stem cells. *BioMed Res. Int.* 2014, 1–18. doi:10.1155/2014/316803

Liu, L., Yuan, W., and Wang, J. (2010). Mechanisms for osteogenic differentiation of human mesenchymal stem cells induced by fluid shear stress. *Biomech. Model. Mechanobiol.* 9 (6), 659–670. doi:10.1007/s10237-010-0206-x

Liu, Y.-S., Liu, Y.-A., Huang, C.-J., Yen, M.-H., Tseng, C.-T., Chien, S., et al. (2015). Mechanosensitive TRPM7 mediates shear stress and modulates osteogenic differentiation of mesenchymal stromal cells through Osterix pathway. *Sci. Rep.* 5 (1), 16522–16613. doi:10.1038/srep16522

Lorthongpanich, C., Thumanu, K., Tangkiettrakul, K., Jiamvoraphong, N., Laowtammathron, C., Damkham, N., et al. (2019). YAP as a key regulator of adipo-osteogenic differentiation in human MSCs. *Stem Cell Res. Ther.* 10 (1), 402–412. doi:10.1186/s13287-019-1494-4

Mizutani, K.-i., Yoon, K., Dang, L., Tokunaga, A., and Gaiano, N. (2007). Differential Notch signalling distinguishes neural stem cells from intermediate progenitors. *Nature* 449 (7160), 351–355. doi:10.1038/nature06090

Moreira, B. G., You, Y., Behlke, M. A., and Owczarzy, R. (2005). Effects of fluorescent dyes, quenchers, and dangling ends on DNA duplex stability. *Biochem. Biophys. Res. Commun.* 327 (2), 473–484. doi:10.1016/j.bbrc.2004.12.035

Navran, S. (2008). The application of low shear modeled microgravity to 3-D cell biology and tissue engineering. *Biotechnol. Annu. Rev.* 14, 275–296. doi:10.1016/s1387-2656(08)00011-2

Nelson, B. R., Hartman, B. H., Georgi, S. A., Lan, M. S., and Reh, T. A. (2007). Transient inactivation of Notch signaling synchronizes differentiation of neural progenitor cells. *Dev. Biol.* 304 (2), 479–498. doi:10.1016/j.ydbio.2007.01.001

Pape, H. C., Evans, A., and Kobbe, P. (2010). Autologous bone graft: Properties and techniques. *J. Orthop. Trauma* 24, S36–S40. doi:10.1097/bot.0b013e3181cec4a1

Poon, C. (2022). Measuring the density and viscosity of culture media for optimized computational fluid dynamics analysis of *in vitro* devices. *J. Mech. Behav. Biomed. Mater.* 126, 105024. doi:10.1016/j.jmbbm.2021.105024

Qin, X., Li, J., Sun, J., Liu, L., Chen, D., and Liu, Y. (2019). Low shear stress induces ERK nuclear localization and YAP activation to control the proliferation of breast cancer cells. *Biochem. Biophys. Res. Commun.* 510 (2), 219–223. doi:10.1016/j.bbrc.2019.01.065

Raisz, L. G. (2005). Pathogenesis of osteoporosis: concepts, conflicts, and prospects. *J. Clin. Invest.* 115 (12), 3318–3325. doi:10.1172/jci27071

Rath, S., Salinas, M., Villegas, A. G., and Ramaswamy, S. (2015). Differentiation and distribution of marrow stem cells in flex-flow environments demonstrate support of the valvular phenotype. *PloS one* 10 (11), e0141802. doi:10.1371/journal.pone.0141802

Reible, B., Schmidmaier, G., Prokscha, M., Moghaddam, A., and Westhauser, F. (2017). Continuous stimulation with differentiation factors is necessary to enhance osteogenic differentiation of human mesenchymal stem cells *in-vitro*. *Growth factors.* 35 (4-5), 179–188. doi:10.1080/08977194.2017.1401618

Riahi, R., Wang, S., Long, M., Li, N., Chiou, P.-Y., Zhang, D. D., et al. (2014). Mapping photothermally induced gene expression in living cells and tissues by nanorod-locked nucleic acid complexes. *Acs Nano* 8 (4), 3597–3605. doi:10.1021/nn500107g

Riahi, R., Sun, J., Wang, S., Long, M., Zhang, D. D., and Wong, P. K. (2015). Notch1–Dll4 signalling and mechanical force regulate leader cell formation during collective cell migration. *Nat. Commun.* 6 (1), 6556–6611. doi:10.1038/ncomms7556

Sacks, M. S., and Yoganathan, A. P. (2008). Heart valve function: a biomechanical perspective. *Phil. Trans. R. Soc. B* 363 (1502), 2481. doi:10.1098/rstb.2008.0062

Saghati, S., Nasrabadi, H. T., Khoshfetrat, A. B., Moharamzadeh, K., Hassani, A., Mohammadi, S. M., et al. (2021). Tissue engineering strategies to increase osteochondral regeneration of stem cells; a close look at different modalities. *Stem Cell Rev. Rep.* 17, 1294–1311. doi:10.1007/s12015-021-10130-0

Song, B.-q., Chi, Y., Li, X., Du, W.-j., Han, Z.-B., Tian, J.-j., et al. (2015). Inhibition of Notch signaling promotes the adipogenic differentiation of mesenchymal stem cells through autophagy activation and PTEN-PI3K/AKT/mTOR pathway. *Cell. Physiol. biochem.* 36 (5), 1991–2002. doi:10.1159/000430167

Tao, S., Wang, S., Moghaddam, S. J., Ooi, A., Chapman, E., Wong, P. K., et al. (2014). Oncogenic KRAS confers chemoresistance by upregulating NRF2. *Cancer Res.* 74 (24), 7430–7441. doi:10.1158/0008-5472.can-14-1439

Wagley, Y., Chesi, A., Acevedo, P. K., Lu, S., Wells, A. D., Johnson, M. E., et al. (2020). Canonical Notch signaling is required for bone morphogenetic protein-mediated human osteoblast differentiation. *Stem Cells* 38 (10), 1332–1347. doi:10.1002/stem.3245

Wang, F., Flanagan, J., Su, N., Wang, L.-C., Bui, S., Nielson, A., et al. (2012). RNAscope: a novel *in situ* RNA analysis platform for formalin-fixed, paraffin-embedded tissues. *J. Mol. Diagn.* 14 (1), 22–29. doi:10.1016/j.jmoldx.2011.08.002

Wang, Y.-K., Yu, X., Cohen, D. M., Wozniak, M. A., Yang, M. T., Gao, L., et al. (2012). Bone morphogenetic protein-2-induced signaling and osteogenesis is regulated by cell shape, RhoA/ROCK, and cytoskeletal tension. *Stem cells Dev.* 21 (7), 1176–1186. doi:10.1089/scd.2011.0293

Wang, S., Riahi, R., Li, N., Zhang, D. D., and Wong, P. K. (2015). Single cell nanobiosensors for dynamic gene expression profiling in native tissue microenvironments. *Adv. Mater.* 27 (39), 6034–6038. doi:10.1002/adma.201502814

Wang, S., Sun, J., Xiao, Y., Lu, Y., Zhang, D. D., and Wong, P. K. (2017). Intercellular tension negatively regulates angiogenic sprouting of endothelial tip cells via notch1-dll4 signaling. *Adv. Biosyst.* 1 (1-2), 1600019. doi:10.1002/adbi.201600019

Wang, S., Majumder, S., Emery, N. J., and Liu, A. P. (2018a). Simultaneous monitoring of transcription and translation in mammalian cell-free expression in bulk and in cell-sized droplets. *Synth. Biol.* 3 (1), ysy005. doi:10.1093/synbio/ysy005

Wang, S., Xiao, Y., Zhang, D. D., and Wong, P. K. (2018b). A gapmer aptamer nanobiosensor for real-time monitoring of transcription and translation in single cells. *Biomaterials* 156, 56–64. doi:10.1016/j.biomaterials.2017.11.026

Wang, S., Emery, N. J., and Liu, A. P. (2019). A novel synthetic toehold switch for MicroRNA detection in mammalian cells. *ACS Synth. Biol.* 8 (5), 1079–1088. doi:10.1021/acssynbio.8b00530

Weber, M., Kim, S., Patterson, N., and Searles, C. D. (2012). Shear-responsive miR-155 regulates endothelial cell phenotype and function. *FASEB J.* 26, 1151–1157. doi:10.1096/fasebj.26.1_supplement.1151.7

Weycker, D., Li, X., Barron, R., Bornheimer, R., and Chandler, D. (2016). Hospitalizations for osteoporosis-related fractures: Economic costs and clinical outcomes. *Bone Rep.* 5, 186–191. doi:10.1016/j.bonr.2016.07.005

Williams, A., Nasim, S., Salinas, M., Moshkforoush, A., Tsoukias, N., and Ramaswamy, S. (2017). A "sweet-spot" for fluid-induced oscillations in the conditioning of stem cell-based engineered heart valve tissues. *J. Biomech.* 65, 40–48. doi:10.1016/j.jbiomech.2017.09.035

Xu, C., Kruse, K., Jeong, H.-W., Watson, E. C., Adams, S., Berkenfeld, F., et al. (2022). Induction of osteogenesis by bone-targeted Notch activation. *Elife* 11, e60183. doi:10.7554/elife.60183

Xue, X., Hong, X., Fu, J., and Deng, C. (2016). Regulation of cytoskeleton contractility and osteogenesis of human mesenchymal stem cells using acoustic tweezing cytometry (ATC). *Biophysical J.* 110 (3), 134a. doi:10.1016/j.bpj.2015.11.768

Xue, X., Hong, X., Li, Z., Deng, C. X., and Fu, J. (2017). Acoustic tweezing cytometry enhances osteogenesis of human mesenchymal stem cells through cytoskeletal contractility and YAP activation. *Biomaterials* 134, 22–30. doi:10.1016/j.biomaterials.2017.04.039

Yang, L., Ge, L., and van Rijn, P. (2020). Synergistic effect of cell-derived extracellular matrices and topography on osteogenesis of mesenchymal stem cells. *ACS Appl. Mater. Interfaces* 12 (23), 25591–25603. doi:10.1021/acsami.0c05012

Yourek, G., McCormick, S. M., Mao, J. J., and Reilly, G. C. (2010). Shear stress induces osteogenic differentiation of human mesenchymal stem cells. *Regen. Med.* 5 (5), 713–724. doi:10.2217/rme.10.60

Yu, J., and Canalis, E. (2020). Notch and the regulation of osteoclast differentiation and function. *Bone* 138, 115474. doi:10.1016/j.bone.2020.115474

Yu, J., Xiao, J., Ren, X., Lao, K., and Xie, X. S. (2006). Probing gene expression in live cells, one protein molecule at a time. *Science* 311 (5767), 1600–1603. doi:10.1126/science.1119623

Zhao, Y., Yang, R., Bousraou, Z., Richardson, K., and Wang, S. (2022). Probing notch1-dll4 signaling in regulating osteogenic differentiation of human mesenchymal stem cells using single cell nanobiosensor. *Sci. Rep.* 12, 10315. doi:10.1038/s41598-022-14437-x

Zheng, Y., Wang, S., Xue, X., Xu, A., Liao, W., Deng, A., et al. (2017). Notch signaling in regulating angiogenesis in a 3D biomimetic environment. *Lab. Chip* 17 (11), 1948–1959. doi:10.1039/c7lc00186j

frontiers | Frontiers in Bioengineering and Biotechnology

TYPE Original Research
PUBLISHED 03 November 2022
DOI 10.3389/fbioe.2022.1011753

OPEN ACCESS

EDITED BY
Jingwei Xie,
University of Nebraska Medical Center, United States

REVIEWED BY
Hemin Nie,
Hunan University, China
Johnson V. John,
Terasaki Institute for Biomedical Innovation, United States

*CORRESPONDENCE
Bin Huang,
binhuang20210101@163.com
Shilin Chen,
chenshlin@163.com

†These authors have contributed equally to this work

SPECIALTY SECTION
This article was submitted to Biomaterials, a section of the journal Frontiers in Bioengineering and Biotechnology

RECEIVED 04 August 2022
ACCEPTED 17 October 2022
PUBLISHED 03 November 2022

CITATION
Shen X, Chen T, Liu N, Yang B, Feng G, Yu P, Zhan C, Yin N, Wang Y, Huang B and Chen S (2022), MRI-guided microwave ablation and albumin-bound paclitaxel for lung tumors: Initial experience.
Front. Bioeng. Biotechnol. 10:1011753.
doi: 10.3389/fbioe.2022.1011753

MRI-guided microwave ablation and albumin-bound paclitaxel for lung tumors: Initial experience

Xiaokang Shen[1,2†], TianMing Chen[3†], Nianlong Liu[5], Bo Yang[5], GuoDong Feng[6], Pengcheng Yu[4], Chuanfei Zhan[4], Na Yin[5], YuHuang Wang[5], Bin Huang[7,8]* and Shilin Chen[1,4]*

[1]Department of Thoracic Surgery, Jiangsu Cancer Hospital, Nanjing, China, [2]Department of Cardiothoracic Surgery, Nanjing First Hospital, Nanjing Medical University, Nanjing, China, [3]Department of General Surgery, Nanjing Drum Tower Hospital, The Affiliated Hospital of Nanjing University Medical School, Nanjing, China, [4]Department of Thoracic Surgery, The Affiliated Cancer Hospital of Nanjing Medical University, Jiangsu Cancer Hospital, Jiangsu Institute of Cancer Research, Nanjing, Jiangsu, China, [5]Department of Medical Imaging, Jiangsu Cancer Hospital, Jiangsu Institute of Cancer Research, The Affiliated Cancer Hospital of Nanjing Medical University, Nanjing, Jiangsu, China, [6]Department of Interventional Therapy, Jiangsu Institute of Cancer Research, The Affiliated Cancer Hospital of Nanjing Medical University, Nanjing, China, [7]The Comprehensive Cancer Center of Nanjing Drum Tower Hospital, The Affiliated Hospital of Nanjing University Medical School, Clinical Cancer Institute of Nanjing University, Nanjing, China, [8]The Comprehensive Cancer Centre of Nanjing Drum Tower Hospital, Clinical College of Nanjing Medical University and Clinical College of Traditional Chinese and Western Medicine, Nanjing University of Chinese Medicine, Nanjing Drum Tower Hospital, Medical School of Southeast University, Nanjing, China

Magnetic resonance-guided microwave ablation (MRI-guided MWA) is a new, minimally invasive ablation method for cancer. This study sought to analyze the clinical value of MRI-guided MWA in non-small cell lung cancer (NSCLC). We compared the precision, efficiency, and clinical efficacy of treatment in patients who underwent MRI-guided MWA or computed tomography (CT)-guided microwave ablation (CT-guided MWA). Propensity score matching was used on the prospective cohort (MRI-MWA group, n = 45) and the retrospective observational cohort (CT-MWA group, n = 305). To evaluate the advantages and efficacy of MRI-guided MWA, data including the accuracy of needle placement, scan duration, ablation time, total operation time, length of hospital stay, progression-free survival (PFS), and overall survival (OS) were collected and compared between the two groups. The mean number of machine scans required to adjust the needle position was 7.62 ± 1.69 (range 4–12) for the MRI-MWA group and 9.64 ± 2.14 (range 5–16) for the CT-MWA group (p < 0.001). The mean time for antenna placement was comparable between the MRI and CT groups (54.41 ± 12.32 min and 53.03 ± 11.29 min, p = 0.607). The microwave ablation time of the two groups was significantly different (7.62 ± 2.65 min and 9.41 ± 2.86 min, p = 0.017), while the overall procedure time was comparable (91.28 ± 16.69 min vs. 93.41 ± 16.03 min, p = 0.568). The overall complication rate in the MRI-MWA group was significantly lower than in the CT-MWA group (12% vs. 51%, p = 0.185). The median time to progression was longer in the MRI-MWA group than in the CT-MWA group (11 months [95% CI 10.24–11.75] vs. 9 months [95% CI 8.00–9.99], p = 0.0003; hazard ratio 0.3690 [95% CI 0.2159–0.6306]). OS was comparable in both groups (MRI group 26.0 months [95% CI 25.022–26.978] vs. CT group 23.0 months [95% CI 18.646–27.354], p = 0.18). This study provides hitherto-undocumented

evidence of the clinical effects of MRI-guided MWA on patients with NSCLC and determines the relative safety and efficiency of MRI- and CT-guided MWA.

KEYWORDS

albumin-bound paclitaxel, magnetic resonance imaging, microwave ablation, non-small cell lung cancer, safety and efficiency

Introduction

Percutaneous thermal ablation under imaging guidance is a minimally invasive technique used for the palliative treatment of nonoperative patients with non-small cell lung cancer (NSCLC) and pulmonary metastasis (Dupuy, 2011). As a heat-based ablation technique, microwave ablation destroys tissues using an electromagnetic field (typically 50–60 W), and the feasibility and efficacy of this approach have been extensively validated (Goldberg et al., 2000; Vietti Violi et al., 2018). Computed tomography (CT) and ultrasound are the most widely used traditional imaging modalities for ablation guidance. It is widely acknowledged that CT-guided treatment of lung cancer via microwave ablation entails significant limitations, such as inaccurate ablation-needle puncturing and inaccurate assessment of the ablation boundary, which affect its therapeutic efficacy to a certain extent (Lu et al., 2012; An et al., 2022). Magnetic resonance imaging (MRI) has limited value for diagnosing and treating lung diseases due to motion artifacts and low signals (Boiselle et al., 2013; Ciet et al., 2015). Over the years, MRI has gained significant momentum with the emergence of new imaging techniques such as multi-channel MRI, systems with strong gradients, and innovative pulse-train techniques for parallel imaging (Puderbach et al., 2007). MRI brings many advantages, including arbitrary direction imaging and high tissue resolution, and can identify changes in the ablation zone during the entire process of ablation, which is useful for monitoring changes in the ablation region (Li et al., 2017; Shono et al., 2020; Shen et al., 2021). However, few studies have assessed the clinical utility and economic value of MRI-guided MWA. To our knowledge, this is the first study to evaluate the accuracy and applicability of MRI-guided MWA therapy.

Materials and methods

Patients and tumor criteria

This prospective study was approved by the Ethics Committee of Jiangsu Provincial Hospital, affiliated with Nanjing Medical University. All patients included in the study provided written informed consent.

Subjects in this study included a prospective cohort (MRI-MWA group, $n = 45$) with lung tumors treated with MRI-guided MWA combined with chemotherapy from February 2018 to August 2021 and a retrospective, observational cohort ($n = 305$) of consecutive patients who underwent CT-guided MWA combined with chemotherapy (CT-MWA group) at our hospital between January 2018 and June 2021. One-to-one propensity score matching (PSM) analysis was performed to remove confounding, selection, and information biases based on the following variables: gender (male/female), age (± 5 years), tumor size (± 4 mm), tumor location (peripheral third of lung, middle third of lung, or inner third of lung), histology, and TNM stage, yielding 39 patients in the MRI-MWA group and 39 patients in the CT-MWA group (Figure1).

For inclusion in the study, patients were required to be adults aged ≥ 18 years; to have a pathological diagnosis of NSCLC, a maximum tumor diameter of 3~5 cm, and cytopathological or histopathological evidence of stage III or IV NSCLC; and to be patients in good general condition, with performance scores of 0–1 and an absence of significant comorbidities involving the heart, liver, kidney, and other major organs.

The exclusion criteria removed patients who could not tolerate additional surgery due to severe cardiopulmonary comorbidities and those in poor physical condition, such as those with insufficient pulmonary function.

Microwave ablation protocol

MRI scanning program and parameters

The Philips Ingenia TM 3.0T system (Philips Medical Systems, Amsterdam, Netherlands) was used to guide and to monitor the microwave ablation procedures with a 16-channel phased array coil. MRI-guided MWA was performed using an ECO-100A MWA system (ECO Medical Instruments Co., Ltd. Nanjing, China; CFDA Certificated No. 20173251268). Moreover, the cooled-shaft ceramic antenna (ECO-100CI8) was made of nonmagnetic ceramic material. The scanning parameters used are shown in Table 1.

CT scanning program and parameters

All lung microwave ablations were performed using CT fluoroscopic guidance (Somatom Sensation 64; Siemens, Erlangen, Germany) with the following parameters: 5-mm collimation, 30 mAs, 120 kV, and 5-mm section thickness. The microwave system consisted of the ECO-100A MWA delivery system (ECO Medical Instruments Co., Ltd. Nanjing,

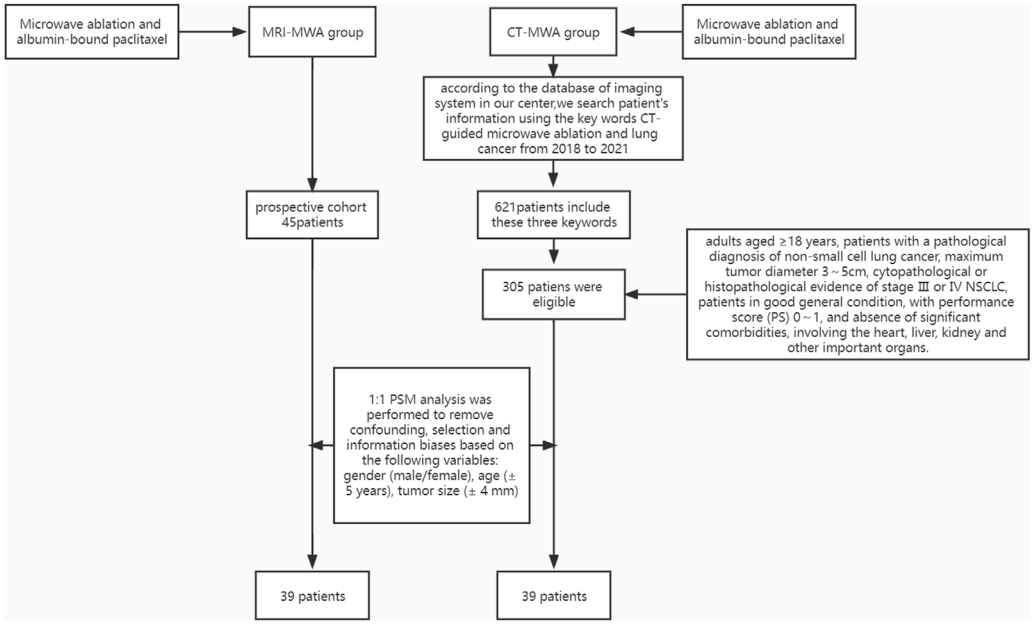

FIGURE 1
Screening process for eligible patients.

TABLE 1 Summary of sequence parameters used for imaging.

Sequence	T_1-TFE	T_2-TSE	DWI
TR (ms)	10	1129	749
TE (ms)	2.3 ACT	80	70
Time(s)	14	17	36
REC Voxel (mm)	0.93/0.93/4.00	0.78/0.78/4.00	1.25/125/4.00
Flip Angle (deg)	15	125	90
FOV(mm)	400 × 330	400 × 330	400 × 330
Slice thickness (mm)	4.0	4.0	4.0

China; CFDA Certificated No. 20173251268), and the cooled-shaft antenna (ECO-100AI13) was made of composite metal materials.

Ablation procedure

The microwave ablation procedure was performed under aseptic conditions by three interventional radiologists with more than eight years of experience in thoracic intervention, a technician, and two experienced radiologists. Codeine phosphate tablets were used to relieve cough (30 mg per patient). Local anesthesia (1% lidocaine) was provided to ensure patients could tolerate the ablation procedure. Electrophysiological monitoring and pulse oximetry were conducted and recorded throughout the procedure. Power was generally 40–60 W, and the treatment duration was 8–16 min. At the end of treatment, patients were instructed to hold their breath. A 20-W power-track ablation was performed immediately to avoid tumor implantation metastasis. After therapy, MRI/CT scanning was performed to observe the incidence of complications and to evaluate treatment outcomes in order to determine whether additional ablation was needed.

MRI-guided MWA

Multiple cod liver oil capsules were used as skin markers and were placed on the skin surface to determine the needle insertion site under MRI. The T1 and T2 sequences were combined to locate the puncture point and plan the preoperative puncture route. The whole-lung scan was performed on T2WI. Then, a breath-hold T1WI scan of the target region was performed. The microwave antenna has a low signal on the image. During the insertion process, horizontal, coronal, and sagittal MRI scanning was conducted during T1WI/TFE, providing a three-dimensional spatial relationship between the ablation needle and the tumor lesion, especially for irregular lesions. A vascular flow void on T2WI ensured that the puncture-ablation needle could effectively avoid important pulmonary vessels and prevent bleeding complications. T2WI/TSE, T1WI/TFE, and DWI sequences were scanned during MRI-guided ablation, and MWA dynamic intraoperative scans monitored changes in the MRI signals in the ablation foci. On T2WI, a low signal was found in the center of the

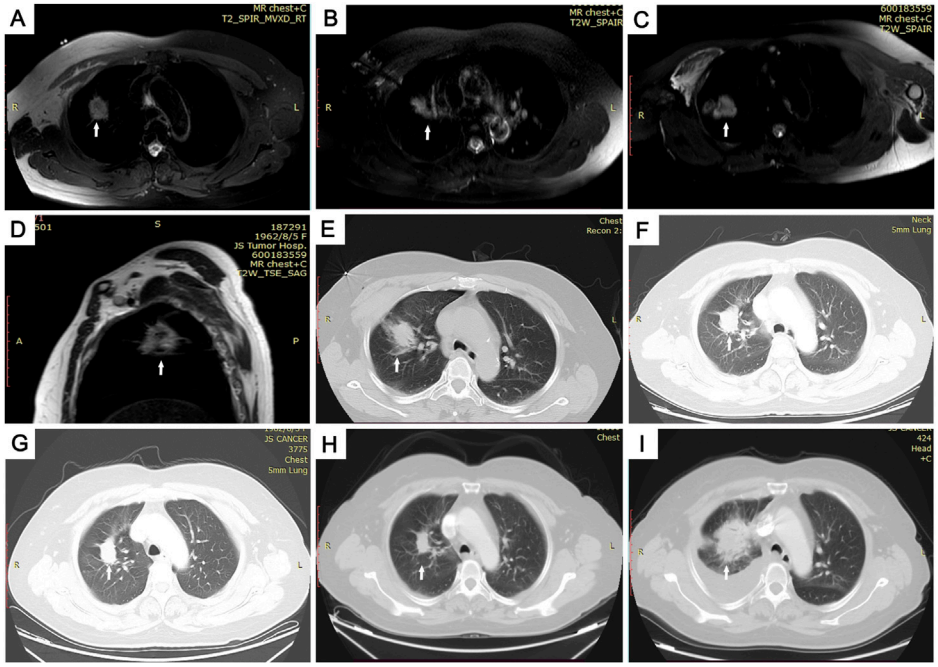

FIGURE 2
Images of the MRI-guided MWA procedure and follow-up in 59-year-old woman with pulmonary adenocarcinoma in superior lobe of right lung. **(A)** Skin markers were applied to locate the needle insertion site under magnetic resonance imaging (MRI) guidance. **(B)** Guided by magnetic-resonance T1WI image, 16G-ablation antenna was punctured to the center of the tumor lesion. **(C–E)** After two 8-min ablation cycles, we achieved a satisfactory ablation area, which is clearly seen in axial- **(C)** and sagittal- **(D)** phase images, and a large area of ground glass covers the entire tumor on the lung window of CT **I**. **(F–I)** Computed tomography (CT) images of follow-up. Follow-up CT scans at 3 **(F)**, 6 **(G)**, and 12 **(H)** months show significantly shrinking, and follow-up CT scan at 21 months **(I)** showed the tumor had increased in size.

ablated tumor, and the high signal area of the primary tumor disappeared and was surrounded by hyperemia and edema with a high signal, which was 5–10 mm beyond the primary tumor area, indicating successful ablation (Figure 2–4).

CT-guided MWA

CT scans were performed to determine the puncture point as well as the angle and depth of the needle. Scans were repeated until the ablation needle reached the center of the tumor. The effect of ablation was evaluated by observing the change in lesion density on CT imaging. After ablation, the tumor lesions showed extensive high density with features such as the “honeycomb sign” and the “bubble sign.”

Chemotherapy protocol

Three courses of albumin-bound paclitaxel combined with carboplatin were used after microwave ablation. Albumin-bound paclitaxel was used at a dose of 125 mg/m^2 (injected for over 30 min). The drug was administered every three weeks on days 1 and 8. Cisplatin was administered at 75 mg/m^2 every 3 weeks on day 1 (injected for over 60 min). The original protocol, when effective, was maintained for three cycles.

Post-ablation follow-up

A chest X-ray or CT scan was performed after 24–48 h to identify any complications. Conservative treatment was adopted if the patient had developed a small asymptomatic pneumothorax or pleural effusion without significant complications. Follow-up CT was performed at 1-, 3-, 6-, and 12-month intervals after the initial ablation session using a multidetector-row helical CT scanner. Contrast-enhanced chest CT images were used to evaluate outcomes.

Outcome evaluation and statistical analysis

The primary outcomes were the accuracy of needle positioning and the efficiency and safety of ablation, as guided by the two imaging methods.

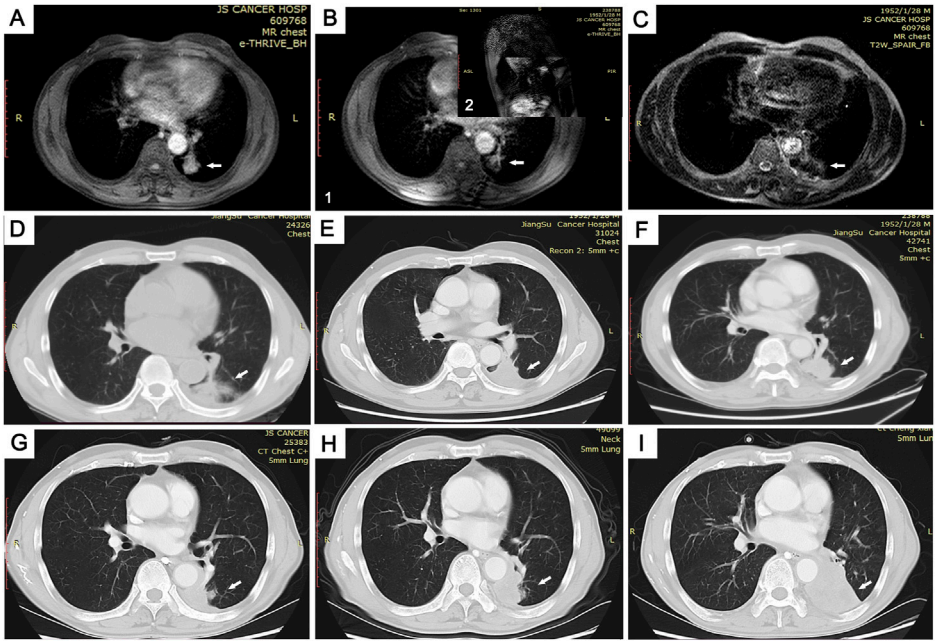

FIGURE 3
Images of the MRI-guided MWA procedure and follow-up in 69-year-old man with pulmonary adenocarcinoma in inferior lobe of left lung. **(A)** Tumor lesion seen on MRI immediately prior to MWA. **(B)** Combined with axial (1) and sagittal (2) MRI scans, the ablation needle reached the tumor site **(C,D)**. By comparing T2WI MRI scan images **(C)** and lung window CT images **(D)**, we found MRI to be more accurate in the assessment of microwave-ablation boundaries. **(E-I)** Follow-up CT scans at 3 **(E)**, 6 **(F)**, 12 **(G)**, and 20 **(H)** months showed no change in the GGO size. At the 26-month follow-up **(I)**, the tumor size was increased.

The accuracy of ablation-needle puncture was defined as the targeting duration and number of scans required for ablation-needle placement.

The ablation efficiency included the microwave ablation time (min) and overall procedure time (min). The overall procedure time was determined as the time between the patient's arrival in the CT or MRI room and the time of their departure. In most cases, less than two ablation cycles were required, ranging from 4 to 8 min. Ablation cycle duration depended on lesion size and power output.

Safety was assessed based on the presence of treatment-related complications, defined according to the Society of Interventional Radiology standard (Ahmed et al., 2014). Secondary outcomes consisted of indicators for evaluating curative effects, including the frequency of residual unablated tumors at 1 month after ablation, the median time to local tumor progression (PFS), and overall survival (OS) at 3 years.

Improved criteria from the Response Evaluation Criteria in Solid Tumors guidelines were used to evaluate the local tumor progression of patients at 3 years of follow-up (Watanabe et al., 2006; Nishino et al., 2010).

The variables were analyzed by SPSS 16.0 software. The means and standard deviations were determined for measurement data and were compared using the independent samples *t*-test or Wilcoxon rank-sum test. The $\chi 2$ test or Fisher's exact test was used to compare categorical variables. The Kaplan–Meier method and log-rank test were applied to compare progression-free survival (PFS) and OS between groups. A *p*-value less than 0.05 was considered statistically significant.

Results

Seventy-eight patients with lung cancer who underwent microwave ablation were included in this study. Patient demographics at baseline did not differ between the MRI and CT groups ($p > 0.05$; Table 2).

There was no difference in the characteristics of the lesions, such as tumor size and depth. The mean number of scans required to adjust needle position was significantly less in the MRI group than in the CT group [7.62 ± 1.69 (range 4–12) vs. 9.64 ± 2.14 (range 5–16), $p < 0.001$]. The mean duration of antenna placement was comparable between the MRI and CT groups (54.41 ± 12.32 min and 53.03 ± 11.29 min, $p = 0.607$).

Microwave ablation duration was significantly different between the two groups (7.97 ± 2.311 min and 9.41 ± 2.86 min, $p = 0.017$).

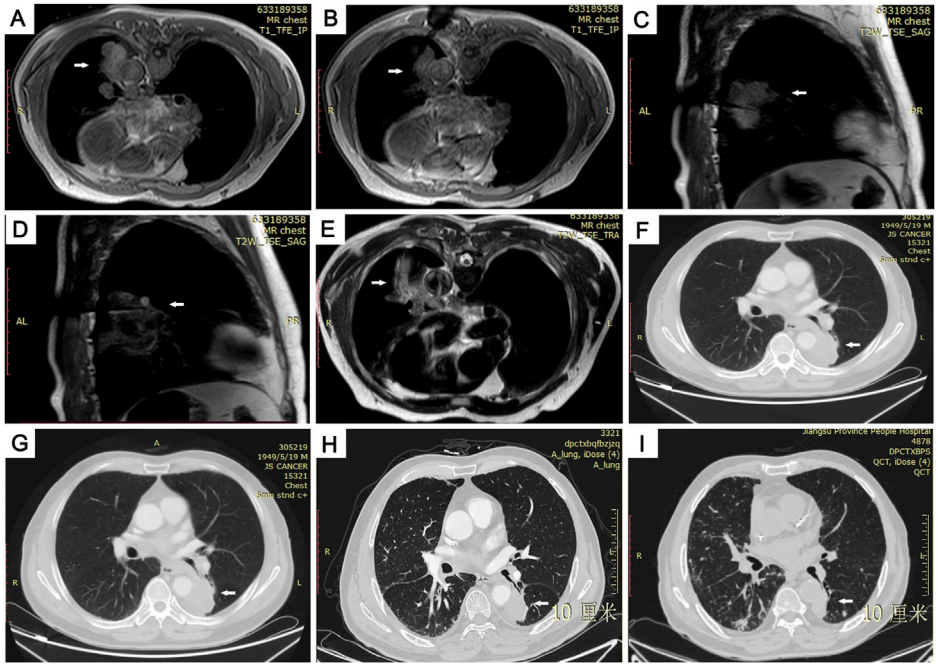

FIGURE 4
Images from 72-year-old man with 50 × 36 mm primary pulmonary adenocarcinoma in lower lobe of left lung. **(A)** Preoperative MRI scan and external puncture site location. **(B)** Ablation needle puncture reached the center of the lesion. **(C,D)** Due to the large lesion, a second ablation was performed by adjusting the ablation needle in real time under the sagittal image. **(E)** T2WI MRI scan immediately after the operation showing the surrounding ring-shaped high-signal thermal-injury response zone completely covered the ablation area with low signal and was well demarcated from the adjacent abdominal aorta. **(F–I)** Follow-up CT images showing the ablative zone was gradually shrinking at postoperative months 3 **(F)** 6 **(G)** 12 **(H)** and 16 **(I)**.

TABLE 2 Clinical characteristics of patients undergoing MRI-guided microwave ablation (MRI-MWA group) or CT-guided microwave ablation (CT-MWA group) to treat pulmonary malignancies.

Characteristic	Total patients (n = 78)	MRI-MWA group (n = 39)	CT-MWA group (n = 39)	χ^2 value/t-value	p-value
Age	62.47 ± 8.61	61.89 ± 9.09	62.71 ± 8.18	0.188	0.666
Gender					
Male	48	23	25	0.217	0.642
Female	30	16	14		
Tumor size	7.77 ± 7.59	8.15 ± 8.64	7.39 ± 6.47	0.189	0.665
Location				0.665	0.717
Peripheral	39	18	21		
Middle	29	15	14		
Inner	10	6	4		
Pathology					
Adenocarcinoma	51	27	24	0.510	0.475
Non-adenocarcinoma	27	12	15		
TNM stage				0.228	0.892
IIIa	31	16	15		
IIIb	19	10	9		
IV	28	13	15		

Note—Data are means ±standard deviations or medians with interquartile ranges in parentheses for continuous variables.

TABLE 3 Comparison of observational data in both study groups.

Parameter	MRI-MWA group (n = 39)	CT-MWA group (n = 39)	t-value	p-value
Number of machine scans for adjusting needle position	7.62 ± 1.69	9.64 ± 2.14	21.396	<0.001
Time for antenna placement (min)	54.41 ± 12.32	53.03 ± 11.29	0.267	0.607
Microwave ablation time (min)	7.62 ± 2.65	9.41 ± 2.86	8.251	0.005
Total procedure time (min)	91.28 ± 16.69	93.41 ± 16.03	0.330	0.568
Residual unablated tumors	3 (7.69%)	4 (10.2%)	0.157	0.692

Note.—Unless otherwise specified, data are presented as mean with the range in parentheses.

TABLE 4 Complications.

Complication	MRI-MWA group (n = 39)	CT-MWA group (n = 39)	χ^2 value	p-value
	12 (30%)	20 (51%)	6.203	0.185
Hemorrhage	1	4		
Pleural effusion	3	4		
Pneumothorax	6	5		
Cavitation of the ablation zone	2	7		

Note.—Data are numbers of patients with percentages in parentheses for categorical variables.

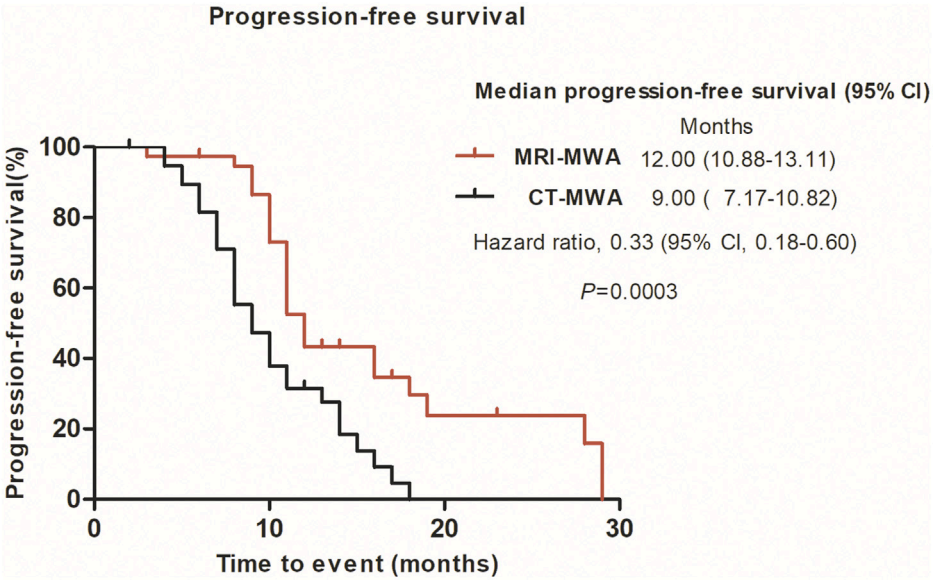

FIGURE 5
Graphs show Kaplan–Meier survival estimates for progression-free survival between MRI-MWA group and CT-MWA group.

The overall procedure duration was comparable between the MRI and CT groups (91.28 ± 16.69 min and 93.41 ± 16.03 min, p = 0.568) (Table 3).

Four major complications related to the ablation procedure were observed within 30 days in the MRI- and CT-MWA groups, including hemoptysis (n = 1 and n = 4, respectively), pleural

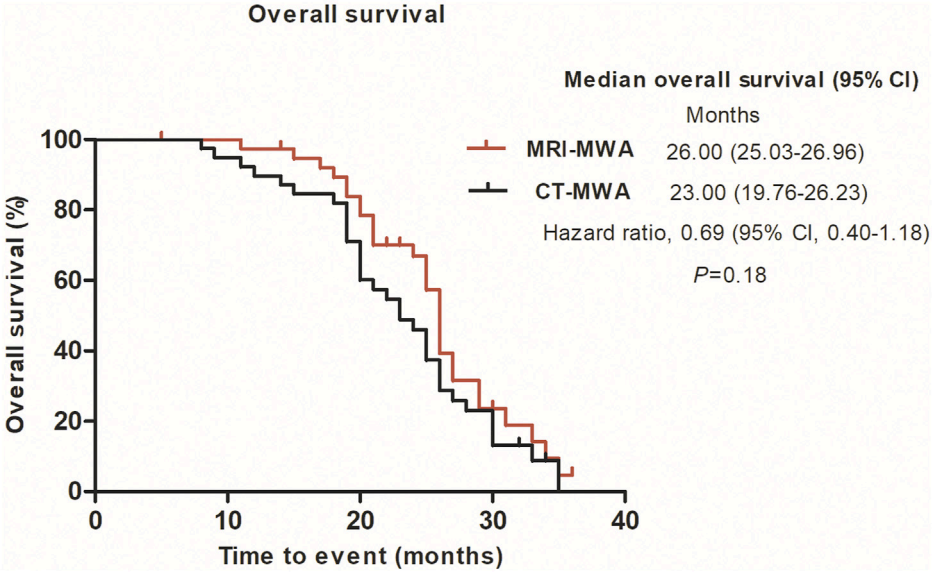

FIGURE 6
Graphs show Kaplan–Meier survival estimates for overall survival between MRI-MWA group and CT-MWA group.

effusion ($n = 3$ and $n = 4$, respectively), pneumothorax ($n = 6$ and $n = 5$, respectively), and cavitation of the ablation zone ($n = 2$ and $n = 7$, respectively) (Table 4). The overall complication rates were 12% and 51% in the MRI- and CT-MWA groups, respectively ($p = 0.185$).

The median time to progression was significantly longer in the MRI-MWA group than in the CT-MWA group (11 months [95% CI 10.24–11.75] vs. 9 months [95% CI 8.00–9.99], $p = 0.0003$; hazard ratio 0.3690 [95% CI 0.2159–0.6306]). As shown in Figure 5, Kaplan–Meier analysis revealed a significant difference in PFS between both groups.

The median OS was 26.0 months [95% CI 25.022–26.978] in the MRI group and 23.0 months [95% CI 18.646–27.354] in the CT group ($p = 0.18$) (Figure 6).

Discussion

It is well-established that CT-guided microwave ablation provides a minimally invasive approach to eradicating tumors, especially for solid lung neoplasms (Wolf et al., 2008; Ko et al., 2016; Huang et al., 2020). The advantages of microwave ablation include higher intratumoral temperatures, the ability to use multiple applicators, more rapid and homogeneous ablations, and little influence of heat dispersion on blood circulation (Skinner et al., 1998; Stauffer et al., 2003; Wright et al., 2003; Shock et al., 2004). Although microwave ablation for lung cancer has achieved remarkable results, there are still some issues, such as inaccurate localization, subjective selection of ablation parameters, incomplete ablation, and excessive ablation, which directly affect the safety and effectiveness of this approach (Liang et al., 2009; Chen et al., 2020). MRI-guided MWA can compensate for the limitations of CT-guided ablation and has similar advantages to CT. Indeed, MRI-guided microwave ablation does not use ionizing radiation and provides high soft-tissue resolution, arbitrary orientation, and multi-parameter imaging for the ablation of liver, kidney, prostate, and other tumors (Lin et al., 2019; Faridi et al., 2020; Yang et al., 2020).

Our preliminary results show that MRI imaging yields superior accuracy, relative to CT, during ablation needle puncture. It is well-established that a fast sequence, such as the T1-TFE sequence, can distinguish anatomical structures for precise puncture. MRI can be used for arbitrary multidirectional imaging to ensure that the overall microwave antenna and the relationship between the microwave antenna and the lesion can be displayed during puncture, shortening the operation time and achieving a rapid, accurate puncture location. Moreover, the metal artifact produced by the ablation needle during CT can cover the ablation target. Importantly, magnetic resonance multisequence imaging and MR-functional imaging methods such as DWI, MRS, and PWI provide more accurate and abundant information than CT does for assessing the relationship between lung tumor lesions and surrounding tissues, cardiac great vessels, and the ablation boundary, making the puncture process simpler, safer, and more

accurate (Biederer et al., 2012). In our study, the number of scans required for ablation-needle puncture in the MRI-MWA group was significantly less than in the CT-MWA group (7.62 ± 1.69 vs. 9.64 ± 2.14, $p < 0.001$). Although the average single-scan duration for MRI was slightly longer than for CT, the average times for antenna placement were comparable for the MRI-MWA group and the CT group (53.03 ± 11.29 min and 54.41 ± 12.32 min, $p = 0.607$). The total procedure duration was comparable between both groups (91.28 ± 16.69 min vs. 93.41 ± 16.03 min, $p > 0.05$). Based on the accuracy of MRI-guided localization and the application of rapid sequence, the overall scanning duration and operation duration were comparable to the CT-MWA group. Taken together, the aforementioned findings suggest that the overall efficiency of MRI-guided microwave ablation is consistent with that of CT-guided microwave ablation and yields less damage due to a significant reduction in the number of needle adjustments.

Indeed, the effect of ionizing radiation produced by CT scans, especially for tumor patients, should not be overstated (Pearce et al., 2012; Hu et al., 2016; Meulepas et al., 2019). Importantly, microwave ablation guided by magnetic resonance produces no ionizing radiation.

In a previous study, we demonstrated a significant difference between the ablation power and the actual ablation power, and it was challenging to accurately control the ablation range (Li et al., 2020). Excessively high temperatures may lead to carbonization of surrounding tissues, reduced ablation volume, or breakdown of the ablation needle due to the standing wave effect. If the ablation-zone temperature is too low, the tumor cannot be completely ablated. Therefore, real-time monitoring during ablation is important. CT is the primary imaging modality used to assess ablation results. Successful ablation is defined as a region of low attenuation covering the lesion area and a lack of contrast enhancement (Abtin et al., 2012; Iguchi et al., 2015; Ye et al., 2018; Ye et al., 2021). It has been shown that in well-demarcated ablation areas, necrosis is surrounded by a darker, patchy rim of acute inflammation, marked congestion, edema, and diffuse alveolar hemorrhage (Goldberg et al., 1995). However, these changes are not obvious on CT, especially in the marginal areas, and there is no guarantee that the potential residual foci near blood vessels could be completely removed. However, based on our team's experience, ground-glass shadow after ablation is often confused with bleeding caused by mechanical lung-tissue injury during puncture in plain CT scanning. Thus, CT does not bring significant advantages during intraprocedural therapeutic evaluation (Harada et al., 2011). It is well-established that MRI is sensitive to changes in the water content of ablated lesions (Lazebnik et al., 2003; Lin et al., 2019). Importantly, high-contrast MRI provides high-definition images of soft tissue, clarifies the lesion's scope, and distinguishes liquefied necrotic tissue from active tumor lesions. Current evidence suggests that MRI enables visualization of coagulated necrotic areas of 2–3 mm (Song et al., 2020). Multi-parameter imaging, such as tissue-diffusion and perfusion imaging, provides a more accurate evaluation of the therapeutic effect (Hayashida et al., 2006; Kamel et al., 2006; Ohira et al., 2009; Olin et al., 2019). Any azimuth fault can clearly display the boundary and formation process of ablation foci. Therefore, the parameters measured by MRI can be used to determine the ablation effect and endpoint to improve the local ablation-control rate, reduce tumor residue, and reduce the incidence of complications (Li et al., 2017).

In the present study, we quantified the maximum diameter, including the ablation area, of isointense signal intensity on T1WI and of high signal intensity on T2WI images, without using contrast enhancement. These findings suggest that, compared with CT, MRI can provide a more accurate real-time evaluation of MWA. T2WI can be used to evaluate the effect of WMA. In the present study, the mean PFS was 11 months in the MRI-MWA group and 9 months in the CT-MWA group, and the difference was significant ($\chi^2 = 11.237$, $p < 0.01$), while no difference in OS was observed between the groups at 3-year follow-up ($\chi^2 = 2.256$, $p = 0.132$).

Although both groups had similar survival rates, higher PFS was observed in the MRI-MWA group, suggesting that these patients had a better quality of life. Nonetheless, it remains unclear whether MRI-guided MWA could improve the survival rate, and further studies with longer-term follow-ups are warranted.

Compared with the literature, PFS was significantly improved between the experimental and control groups in this study, which may be related to albumin-bound paclitaxel (Jung et al., 2020; Xu et al., 2021). Nab-paclitaxel is a nanoparticle-sized anti-tumor drug formed from paclitaxel and albumin (West et al., 2019). It has been found that nab-paclitaxel can be used instead of regular paclitaxel to reduce hypersensitivity reactions in the treatment of advanced breast cancer (Schmid et al., 2018; Emens et al., 2021). In addition, nab-paclitaxel has targeting properties which, combined with the natural transport mechanism of albumin, allow paclitaxel to act on tumor tissues and achieve higher drug levels within a short period, thereby achieving better anti-tumor effects. Its main mechanism of action is similar to paclitaxel—promoting microtubulin polymerization and hindering microtubulin depolymerization—and thus it inhibits tumor cell proliferation and growth (Yardley, 2013). Moreover, overwhelming evidence has substantiated that nab-paclitaxel is effective as the first-line treatment of advanced NSCLC. A large phase-III clinical study showed that nab-paclitaxel combined with carboplatin was cost-effective, compared to paclitaxel injection combined with carboplatin, for the first-line treatment of advanced NSCLC (Jotte et al., 2020).

Although survival was similar between the two groups in this study, the higher PFS rate in the MRI-MWA group suggested that its patients had a better quality of life. However, it remains unclear whether MRI-guided microwave ablation could improve the survival rate; this uncertainty emphasizes the need for further studies with longer follow-ups to validate this hypothesis.

Similar to percutaneous ablation therapies, MRI-guided microwave ablation is associated with common complications such as hemorrhage, pleural effusion, pneumothorax, and cavitation of the ablation zone (Chen et al., 2020). Other complications, such as pulmonary-artery aneurysms and postprocedural pneumonia, are rare and were not observed in our study. Moreover, we found no difference in the incidence of complications, although the incidence of ablation-zone cavitation was slightly higher in the CT-MWA group than in the MRI-MWA group, which may be related to the longer ablation time (Carrafiello et al., 2012; Zheng et al., 2014; Welch et al., 2015). Although cavitation of the ablation zone is usually clinically insignificant, rupture may occur, leading to pneumothorax and bleeding. Cavities may also serve as scaffolds for fungal colonization. Precautions to minimize these risks should be taken whenever possible. In most cases, patients in the MRI-WMA group did not experience any symptoms, with only one experiencing an increased heart rate (90 bpm) that was resolved by manual aspiration.

The present study had some limitations, including its small sample size and the retrospective nature of the data obtained for the CT-MWA group. Moreover, our findings were based on data from a single center, emphasizing the need for multi-center studies. In this study, ablations were performed by experienced interventionists; it remains unclear whether the same benefits in accuracy and time would be observed with less-experienced radiologists. Moreover, the management of patients (i.e., whether they received targeted therapy, immunotherapy, or systemic chemotherapy) after local tumor progression was not assessed in the 3-year follow-up, but this will be carried out during follow-up analysis. Additionally, the quality of life and other measures of patient experience of the treatment were not directly studied and should be considered in the future to truly reflect the value of MRI-guided microwave ablation for the treatment of NSCLC. Indeed, the follow-up period (3 years) was relatively short. A longer follow-up period may reveal differences in survival rates between the two groups.

Conclusion

Overall, the results of our matched-cohort study suggest that MRI-guided percutaneous ablation has significant prospects for the treatment of lung tumors as a feasible, safe, effective, and minimally invasive approach and provides a satisfactory outcome.

Data availability statement

The original contributions presented in the study are included in the article/Supplementary Material; further inquiries can be directed to the corresponding author.

Ethics statement

This prospective study was reviewed and approved by the Ethics Committee of Jiangsu Provincial Hospital Affiliated to Nanjing Medical University. All patients included in the study provided informed consent and paper-based written consent to publish the related research results was acquired.

Author contributions

XS and TC drafted the manuscript and analyzed the data; NL, PY, GF, and BY generated the figure. NY, CZ, and YW performed the background research. BH and SC edited the manuscript. All authors have read and approved the content of the manuscript.

Funding

The study was supported by the Health Planning Commission of Jiangsu Province (no. BE2017758) and the Scientific Research Project of the Health Commission of Jiangsu Province (no. BJ18034).

Acknowledgments

The authors wish to thank all their colleagues in the Department of Thoracic Surgery, Jiangsu Cancer Hospital.

Conflict of interest

The authors declare that the research was conducted in the absence of any commercial or financial relationships that could be construed as a potential conflict of interest.

Publisher's note

References

Abtin, F. G., Eradat, J., Gutierrez, A. J., Lee, C., Fishbein, M. C., and Suh, R. D. (2012). Radiofrequency ablation of lung tumors: Imaging features of the postablation zone. *Radiographics* 32 (4), 947–969. doi:10.1148/rg.324105181

Ahmed, M., Solbiati, L., Brace, C. L., Breen, D. J., Callstrom, M. R., Charboneau, J. W., et al. (2014). Image-guided tumor ablation: Standardization of terminology and reporting criteria--a 10-year update. *Radiology* 273 (1), 241–260. doi:10.1148/radiol.14132958

An, W., Zhang, H., Wang, B., Zhong, F., Wang, S., and Liao, M. (2022). Comparison of CT-guided core needle biopsy in pulmonary ground-glass and solid nodules based on propensity score matching analysis. *Technol. Cancer Res. Treat.* 21, 153303382210853. doi:10.1177/15330338221085357

Biederer, J., Beer, M., Hirsch, W., Wild, J., Fabel, M., Puderbach, M., et al. (2012). MRI of the lung (2/3). Why . when. how? *Insights Imaging* 3 (4), 355–371. doi:10.1007/s13244-011-0146-8

Boiselle, P. M., Biederer, J., Gefter, W. B., and Lee, E. Y. (2013). Expert opinion: Why is MRI still an under-utilized modality for evaluating thoracic disorders? *J. Thorac. Imaging* 28 (3), 137. doi:10.1097/RTI.0b013e31828cafe7

Carrafiello, G., Mangini, M., Fontana, F., Di Massa, A., Ierardi, A. M., Cotta, E., et al. (2012). Complications of microwave and radiofrequency lung ablation: Personal experience and review of the literature. *Radiol. Med.* 117 (2), 201–213. doi:10.1007/s11547-011-0741-2

Chen, B., Li, W., Liu, Y., Ren, S., Wang, L., Wang, H., et al. (2020). The efficacy and complications of computed tomography guided microwave ablation in lung cancer. *Ann. Palliat. Med.* 9 (5), 2760–2765. doi:10.21037/apm-20-255

Ciet, P., Tiddens, H. A., Wielopolski, P. A., Wild, J. M., Lee, E. Y., Morana, G., et al. (2015). Magnetic resonance imaging in children: Common problems and possible solutions for lung and airways imaging. *Pediatr. Radiol.* 45 (13), 1901–1915. doi:10.1007/s00247-015-3420-y

Dupuy, D. E. (2011). Image-guided thermal ablation of lung malignancies. *Radiology* 260 (3), 633–655. doi:10.1148/radiol.11091126

Emens, L. A., Adams, S., Barrios, C. H., Dieras, V., Iwata, H., Loi, S., et al. (2021). First-line atezolizumab plus nab-paclitaxel for unresectable, locally advanced, or metastatic triple-negative breast cancer: IMpassion130 final overall survival analysis. *Ann. Oncol.* 32 (8), 983–993. doi:10.1016/j.annonc.2021.05.355

Faridi, P., Keselman, P., Fallahi, H., and Prakash, P. (2020). Experimental assessment of microwave ablation computational modeling with MR thermometry. *Med. Phys.* 47 (9), 3777–3788. doi:10.1002/mp.14318

Goldberg, S. N., Gazelle, G. S., Compton, C. C., and McLoud, T. C. (1995). Radiofrequency tissue ablation in the rabbit lung: Efficacy and complications. *Acad. Radiol.* 2 (9), 776–784. doi:10.1016/s1076-6332(05)80852-9

Goldberg, S. N., Gazelle, G. S., and Mueller, P. R. (2000). Thermal ablation therapy for focal malignancy: A unified approach to underlying principles, techniques, and diagnostic imaging guidance. *Am. J. Roentgenol.* 174 (2), 323–331. doi:10.2214/ajr.174.2.1740323

Harada, S., Sato, S., Suzuki, E., Okumura, Y., Hiraki, T., Gobara, H., et al. (2011). The usefulness of pre-radiofrequency ablation SUV(max) in 18F-FDG PET/CT to predict the risk of a local recurrence of malignant lung tumors after lung radiofrequency ablation. *Acta Med. Okayama* 65 (6), 395–402. doi:10.18926/AMO/47265

Hayashida, Y., Yakushiji, T., Awai, K., Katahira, K., Nakayama, Y., Shimomura, O., et al. (2006). Monitoring therapeutic responses of primary bone tumors by diffusion-weighted image: Initial results. *Eur. Radiol.* 16 (12), 2637–2643. doi:10.1007/s00330-006-0342-y

Hu, B., Jin, C., Li, H. B., Tong, J., Ouyang, X., Cetinbas, N. M., et al. (2016). The DNA-sensing AIM2 inflammasome controls radiation-induced cell death and tissue injury. *Science* 354 (6313), 765–768. doi:10.1126/science.aaf7532

Huang, G., Yang, X., Li, W., Wang, J., Han, X., Wei, Z., et al. (2020). A feasibility and safety study of computed tomography-guided percutaneous microwave ablation: A novel therapy for multiple synchronous ground-glass opacities of the lung. *Int. J. Hyperth.* 37 (1), 414–422. doi:10.1080/02656736.2020.1756467

Iguchi, T., Hiraki, T., Gobara, H., Fujiwara, H., Matsui, Y., Soh, J., et al. (2015). Percutaneous radiofrequency ablation of lung cancer presenting as ground-glass opacity. *Cardiovasc. Interv. Radiol.* 38 (2), 409–415. doi:10.1007/s00270-014-0926-x

Jotte, R., Cappuzzo, F., Vynnychenko, I., Stroyakovskiy, D., Rodriguez-Abreu, D., Hussein, M., et al. (2020). Atezolizumab in combination with carboplatin and nab-paclitaxel in advanced squamous NSCLC (IMpower131): Results from a randomized phase III trial. *J. Thorac. Oncol.* 15 (8), 1351–1360. doi:10.1016/j.jtho.2020.03.028

Jung, H. A., Noh, J. M., Sun, J. M., Lee, S. H., Ahn, J. S., Ahn, M. J., et al. (2020). Real world data of durvalumab consolidation after chemoradiotherapy in stage III non-small-cell lung cancer. *Lung Cancer* 146, 23–29. doi:10.1016/j.lungcan.2020.05.035

Kamel, I. R., Bluemke, D. A., Eng, J., Liapi, E., Messersmith, W., Reyes, D. K., et al. (2006). The role of functional MR imaging in the assessment of tumor response after chemoembolization in patients with hepatocellular carcinoma. *J. Vasc. Interv. Radiol.* 17 (3), 505–512. doi:10.1097/01.RVI.0000200052.02183.92

Ko, W. C., Lee, Y. F., Chen, Y. C., Chien, N., Huang, Y. S., Tseng, Y. H., et al. (2016). CT-guided percutaneous microwave ablation of pulmonary malignant tumors. *J. Thorac. Dis.* 8 (9), S659–S665. doi:10.21037/jtd.2016.09.44

Lazebnik, R. S., Breen, M. S., Fitzmaurice, M., Nour, S. G., Lewin, J. S., and Wilson, D. L. (2003). Radio-frequency-induced thermal lesions: Subacute magnetic resonance appearance and histological correlation. *J. Magn. Reson. Imaging* 18 (4), 487–495. doi:10.1002/jmri.10382

Li, H., Fan, Z., Nan, Q., and Cheng, Y. (2020). Numerical simulation of electromagnetic heating process of biological tissue via time-fractional Cattaneo transfer equation. *J. Therm. Biol.* 94, 102789. doi:10.1016/j.jtherbio.2020.102789

Li, J., Qu, J., Zhang, H., Wang, Y., Zheng, L., Geng, X., et al. (2017). 3.0T MRI for long-term observation of lung nodules post cryoablation: A pilot study. *Cancer Imaging* 17 (1), 29. doi:10.1186/s40644-017-0131-7

Liang, P., Wang, Y., Yu, X., and Dong, B. (2009). Malignant liver tumors: Treatment with percutaneous microwave ablation--complications among cohort of 1136 patients. *Radiology* 251 (3), 933–940. doi:10.1148/radiol.2513081740

Lin, Z., Chen, J., Yan, Y., Chen, J., and Li, Y. (2019). Microwave ablation of hepatic malignant tumors using 1.5T MRI guidance and monitoring: Feasibility and preliminary clinical experience. *Int. J. Hyperth.* 36 (1), 1215–1221. doi:10.1080/02656736.2019.1690166

Lu, Q., Cao, W., Huang, L., Wan, Y., Liu, T., Cheng, Q., et al. (2012). CT-guided percutaneous microwave ablation of pulmonary malignancies: Results in 69 cases. *World J. Surg. Oncol.* 10, 80. doi:10.1186/1477-7819-10-80

Meulepas, J. M., Ronckers, C. M., Smets, A., Nievelstein, R. A. J., Gradowska, P., Lee, C., et al. (2019). Radiation exposure from pediatric CT scans and subsequent cancer risk in The Netherlands. *J. Natl. Cancer Inst.* 111 (3), 256–263. doi:10.1093/jnci/djy104

Nishino, M., Jackman, D. M., Hatabu, H., Yeap, B. Y., Cioffredi, L. A., Yap, J. T., et al. (2010). New response evaluation criteria in solid tumors (RECIST) guidelines for advanced non-small cell lung cancer: Comparison with original RECIST and impact on assessment of tumor response to targeted therapy. *Am. J. Roentgenol.* 195 (3), W221–W228. doi:10.2214/AJR.09.3928

Ohira, T., Okuma, T., Matsuoka, T., Wada, Y., Nakamura, K., Watanabe, Y., et al. (2009). FDG-MicroPET and diffusion-weighted MR image evaluation of early changes after radiofrequency ablation in implanted VX2 tumors in rabbits. *Cardiovasc. Interv. Radiol.* 32 (1), 114–120. doi:10.1007/s00270-008-9394-5

Olin, A., Krogager, L., Rasmussen, J. H., Andersen, F. L., Specht, L., Beyer, T., et al. (2019). Preparing data for multiparametric PET/MR imaging: Influence of PET point spread function modelling and EPI distortion correction on the spatial correlation of [(18)F]FDG-PET and diffusion-weighted MRI in head and neck cancer. *Phys. Medica* 61, 1–7. doi:10.1016/j.ejmp.2019.04.006

Pearce, M. S., Salotti, J. A., Little, M. P., McHugh, K., Lee, C., Kim, K. P., et al. (2012). Radiation exposure from CT scans in childhood and subsequent risk of leukaemia and brain tumours: A retrospective cohort study. *Lancet* 380 (9840), 499–505. doi:10.1016/S0140-6736(12)60815-0

Puderbach, M., Hintze, C., Ley, S., Eichinger, M., Kauczor, H. U., and Biederer, J. (2007). MR imaging of the chest: A practical approach at 1.5T. *Eur. J. Radiol.* 64 (3), 345–355. doi:10.1016/j.ejrad.2007.08.009

Schmid, P., Adams, S., Rugo, H. S., Schneeweiss, A., Barrios, C. H., Iwata, H., et al. (2018). Atezolizumab and nab-paclitaxel in advanced triple-negative breast cancer. *N. Engl. J. Med. Overseas. Ed.* 379 (22), 2108–2121. doi:10.1056/NEJMoa1809615

Shen, X., Chen, T., Yang, B., Liu, N., Qian, X., Xia, B., et al. (2021). Magnetic resonance imaging-guided microwave ablation for lung tumor: A case report. *Quant. Imaging Med. Surg.* 11 (6), 2780–2784. doi:10.21037/qims-20-667

Shock, S. A., Meredith, K., Warner, T. F., Sampson, L. A., Wright, A. S., Winter, T. C., 3rd, et al. (2004). Microwave ablation with loop antenna: *In vivo* porcine liver model. *Radiology* 231 (1), 143–149. doi:10.1148/radiol.2311021342

Shono, N., Ninni, B., King, F., Kato, T., Tokuda, J., Fujimoto, T., et al. (2020). Simulated accuracy assessment of small footprint body-mounted probe alignment device for MRI-guided cryotherapy of abdominal lesions. *Med. Phys.* 47 (6), 2337–2349. doi:10.1002/mp.14116

Skinner, M. G., Iizuka, M. N., Kolios, M. C., and Sherar, M. D. (1998). A theoretical comparison of energy sources--microwave, ultrasound and laser--for

interstitial thermal therapy. *Phys. Med. Biol.* 43 (12), 3535–3547. doi:10.1088/0031-9155/43/12/011

Song, D., Chen, T., Wang, S., Chen, S., Li, H., Yu, F., et al. (2020). Study on the biochemical mechanisms of the micro-wave ablation treatment of lung cancer by *ex vivo* confocal Raman microspectral imaging. *Analyst* 145 (2), 626–635. doi:10.1039/c9an01524h

Stauffer, P. R., Rossetto, F., Prakash, M., Neuman, D. G., and Lee, T. (2003). Phantom and animal tissues for modelling the electrical properties of human liver. *Int. J. Hyperth.* 19 (1), 89–101. doi:10.1080/0265673021000017064

Vietti Violi, N., Duran, R., Guiu, B., Cercueil, J. P., Aube, C., Digklia, A., et al. (2018). Efficacy of microwave ablation versus radiofrequency ablation for the treatment of hepatocellular carcinoma in patients with chronic liver disease: A randomised controlled phase 2 trial. *Lancet Gastroenterol. Hepatol.* 3 (5), 317–325. doi:10.1016/S2468-1253(18)30029-3

Watanabe, H., Kunitoh, H., Yamamoto, S., Kawasaki, S., Inoue, A., Hotta, K., et al. (2006). Effect of the introduction of minimum lesion size on interobserver reproducibility using RECIST guidelines in non-small cell lung cancer patients. *Cancer Sci.* 97 (3), 214–218. doi:10.1111/j.1349-7006.2006.00157.x

Welch, B. T., Brinjikji, W., Schmit, G. D., Callstrom, M. R., Kurup, A. N., Cloft, H. J., et al. (2015). A national analysis of the complications, cost, and mortality of percutaneous lung ablation. *J. Vasc. Interv. Radiol.* 26 (6), 787–791. doi:10.1016/j.jvir.2015.02.019

West, H., McCleod, M., Hussein, M., Morabito, A., Rittmeyer, A., Conter, H. J., et al. (2019). Atezolizumab in combination with carboplatin plus nab-paclitaxel chemotherapy compared with chemotherapy alone as first-line treatment for metastatic non-squamous non-small-cell lung cancer (IMpower130): A multicentre, randomised, open-label, phase 3 trial. *Lancet Oncol.* 20 (7), 924–937. doi:10.1016/S1470-2045(19)30167-6

Wolf, F. J., Grand, D. J., Machan, J. T., Dipetrillo, T. A., Mayo-Smith, W. W., and Dupuy, D. E. (2008). Microwave ablation of lung malignancies: Effectiveness, CT findings, and safety in 50 patients. *Radiology* 247 (3), 871–879. doi:10.1148/radiol.2473070996

Wright, A. S., Lee, F. T., Jr., and Mahvi, D. M. (2003). Hepatic microwave ablation with multiple antennae results in synergistically larger zones of coagulation necrosis. *Ann. Surg. Oncol.* 10 (3), 275–283. doi:10.1245/aso.2003.03.045

Xu, S., Qi, J., Li, B., and Li, X. G. (2021). Survival prediction for non-small cell lung cancer patients treated with CT-guided microwave ablation: Development of a prognostic nomogram. *Int. J. Hyperth.* 38 (1), 640–649. doi:10.1080/02656736.2021.1914353

Yang, N., Gong, J., Yao, L., Wang, C., Chen, J., Liu, J., et al. (2020). Magnetic resonance imaging-guided microwave ablation of hepatic malignancies: Feasibility, efficacy, safety, and follow-up. *J. Cancer Res. Ther.* 16 (5), 1151–1156. doi:10.4103/jcrt.JCRT_1_20

Yardley, D. A. (2013). nab-Paclitaxel mechanisms of action and delivery. *J. Control. Release* 170 (3), 365–372. doi:10.1016/j.jconrel.2013.05.041

Ye, X., Fan, W., Wang, H., Wang, J., Wang, Z., Gu, S., et al. (2018). Expert consensus workshop report: Guidelines for thermal ablation of primary and metastatic lung tumors (2018 edition). *J. Cancer Res. Ther.* 14 (4), 730–744. doi:10.4103/jcrt.JCRT_221_18

Ye, X., Fan, W., Wang, Z., Wang, J., Wang, H., Wang, J., et al. (2021). Expert consensus for thermal ablation of pulmonary subsolid nodules (2021 edition). *Zhongguo Fei Ai Za Zhi* 24 (5), 305–322. doi:10.3779/j.issn.1009-3419.2021.101.14

Zheng, A., Wang, X., Yang, X., Wang, W., Huang, G., Gai, Y., et al. (2014). Major complications after lung microwave ablation: A single-center experience on 204 sessions. *Ann. Thorac. Surg.* 98 (1), 243–248. doi:10.1016/j.athoracsur.2014.03.008

frontiers | Frontiers in Bioengineering and Biotechnology

TYPE Review
PUBLISHED 20 December 2022
DOI 10.3389/fbioe.2022.1083640

OPEN ACCESS

EDITED BY
Jingwei Xie,
University of Nebraska Medical Center, United States

REVIEWED BY
Shixuan Chen,
University of Chinese Academy of Sciences, China
Beklem Bostancioglu,
Karolinska Institutet (KI), Sweden
Alec McCarthy,
Merz Pharmaceuticals GmbH, Germany

*CORRESPONDENCE
Tao Xiong,
xiongtao@hotmail.com
Han Shen,
shenhan10366@sina.com
Zhiyang Li,
lizhiyang@nju.edu.cn

SPECIALTY SECTION
This article was submitted to Tissue Engineering and Regenerative Medicine, a section of the journal Frontiers in Bioengineering and Biotechnology

RECEIVED 29 October 2022
ACCEPTED 05 December 2022
PUBLISHED 20 December 2022

CITATION
Zhang B, Gong J, He L, Khan A, Xiong T, Shen H and Li Z (2022), Exosomes based advancements for application in medical aesthetics.
Front. Bioeng. Biotechnol. 10:1083640. doi: 10.3389/fbioe.2022.1083640

Exosomes based advancements for application in medical aesthetics

Bin Zhang[1,2], Jianmin Gong[1,2], Lei He[2], Adeel Khan[3], Tao Xiong[1]*, Han Shen[2]* and Zhiyang Li[2]*

[1]College of Life Science, Yangtze University, Jingzhou, China, [2]Department of Clinical Laboratory, The Affiliated Drum Tower Hospital of Nanjing University Medical School, Nanjing, China, [3]State Key Laboratory of Bioelectronics, School of Biological Science and Medical Engineering, National Demonstration Center for Experimental Biomedical Engineering Education, Southeast University, Nanjing, China

Beauty is an eternal pursuit of all people. Wound repair, anti-aging, inhibiting hyperpigmentation and hair loss are the main demands for medical aesthetics. At present, the repair and remodeling of human body shape and function in medical aesthetics are often achieved by injection of antioxidants, hyaluronic acid and botulinum toxin, stem cell therapy. However, there are some challenges, such as difficulty controlling the injection dose, abnormal local contour, increased foreign body sensation, and the risk of tumor occurrence and deformity induced by stem cell therapy. Exosomes are tiny vesicles secreted by cells, which are rich in proteins, nucleic acids and other bioactive molecules. They have the characteristics of low immunogenicity and strong tissue penetration, making them ideal for applications in medical aesthetics. However, their low yield, strong heterogeneity, and long-term preservation still hinder their application in medical aesthetics. In this review, we summarize the mechanism of action, administration methods, engineered production and preservation technologies for exosomes in medical aesthetics in recent years to further promote their research and industrialization in the field of medical aesthetics.

KEYWORDS

exosomes, engineering production, preserve, separate, medical aesthetics

1 Introduction

Beauty is the eternal pursuit of all people. Wound repair (Prasai et al., 2022), anti-aging (Hu et al., 2019), inhibiting hyperpigmentation (Wang et al., 2021) and inhibiting hair loss (Yang G. et al., 2019) are the main demands for medical aesthetics. Medical aesthetics is a perfect combination of regenerative medicine and improvement of one's looks (Edmonds, 2013). It repairs, replaces, or regenerates human cells and tissues by using regenerative medicine technologies such as cells, natural or artificial scaffold materials and growth factors (Lee J. et al., 2020; Huang et al., 2021). At the same time, it is used in medical aesthetics to achieve the repair, remodeling and improvement of human appearance, shape and function, so as to achieve the harmony and improvement

of aesthetics, medicine, shape and function of the human body (Martínez-González et al., 2019; Xiong et al., 2021).

At present, in the field of medical aesthetics, anti-oxidants such as vitamin C (Odrobinska et al., 2020) and resveratrol (Ratz-Lyko and Arct, 2019), hyaluronic acid (Shekhter et al., 2019; Gazitaeva et al., 2021) and botulinum toxin (Naik, 2021) are often injected to remove wrinkles, reduce color spots and promote wound healing. However, there are still many challenges in aesthetics, for example, it is difficult to control the dose of anti-oxidant injection (Shekhter et al., 2019; Gazitaeva et al., 2021). In clinical practice, fat transplantation is often used in medical aesthetics, but it may lead abnormal local contour shape and to increase foreign body sensation (Yan et al., 2021). Subsequently, stem cell therapy was gradually applied to regenerative medicine due to its pluripotency, self-renewal and ability to promote the secretion of regenerative cytokines (Johari et al., 2019; Li W. et al., 2022), but stem cell therapy may induce the risk of tumorigenesis and malformation (Trounson and McDonald, 2015). Moreover, exosomes are nano vesicles secreted by cells, which belong to one kind of extracellular vesicles and play an important role in intercellular communication (Mehryab et al., 2020). Compared with drugs, plant/herbal extracts and bioactive molecules, exosomes have the advantages of low immunogenicity, good biocompatibility, targeting specificity and strong tissue permeability (Ha et al., 2016; Liang et al., 2021; Rao et al., 2021). They are often used as drug delivery vehicles and can play a role in medical aesthetics (Li M. et al., 2020). Here, we summarize the mechanism of action, administration methods, engineered production, separation, purification and presser-vation methods of exosomes in the field of medical aesthetics in recent years with a view to furthering the research and industrialization process of exosomes in the field of medical aesthetics.

2 Biological properties of exosomes

Exosomes have unique physicochemical properties, such as their ability to pass through tissue barriers, mononuclear phagocytic cell systems and certain targeting properties (Marcus and Leonard, 2013) when carrying drugs, and they are often used as therapeutic drug delivery carriers in medical aesthetics. For example, exosomes' lipid bilayer structure can prolong drug circulation time *in vivo*, escaping the elimination by mononuclear phagocytosis system, increasing the local drug concentration, and effectively controlling the drug release (Nam et al., 2020). Compared with traditional nanomaterials, exosomes have good biocompatibility, degradability, low toxicity, and low immunogenicity, so they are more suitable as drug delivery carriers (O'Brien et al., 2020).

2.1 Structure and composition of exosomes

The lipid bilayer membrane structure of exosomes protects the abundant proteins, nucleic acids, microRNAs (miRNAs), cholesterol and sphingomyelin in the membrane from being degraded (Pegtel and Gould, 2019; Li X. et al., 2020; Foo et al., 2021; Gurunathan et al., 2021) (Figure 1). A common cytoplasmic protein in exosomes is the RAB protein, a member of the guanylate triphosphatase (GTPases) family, which regulates the fusion of exosome membranes with recipient cells (An et al., 2021). In addition to RAB proteins, exosomes are rich in annexins that have exosomal membrane exchange and fusion effects (Tan et al., 2017; Keklikoglou et al., 2019). Exosomes membrane is rich in tetraspanins involved in exosomes transport family (CD63, CD81, and CD9) (Barranco et al., 2019) and heat shock protein family (HSP60, HSP70, and HSP90) (Regimbeau et al., 2021). Exosomes transport cargoes through the lipid bilayer membrane, and can deliver active ingredients (including proteins, nucleic acids, and lipids) from parent cells to recipient cells (Villarroya-Beltri et al., 2014; van Niel et al., 2018), and they can selectively enter target cells (Li M. et al., 2020) by homing to target tissues. Their active ingredients are delivered to the target cells' cytoplasm, thereby changing recipient cells' physiological state (Tkach and Thery, 2016).

2.2 Biogenesis

In the aspect of medical aesthetics, the research of exosomes biogenesis is crucial to the engineering transformation of exosomes and the production of larger quantities. A short overview of exosomes biogenesis can be stated as the inward movement of cytoplasmic membranes results in wrapping around extracellular entities and various membrane proteins forming the early sorting endosomes (ESEs), the ESEs fuses with other ESEs to form late sorting exosomes (LSEs). The LSEs develop into multivesicular bodies (MVBs). MVBs contain many intraluminal vesicles (ILVs) that are released into exosomes. After its formation, the MVBs can either be degraded by fusion with lysosomes or fuse with the plasma membrane with ILVs in it, the final exosomes (Borges et al., 2013; Matic et al., 2020; Ras-Carmona et al., 2021).

Because the biogenesis of exosomes is mainly divided into two ways: dependent on the transport of necessary endosome sorting complex (ESCRT) pathway and independent of ESCRT. Therefore, we herein discuss some ESCRT-dependent and ESCRT-independent mechanisms to increase exosome production (Figure 2). These following methods provide important ideas on engineering preparation of related exosomes in the field of later medical aesthetics and improve their production rate. ESCRT-dependent pathways: Genetic manipulation of gene generation pathways to overexpress

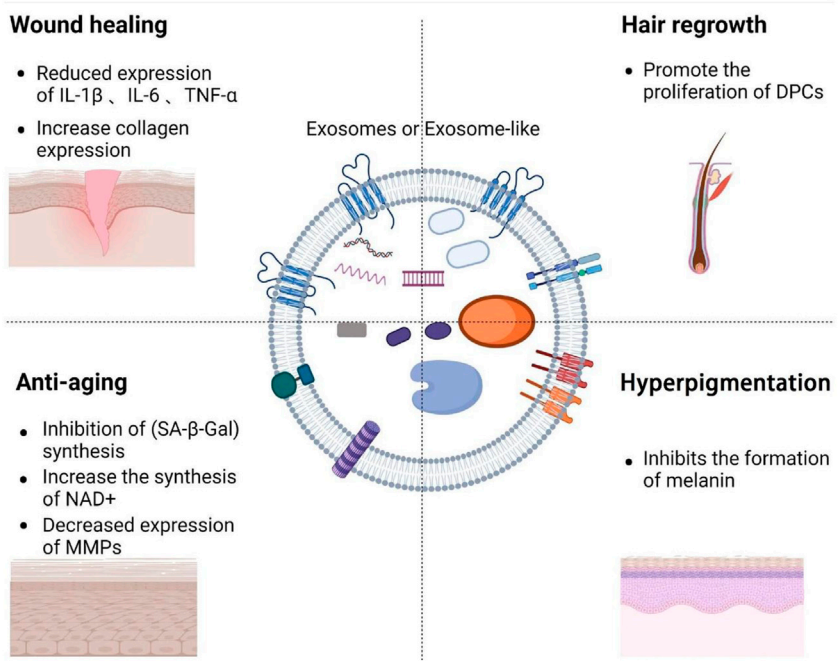

FIGURE 1
Overview of the composition of exosomes and the role of exosomes in medical aesthetics.

activating genes for exosome biogenesis and downregulating key regulatory genes involved in exosome transport, storage, secretion, or recycling. In most of these pathways, genes have a directly positive effect on exosome production (Jafari et al., 2020). For example, Wang et al. found that overexpression of HSP20 attenuated diabetes-induced cardiac damage. In addition, the elevation of HSP20 promoted the secretion of exosomes by directly interacting with Tsg101, a promoter of the exosome biogenesis pathway, and the production of exosomes was increased by 1.8-fold compared with the control group (Wang et al., 2016) (Table 1 for details).

ESCRT independent pathway involves steps such as cell culture manipulation *via* altering the media, use of specific drugs and harsh conditions to accelerate the production of exosomes. For example, Ban et al. isolated exosomes from cell culture media at pH 4, 7 and 11, and found that the concentration of exosomes protein and RNA in pH 4 medium was 5 times higher than that in pH 7 medium (Ban et al., 2015). However, one study showed that storage at pH 4 would reduce the concentration of exosomes and increased the absorption of exosomes by cells (Cheng et al., 2019), but at present many reports still use pH 7 buffer to preserve exosomes (Salimu et al., 2017; Petersen et al., 2018). Therefore, the influence of pH value on exosomes still needs to be further explored in the future. Together, we can broaden, change or improve the therapeutic capacity of exosomes by studying or engineering their structure, biogenesis, and properties (Table 2 for detailed data).

3 The regulatory mechanism of exosomes in medical aesthetics

At present, several studies have proved that miRNAs (Zhai et al., 2020), related active factors (Yoshida et al., 2019) in exosomes mediate wound repair (Li and Wu, 2022), anti-aging (Han et al., 2022), inhibiting hyperpigmentation (Liu et al., 2019), and inhibiting hair loss (Bae and Kim, 2021) and other related signaling pathways, regulating inflammatory factors interleukin-1β (IL-1β) (Li Z. Q. et al., 2020), matrix metalloproteinase 1 (MMP-1) (Liu et al., 2021), matrix metalloproteinase 3 (MMP-3) (Wang et al., 2017), collagen 1 (COL1A) and collagen 3 (COL3A) (Qi et al., 2020) expression of related genes, thus playing a role in medical aesthetics. For example, mesenchymal stem cell exosomes (MSCs-EXOs) encapsulated miR-223 regulate the polarization of macrophage M2 by targeting pknox1 and reducing the related inflammatory factor IL-10,TNF-α expression, thereby controlling the inflammatory response (He et al., 2019). Below we specifically explore exosomes' role and regulatory mechanism in wound repair, anti-aging, inhibiting hyperpigmentation, and inhibiting hair loss (Table 3 for details).

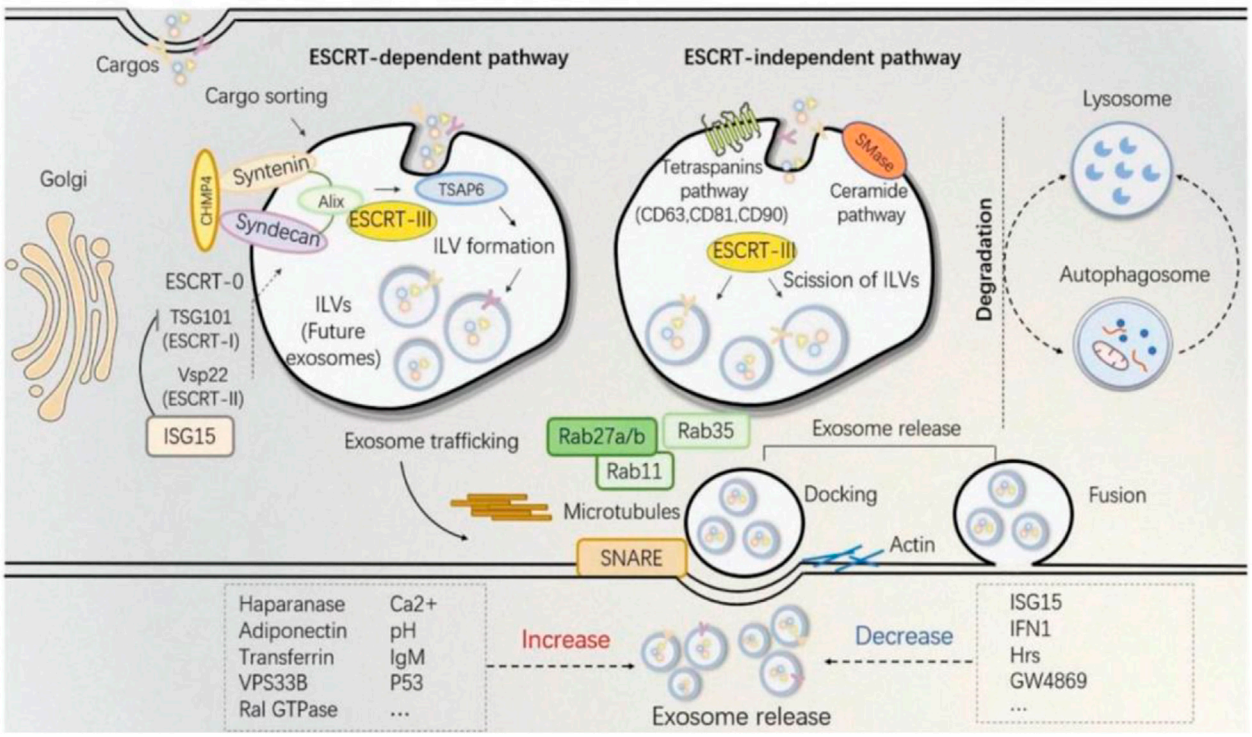

FIGURE 2
The established theory of exosomes biogenesis indicates different pathways distinguished as ESCRT-dependent and ESCRT-independent (Shi et al., 2021).

TABLE 1 Take parts as an example: Gene manipulation promotes exosome release.

Modification	Cell line	Outcome	Mechanism of action	References
Overexpression of HSP20	Cardiomyocyte	Increased generation of exosomes	Direct interaction of Hsp20 with Tsg101	Wang et al. (2016)
Overexpression of LMP1	HEK293	Separation EV increased 2–4 times	CD63-mediated exosomes LMP1 release	Hurwitz et al. (2017)
Overexpression of TSPAN6	HEK293	Exosome release increased by 60%	Interaction with syntenic	Guix et al. (2017)
Cortactin overexpression	SCC61	Exosome secretion increased 1.5–2 times	Interaction with Arp2/3 complex and F-actin	Sinha et al. (2016)
Overexpression of the tetraspanin CD9	Standard HEK-AAV producer	The production of exosomes increased 3.75 times	Not mentioned	Schiller et al. (2018)
Combined expression of STEAP3, syndecan-4	HEK293	The production of exosomes increased 15–40 times	Not mentioned	Kojima et al. (2018)
miR-126-3p-overexpressing combined with chitosan wound dressing	SMSCs	Increased exosome release	Not mentioned	Tao et al. (2017)

TABLE 2 Physical or chemical methods promote the release of exosomes.

Condition	Cell line	Outcome	Mechanism of action	References
Acidic pH	HEK293	Production of exosomes increased 5 times	Acidic pH could increase the stability of exosomes	Ban et al. (2015)
Oxidative stress	ARPE-19	The release of the exosomes containing the VEGR receptor was increased 4 times	RPE cells release higher amounts of exosomes when they are under oxidative stress	Atienzar-Aroca et al. (2016)
Glucose starvation	H9C2	Increased exosome release	Not mentioned	Garcia et al. (2015)
Hypoxia	MCF7, SKBR3, and MDA-MB-231	Exosome release increases 1.4-2 times	Activation of hypoxic signaling by dimethyloxalylglycine, elevation of miR-210	King et al. (2012)
Incubation with IgM	CLL	Secretion of exosomes increases by about 2 times, expression of miR-150 and miR-155 in exosomes	B cell receptor activation by a-immunoglobulin (Ig)M induces exosome secretion	Yeh et al. (2015)
Cyclophosphamide	LBC T cell	Exosomes increased by 61%	Not mentioned	Cocozza et al. (2019)
Recombinant WNT5A	Melanoma cells	Increased exosome release	Ca^{2+}-dependent release of exosomes containing IL-6, VEGF and MMP2 proteins	Ekström et al. (2014)
Extracellular Ca^{2+}	SJSA-1, Hs578T	The production of tumor microvesicles and the formation of tumor globules increased about 3 times	Not mentioned	Crawford et al. (2010)

TABLE 3 Role of exosomes in medical aesthetics.

Source	Mechanism of action	Function	References
Mesenchymal stem cell exosomes	miR-223 coated by MSCS-Exos regulates M2 polarization of macrophages by targeting Pknox1	Wound healing	He et al. (2019)
Keratinocyte-derived exosomes	Carrying miR-330-5p inhibits melanin production by targeting TYR	Hyperpigmentation	Liu et al. (2019)
Exosomes derived from human amniotic stem cells	miR-181a-5p and miR-199a, respectively, inhibit melanin production by reducing MITF expression	Hyperpigmentation	Wang et al. (2021)
Milk exosomes	miR-2478 directly targets rap1a *via* the Akt-GSK3 β pathway as a regulator of Melanin production, which reduces Melanin content in melanocytes and inhibits Melanin formation	Hyperpigmentation	Bae and Kim, (2021), Han et al. (2022)
Fat Mesenchymal stem cell exosomes	By regulating miR-22, Wnt/β-catenin signal pathway and TNF-α signal pathway, the proliferation and migration of DPCs and expression of ALP, versican and Alpha-smooth muscle actin (α-SMA) proteins were promoted	Control hair loss	Nilforoushzadeh et al. (2020), Li et al. (2022b)
Human-induced potent stem cell-derived exosomes	It decreased the activity of SA-β-Gal and inhibited the expression of P53 and P21 in HDFs	Anti-aging	Lee et al. (2020a)
Blood exosomes	NAMPT carried in exosomes increases the biosynthesis of NAD	Anti-aging	Yoshida et al. (2019)
Endothelial progenitor cells exosomes	Activation of ERK1/2 signal pathway enhances the ability of human endothelium to proliferate, migrate and become tube	Wound healing	Zhang et al. (2016b)
Exosomes derived from human umbilical Mesenchymal stem cell	Activation of ERK pathway significantly inhibits Melanin Synthesis during MITF degradation	Hyperpigmentation	Kim et al. (2015)
Exosomes derived from Dermal Papilla cells	Down-regulation of relevant hair follicle inhibitory signal proteins by genes involved in the key pathways of β-catenin, WNT, BMP2 and BMP4 promotes the proliferation of hair follicle stem cells	Control hair loss	Zhou et al. (2018), Zhang et al. (2022)
Exosomes derived from Human Mesenchymal stem cell	Activation of hair inductivity of DPCs, AKT phosphorylation, Bcl-2 in Dermal Papilla, and regulation of proliferation of DPCs	Control hair loss	Rajendran et al. (2017), Taghiabadi et al. (2020)
Fat Mesenchymal stem cell exosomes	Inhibit the over-expression of MMP-1, MMP-2, MMP-3 and MMP-9 induced by UV irradiation, and enhance the expression of Collagen type I and III and Elastin	Anti-aging	Choi et al. (2019)
Wheat exosomes	The gene expression related to wound healing was enhanced and gene modification coordinated the formation of blood vessel	Wound healing	Sahin et al. (2019)

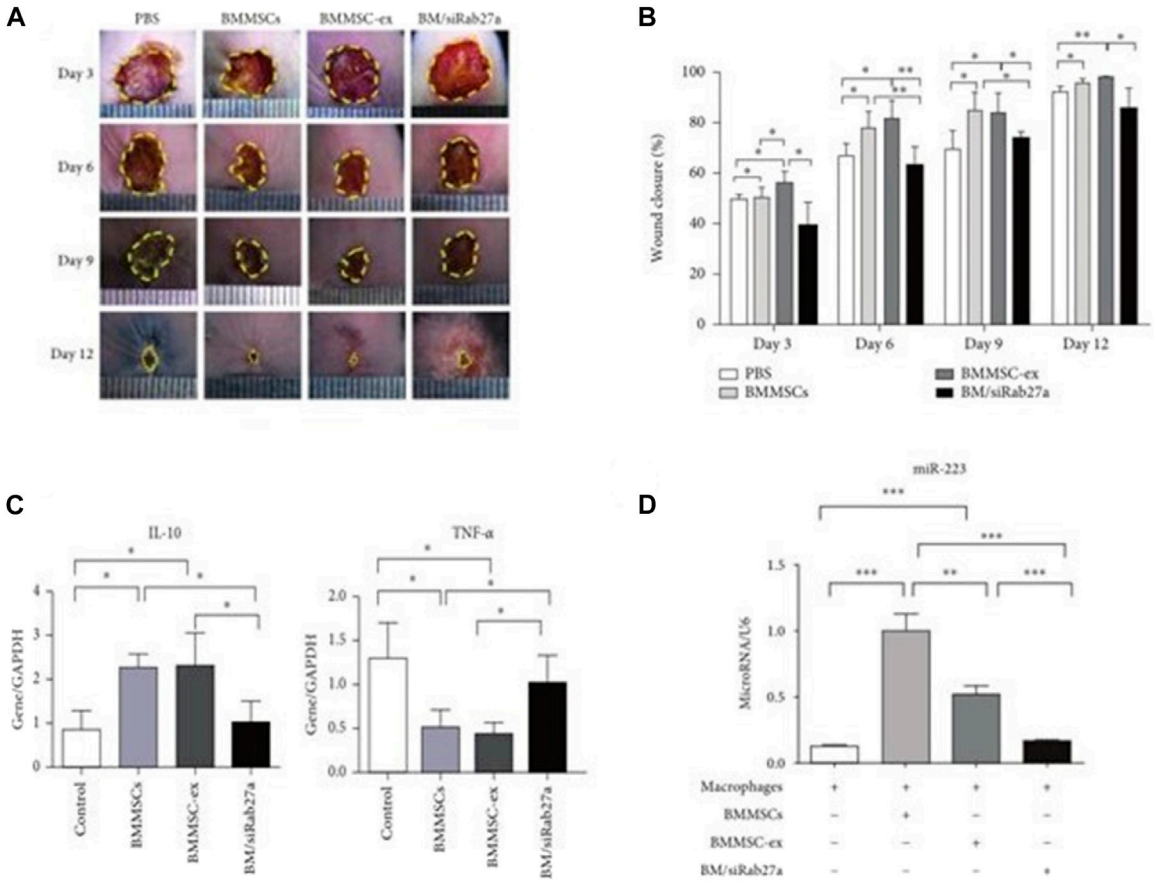

FIGURE 3
Utlization of MSCs derived exosomes for wound healing. **(A)** Depicts the light field photographs of cutaneous wounds post treatment with PBS, BMMSCs, BMMSC-ex, and BM/siRab27a. **(B)** Percentage of the wound closure on day 3–day 12 in reference to the day 0 wounds (n = 4). **(C)** qRT-PCR analysis of IL-10 and TNF-α in macrophages after being cocultured with BMMSC-, BMMSC/siRab27a-, or BMMSC-derived exosomes (n = 3). **(D)** qRT-PCR analysis of miR-223 in macrophages cocultured with BMMSCs, BMMSC-ex, and BM/siRab27a (He et al., 2019).

3.1 The role and mechanism of exosomes in wound repair

Skin wound repair is a complex dynamic physiological process (Jackson et al., 2012; Ogawa, 2017). Studies have shown that exosomes play a role in promoting blood coagulation (Zifkos et al., 2021), reducing inflammation (Chamberlain et al., 2021), accelerating tissue remodeling (Das et al., 2019), and inhibiting scar formation (An et al., 2021) by mediating wound repair-related signaling pathways such as MAPK (Gartz et al., 2018) and ERK (Geng et al., 2021). Exosomes can be vital in wound repair.

3.1.1 Procoagulant

At present, the mechanism and physiological relevance of exosomes for procoagulant effect in wound repair is still unclear. However, exosomes are rich in active components and have unique physicochemical properties, such as passing through tissue barriers, which are beneficial in reducing blood coagulation in human blood. Studies have found that salivary exosomes can activate TF and coagulation factor VII-mediated coagulation in human plasma, helping coagulation, thereby reducing the risk of blood loss and pathogens entering the blood, thus contributing to innate immunity and host defense (Berckmans et al., 2011).

3.1.2 Reduction of inflammation

Skin damage causes an inflammatory response, and there are also changes in the secretion of inflammatory factors (Marofi et al., 2021). Exosomes can reduce the time from wound repair inflammation to remodeling by reducing the expression of related inflammatory factors. Studies have shown that mesenchymal stem cell exosomes (MSCs-EXOs) encapsulated miR-223 regulate the macrophage M2 polarization by targeting pknox1 and reduces the related inflammatory factor IL-10, NF-α expression,

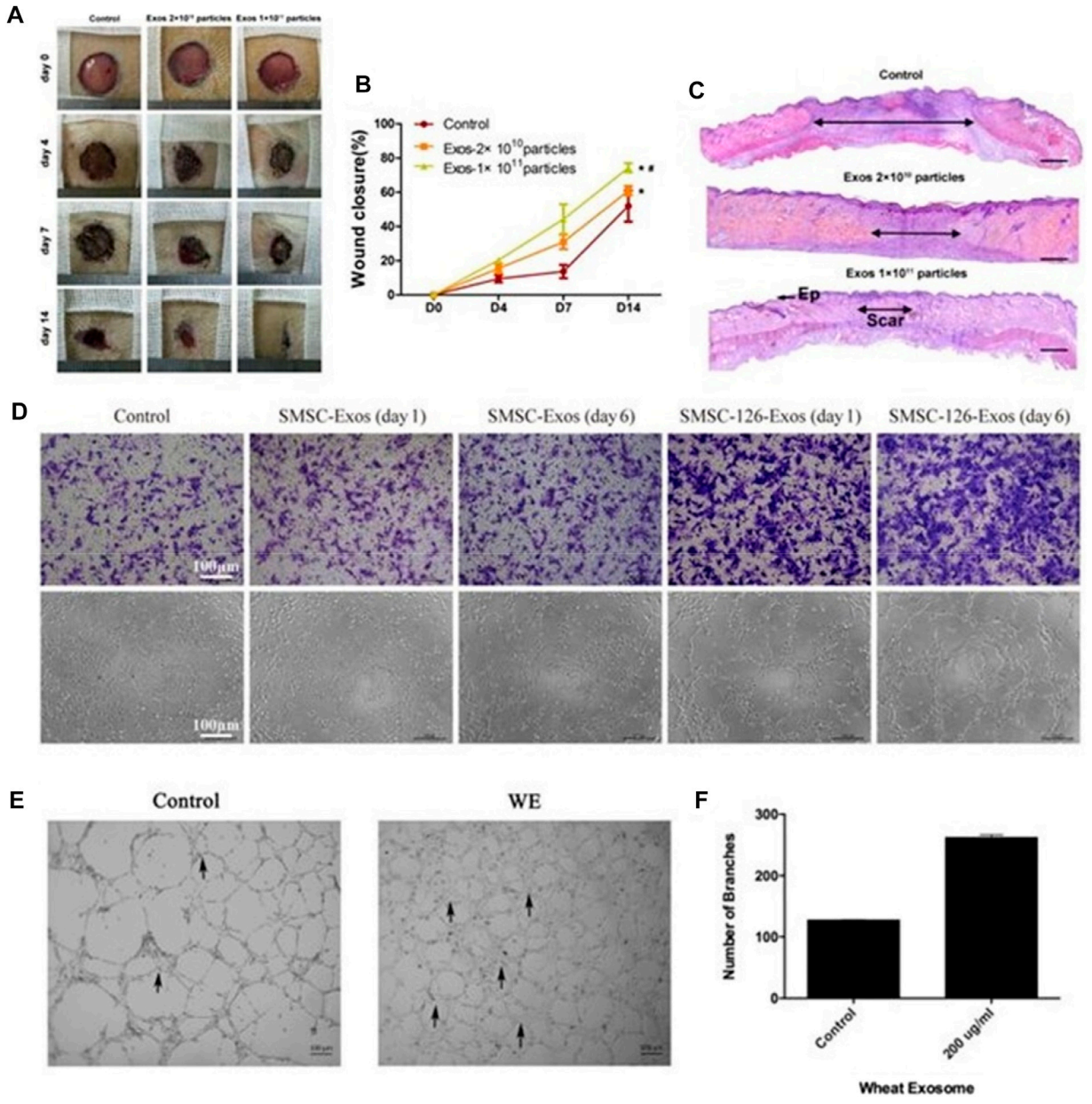

FIGURE 4
Exosomes can accelerate tissue remodeling. **(A)** General view of wounds treated with PBS or EPC exosomes of different concentrations on the 4th, 7th, and 14th days after trauma. **(B)** The rate of wound-closure on different days in wounds receiving different treatments. **(C)** On the 14th day after trauma, the wounds were treated with PBS or EPC exosomes of different concentrations and then stained with H&E (Zhang J. et al., 2016). **(D)** Representative photographs showing the effect of conditioned medium from days 0 to 6 on the transwell migration and tubule formation of HMEC-1 (Tao et al., 2017). **(E, F)** Control cells and 200 μg/ml wheat exosome (WE)–treated cells were incubated (37°C, 5% CO_2) in DMEM medium supplemented with 10% FBS. Average number of branches formed by both control and treated cells (Sahin et al., 2019).

thereby controlling the inflammatory response (He et al., 2019) (Figure 3). These results indicate that exosomes can accelerate the transition of wound repair from the inflammatory phase to the remodeling phase, thereby promoting wound repair.

3.1.3 Accelerated tissue remodeling

Exosomes accelerate tissue remodeling by activating endothelial cells and fibroblasts, promoting pro-angiogenesis and initiating extracellular matrix deposition (Zhang J. et al., 2015; Shabbir et al., 2015; Zhao et al., 2018; Ma et al., 2019; Xu

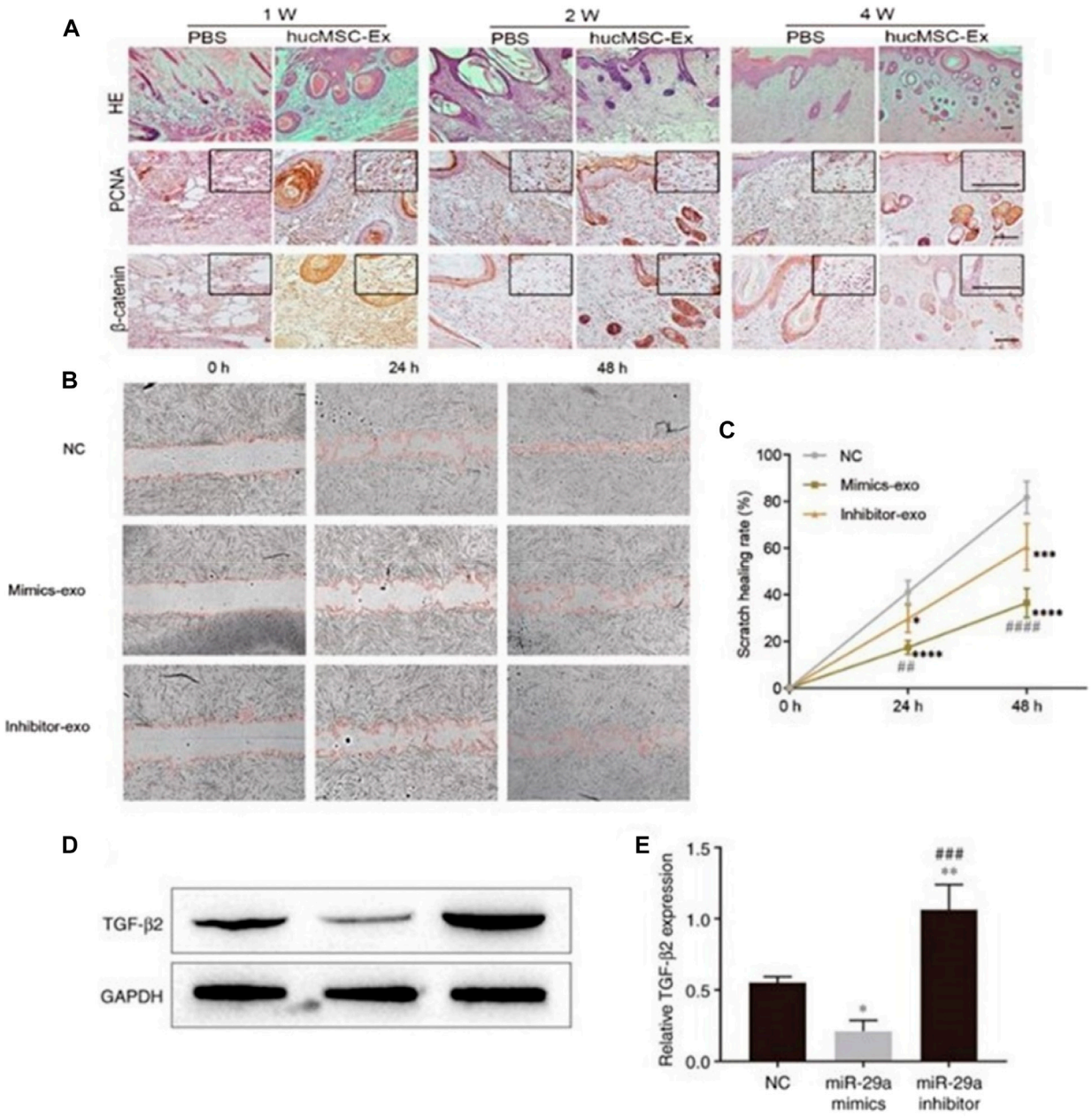

FIGURE 5
Exosomes inhibits the formation of scar by inhibiting the excessive proliferation of tissues. **(A)** Representative images of immunohistochemical staining of PCNA and β-catenin in each group. Scale bar = 100 μm (Zhang B. et al., 2016). **(B, C)** Effect of miR-29a-modified hADSCs-exo on the scratch healing of HSFBs. **(D, E)** Effect of miR-29a overexpression and knockdown on the expression level of TGF-β2 in HSFBs (Yuan et al., 2021).

et al., 2020). In mouse wound experiments, Zhang J. et al. (2016) injected exosomes derived from endothelial progenitor cells (EPCs) into a mouse abdomen and found that the EPCs-Exos can enhance human microvessels by activating the ERK1/2 signaling pathway. The ability of endothelial cells to proliferate, migrate and form tubes, thereby improving the rate of skin wound healing in diabetic rats, enhancing neovascularization, epidermal and collagen tissue regeneration, and then accelerating tissue remodeling (Figures 4A–C). It can be seen that synovial MSCs-EXOs can function in promoting the formation of blood vessels by activating protein kinase B (AKT) and extracellular signal-regulated kinase (ERK) pathways. Endothelial cells proliferate and promote fibroblast migration to the wound site and capillary angiogenesis through HSP70 and

HSP90, accelerating tissue remodeling (Tao et al., 2017) (Figure 4D).

Additionally, it has been discovered that wheat-derived nano-vesicles can encourage human endothelial cell proliferation and migration and to improve the synthesis of endothelial cell tubular structures. Moreover, increased expression of Collagen 1 contributes to tissue remodeling (Sahin et al., 2019) (Figures 4E, F). The study of wheat-derived nano-vesicles provides a new solution for wound repair and lays a foundation for future research on wound repair mechanisms and the development of wound repair-related drugs.

3.1.4 Inhibition of scarring

Exosomes inhibit scarring by inhibiting tissue hyperproliferation. The study found that human mesenchymal stem cell-derived exosomes (hucMSC-Exos) promoted wound repair by activating the Hippo signaling pathway in a rat skin burn model, inhibiting excessive tissue proliferation and scar formation (Zhang B. et al., 2016) (Figure 5A). HucMSC-Exos also inhibits scarring by inhibiting the activation of TGF-β/SMAD2 pathway in fibroblasts by transporting miR-29a (Chen et al., 2019; Yuan et al., 2021) (Figures 5B–E). All of the above proves that exosomes are important medium for information transfer between cells and cytokines, which can be used as a new hope for cell-free therapy for non-invasive wound repair.

3.2 The role and mechanism of exosomes in anti-aging

The essence of human aging involves the aging of cells. Cell aging is due to the accumulation of damage that induces the activation of cell cycle inhibition pathways. Cells permanently exit the cell proliferation cycle, and cellular aging has permanent cell cycle arrest, reduction of NAD^+, apoptosis resistance, aging-associated inflammatory cytokine secretion, and altered metabolic and epigenetic signatures (Kirkland and Tchkonia, 2017). Exosomes often contain biologically active proteins and genetic information, all of which play an important role in delaying cell aging (Liao et al., 2021), such as inhibiting the synthesis of related aging factor-β-galactosidase (SA-β-Gal) (Kim et al., 2021), and inhibiting skin photoaging (Gao et al., 2021).

3.2.1 Exosomes delay cell senescence

Exosomes can delay cell senescence by inhibiting the synthesis of related senescence factor-β-galactosidase (SA-β-Gal) (Kim et al., 2021) and promoting the synthesis of nicotinamide adenine dinucleotide (NAD^+) (McReynolds et al., 2021). Studies have shown that human-induced potent stem cell-derived exosomes (iPSC-EXO) can delay fibroblast senescence by inhibiting the synthesis of senescence-related factor-β-galactosidase (SA-β-Gal). Lee et al. (2020a) fabricated cell-engineered nanovesicles (CENVs) by continuously extruding iPSCs through membrane filters. They discovered that IPSC-CENVs had characteristics with IPSC-EXOs, and iPSC-CNEVs greatly diminished fibroblasts (HDFs), senescence-associated-galactosidase (SA-Gal), expression of p53 and p21, and SA-Gal activity, thus delaying cellular senescence (Figures 6A–C). These results suggest that the iPSC-CENVs can serve as an excellent surrogate for iPSC-EXO, and as well as a source of drugs for treating skin aging.

In addition, multiple studies have confirmed that NAD^+ is a major player in cellular aging. Studies have shown that NAD^+ levels in the circulatory system are decreased significantly with age in mice and humans during aging (Clement et al., 2019; McReynolds et al., 2020). Aging and muscle contraction enhance NAD^+ utilization, and under normal physiological conditions, NAD^+ depletion occurs primarily through salvage pathways catalyzed by nicotinamide phosphoribosyl transferase (NAMPT). Studies by Yoshida et al. (2019) have shown that blood transfusion into neonatal mice can prolong the lifespan and improve the health status of aging mice, mainly because NAMPT carried in blood exosomes increases the biosynthesis of NAD^+, thereby prolonging the lifespan of mice (Figures 6D–F). These results indicate that NAMPT carried by blood exosomes has the effect of delaying cell senescence, laying a foundation for the development of later anti-aging drugs.

3.2.2 Exosomes inhibit skin photoaging

Skin photoaging is the most direct manifestation of human aging, mainly due to the abnormal up-regulation of matrix metalloproteinases (MMPs) after UV exposure, resulting in obvious skin wrinkles (Mazini et al., 2021). The researchers used a needle-free syringe to inject human dermal fibroblasts (HDFs) exosomes cultured in three-dimensional spheroids (3D-HDF-XOs) and monolayers (2D-HDF-XOs) *in vitro* and in a nude mouse model for photoaging, respectively. They found that the 3D-HDF-XOs cultured exosomes caused a significant decrease in MMP-1 expression and increased type I procollagen expression, mainly by down-regulating tumor necrosis factor-α (TNF-α) and up-regulating transforming growth factor-β (TGF-β) (Figure 7A). These findings imply that exosomes produced from 3D grown HDF spheroids have anti-aging capabilities and can also be used to treat and prevent the aging process of skin (Hu et al., 2019) (Figure 7B). In addition, human induced pluripotent stem cell exosomes (iPSCs-Exo) can inhibit UVB radiation-induced HDFs damage and matrix metalloproteinase 1/3 (MMP-1/3) overexpression. Increased expression level of collagen type I in photoaged HDFs was investigated (Oh et al., 2018) (Figure 7C). Exosomes (EXO) from human adipose-derived stem cells (HASCs) were also studied for their impact on photodamaged human dermal fibroblasts (HDFs), and it was discovered that adipose-derived mesenchymal stem cell exosomes (ADSCs-Exo) significantly

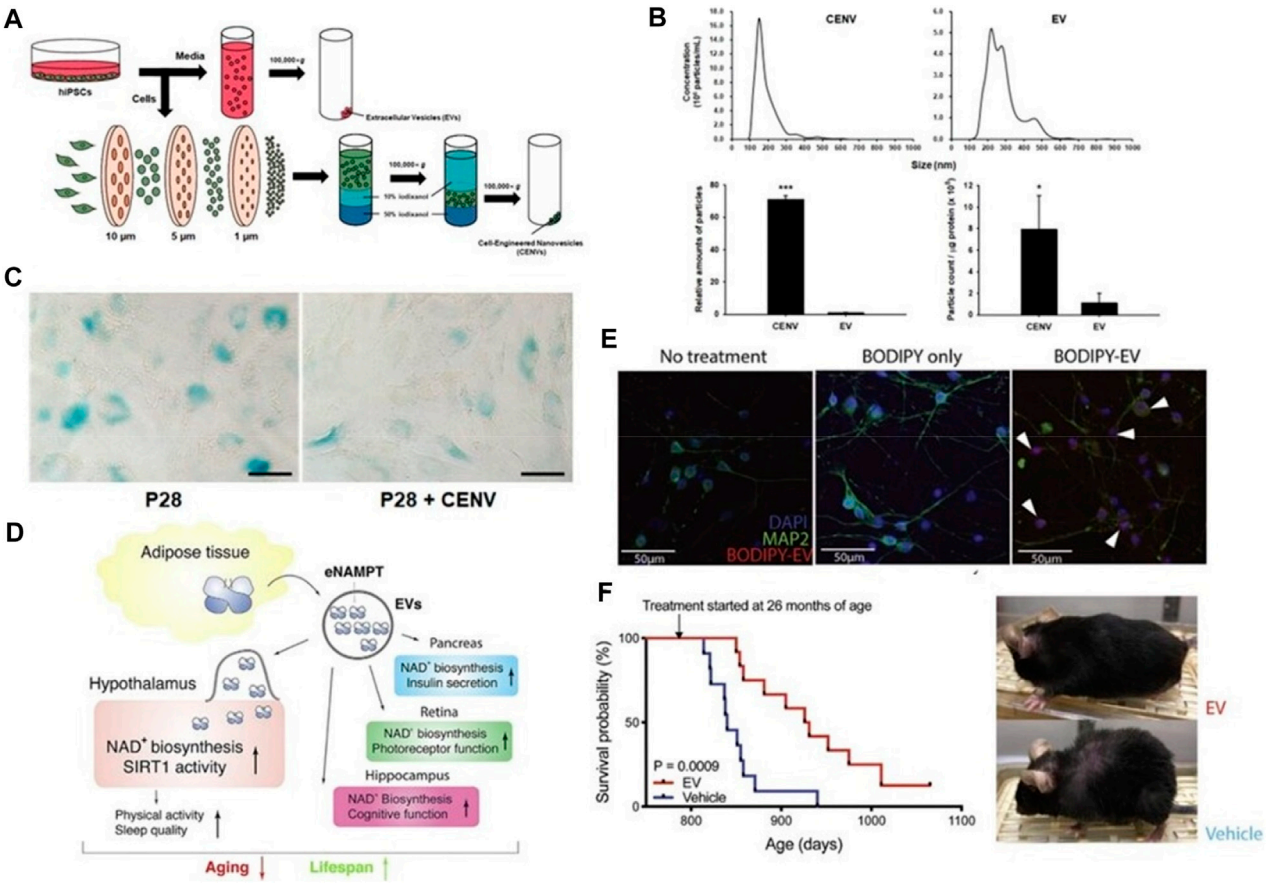

FIGURE 6
Exosomes delay cell senescence. **(A)** Schematic of the preparation of extracellular vesicles (EVs), and cell-engineered nanovesicles (CENVs) from human induced pluripotent stem cells (iPSCs). **(B, C)** Comparison of human iPSC-derived CENV and EV (Lee H. et al., 2020). **(D)** Mechanism Diagram of eNAMPT Containing Extracellular Vesicles Delaying Cell Aging. **(E)** Fluorescent images of primary hypothalamic neurons following the incubation with BODIPY-labeled EVs. **(F)** Kaplan-Meier curves and representative images of aged female mice injected with vehicle or EVs isolated from 4- to 12-month-old mice (n = 11–12). The mouse images were taken after 3 months of treatment (Yoshida et al., 2019).

inhibited UV-irradiation-induced overexpression of MMP-1, 2, 3, and 9, and enhanced I (from 119.6% ± 35.8% to 262.6% ± 54.1%), type III (from 61.2% ± 4.5% to 80.8% ± 2.7%) collagen and elastin expression (Choi et al., 2019) (Figures 7D, E).

These above results revealed that exosomes have the potential to be combined with cosmetics or drugs. However, the transformational application of exosome anti-aging effect is still in its infancy, and there is no clear clinical report, but its huge application potential deserves attention.

3.3 The role and mechanism for exosomes in hyperpigmentation

Asian women have long had a penchant for inhibiting hyperpigmentation (Hakozaki et al., 2002; Boo, 2022). Since skin color is mainly determined by the content and distribution of skin pigments, melanin is the most important determinant. Therefore, inhibiting melanin formation is one of the main ways to reduce skin pigmentation (Hwang and Hong, 2017). Human skin, mucous membranes, the retina, the pia mater, the gallbladder and ovary are all rich in melanin. Exosomes may have the effect of reducing hyperpigmentation by inhibiting the production of melanin (Lo Cicero et al., 2015).

Studies have shown that miR-181a-5p and miR-199a in human amniotic stem cell-derived exosomes promote melanosome degradation in skin hyperpigmentation by inhibiting melanogenesis by reducing MITF expression, respectively. Exosomes derived from human umbilical cord mesenchymal stem cells are activated *via* the ERK pathway (Figures 8A–C), which significantly inhibits melanin synthesis during the degradation of MITF gene (Kim et al., 2015) (Figures 8D–F). In addition, miR-2478 in milk exosomes directly targets rap1a *via* the Akt-GSK3β pathway as a regulator of melanin

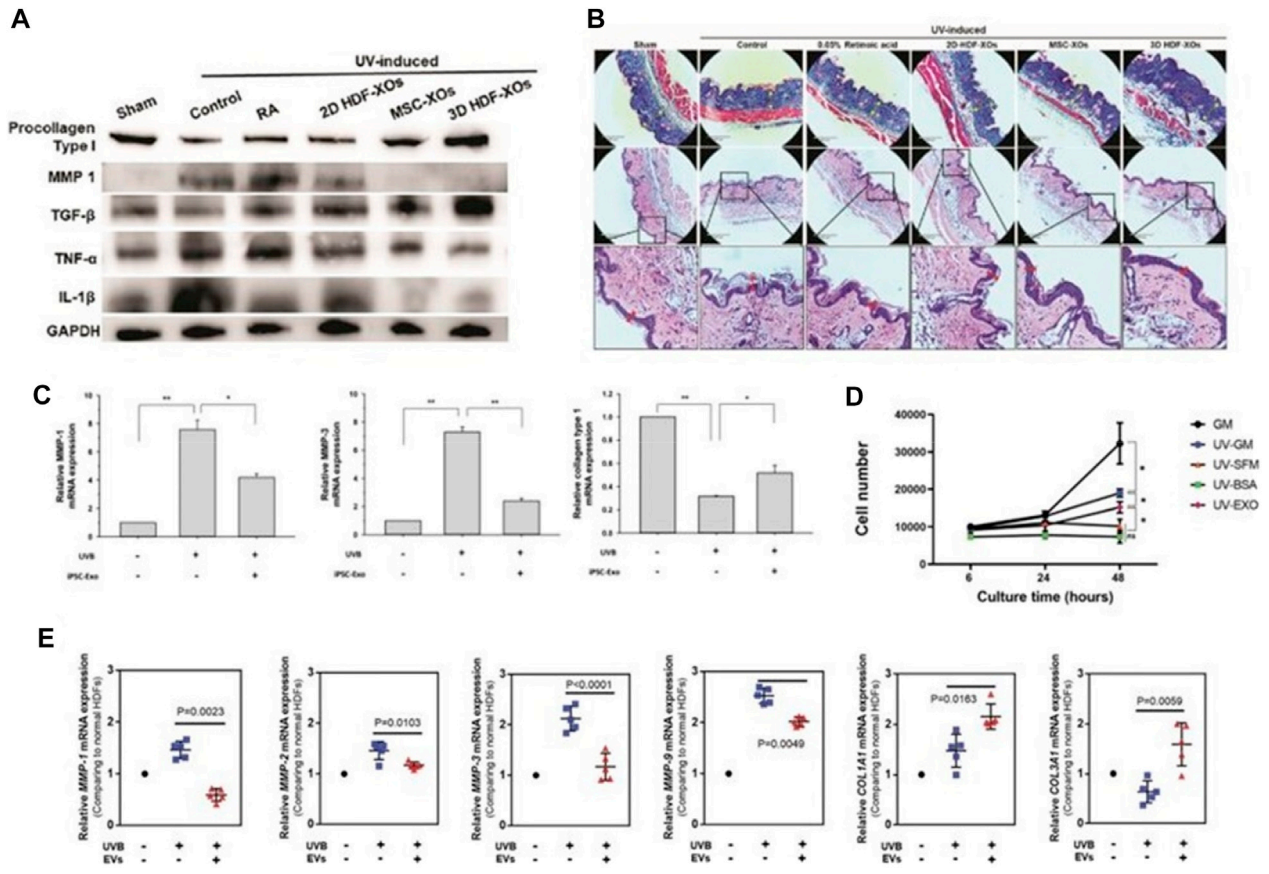

FIGURE 7
The mechanism for exosome regulation of MMPs. **(A)** Western blot of dorsal skin of different groups. **(B)** Masson's Trichrome staining and Corresponding H & E staining. scale bar: 290 μm (Hu et al., 2019). **(C)** The mRNA expression levels of MMP-1, MMP-3 and collagen type I were quantified by quantitative real-time RT-PCR (Oh et al., 2018). **(D, E)** The proliferation of HDFs in different groups was measured by CCK-8 method. Gene expression in HDFs with or without HASC-derived EVs treatment after UV irradiation (Choi et al., 2019).

production, reducing melanin content in melanocytes and thereby inhibiting the formation of melanin (Bae and Kim, 2021; Han et al., 2022) (Figures 8G, H). These results indicate that the exosomes can be used as an effective cosmetic ingredient to inhibit hyperpigmentation, and have great application potential in regulating skin pigment. The huge application potential of exosomes is expected to boost for the commercialization of exosomes based cosmeceutical products in the future.

3.4 The role and mechanism of exosomes in inhibiting hair loss

Hair loss is affected by various internal and external factors such as genetics, endocrine function (thyroid organ disease, changes in sex hormone levels), immune system diseases, malnutrition, drugs, mental state and natural aging. The above factors can affect the hair cycle (HC), reducing the activity and repair ability of hair follicle stem cells (Gentile and Garcovich, 2019). Dermal papilla cells (DPCs) are located in the hair bulb at the bottom of the hair follicle, surrounded by the dermal sheath and hair matrix cells, and are considered a unique type of mesenchymal stem cells. DPCs serve as signaling centers in the hair follicle (HF) and play an important role in regulating hair growth, formation, and circulation. Exosomes can inhibit hair loss by inducing HF regeneration by promoting the proliferation of DPCs (Kost et al., 2022).

Studies have shown that the DPCs-Exos affect the hair follicle signaling pathway through the miRNAs it carries. By acting on key pathway genes such as β-catenin, Wnt, BMP2, BMP4, and downregulating related hair follicle inhibitory signaling proteins, the DPCs-Exos promotes hair follicle stem cell proliferation, hair follicle regeneration, and hair follicle formation. The telogen phase transitions to the growth phase (Zhou et al., 2018; Zhang et al., 2022). ADSC-Exos significantly promoted the proliferation and migration of DPCs by regulating miR-22, Wnt/β-catenin signaling pathway, and TNF-α signaling pathway, and promoting

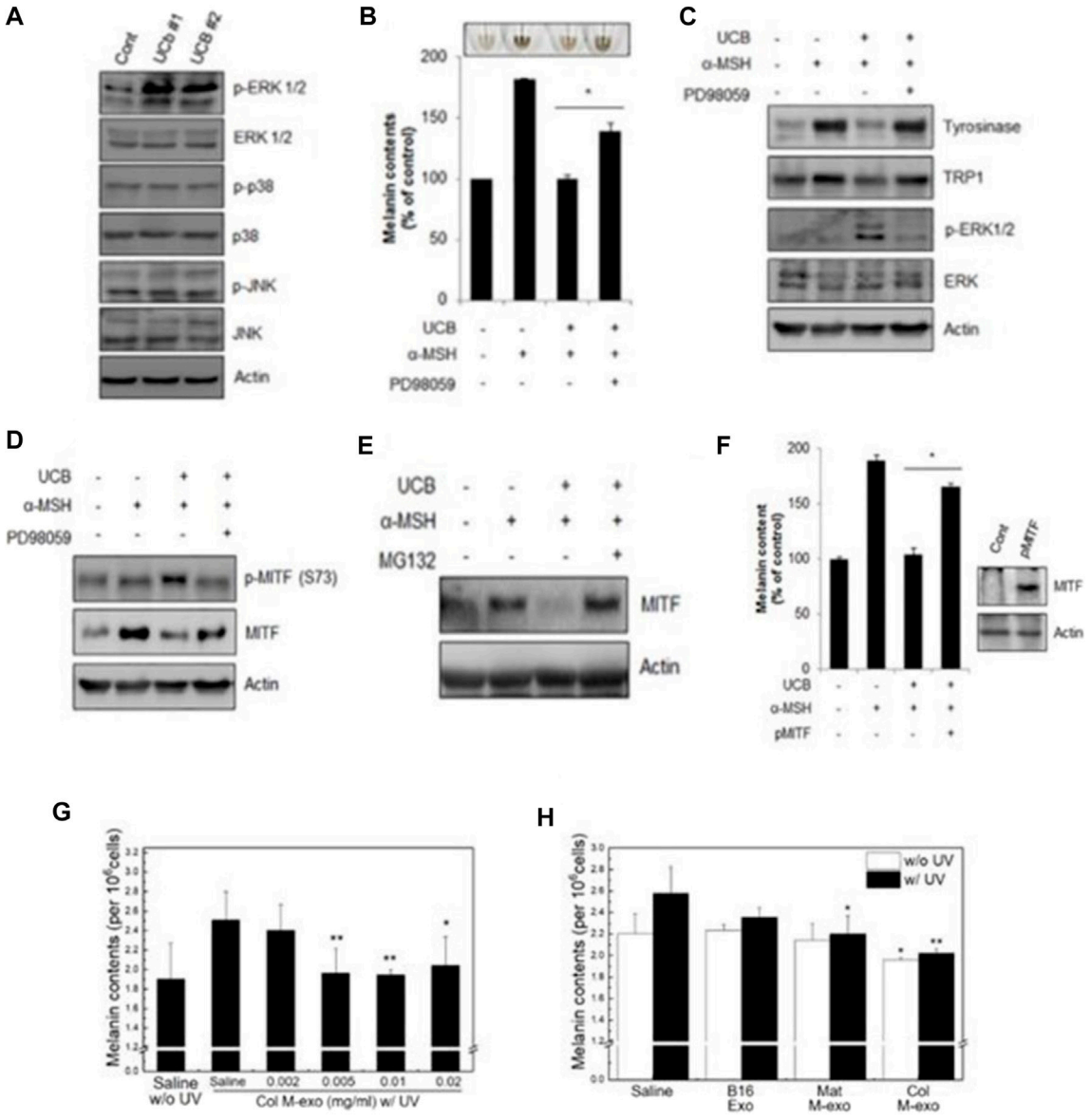

FIGURE 8
Exosomes inhibit melanin production. **(A–C)** Western blot was used to analyze the expression of related proteins. Melanin content in cells under different conditions.Western blot analysis of protein expression levels of tyrosinase, TRP1, p-ERK1/2 and ERK1/2 in cells. **(D–F)** Western blot analysis was used to detect the level of MITF under different conditions (Kim et al., 2015). **(G, H)** Melanin content of UV irradiated cells under different conditions (Han et al., 2022).

the expression of ALP, versican, and α-SMA proteins while maintaining their hair-inducibility, finally having a positive effect on hair follicle regeneration (Nilforoushzadeh et al., 2020). Human mesenchymal stem cell-derived exosomes activate the hair-inducibility of DPCs by stimulating Akt phosphorylation, and increasing Bcl-2 in the dermal papilla, thereby regulating the proliferation of DPCs and transforming hair follicles from dormant to anagen phase (Rajendran et al., 2017; Taghiabadi et al., 2020) (Figures 9A, B).

Recently, Kou et al. proposed for the first time that apoEVs play an important role in maintaining stem cell homeostasis *in vivo*. They found that exogenous apoEVs are metabolized through skin and hair follicles in a wave-like manner. At the same time, exogenous apoEVs can activate skin and hair follicle mesenchymal stem cells through the Wnt/β-catenin pathway to promote hair regeneration (Ma et al., 2023) (Figures 9C–F). All of the above implies that the exosomes may be a promising cell-free

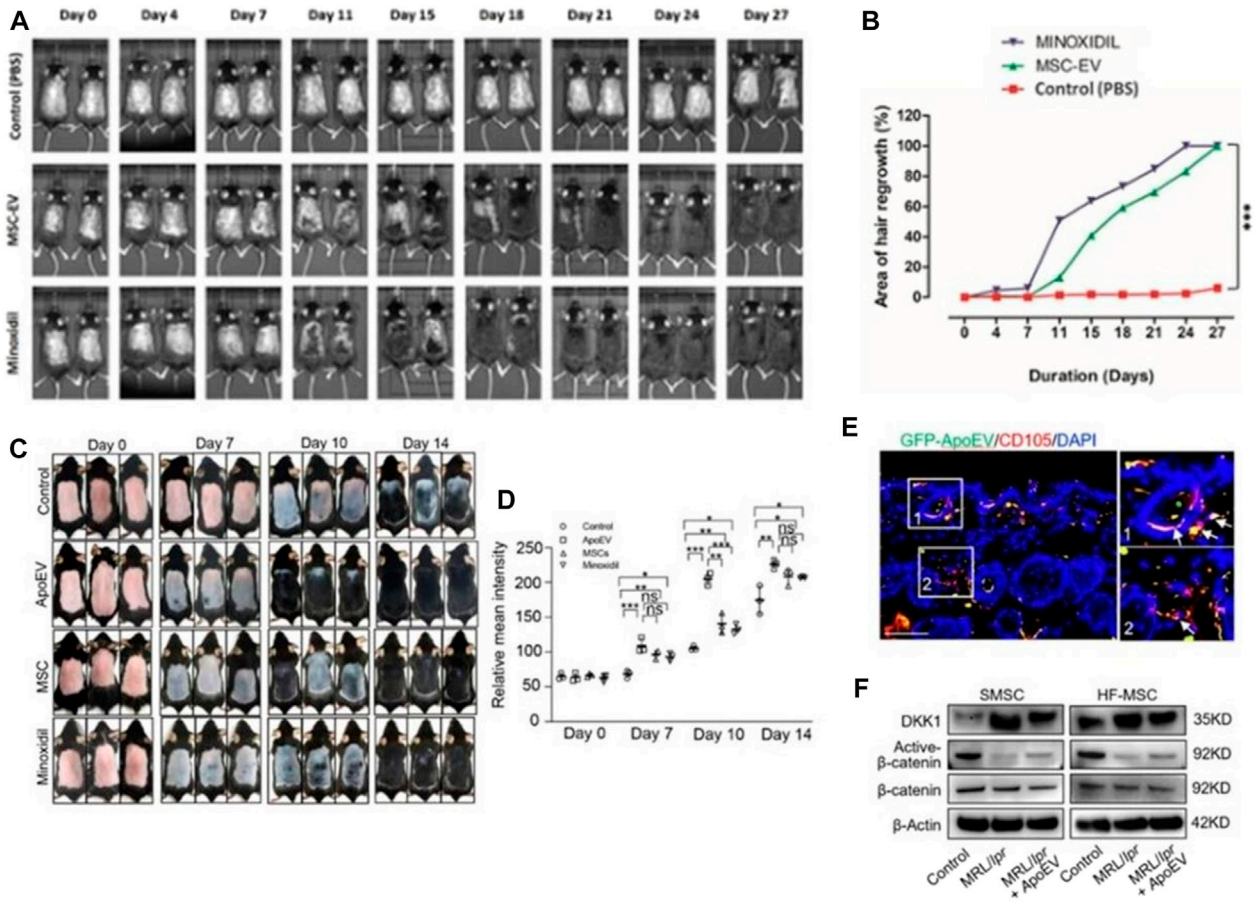

FIGURE 9
Hair regeneration induced by exosomes. **(A, B)** Take skin photos on days 0, 4, 11, 15, 18, 21, 24, and 28. Then, the hair regeneration area quantized by imageJ software is expressed in percentage (Rajendran et al., 2017). **(C, D)** Representative photos of mice showing skin color darkness and hair regrowth at 0, 7, 10 and 14 days post-injection. The level of pigmentation was quantified by the intensity of the darkness of the back skin in the same area. **(E)** Immunofluore-scent images show that GFP-ApoEV (green) were engulfed by skin MSCs (SMSCs) (1 and 2), as indicated by co-staining with CD105 at 7 days post-injection. **(F)** Western blotting shows Wnt/β-catenin signaling is activated and DKK1 expression is decreased in SMSCs and hair follicle MSCs (HF-MSCs) from MRL/lpr mice after apoEVs injection (Ma et al., 2023).

therapeutic strategy for immune-mediated hair loss (Li Y. et al., 2022). However, exosome-based treatments for hair loss are still in their infancy, and more robust clinical studies are needed to better evaluate their mechanisms of action, efficacy, safety, benefits, and limitations (Egger et al., 2020).

3.5 Clinical trials

At present, in the aspect of medical aesthetics, only 3 studies are based on the clinical trial registration related to wound healing of exosomes (17 November 2022) (Li et al., 2021a). The clinical trials of exosomes in anti-aging, inhibition of hyperpigmentation and hair loss have not yet been reported. Previous studies have found that exosomes from serum can accelerate the healing of skin wounds in BALB/c mice (Li et al., 2021b; Lee et al., 2021). Therefore, a trial is currently under way, in which autologous exosomes from plasma will be applied to the ulcer of the participants every day for 28 days. Then evaluate the healing of the skin wound according to the length, width and depth of the wound (ClinicalTrials.gov: NCT02565264). In addition, there is also a single arm pilot study. All patients were recruited on an outpatient basis. Debridement and photography were performed on the patient's wound surface, and the wound area was measured. Then provide fat tissue exocrine dressing for patients in the intervention group. Exosomes were mixed with sterile hydrogel and applied directly to the wound surface, and the wound was covered with inert protective dressing. Patients who meet the inclusion and exclusion criteria at the end of the induction period will receive treatment twice a week for 4 weeks or until recovery (ClinicalTrials.gov: NCT05475418). To conduct a pilot clinical

trial in diabetes patients with chronic skin ulcer (CCU), and evaluate the effect of the exosomes of mesenchymal stem cells (MSC) on the healing and regeneration ability of personalized nutritional supplementation (ClinicalTrials.gov: NCT05243368). Furthermore, there are currently five registered clinical trials based on plant exosome-like nanovesicles, including those from grape, lemon, aloe and ginger (ClinicalTrials.gov: NCT01668849; NCT04698447; NCT03493984; NCT01294072; NCT04879810), which are respectively studies on reducing the incidence rate of oral mucositis, cardiovascular risk factors, polycystic ovary syndrome, colon cancer and inflammatory bowel disease. Although there is no clinical trial related to medical aesthetics for these plant exosome-like nanovesicles, it has been reported that the plant exosome-like nanovesicles of grapefruit (Savcı et al., 2021), lemon (Manconi et al., 2016) and aloe (Zeng et al., 2021; Kim and Park, 2022) have potential application value in wound healing and anti-aging, and are expected to conduct clinical trials in the future (Leggio et al., 2020; Dad et al., 2021).

4 Administration of exosomes in medical aesthetics

At present, exosomes are mainly used for medical aesthetics research through topical application and local injection (Yari et al., 2022). Topical application (Li L. et al., 2020) can be directly applied locally to the skin or by means of microneedles (Zhang K. et al., 2020) or transdermal drug delivery (Shang et al., 2022) to increase the transdermal effect of exosomes. Local injection works mainly through subcutaneous injection (Cao et al., 2021). At present, there is no unified standard to judge which exosomes administration mode has the most obvious effect. The effect of exosomes from different sources may vary depending on the mode of administration. Therefore, which management mode to adopt is still a question and the focus of our discussion.

4.1 Topical application

Topical application can be applied to different areas according to different effects, and the dosage can be freely controlled. Xu et al. (2020) constructed a mouse skin injury model and found that both exosomes and miRNA-221-3p can promote wound healing in normal and diabetic mice by smearing endothelial progenitor cell exosomes or miRNA-221-3p. However, transdermal drug delivery can directly deliver active ingredients under the epidermis, opening the stratum corneum barrier, greatly improving the skin's absorption rate of active substances, and reducing the loss of active ingredients. A detachable microneedle device-mediated drug delivery system for extended distribution of hair follicle stem cell activators was designed by Yang et al. (2017). The combination of this microneedle technology with small molecule medication UK5099 and exosomes produced from mesenchymal stem cells (MSCs) increased treatment efficacy at a lower dose and encouraged pigmentation and hair regrowth within six days through two rounds of treatment, according to their findings. In addition, this microneedle-based transdermal delivery technique demonstrated greater efficacy compared to topical UK5099 distribution and subcutaneous exosome injection. Additionally, human amniotic mesenchymal stem cells (hAMSCs) exosomes and hair nanoparticles were coupled with soluble microneedle patches (MNs) (HNP). They discovered that HNP-modified microneedle patches (HMNs) can efficiently permeate the stratum corneum and help deliver hAMSC exosomes into the dermis to stimulate proliferation of hair follicle stem cells and promote hair regeneration by causing the hair follicle to transition from telogen to anagen (Hong et al., 2021). Compared to direct administration, these combination transdermal treatments are more effective and safer (Shang et al., 2022). Some regenerative medicine companies, such as BENEV and Kimera Labs, have developed health care products involving exosomes for skin damage, anti-aging, pigment regulation and inhibition of hair loss. These products have been approved by the US Food and Drug Administration (FDA) (Peña-Juárez et al., 2022).

4.2 Local injection

Local injection has advantages such as less adverse reactions and simple operation. Here we mainly discuss subcutaneous injection. Han et al. (2021) *in vitro* studies on mice revealed that subcutaneous injection of DF-Exo markedly expedited the healing of diabetic skin lesions by boosting re-epithelialization, collagen deposition, skin cell proliferation, and angiogenesis. In addition, according to Shin et al., subcutaneous injection of adipose-derived mesenchymal stem cell exosomes significantly decreased trans epidermal water loss, increased stratum corneum (SC) hydration, and significantly decreased the expression of inflammatory cytokines like IL-4, etc., promoting wound healing (Shin et al., 2020). In addition, exosomes are often incorporated into hydrogels to function. Some researchers assembled MSC-derived exosomes in chitosan/silk hydrogels (Shiekh et al., 2020) and self-healing antibacterial polypeptide hydrogels (Wang C. et al., 2019), and found that exosome-assembled hydrogels can promote wound healing in diabetic patients and can also be placed directly in or near the target area, the dose of exosomes is more concentrated and more targeted (Riau et al., 2019). It has been shown to have the ability to rapidly heal wounds and is more effective than single exosome therapy, and reduces scarring (Wang C. et al., 2019; Wang M. et al., 2019). These results suggest that the exosomes can potentially be used as therapeutic agents to repair skin

damage. However, there are still many problems, such as standardization of research methods, clarification of the mechanism of action, and validity of application (Mehryab et al., 2020). There are a few clinical studies on exosomes in medical aesthetics. At present, it is still in the primary stage of research (Jing et al., 2018; Hade et al., 2021) and has not been approved by the US Food and Drug Administration (FDA).

The above results indicate that exosomes can play a role in the field of medical aesthetics through different delivery methods. However, in terms of medical aesthetics, we recommend transdermal drug delivery. Compared to the direct application of exosomes, transdermal drug delivery can penetrate the cuticle, greatly improve the skin's absorption rate of effective substances, and reduce the effective loss of ingredients. Compared to the injection of exosomes, transdermal drug delivery is more convenient, has fewer side effects, and is safer. It has huge application potential in the future medical beauty industry (Yang et al., 2021).

5 Exosome engineering production and preservation

The application of exosomes in medical aesthetics is inseparable from their large-scale production and preservation. The unique heterogeneity and other characteristics of exosomes hinder their engineering production. Secondly, different separation, purification and preservation methods have a greater impact on the yield and active components of exosomes. Therefore, it is crucial to adopt appropriate engineered production, separation and purification techniques and preservation methods of exosomes. Next, we specifically discuss the engineering production, separation, purification technology, and preservation methods of exosomes in recent years, laying the foundation for their application in medical aesthetics in the later period.

5.1 Exosome engineering production technology

At present, many companies and researchers are working hard to develop engineered exosomes for medical aesthetics (Gimona et al., 2017). To improve cell-to-cell communication, Cha et al. (2018) established the usage of a polyethylene glycol (PEG) hydrogel for cell aggregation and MSC spheroid formation. In addition, they employed a programmable dynamic culture method in the planned microwells, which increased EV production 100 times more than 2D cell culture. Cao et al. (2020) utilized a three-dimensional (3D) culture system of hollow fiber bioreactors to produce MSC-exos and evaluated the therapeutic effect of 3D-exosomes (3D-exos) on acute kidney injury (AKI). They discovered that compared to 2D culture, 3D culture did not significantly change the surface indicators of MSCs or their morphology, size, or exosome labelling. Tubular epithelial cells (TECs) absorbed the 3D-exos more effectively, leading to better anti-inflammatory efficacy and increased TEC viability *in vitro*. The total exosome yield was also raised by 19.4 times in the 3D culture system, and the hollow fiber technology provides benefits, including exosome concentration, immunity to serum exosome contamination, and a reduction in other contaminants. Based on the advantages of 3D culture technology, Enze Kangtai Company has successfully built an engineered exosome research and transformation platform with independent intellectual property rights - ModiExo™. Based on mature site-directed insertion technology and backbone plasmids, the ModiExo™ platform can rapidly construct exosome scaffold protein-engineered cell lines and combine with 3D microcarrier culture technology to efficiently and stably mass-produce projects targeting specific organs or loading specific proteins/RNAs exosomes. The establishment of this platform has promoted the rapid development of exosome clinical transformation.

In addition, by using MYC gene to genetically modify human embryonic stem cell mesenchymal stem cells, we have created immortal cell lines that can permanently produce exosomes without batch renewal. However, this approach has not been well received by other researchers, and a biological function investigation alone cannot vouch that the exosomes' characteristics are unaffected by cell transformation. Therefore, additional research is necessary to ascertain the potential alterations in exosome content (Chen et al., 2011). Therefore, the generation of exosomes by manipulating cellular sources or conditions requires further characterization of their composition and provides ideas for the development of new methods for exosomes in medical aesthetic applications.

However, the engineering application of exosomes still faces many challenges in medical aesthetics. At each step of large-scale exosomes production should be according to good manufacturing practice protocol (GMP). Further exploration is still needed in this field because systems based on GMP protocols and adequate quality control, and quality certification processes are still essential (Lener et al., 2015).

5.2 Engineering isolation and purification of exosomes

The putative use of exosomes in medical cosmetics has been continuously explored as exosome research has progressed. Exosome enrichment and reproducible isolation will make it easier to establish their biological activities (Zhang Y. et al., 2020). Conversely, exosomes collection and purification are complicated because exosomes from diverse sources fluctuate in size, composition, and function (Kalluri and LeBleu, 2020).

TABLE 4 Isolation of exosomes.

Isolation technique	Isolation principle	Advantages	Disadvantages
Ultracentrifugation Techniques	Precipitate and isolate exosomes based on density and size	Separation of gold standard exosomes, and the most widely used	Time consumption, high cost, structural damage
Ultrafiltration technique	Filtration with different relative molecular mass	Low cost, high enrichment efficiency and exosomes activity are not affected	Low purity and non-specific bind-ing of exosomes and reduced recovery through exosomes and ultrafiltration membranes
Size-based isolation techniques	This technique mainly refers to ultrafiltration and size exclusion chromatography. Both are exclusively based on the differences in diameter between exosomes and other components	The structure and integrity of exosomes separated from SEC are usually not affected by shear force	It usually requires a long running time, which limits its application in processing a variety of biological samples
Polymer precipitation	Collect exosomes under centrifugation by reducing the solubility of exosomes, such as PEG	Relatively easy to operate with short analysis time and is suitable for processing large doses of samples	Expensive and other non-exosomal contaminants proteins and polymeric materials may co-precipitate, resulting in low purity exosomes
Immunoaffinity capture techniques	Based on specific binding of antibodies and ligands to separate desired substances from heterogeneous mixtures	This method is applicable to the isolation of exosomes with the same membrane protein expression, as well as the qualitative and quantitative determination of exosomes	The reagent cost is high. This method is not suitable for the mass separation of exosomes, and the separated exosomes may lose their activity
Microfluidics-derived chip isolation techniques	It is a microscale separation technique based on difference between biochemical and physical properties of exosomes, such as density, size and immunoaffinity	Fast sample processing, low cost and portability	Low yield, high sensitivity, only for diagnostic purposes, and a large amount of raw materials are needed to increase the output
Flow field-flow fractionation (FlFFF)	Particle size separation of sample components is realized by increasing the molecular weight or hydrodynamic diameter	Once the lipid target or marker is determined, you can use FlFFF ESI MS/MS for top-down lipid analysis to directly analyze the lipids in the exosomes without collecting the exosomes for lipid extraction	The lack of adequate sample validation has its limitations

Consequently, one of the current biggest issues is how to efficiently enrich exosomes, which is vital for the engineering production of exosomes. For varied uses and goals, different separation techniques are frequently used. At present, ultracentrifugation technology is one of the frequently employed exosome separation techniques in medical cosmetic applications (Livshits et al., 2015), polymer precipitation technology (Domenis et al., 2017), immunoaffinity capture technology (He et al., 2017) and asymmetric flow field-flow fractionation technology (Yang et al., 2017; Willms et al., 2018). However, the equipment required for ultracentrifugation technology is expensive and complex to operate. The polymer precipitation technology may be contaminated with other proteins and the purity of exosomes is low. The reagents required for immunoaffinity capture technology are expensive, and the isolated exosomes may lose activity. Asymmetric flow field-flow fractionation technology requires large sample size and low yield, which is easily limited in medical cosmetic applications (Yang X. X. et al., 2019; Alzhrani et al., 2021) (Table 4 for details)

Secondly, the research progress of exosomes in medical aesthetics is hindered to a certain extent by the heterogeneity of their application preparation process, and the purification efficiency of different separation methods is significantly different (Hettich et al., 2020). It is said that, size-based separation techniques, such as gravity size exclusion chromatography (SEC), are a faster purification method with higher purification efficiency and can obtain high-purity and intact exosomes (Lobb et al., 2015; Nordin et al., 2015; Mol et al., 2017), which are favored by many researchers. Size exclusion chromatography (SEC) was employed by Vaswani et al. (2017) to concentrate milk-derived exosomes from extracellular carriers (EVs) that could be enriched in about 30 min, and exosomes produced by SEC yield (3×10^{12} particles/ml) was higher that density gradient centrifugation (7×10^{10} particles/ml). However, there may be contamination of microvesicles in it.

Chen et al. (2021) invented an exosome detection method *via* ultra-fast separation system (EXODUS) (Figures 10A, B). EXODUS is based on the creation of negative pressure switching technology (NPO) and NPO-HO technology that simultaneously generates high and low-frequency vibration (HO) on nanomembranes and devices. Negative pressure oscillation and membrane vibration activated by double-coupled harmonic oscillators were used to ultra-effectively purify exosomes. This approach can quickly finish exosome separation in less than 10 min, compared to existing separation and purifying techniques. Exosomes isolated by EXODUS had the highest signal intensities from all chosen

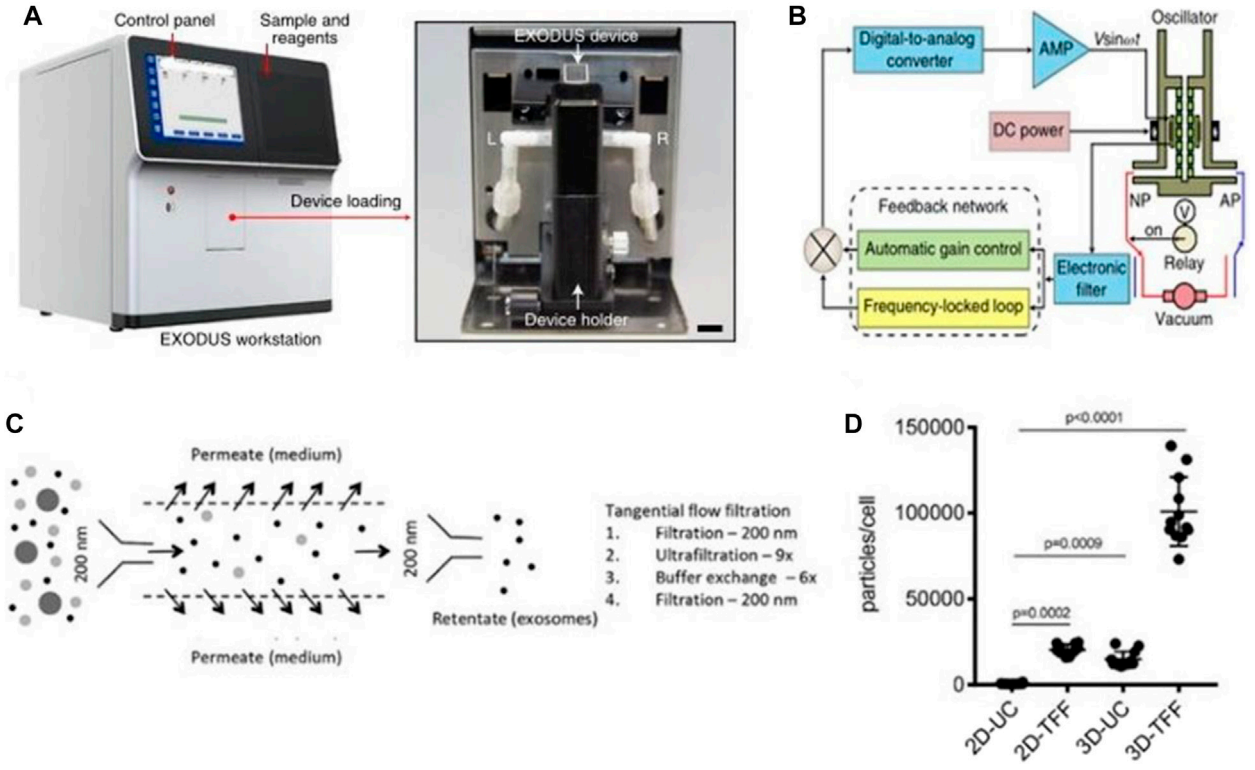

FIGURE 10
Exosomes separation device. **(A, B)** A photograph of the EXODUS station and Schematic diagram of the control module for the resonator (Chen et al., 2021). **(C, D)** Separation of exosomes by tangential flow filtration. Exosomes were enriched from the culture supernatant by tangential flow filtration with a 500 kDa cut-off filter cartridge (Haraszti et al., 2018).

exosomal proteins and the lowest signal intensities from chosen protein contaminants, demonstrating the benefits of exosome isolation and purification. Concerning a variety of sample types, sample quantities, and exosome concentrations, the EXODUS system enables reproducible procedures, and reproducible results.

In addition, tangential flow filtration (TFF) is also considered to be an ideal method for engineering the isolation of exosomes (Reiner et al., 2017; Ha et al., 2020a; Ha et al., 2020b; Yi et al., 2020). The TFF system complies with Good Manufacturing Practice (GMP), which is a method for separating exosomes, concentrated proteins or viruses from a large number of cell culture media. (Potter et al., 2014; Haraszti et al., 2018) (Figures 10C, D). Lee et al. (2020c) used TFF technique to isolate exosomes from adipose tissue-derived adipose-derived mesenchymal stem cells on a large scale with positive effects on kidney injury. Several studies have proved that the yield and purity of TFF-isolated exosomes are comparable to methods based on size exclusion chromatography (Reiner et al., 2017; Busatto et al., 2018; Haraszti et al., 2018; Ha et al., 2020a; Ha et al., 2020b; Yi et al., 2020) and have been gradually applied in the field of medical aesthetics.

There is no absolute best separation method for exosomes, and their separation effect is closely related to downstream applications and scientific issues, but high recovery and high specificity are two recognized basic requirements. In addition, the complexity of the operating procedure, extraction cost, biological activity, and throughput still need to be considered. Due to the limitations of the separation principle, the current exosome separation and purification technology has bottlenecks such as contamination with other components and exosome aggregation. Therefore, selecting appropriate methods for exosome isolation from different sources according to their characteristics is crucial.

5.3 Preservation of exosomes

Exosome utilisation in medical aesthetics depends on a suitable storage environment. It is an essential step to keep the biological activity stable throughout preservation. Exosome function may be more affected by various storage conditions. It is crucial to maintain a specific storage state. Currently, cryopreservation, freeze-drying and spray-drying are the three main preservation procedures used.

5.3.1 Cryopreservation

Cryopreservation is currently the storage technique that is most frequently employed (Mahdavinezhad et al., 2022). In order to preserve the functional stability of biological microparticles, a storage method known cryopreservation lowers the temperature below that needed for biochemical reactions. It is typically used at temperatures of 4°C, −20°C, −80°C, and −196°C (Saadeldin et al., 2020). But this way of preservation is prone to "frost burn". The term "frozen injury" used here refers to ice crystal development inside biological particles and the imbalance of osmosis that occurs during freezing. In addition, repeated freezing and thawing changes the biological properties, content and marker composition of exosome surface molecules (Maroto et al., 2017). Therefore, an appropriate concentration of antifreeze is often selectively added to prolong shelf life. The most effective disaccharide antifreeze for exosomes is trehalose, which is mentioned as the best alternative (Nakanishi et al., 2020). Trehalose and other membrane stabilisers have been used to store labile proteins, vaccines, liposomes, and cryopreserve tissues and stem cells, thus it makes sense to utilise them to keep exosomes stable (Zhang X. G. et al., 2015; Bosch et al., 2016; Shinde et al., 2019). Budgude et al. added 25 mM trehalose to exosomes in PBS at −80°C and found that these cryopreserved exosomes could be taken up by hematopoietic stem cells as efficiently as freshly isolated exosomes and that trehalose was as effective forfreshly isolated exosomes (Budgude et al., 2021). The addition will not alter the form of the exosomes and can successfully prevent exosome aggregation during the freeze-drying process, boosting stability.

5.3.2 Freeze drying

For heat-sensitive molecules such as proteins, peptides, vaccines, colloidal carriers, vesicles, and viruses, freeze-drying is currently thought to be the most dependable technique (Hansen et al., 2015; Muramatsu et al., 2022). In order to meet storage needs, a process known as freeze-drying pre-cools materials containing moisture to below freezing point, causes them to solidify. The ice is then directly sublimated in a vacuum and removed as water vapour Wang et al. (2022) have developed an inhaled, room temperature-stable virus-like particle (exosome) vaccine as a promising COVID-19 vaccine candidate. The new coronavirus vaccine consists of a recombinant new coronavirus receptor-binding domain (RBD) that binds to pulmonary exosomes, which can enhance the retention of RBD in the respiratory tract and lungs, and the new coronavirus vaccine can be lyophilized at room temperature for more than 3 months. However, the freezing and dehydration pressures generated during freeze-drying may cause the molecular structure of biomolecules to be destroyed. Therefore, it is also necessary to selectively add antifreeze, such as trehalose, to protect biological materials.

5.3.3 Spray drying

Simple, quick, repeatable, and scalable drying methods include spray drying (Arpagaus et al., 2018). Compared to freeze-drying, spray drying is a continuous process, which does not require freezing steps, and can directly transform various liquids into solid particles with adjustable size, distribution, shape, porosity, density and chemical composition. Powders that have been sprayed-dried are of a high calibre, often have a reduced moisture content, and are more stable (Arpagaus et al., 2018; Kusuma et al., 2018). However, spray drying is currently mainly concentrated in food applications and capsule and tablet applications, and the preservation and transportation of exosomes have not yet been covered. If it can be applied to the field of medical aesthetics in the future, it will solve a major problem in the preservation and transportation of exosomes.

Overall, research is underway to determine the ideal storage conditions for exosomes in medical aesthetics. Exosomes should be kept at −80°C for long-term storage and at 4°C for short-term storage. For preparation and transportation of exosome-related drugs, a freeze-drying method is used, but cryoprotectants such as trehalose, albumin., need to be added during the freezing process to reduce the loss of extracellular vesicles during separation and preservation (Bosch et al., 2016).

6 Conclusion and future perceptive

This paper discusses the regulatory mechanism of exosomes in wound repair, anti-aging, inhibition of hyperpigmentation and hair loss, also summarizes the engineering production technology, administration methods, and preservation methods for exosomes in medical beauty, with further explanations of exosomes applications in the medical aesthetics industry.

As a new type of tissue engineering material, exosomes have been gradually applied in the medical aesthetics industry. However, the research on the function of exosomes is still in the early stage, and there is an urgent need to conduct comprehensive research on the functions of exosomes in absorption, distribution, and metabolism (Cheng et al., 2020). Second, the uncertainty about the accuracy and content of components in exosomes (Lee et al., 2012), such as miRNA, proteins, and lipids, their high cost for separation procedures, and low purity of exosomes have always been problems in their application in medical aesthetics (Golchin, 2021).

The widespread use of exosomes still faces several difficulties, which we must continue to investigate in the future from various angles. First, stem cell exosomes are the main exosomes used in medical aesthetics. However, more research is needed to determine the significant usefulness of a wide range of exosomes, including plant nanovesicles and microbial nanovesicles. The route and dose of administration of

exosomes will also affect the biological distribution pattern (Wiklander et al., 2015). As a drug delivery carrier, how to achieve local administration suitable for home use and how to improve its efficacy is still a problem worth exploring. Secondly, the small automatic preparation device has a huge application market at home, and how to develop a small automatic exosome extraction device suitable for home use is also a direction worth exploring. At the same time, large-scale preparation technology combined with long-term effective preservation technology is also a direction worthy of research.

Exosomes still face many challenges in clinical practice. In clinical practice and medical aesthetics, allogeneic exosomes are often applied to individuals. Although allogeneic exosomes can induce T cell proinflammatory allogeneic immune response *in vitro* and *in vivo*, due to different donors, the drug formation ability of allogeneic exosomes needs further study. (Marino et al., 2016; Lu et al., 2019). How to improve the curative effect of exosomes is the key point worth studying. In addition, due to heterogeneity and donor age, sex, body mass index, drug use, race and other factors that affect the level of exosomes (Witwer et al., 2013). With the in-depth study of engineered exosomes, the selection of engineered cells for different indications, production standards and standardization of clinical trials are also an important direction.

Author contributions

BZ: first draft and illustrations. JG, LH, and AK: subsequentre visions of manuscript. TX, HS, and ZL: revisions of the manuscript and funding of effort. All authors contributed to the article and approved the submitted version.

Funding

This study was supported by the National Natural Science Foundation of China (61971216, 82002242, and 81972310), the Key Research and Development Project of Jiangsu Province (BE2019603 and BE2020768), Nanjing Important Science & Technology Specific Projects (2021-11005).

Conflict of interest

The authors declare that the research was conducted in the absence of any commercial or financial relationships that could be construed as a potential conflict of interest.

Publisher's note

References

Alzhrani, G. N., Alanazi, S. T., Alsharif, S. Y., Albalawi, A. M., Alsharif, A. A., Abdel-Maksoud, M. S., et al. (2021). Exosomes: Isolation, characterization, and biomedical applications. *Cell. Biol. Int.* 45 (9), 1807–1831. doi:10.1002/cbin.11620

An, Y., Lin, S., Tan, X., Zhu, S., Nie, F., Zhen, Y., et al. (2021). Exosomes from adipose-derived stem cells and application to skin wound healing. *Cell. Prolif.* 54 (3), e12993. doi:10.1111/cpr.12993

Arpagaus, C., Collenberg, A., Rutti, D., Assadpour, E., and Jafari, S. M. (2018). Nano spray drying for encapsulation of pharmaceuticals. *Int. J. Pharm. X.* 546 (1-2), 194–214. doi:10.1016/j.ijpharm.2018.05.037

Atienzar-Aroca, S., Flores-Bellver, M., Serrano-Heras, G., Martinez-Gil, N., Barcia, J. M., Aparicio, S., et al. (2016). Oxidative stress in retinal pigment epithelium cells increases exosome secretion and promotes angiogenesis in endothelial cells. *J. Cell. Mol. Med.* 20 (8), 1457–1466. doi:10.1111/jcmm.12834

Bae, I. S., and Kim, S. H. (2021). Milk exosome-derived MicroRNA-2478 suppresses melanogenesis through the akt-gsk3β pathway. *Cells* 10 (11), 2848. doi:10.3390/cells10112848

Ban, J. J., Lee, M., Im, W., and Kim, M. (2015). Low pH increases the yield of exosome isolation. *Biochem. Biophys. Res. Commun.* 461 (1), 76–79. doi:10.1016/j.bbrc.2015.03.172

Barranco, I., Padilla, L., Parrilla, I., Alvarez-Barrientos, A., Perez-Patino, C., Pena, F. J., et al. (2019). Extracellular vesicles isolated from porcine seminal plasma exhibit different tetraspanin expression profiles. *Sci. Rep.* 9 (1), 11584. doi:10.1038/s41598-019-48095-3

Berckmans, R. J., Sturk, A., van Tienen, L. M., Schaap, M. C., and Nieuwland, R. (2011). Cell-derived vesicles exposing coagulant tissue factor in saliva. *Blood* 117 (11), 3172–3180. doi:10.1182/blood-2010-06-290460

Boo, Y. C. (2022). Metabolic basis and clinical evidence for skin lightening effects of thiol compounds. *Antioxidants (Basel)* 11 (3), 503. doi:10.3390/antiox11030503

Borges, F. T., Reis, L. A., and Schor, N. (2013). Extracellular vesicles: Structure, function, and potential clinical uses in renal diseases. *Braz. J. Med. Biol. Res.* 46 (10), 824–830. doi:10.1590/1414-431X20132964

Bosch, S., de Beaurepaire, L., Allard, M., Mosser, M., Heichette, C., Chretien, D., et al. (2016). Trehalose prevents aggregation of exosomes and cryodamage. *Sci. Rep.* 6, 36162. doi:10.1038/srep36162

Budgude, P., Kale, V., and Vaidya, A. (2021). Cryopreservation of mesenchymal stromal cell-derived extracellular vesicles using trehalose maintains their ability to expand hematopoietic stem cells *in vitro*. *Cryobiology* 98, 152–163. doi:10.1016/j.cryobiol.2020.11.009

Busatto, S., Vilanilam, G., Ticer, T., Lin, W. L., Dickson, D. W., Shapiro, S., et al. (2018). Tangential flow filtration for highly efficient concentration of extracellular vesicles from large volumes of fluid. *Cells* 7 (12), 273. doi:10.3390/cells7120273

Cao, J., Wang, B., Tang, T., Lv, L., Ding, Z., Li, Z., et al. (2020). Three-dimensional culture of MSCs produces exosomes with improved yield and enhanced therapeutic efficacy for cisplatin-induced acute kidney injury. *Stem Cell. Res. Ther.* 11 (1), 206. doi:10.1186/s13287-020-01719-2

Cao, L., Tian, T., Huang, Y., Tao, S., Zhu, X., Yang, M., et al. (2021). Neural progenitor cell-derived nanovesicles promote hair follicle growth via miR-100. *J. Nanobiotechnology* 19 (1), 20. doi:10.1186/s12951-020-00757-5

Cha, J. M., Shin, E. K., Sung, J. H., Moon, G. J., Kim, E. H., Cho, Y. H., et al. (2018). Efficient scalable production of therapeutic microvesicles derived from human mesenchymal stem cells. *Sci. Rep.* 8 (1), 1171. doi:10.1038/s41598-018-19211-6

Chamberlain, C. S., Kink, J. A., Wildenauer, L. A., McCaughey, M., Henry, K., Spiker, A. M., et al. (2021). Exosome-educated macrophages and exosomes

differentially improve ligament healing. *Stem Cells* 39 (1), 55–61. doi:10.1002/stem.3291

Chen, J., Zhou, R., Liang, Y., Fu, X., Wang, D., and Wang, C. (2019). Blockade of lncRNA-ASLNCS5088-enriched exosome generation in M2 macrophages by GW4869 dampens the effect of M2 macrophages on orchestrating fibroblast activation. *FASEB J.* 33 (11), 12200–12212. doi:10.1096/fj.201901610

Chen, T. S., Arslan, F., Yin, Y., Tan, S. S., Lai, R. C., Choo, A. B., et al. (2011). Enabling a robust scalable manufacturing process for therapeutic exosomes through oncogenic immortalization of human ESC-derived MSCs. *J. Transl. Med.* 9, 47. doi:10.1186/1479-5876-9-47

Chen, Y., Zhu, Q., Cheng, L., Wang, Y., Li, M., Yang, Q., et al. (2021). Exosome detection via the ultrafast-isolation system: Exodus. *Nat. Methods* 18 (2), 212–218. doi:10.1038/s41592-020-01034-x

Cheng, J., Zhao, Z. W., Wen, J. R., Wang, L., Huang, L. W., Yang, Y. L., et al. (2020). Status, challenges, and future prospects of stem cell therapy in pelvic floor disorders. *World J. Clin. Cases* 8 (8), 1400–1413. doi:10.12998/wjcc.v8.i8.1400

Cheng, Y., Zeng, Q., Han, Q., and Xia, W. (2019). Effect of pH, temperature and freezing-thawing on quantity changes and cellular uptake of exosomes. *Protein Cell.* 10 (4), 295–299. doi:10.1007/s13238-018-0529-4

Choi, J. S., Cho, W. L., Choi, Y. J., Kim, J. D., Park, H. A., Kim, S. Y., et al. (2019). Functional recovery in photo-damaged human dermal fibroblasts by human adipose-derived stem cell extracellular vesicles. *J. Extracell. Vesicles* 8 (1), 1565885. doi:10.1080/20013078.2019.1565885

Clement, J., Wong, M., Poljak, A., Sachdev, P., and Braidy, N. (2019). The plasma NAD(+) metabolome is dysregulated in "normal" aging. *Rejuvenation Res.* 22 (2), 121–130. doi:10.1089/rej.2018.2077

Cocozza, F., Menay, F., Tsacalian, R., Elisei, A., Sampedro, P., Soria, I., et al. (2019). Cyclophosphamide enhances the release of tumor exosomes that elicit a specific immune response *in vivo* in a murine T-cell lymphoma. *Vaccine* 37 (12), 1565–1576. doi:10.1016/j.vaccine.2019.02.004

Crawford, S., Diamond, D., Brustolon, L., and Penarreta, R. (2010). Effect of increased extracellular Ca++ on microvesicle production and tumor spheroid formation. *Cancer Microenviron.* 4 (1), 93–103. doi:10.1007/s12307-010-0049-0

Dad, H. A., Gu, T. W., Zhu, A. Q., Huang, L. Q., and Peng, L. H. (2021). Plant exosome-like nanovesicles: Emerging therapeutics and drug delivery nanoplatforms. *Mol. Ther.* 29 (1), 13–31. doi:10.1016/j.ymthe.2020.11.030

Das, A., Mohan, V., Krishnaswamy, V. R., Solomonov, I., and Sagi, I. (2019). Exosomes as a storehouse of tissue remodeling proteases and mediators of cancer progression. *Cancer Metastasis Rev.* 38 (3), 455–468. doi:10.1007/s10555-019-09813-5

Domenis, R., Zanutel, R., Caponnetto, F., Toffoletto, B., Cifu, A., Pistis, C., et al. (2017). Characterization of the proinflammatory profile of synovial fluid-derived exosomes of patients with osteoarthritis. *Mediat. Inflamm.* 2017, 1–11. doi:10.1155/2017/4814987

Edmonds, A. (2013). Can medicine be aesthetic? Disentangling beauty and health in elective surgeries. *Med. Anthropol. Q.* 27 (2), 233–252. doi:10.1111/maq.12025

Egger, A., Tomic-Canic, M., and Tosti, A. (2020). Advances in stem cell-based therapy for hair loss. *CellR4. Repair Replace. Regen. Reprogr.* 8, e2894.

Ekström, E. J., Bergenfelz, C., von Bülow, V., Serifler, F., Carlemalm, E., Jönsson, G., et al. (2014). WNT5A induces release of exosomes containing pro-angiogenic and immunosuppressive factors from malignant melanoma cells. *Mol. Cancer* 13, 88. doi:10.1186/1476-4598-13-88

Foo, J. B., Looi, Q. H., How, C. W., Lee, S. H., Al-Masawa, M. E., Chong, P. P., et al. (2021). Mesenchymal stem cell-derived exosomes and MicroRNAs in cartilage regeneration: Biogenesis, efficacy, miRNA enrichment and delivery. *Pharm. (Basel)* 14 (11), 1093. doi:10.3390/ph14111093

Gao, W., Wang, X., Si, Y., Pang, J., Liu, H., Li, S., et al. (2021). Exosome derived from ADSCs attenuates ultraviolet B-mediated photoaging in human dermal fibroblasts. *Photochem. Photobiol.* 97 (4), 795–804. doi:10.1111/php.13370

Garcia, N. A., Ontoria-Oviedo, I., Gonzalez-King, H., Diez-Juan, A., and Sepulveda, P. (2015). Glucose starvation in cardiomyocytes enhances exosome secretion and promotes angiogenesis in endothelial cells. *PLoS One* 10 (9), e0138849. doi:10.1371/journal.pone.0138849

Gartz, M., Darlington, A., Afzal, M. Z., and Strande, J. L. (2018). Exosomes exert cardioprotection in dystrophin-deficient cardiomyocytes via ERK1/2-p38/MAPK signaling. *Sci. Rep.* 8 (1), 16519. doi:10.1038/s41598-018-34879-6

Gazitaeva, Z. I., Drobintseva, A. O., Prokopov, A. Y., Sidorina, A. N., Leonteva, D. O., and Kvetnoy, I. M. (2021). Signaling molecules of human skin cells as the targets for injection cosmetology. *Clin. Cosmet. Investig. Dermatol.* 14, 1473–1480. doi:10.2147/CCID.S321104

Geng, H. Y., Feng, Z. J., Zhang, J. J., and Li, G. Y. (2021). Exosomal CLIC1 released by CLL promotes HUVECs angiogenesis by regulating ITGβ1-MAPK/ERK axis. *Kaohsiung J. Med. Sci.* 37 (3), 226–235. doi:10.1002/kjm2.12287

Gentile, P., and Garcovich, S. (2019). Advances in regenerative stem cell therapy in androgenic alopecia and hair loss: Wnt pathway, growth-factor, and mesenchymal stem cell signaling impact analysis on cell growth and hair follicle development. *Cells* 8 (5), 466. doi:10.3390/cells8050466

Gimona, M., Pachler, K., Laner-Plamberger, S., Schallmoser, K., and Rohde, E. (2017). Manufacturing of human extracellular vesicle-based therapeutics for clinical use. *Int. J. Mol. Sci.* 18 (6), 1190. doi:10.3390/ijms18061190

Golchin, A. (2021). Cell-based therapy for severe COVID-19 patients: Clinical trials and cost-utility. *Stem Cell. Rev. Rep.* 17 (1), 56–62. doi:10.1007/s12015-020-10046-1

Guix, F. X., Sannerud, R., Berditchevski, F., Arranz, A. M., Horre, K., Snellinx, A., et al. (2017). Tetraspanin 6: A pivotal protein of the multiple vesicular body determining exosome release and lysosomal degradation of amyloid precursor protein fragments. *Mol. Neurodegener.* 12 (1), 25. doi:10.1186/s13024-017-0165-0

Gurunathan, S., Kang, M. H., Qasim, M., Khan, K., and Kim, J. H. (2021). Biogenesis, membrane trafficking, functions, and next generation nanotherapeutics medicine of extracellular vesicles. *Int. J. Nanomedicine* 16, 3357–3383. doi:10.2147/IJN.S310357

Ha, D. H., Kim, H. K., Lee, J., Kwon, H. H., Park, G. H., Yang, S. H., et al. (2020a). Mesenchymal stem/stromal cell-derived exosomes for immunomodulatory therapeutics and skin regeneration. *Cells* 9 (5), 1157. doi:10.3390/cells9051157

Ha, D. H., Kim, S. D., Lee, J., Kwon, H. H., Park, G. H., Yang, S. H., et al. (2020b). Toxicological evaluation of exosomes derived from human adipose tissue-derived mesenchymal stem/stromal cells. *Regul. Toxicol. Pharmacol.* 115, 104686. doi:10.1016/j.yrtph.2020.104686

Ha, D., Yang, N., and Nadithe, V. (2016). Exosomes as therapeutic drug carriers and delivery vehicles across biological membranes: Current perspectives and future challenges. *Acta Pharm. Sin. B* 6 (4), 287–296. doi:10.1016/j.apsb.2016.02.001

Hade, M. D., Suire, C. N., and Suo, Z. (2021). Mesenchymal stem cell-derived exosomes: Applications in regenerative medicine. *Cells* 10 (8), 1959. doi:10.3390/cells10081959

Hakozaki, T., Minwalla, L., Zhuang, J., Chhoa, M., Matsubara, A., Miyamoto, K., et al. (2002). The effect of niacinamide on reducing cutaneous pigmentation and suppression of melanosome transfer. *Br. J. Dermatol.* 147 (1), 20–31. doi:10.1046/j.1365-2133.2002.04834.x

Han, G., Kim, H., Kim, D. E., Ahn, Y., Kim, J., Jang, Y. J., et al. (2022). The potential of bovine colostrum-derived exosomes to repair aged and damaged skin cells. *Pharmaceutics* 14 (2), 307. doi:10.3390/pharmaceutics14020307

Han, X., Wu, P., Li, L., Sahal, H. M., Ji, C., Zhang, J., et al. (2021). Exosomes derived from autologous dermal fibroblasts promote diabetic cutaneous wound healing through the Akt/β-catenin pathway. *Cell. Cycle* 20 (5-6), 616–629. doi:10.1080/15384101.2021.1894813

Hansen, L. J. J., Daoussi, R., Vervaet, C., Remon, J. P., and De Beer, T. R. M. (2015). Freeze-drying of live virus vaccines: A review. *Vaccine* 33 (42), 5507–5519. doi:10.1016/j.vaccine.2015.08.085

Haraszti, R. A., Miller, R., Stoppato, M., Sere, Y. Y., Coles, A., Didiot, M. C., et al. (2018). Exosomes produced from 3D cultures of MSCs by tangential flow filtration show higher yield and improved activity. *Mol. Ther.* 26 (12), 2838–2847. doi:10.1016/j.ymthe.2018.09.015

He, F., Liu, H., Guo, X., Yin, B. C., and Ye, B. C. (2017). Direct exosome quantification via bivalent-cholesterol-labeled DNA anchor for signal amplification. *Anal. Chem.* 89 (23), 12968–12975. doi:10.1021/acs.analchem.7b03919

He, X., Dong, Z., Cao, Y., Wang, H., Liu, S., Liao, L., et al. (2019). MSC-derived exosome promotes M2 polarization and enhances cutaneous wound healing. *Stem Cells Int.* 2019, 1–16. doi:10.1155/2019/7132708

Hettich, B. F., Ben-Yehuda Greenwald, M., Werner, S., and Leroux, J. C. (2020). Exosomes for wound healing: Purification optimization and identification of bioactive components. *Adv. Sci. (Weinh).* 7 (23), 2002596. doi:10.1002/advs.202002596

Hong, C., Zhang, G. L., Zhang, W., Liu, J. Q., Zhang, J., Chen, Y. T., et al. (2021). Hair grows hair: Dual-effective hair regrowth through a hair enhanced dissolvable microneedle patch cooperated with the pure yellow light irradiation. *Appl. Mater. Today* 25, 101188. doi:10.1016/j.apmt.2021.101188

Hu, S., Li, Z., Cores, J., Huang, K., Su, T., Dinh, P. U., et al. (2019). Needle-free injection of exosomes derived from human dermal fibroblast spheroids ameliorates skin photoaging. *ACS Nano* 13 (10), 11273–11282. doi:10.1021/acsnano.9b04384

Huang, J., Xiong, J., Yang, L., Zhang, J., Sun, S., and Liang, Y. (2021). Cell-free exosome-laden scaffolds for tissue repair. *Nanoscale* 13 (19), 8740–8750. doi:10.1039/d1nr01314a

Hurwitz, S. N., Nkosi, D., Conlon, M. M., York, S. B., Liu, X., Tremblay, D. C., et al. (2017). CD63 regulates epstein-barr virus LMP1 exosomal packaging, enhancement of vesicle production, and noncanonical NF-κB signaling. *J. Virol.* 91, e02251. doi:10.1128/JVI.02251-16

Hwang, I., and Hong, S. (2017). Neural stem cells and its derivatives as a new material for melanin inhibition. *Int. J. Mol. Sci.* 19 (1), 36. doi:10.3390/ijms19010036

Jackson, W. M., Nesti, L. J., and Tuan, R. S. (2012). Concise review: Clinical translation of wound healing therapies based on mesenchymal stem cells. *Stem Cells Transl. Med.* 1 (1), 44–50. doi:10.5966/sctm.2011-0024

Jafari, D., Malih, S., Eini, M., Jafari, R., Gholipourmalekabadi, M., Sadeghizadeh, M., et al. (2020). Improvement, scaling-up, and downstream analysis of exosome production. *Crit. Rev. Biotechnol.* 40 (8), 1098–1112. doi:10.1080/07388551.2020.1805406

Jing, H., He, X., and Zheng, J. (2018). Exosomes and regenerative medicine: State of the art and perspectives. *Transl. Res.* 196, 1–16. doi:10.1016/j.trsl.2018.01.005

Johari, B., Asadi, Z., Rismani, E., Maghsood, F., Sheikh Rezaei, Z., Farahani, S., et al. (2019). Inhibition of transcription factor T-cell factor 3 (TCF3) using the oligodeoxynucleotide strategy increases embryonic stem cell stemness: Possible application in regenerative medicine. *Cell. Biol. Int.* 43 (8), 852–862. doi:10.1002/cbin.11153

Kalluri, R., and LeBleu, V. S. (2020). The biology, function, and biomedical applications of exosomes. *Science* 367 (6478), eaau6977. doi:10.1126/science.aau6977

Keklikoglou, I., Cianciaruso, C., Guc, E., Squadrito, M. L., Spring, L. M., Tazzyman, S., et al. (2019). Chemotherapy elicits pro-metastatic extracellular vesicles in breast cancer models. *Nat. Cell. Biol.* 21 (2), 190–202. doi:10.1038/s41556-018-0256-3

Kim, E. S., Jeon, H. B., Lim, H., Shin, J. H., Park, S. J., Jo, Y. K., et al. (2015). Conditioned media from human umbilical cord blood-derived mesenchymal stem cells inhibits melanogenesis by promoting proteasomal degradation of MITF. *PLoS One* 10 (5), e0128078. doi:10.1371/journal.pone.0128078

Kim, M., and Park, J. H. (2022). Isolation of aloe saponaria-derived extracellular vesicles and investigation of their potential for chronic wound healing. *Pharmaceutics* 14 (9), 1905. doi:10.3390/pharmaceutics14091905

Kim, S. R., Zou, X., Tang, H., Puranik, A. S., Abumoawad, A. M., Zhu, X. Y., et al. (2021). Increased cellular senescence in the murine and human stenotic kidney: Effect of mesenchymal stem cells. *J. Cell. Physiol.* 236 (2), 1332–1344. doi:10.1002/jcp.29940

King, H. W., Michael, M. Z., and Gleadle, J. M. (2012). Hypoxic enhancement of exosome release by breast cancer cells. *BMC Cancer* 12, 421. doi:10.1186/1471-2407-12-421

Kirkland, J. L., and Tchkonia, T. (2017). Cellular senescence: A translational perspective. *EBioMedicine* 21, 21–28. doi:10.1016/j.ebiom.2017.04.013

Kojima, R., Bojar, D., Rizzi, G., Hamri, G. C., El-Baba, M. D., Saxena, P., et al. (2018). Designer exosomes produced by implanted cells intracerebrally deliver therapeutic cargo for Parkinson's disease treatment. *Nat. Commun.* 9 (1), 1305. doi:10.1038/s41467-018-03733-8

Kost, Y., Muskat, A., Mhaimeed, N., Nazarian, R. S., and Kobets, K. (2022). Exosome therapy in hair regeneration: A literature review of the evidence, challenges, and future opportunities. *J. Cosmet. Dermatol.* 21, 3226–3231. doi:10.1111/jocd.15008

Kusuma, G. D., Barabadi, M., Tan, J. L., Morton, D. A. V., Frith, J. E., and Lim, R. (2018). To protect and to preserve: Novel preservation strategies for extracellular vesicles. *Front. Pharmacol.* 9, 1199. doi:10.3389/fphar.2018.01199

Lee, H., Cha, H., and Park, J. H. (2020a). Derivation of cell-engineered nanovesicles from human induced pluripotent stem cells and their protective effect on the senescence of dermal fibroblasts. *Int. J. Mol. Sci.* 21 (1), 343. doi:10.3390/ijms21010343

Lee, J. H., Ha, D. H., Go, H. K., Youn, J., Kim, H. K., Jin, R. C., et al. (2020c). Reproducible large-scale isolation of exosomes from adipose tissue-derived mesenchymal stem/stromal cells and their application in acute kidney injury. *Int. J. Mol. Sci.* 21 (13), 4774. doi:10.3390/ijms21134774

Lee, J. H., Yoon, J. Y., Lee, J. H., Lee, H. H., Knowles, J. C., and Kim, H. W. (2021). Emerging biogenesis technologies of extracellular vesicles for tissue regenerative therapeutics. *J. Tissue Eng.* 12, 204173142110190. doi:10.1177/20417314211019015

Lee, J., Seok, J. M., Huh, S. J., Byun, H., Lee, S., Park, S. A., et al. (2020b). 3D printed micro-chambers carrying stem cell spheroids and pro-proliferative growth factors for bone tissue regeneration. *Biofabrication* 13 (1), 015011. doi:10.1088/1758-5090/abc39c

Lee, Y., El Andaloussi, S., and Wood, M. J. (2012). Exosomes and microvesicles: Extracellular vesicles for genetic information transfer and gene therapy. *Hum. Mol. Genet.* 21 (R1), R125–R134. doi:10.1093/hmg/dds317

Leggio, L., Arrabito, G., Ferrara, V., Vivarelli, S., Paternò, G., Marchetti, B., et al. (2020). Mastering the tools: Natural versus artificial vesicles in nanomedicine. *Adv. Healthc. Mat.* 9 (18), e2000731. doi:10.1002/adhm.202000731

Lener, T., Gimona, M., Aigner, L., Borger, V., Buzas, E., Camussi, G., et al. (2015). Applying extracellular vesicles based therapeutics in clinical trials - an ISEV position paper. *J. Extracell. Vesicles* 4, 30087. doi:10.3402/jev.v4.30087

Li, D., and Wu, N. (2022). Mechanism and application of exosomes in the wound healing process in diabetes mellitus. *Diabetes Res. Clin. Pract.* 187, 109882. doi:10.1016/j.diabres.2022.109882

Li, L., Zhang, Y., Mu, J., Chen, J., Zhang, C., Cao, H., et al. (2020a). Transplantation of human mesenchymal stem-cell-derived exosomes immobilized in an adhesive hydrogel for effective treatment of spinal cord injury. *Nano Lett.* 20 (6), 4298–4305. doi:10.1021/acs.nanolett.0c00929

Li, M., Li, S., Du, C., Zhang, Y., Li, Y., Chu, L., et al. (2020b). Exosomes from different cells: Characteristics, modifications, and therapeutic applications. *Eur. J. Med. Chem.* 207, 112784. doi:10.1016/j.ejmech.2020.112784

Li, W., Huang, X., Yu, W., Xu, Y., Huang, R., Park, J., et al. (2022a). Activation of functional somatic stem cells promotes endogenous tissue regeneration. *J. Dent. Res.* 101 (7), 802–811. doi:10.1177/00220345211070222

Li, X., He, X., Wang, J., Wang, D., Cong, P., Zhu, A., et al. (2020c). The regulation of exosome-derived miRNA on heterogeneity of macrophages in atherosclerotic plaques. *Front. Immunol.* 11, 2175. doi:10.3389/fimmu.2020.02175

Li, Y., Wang, G., Wang, Q., Zhang, Y., Cui, L., and Huang, X. (2022b). Exosomes secreted from adipose-derived stem cells are a potential treatment agent for immune-mediated alopecia. *J. Immunol. Res.* 2022, 1–14. doi:10.1155/2022/7471246

Li, Y., Xiao, Q., Tang, J., Xiong, L., and Li, L. (2021a). Extracellular vesicles: Emerging therapeutics in cutaneous lesions. *Int. J. Nanomedicine* 16, 6183–6202. doi:10.2147/ijn.S322356

Li, Y., Zhang, J., Shi, J., Liu, K., Wang, X., Jia, Y., et al. (2021b). Exosomes derived from human adipose mesenchymal stem cells attenuate hypertrophic scar fibrosis by miR-192-5p/IL-17RA/Smad axis. *Stem Cell. Res. Ther.* 12 (1), 221. doi:10.1186/s13287-021-02290-0

Li, Z. Q., Kong, L., Liu, C., and Xu, H. G. (2020d). Human bone marrow mesenchymal stem cell-derived exosomes attenuate IL-1β-induced annulus fibrosus cell damage. *Am. J. Med. Sci.* 360 (6), 693–700. doi:10.1016/j.amjms.2020.07.025

Liang, Y., Duan, L., Lu, J., and Xia, J. (2021). Engineering exosomes for targeted drug delivery. *Theranostics* 11 (7), 3183–3195. doi:10.7150/thno.52570

Liao, C. M., Luo, T., von der Ohe, J., de Juan Mora, B., Schmitt, R., and Hass, R. (2021). Human MSC-derived exosomes reduce cellular senescence in renal epithelial cells. *Int. J. Mol. Sci.* 22 (24), 13562. doi:10.3390/ijms222413562

Liu, S. J., Meng, M. Y., Han, S., Gao, H., Zhao, Y. Y., Yang, Y., et al. (2021). Umbilical cord mesenchymal stem cell-derived exosomes ameliorate HaCaT cell photo-aging. *Rejuvenation Res.* 24 (4), 283–293. doi:10.1089/rej.2020.2313

Liu, Y., Xue, L., Gao, H., Chang, L., Yu, X., Zhu, Z., et al. (2019). Exosomal miRNA derived from keratinocytes regulates pigmentation in melanocytes. *J. Dermatol. Sci.* 93 (3), 159–167. doi:10.1016/j.jdermsci.2019.02.001

Livshits, M. A., Khomyakova, E., Evtushenko, E. G., Lazarev, V. N., Kulemin, N. A., Semina, S. E., et al. (2015). Isolation of exosomes by differential centrifugation: Theoretical analysis of a commonly used protocol. *Sci. Rep.* 5, 17319. doi:10.1038/srep17319

Lo Cicero, A., Delevoye, C., Gilles-Marsens, F., Loew, D., Dingli, F., Guere, C., et al. (2015). Exosomes released by keratinocytes modulate melanocyte pigmentation. *Nat. Commun.* 6, 7506. doi:10.1038/ncomms8506

Lobb, R. J., Becker, M., Wen, S. W., Wong, C. S., Wiegmans, A. P., Leimgruber, A., et al. (2015). Optimized exosome isolation protocol for cell culture supernatant and human plasma. *J. Extracell. Vesicles* 4, 27031. doi:10.3402/jev.v4.27031

Lu, M., Peng, L., Ming, X., Wang, X., Cui, A., Li, Y., et al. (2019). Enhanced wound healing promotion by immune response-free monkey autologous iPSCs and exosomes vs. their allogeneic counterparts. *EBioMedicine* 42, 443–457. doi:10.1016/j.ebiom.2019.03.011

Ma, L., Chen, C., Liu, D., Huang, Z., Li, J., Liu, H., et al. (2023). Apoptotic extracellular vesicles are metabolized regulators nurturing the skin and hair. *Bioact. Mat.* 19, 626–641. doi:10.1016/j.bioactmat.2022.04.022

Ma, T., Fu, B., Yang, X., Xiao, Y., and Pan, M. (2019). Adipose mesenchymal stem cell-derived exosomes promote cell proliferation, migration, and inhibit cell

apoptosis via Wnt/β-catenin signaling in cutaneous wound healing. *J. Cell. Biochem.* 120 (6), 10847–10854. doi:10.1002/jcb.28376

Mahdavinezhad, F., Gilani, M. A. S., Gharaei, R., Ashrafnezhad, Z., Valipour, J., Nashtaei, M. S., et al. (2022). Protective roles of seminal plasma exosomes and microvesicles during human sperm cryopreservation. *Reprod. Biomed. Online* 45 (2), 341–353. doi:10.1016/j.rbmo.2022.03.033

Manconi, M., Manca, M. L., Marongiu, F., Caddeo, C., Castangia, I., Petretto, G. L., et al. (2016). Chemical characterization of Citrus limon var. pompia and incorporation in phospholipid vesicles for skin delivery. *Int. J. Pharm. X.* 506 (1-2), 449–457. doi:10.1016/j.ijpharm.2016.04.014

Marcus, M. E., and Leonard, J. N. (2013). FedExosomes: Engineering therapeutic biological nanoparticles that truly deliver. *Pharm. (Basel)* 6 (5), 659–680. doi:10.3390/ph6050659

Marino, J., Babiker-Mohamed, M. H., Crosby-Bertorini, P., Paster, J. T., LeGuern, C., Germana, S., et al. (2016). Donor exosomes rather than passenger leukocytes initiate alloreactive T cell responses after transplantation. *Sci. Immunol.* 1 (1), aaf8759. doi:10.1126/sciimmunol.aaf8759

Marofi, F., Alexandrovna, K. I., Margiana, R., Bahramali, M., Suksatan, W., Abdelbasset, W. K., et al. (2021). MSCs and their exosomes: A rapidly evolving approach in the context of cutaneous wounds therapy. *Stem Cell. Res. Ther.* 12 (1), 597. doi:10.1186/s13287-021-02662-6

Maroto, R., Zhao, Y., Jamaluddin, M., Popov, V. L., Wang, H., Kalubowilage, M., et al. (2017). Effects of storage temperature on airway exosome integrity for diagnostic and functional analyses. *J. Extracell. Vesicles* 6 (1), 1359478. doi:10.1080/20013078.2017.1359478

Martínez-González, M. C., Martínez-González, R. A., and Guerra-Tapia, A. (2019). Key communication skills in cosmetic dermatology: A 3-pillar model. *Actas Sifiliogr.* 110 (10), 794–799. doi:10.1016/j.adengl.2019.10.003

Matic, S., D'Souza, D. H., Wu, T., Pangloli, P., and Dia, V. P. (2020). Bovine milk exosomes affect proliferation and protect macrophages against cisplatin-induced cytotoxicity. *Immunol. Invest.* 49 (7), 711–725. doi:10.1080/08820139.2020.1769647

Mazini, L., Rochette, L., Hamdan, Y., and Malka, G. (2021). Skin immunomodulation during regeneration: Emerging new targets. *J. Pers. Med.* 11 (2), 85. doi:10.3390/jpm11020085

McReynolds, M. R., Chellappa, K., and Baur, J. A. (2020). Age-related NAD(+) decline. *Exp. Gerontol.* 134, 110888. doi:10.1016/j.exger.2020.110888

McReynolds, M. R., Chellappa, K., Chiles, E., Jankowski, C., Shen, Y., Chen, L., et al. (2021). NAD(+) flux is maintained in aged mice despite lower tissue concentrations. *Cell. Syst.* 12 (12), 1160–1172.e4. e1164. doi:10.1016/j.cels.2021.09.001

Mehryab, F., Rabbani, S., Shahhosseini, S., Shekari, F., Fatahi, Y., Baharvand, H., et al. (2020). Exosomes as a next-generation drug delivery system: An update on drug loading approaches, characterization, and clinical application challenges. *Acta Biomater.* 113, 42–62. doi:10.1016/j.actbio.2020.06.036

Mol, E. A., Goumans, M. J., Doevendans, P. A., Sluijter, J. P. G., and Vader, P. (2017). Higher functionality of extracellular vesicles isolated using size-exclusion chromatography compared to ultracentrifugation. *Nanomedicine Nanotechnol. Biol. Med.* 13 (6), 2061–2065. doi:10.1016/j.nano.2017.03.011

Muramatsu, H., Lam, K., Bajusz, C., Laczkó, D., Karikó, K., Schreiner, P., et al. (2022). Lyophilization provides long-term stability for a lipid nanoparticle-formulated, nucleoside-modified mRNA vaccine. *Mol. Ther.* 30 (5), 1941–1951. doi:10.1016/j.ymthe.2022.02.001

Naik, P. P. (2021). Utilities of botulinum toxins in dermatology and cosmetology. *Clin. Cosmet. Investig. Dermatol.* 14, 1319–1330. doi:10.2147/CCID.S332247

Nakanishi, K., Tomita, M., and Tsumoto, K. (2020). Membrane fusion and infection abilities of baculovirus virions are preserved during freezing and thawing in the presence of trehalose. *Biosci. Biotechnol. Biochem.* 84 (4), 686–694. doi:10.1080/09168451.2019.1704396

Nam, G. H., Choi, Y., Kim, G. B., Kim, S., Kim, S. A., and Kim, I. S. (2020). Emerging prospects of exosomes for cancer treatment: From conventional therapy to immunotherapy. *Adv. Mat.* 32 (51), e2002440. doi:10.1002/adma.202002440

Nilforoushzadeh, M. A., Aghdami, N., and Taghiabadi, E. (2020). Human hair outer root sheath cells and platelet-lysis exosomes promote hair inductivity of dermal papilla cell. *Tissue Eng. Regen. Med.* 17 (4), 525–536. doi:10.1007/s13770-020-00266-4

Nordin, J. Z., Lee, Y., Vader, P., Mager, I., Johansson, H. J., Heusermann, W., et al. (2015). Ultrafiltration with size-exclusion liquid chromatography for high yield isolation of extracellular vesicles preserving intact biophysical and functional properties. *Nanomedicine Nanotechnol. Biol. Med.* 11 (4), 879–883. doi:10.1016/j.nano.2015.01.003

O'Brien, K., Breyne, K., Ughetto, S., Laurent, L. C., and Breakefield, X. O. (2020). RNA delivery by extracellular vesicles in mammalian cells and its applications. *Nat. Rev. Mol. Cell. Biol.* 21 (10), 585–606. doi:10.1038/s41580-020-0251-y

Odrobinska, J., Mielanczyk, L., and Neugebauer, D. (2020). 4-n-Butylresorcinol-Based linear and graft polymethacrylates for arbutin and vitamins delivery by micellar systems. *Polym. (Basel)* 12 (2), 330. doi:10.3390/polym12020330

Ogawa, R. (2017). Keloid and hypertrophic scars are the result of chronic inflammation in the reticular dermis. *Int. J. Mol. Sci.* 18 (3), 606. doi:10.3390/ijms18030606

Oh, M., Lee, J., Kim, Y. J., Rhee, W. J., and Park, J. H. (2018). Exosomes derived from human induced pluripotent stem cells ameliorate the aging of skin fibroblasts. *Int. J. Mol. Sci.* 19 (6), 1715. doi:10.3390/ijms19061715

Pegtel, D. M., and Gould, S. J. (2019). Exosomes. *Annu. Rev. Biochem.* 88, 487–514. doi:10.1146/annurev-biochem-013118-111902

Peña-Juárez, M. C., Guadarrama-Escobar, O. R., and Escobar-Chávez, J. J. (2022). Transdermal delivery systems for biomolecules. *J. Pharm. Innov.* 17 (2), 319–332. doi:10.1007/s12247-020-09525-2

Petersen, K. E., Shiri, F., White, T., Bardi, G. T., Sant, H., Gale, B. K., et al. (2018). Exosome isolation: Cyclical electrical field flow fractionation in low-ionic-strength fluids. *Anal. Chem.* 90 (21), 12783–12790. doi:10.1021/acs.analchem.8b03146

Potter, M., Lins, B., Mietzsch, M., Heilbronn, R., Van Vliet, K., Chipman, P., et al. (2014). A simplified purification protocol for recombinant adeno-associated virus vectors. *Mol. Ther. - Methods & Clin. Dev.* 1, 14034. doi:10.1038/mtm.2014.34

Prasai, A., Jay, J. W., Jupiter, D., Wolf, S. E., and El Ayadi, A. (2022). Role of exosomes in dermal wound healing: A systematic review. *J. Invest. Dermatol.* 142, 662–678.e8. e668. doi:10.1016/j.jid.2021.07.167

Qi, J., Liu, Q., Reisdorf, R. L., Boroumand, S., Behfar, A., Moran, S. L., et al. (2020). Characterization of a purified exosome product and its effects on canine flexor tenocyte biology. *J. Orthop. Res.* 38 (8), 1845–1855. doi:10.1002/jor.24587

Rajendran, R. L., Gangadaran, P., Bak, S. S., Oh, J. M., Kalimuthu, S., Lee, H. W., et al. (2017). Extracellular vesicles derived from MSCs activates dermal papilla cell *in vitro* and promotes hair follicle conversion from telogen to anagen in mice. *Sci. Rep.* 7 (1), 15560. doi:10.1038/s41598-017-15505-3

Rao, D., Huang, D., Sang, C., Zhong, T., Zhang, Z., and Tang, Z. (2021). Advances in mesenchymal stem cell-derived exosomes as drug delivery vehicles. *Front. Bioeng. Biotechnol.* 9, 797359. doi:10.3389/fbioe.2021.797359

Ras-Carmona, A., Gomez-Perosanz, M., and Reche, P. A. (2021). Prediction of unconventional protein secretion by exosomes. *BMC Bioinforma.* 22 (1), 333. doi:10.1186/s12859-021-04219-z

Ratz-Lyko, A., and Arct, J. (2019). Resveratrol as an active ingredient for cosmetic and dermatological applications: A review. *J. Cosmet. Laser Ther.* 21 (2), 84–90. doi:10.1080/14764172.2018.1469767

Regimbeau, M., Abrey, J., Vautrot, V., Causse, S., Gobbo, J., and Garrido, C. (2021). Heat shock proteins and exosomes in cancer theranostics. *Semin. Cancer Biol.* 86, 46–57. doi:10.1016/j.semcancer.2021.07.014

Reiner, A. T., Witwer, K. W., van Balkom, B. W. M., de Beer, J., Brodie, C., Corteling, R. L., et al. (2017). Concise review: Developing best-practice models for the therapeutic use of extracellular vesicles. *Stem Cells Transl. Med.* 6 (8), 1730–1739. doi:10.1002/sctm.17-0055

Riau, A. K., Ong, H. S., Yam, G. H. F., and Mehta, J. S. (2019). Sustained delivery system for stem cell-derived exosomes. *Front. Pharmacol.* 10, 1368. doi:10.3389/fphar.2019.01368

Saadeldin, I. M., Khalil, W. A., Alharbi, M. G., and Lee, S. H. (2020). The current trends in using nanoparticles, liposomes, and exosomes for semen cryopreservation. *Anim. (Basel)* 10 (12), 2281. doi:10.3390/ani10122281

Sahin, F., Kocak, P., Gunes, M. Y., Ozkan, I., Yildirim, E., and Kala, E. Y. (2019). *In vitro* wound healing activity of wheat-derived nanovesicles. *Appl. Biochem. Biotechnol.* 188 (2), 381–394. doi:10.1007/s12010-018-2913-1

Salimu, J., Webber, J., Gurney, M., Al-Taei, S., Clayton, A., and Tabi, Z. (2017). Dominant immunosuppression of dendritic cell function by prostate-cancer-derived exosomes. *J. Extracell. Vesicles* 6 (1), 1368823. doi:10.1080/20013078.2017.1368823

Savcı, Y., Kırbaş, O. K., Bozkurt, B. T., Abdik, E. A., Taşlı, P. N., Şahin, F., et al. (2021). Grapefruit-derived extracellular vesicles as a promising cell-free therapeutic tool for wound healing. *Food Funct.* 12 (11), 5144–5156. doi:10.1039/d0fo02953j

Schiller, L. T., Lemus-Diaz, N., Rinaldi Ferreira, R., Boker, K. O., and Gruber, J. (2018). Enhanced production of exosome-associated AAV by overexpression of the tetraspanin CD9. *Mol. Ther. - Methods & Clin. Dev.* 9, 278–287. doi:10.1016/j.omtm.2018.03.008

Shabbir, A., Cox, A., Rodriguez-Menocal, L., Salgado, M., and Van Badiavas, E. (2015). Mesenchymal stem cell exosomes induce proliferation and migration of

normal and chronic wound fibroblasts, and enhance angiogenesis *in vitro*. *Stem Cells Dev.* 24 (14), 1635–1647. doi:10.1089/scd.2014.0316

Shang, H., Younas, A., and Zhang, N. (2022). Recent advances on transdermal delivery systems for the treatment of arthritic injuries: From classical treatment to nanomedicines. *Wiley Interdiscip. Rev. Nanomed. Nanobiotechnol.* 14 (3), e1778. doi:10.1002/wnan.1778

Shekhter, A. B., Fayzullin, A. L., Vukolova, M. N., Rudenko, T. G., Osipycheva, V. D., and Litvitsky, P. F. (2019). Medical applications of collagen and collagen-based materials. *Curr. Med. Chem.* 26 (3), 506–516. doi:10.2174/0929867325666171205170339

Shi, H., Wang, M., Sun, Y., Yang, D., Xu, W., and Qian, H. (2021). Exosomes: Emerging cell-free based therapeutics in dermatologic diseases. *Front. Cell. Dev. Biol.* 9, 736022. doi:10.3389/fcell.2021.736022

Shiekh, P. A., Singh, A., and Kumar, A. (2020). Exosome laden oxygen releasing antioxidant and antibacterial cryogel wound dressing OxOBand alleviate diabetic and infectious wound healing. *Biomaterials* 249, 120020. doi:10.1016/j.biomaterials.2020.120020

Shin, K. O., Ha, D. H., Kim, J. O., Crumrine, D. A., Meyer, J. M., Wakefield, J. S., et al. (2020). Exosomes from human adipose tissue-derived mesenchymal stem cells promote epidermal barrier repair by inducing de Novo synthesis of ceramides in atopic dermatitis. *Cells* 9 (3), 680. doi:10.3390/cells9030680

Shinde, P., Khan, N., Melinkeri, S., Kale, V., and Limaye, L. (2019). Freezing of dendritic cells with trehalose as an additive in the conventional freezing medium results in improved recovery after cryopreservation. *Transfusion* 59 (2), 686–696. doi:10.1111/trf.15028

Sinha, S., Hoshino, D., Hong, N. H., Kirkbride, K. C., Grega-Larson, N. E., Seiki, M., et al. (2016). Cortactin promotes exosome secretion by controlling branched actin dynamics. *J. Cell. Biol.* 214 (2), 197–213. doi:10.1083/jcb.201601025

Taghiabadi, E., Nilforoushzadeh, M. A., and Aghdami, N. (2020). Maintaining hair inductivity in human dermal papilla cells: A review of effective methods. *Skin. Pharmacol. Physiol.* 33 (5), 280–292. doi:10.1159/000510152

Tan, K. H., Tan, S. S., Ng, M. J., Tey, W. S., Sim, W. K., Allen, J. C., et al. (2017). Extracellular vesicles yield predictive pre-eclampsia biomarkers. *J. Extracell. Vesicles* 6 (1), 1408390. doi:10.1080/20013078.2017.1408390

Tao, S. C., Guo, S. C., Li, M., Ke, Q. F., Guo, Y. P., and Zhang, C. Q. (2017). Chitosan wound dressings incorporating exosomes derived from MicroRNA-126-overexpressing synovium mesenchymal stem cells provide sustained release of exosomes and heal full-thickness skin defects in a diabetic rat model. *Stem Cells Transl. Med.* 6 (3), 736–747. doi:10.5966/sctm.2016-0275

Tkach, M., and Thery, C. (2016). Communication by extracellular vesicles: Where we are and where we need to go. *Cell.* 164 (6), 1226–1232. doi:10.1016/j.cell.2016.01.043

Trounson, A., and McDonald, C. (2015). Stem cell therapies in clinical trials: Progress and challenges. *Cell. Stem Cell.* 17 (1), 11–22. doi:10.1016/j.stem.2015.06.007

van Niel, G., D'Angelo, G., and Raposo, G. (2018). Shedding light on the cell biology of extracellular vesicles. *Nat. Rev. Mol. Cell. Biol.* 19 (4), 213–228. doi:10.1038/nrm.2017.125

Vaswani, K., Koh, Y. Q., Almughlliq, F. B., Peiris, H. N., and Mitchell, M. D. (2017). A method for the isolation and enrichment of purified bovine milk exosomes. *Reprod. Biol.* 17 (4), 341–348. doi:10.1016/j.repbio.2017.09.007

Villarroya-Beltri, C., Baixauli, F., Gutierrez-Vazquez, C., Sanchez-Madrid, F., and Mittelbrunn, M. (2014). Sorting it out: Regulation of exosome loading. *Semin. Cancer Biol.* 28, 3–13. doi:10.1016/j.semcancer.2014.04.009

Wang, C., Wang, M., Xu, T., Zhang, X., Lin, C., Gao, W., et al. (2019a). Engineering bioactive self-healing antibacterial exosomes hydrogel for promoting chronic diabetic wound healing and complete skin regeneration. *Theranostics* 9 (1), 65–76. doi:10.7150/thno.29766

Wang, L., Hu, L., Zhou, X., Xiong, Z., Zhang, C., Shehada, H. M. A., et al. (2017). Exosomes secreted by human adipose mesenchymal stem cells promote scarless cutaneous repair by regulating extracellular matrix remodelling. *Sci. Rep.* 7 (1), 13321. doi:10.1038/s41598-017-12919-x

Wang, M., Wang, C., Chen, M., Xi, Y., Cheng, W., Mao, C., et al. (2019b). Efficient angiogenesis-based diabetic wound healing/skin reconstruction through bioactive antibacterial adhesive ultraviolet shielding nanodressing with exosome release. *ACS Nano* 13 (9), 10279–10293. doi:10.1021/acsnano.9b03656

Wang, X., Gu, H., Huang, W., Peng, J., Li, Y., Yang, L., et al. (2016). Hsp20-Mediated activation of exosome biogenesis in cardiomyocytes improves cardiac function and angiogenesis in diabetic mice. *Diabetes* 65 (10), 3111–3128. doi:10.2337/db15-1563

Wang, X. Y., Guan, X. H., Yu, Z. P., Wu, J., Huang, Q. M., Deng, K. Y., et al. (2021). Human amniotic stem cells-derived exosmal miR-181a-5p and miR-199a inhibit melanogenesis and promote melanosome degradation in skin hyperpigmentation, respectively. *Stem Cell. Res. Ther.* 12 (1), 501. doi:10.1186/s13287-021-02570-9

Wang, Z., Popowski, K. D., Zhu, D., de Juan Abad, B. L., Wang, X., Liu, M., et al. (2022). Exosomes decorated with a recombinant SARS-CoV-2 receptor-binding domain as an inhalable COVID-19 vaccine. *Nat. Biomed. Eng.* 6, 791–805. doi:10.1038/s41551-022-00902-5

Willms, E., Cabanas, C., Mager, I., Wood, M. J. A., and Vader, P. (2018). Extracellular vesicle heterogeneity: Subpopulations, isolation techniques, and diverse functions in cancer progression. *Front. Immunol.* 9, 738. doi:10.3389/fimmu.2018.00738

Witwer, K. W., Buzás, E. I., Bemis, L. T., Bora, A., Lässer, C., Lötvall, J., et al. (2013). Standardization of sample collection, isolation and analysis methods in extracellular vesicle research. *J. Extracell. Vesicles* 2, 20360. doi:10.3402/jev.v2i0.20360

Xiong, M., Zhang, Q., Hu, W., Zhao, C., Lv, W., Yi, Y., et al. (2021). The novel mechanisms and applications of exosomes in dermatology and cutaneous medical aesthetics. *Pharmacol. Res.* 166, 105490. doi:10.1016/j.phrs.2021.105490

Xu, J., Bai, S., Cao, Y., Liu, L., Fang, Y., Du, J., et al. (2020). <p>miRNA-221-3p in endothelial progenitor cell-derived exosomes accelerates skin wound healing in diabetic mice</p>. *Diabetes Metab. Syndr. Obes.* 13, 1259–1270. doi:10.2147/DMSO.S243549

Yan, D., Li, S. H., Zhang, A. L., Xiao, Y., and Huang, Z. C. (2021). A clinical study of platelet-rich fibrin combined with autologous high-density fat transplantation in augmentation rhinoplasty. *Ear Nose Throat J.* 2021, 1455613211016902. doi:10.1177/01455613211016902

Yang, G., Chen, G., and Gu, Z. (2021). Transdermal drug delivery for hair regrowth. *Mol. Pharm.* 18 (2), 483–490. doi:10.1021/acs.molpharmaceut.0c00041

Yang, G., Chen, Q., Wen, D., Chen, Z., Wang, J., Chen, G., et al. (2019a). A therapeutic microneedle patch made from hair-derived keratin for promoting hair regrowth. *ACS Nano* 13 (4), 4354–4360. doi:10.1021/acsnano.8b09573

Yang, J. S., Lee, J. C., Byeon, S. K., Rha, K. H., and Moon, M. H. (2017). Size dependent lipidomic analysis of urinary exosomes from patients with prostate cancer by flow field-flow fractionation and nanoflow liquid chromatography-tandem mass spectrometry. *Anal. Chem.* 89 (4), 2488–2496. doi:10.1021/acs.analchem.6b04634

Yang, X. X., Sun, C., Wang, L., and Guo, X. L. (2019b). New insight into isolation, identification techniques and medical applications of exosomes. *J. Control. Release* 308, 119–129. doi:10.1016/j.jconrel.2019.07.021

Yari, H., Mikhailova, M. V., Mardasi, M., Jafarzadehgharehziaaddin, M., Shahrokh, S., Thangavelu, L., et al. (2022). Emerging role of mesenchymal stromal cells (MSCs)-derived exosome in neurodegeneration-associated conditions: A groundbreaking cell-free approach. *Stem Cell. Res. Ther.* 13 (1), 423. doi:10.1186/s13287-022-03122-5

Yeh, Y. Y., Ozer, H. G., Lehman, A. M., Maddocks, K., Yu, L., Johnson, A. J., et al. (2015). Characterization of CLL exosomes reveals a distinct microRNA signature and enhanced secretion by activation of BCR signaling. *Blood* 125 (21), 3297–3305. doi:10.1182/blood-2014-12-618470

Yi, Y. W., Lee, J. H., Kim, S. Y., Pack, C. G., Ha, D. H., Park, S. R., et al. (2020). Advances in analysis of biodistribution of exosomes by molecular imaging. *Int. J. Mol. Sci.* 21 (2), 665. doi:10.3390/ijms21020665

Yoshida, M., Satoh, A., Lin, J. B., Mills, K. F., Sasaki, Y., Rensing, N., et al. (2019). Extracellular vesicle-contained eNAMPT delays aging and extends lifespan in mice. *Cell. Metab.* 30 (2), 329–342.e5. doi:10.1016/j.cmet.2019.05.015

Yuan, R., Dai, X., Li, Y., Li, C., and Liu, L. (2021). Exosomes from miR-29a-modified adipose-derived mesenchymal stem cells reduce excessive scar formation by inhibiting TGF-β2/Smad3 signaling. *Mol. Med. Rep.* 24 (5), 758. doi:10.3892/mmr.2021.12398

Zeng, L., Wang, H., Shi, W., Chen, L., Chen, T., Chen, G., et al. (2021). Aloe derived nanovesicle as a functional carrier for indocyanine green encapsulation and phototherapy. *J. Nanobiotechnology* 19 (1), 439. doi:10.1186/s12951-021-01195-7

Zhai, M., Zhu, Y., Yang, M., and Mao, C. (2020). Human mesenchymal stem cell derived exosomes enhance cell-free bone regeneration by altering their miRNAs profiles. *Adv. Sci. (Weinh).* 7 (19), 2001334. doi:10.1002/advs.202001334

Zhang, B., Shi, Y., Gong, A., Pan, Z., Shi, H., Yang, H., et al. (2016a). HucMSC exosome-delivered 14-3-3ζ orchestrates self-control of the Wnt response via modulation of YAP during cutaneous regeneration. *Stem Cells* 34 (10), 2485–2500. doi:10.1002/stem.2432

Zhang, J., Chen, C., Hu, B., Niu, X., Liu, X., Zhang, G., et al. (2016b). Exosomes derived from human endothelial progenitor cells accelerate cutaneous wound healing by promoting angiogenesis through erk1/2 signaling. *Int. J. Biol. Sci.* 12 (12), 1472–1487. doi:10.7150/ijbs.15514

Zhang, J., Guan, J., Niu, X., Hu, G., Guo, S., Li, Q., et al. (2015a). Exosomes released from human induced pluripotent stem cells-derived MSCs facilitate cutaneous wound healing by promoting collagen synthesis and angiogenesis. *J. Transl. Med.* 13, 49. doi:10.1186/s12967-015-0417-0

Zhang, K., Yu, L., Li, F. R., Li, X., Wang, Z., Zou, X., et al. (2020a). <p>Topical application of exosomes derived from human umbilical cord mesenchymal stem cells in combination with sponge spicules for treatment of photoaging</p>. *Int. J. Nanomedicine* 15, 2859–2872. doi:10.2147/ijn.S249751

Zhang, X. G., Wang, Y. H., Han, C., Hu, S., Wang, L. Q., and Hu, J. H. (2015b). Effects of trehalose supplementation on cell viability and oxidative stress variables in frozen-thawed bovine calf testicular tissue. *Cryobiology* 70 (3), 246–252. doi:10.1016/j.cryobiol.2015.03.004

Zhang, Y., Bi, J., Huang, J., Tang, Y., Du, S., and Li, P. (2020b). <p>Exosome: A review of its classification, isolation techniques, storage, diagnostic and targeted therapy applications</p>. *Int. J. Nanomedicine* 15, 6917–6934. doi:10.2147/IJN.S264498

Zhang, Y., Su, J., Ma, K., Li, H., Fu, X., and Zhang, C. (2022). Photobiomodulation promotes hair regeneration in injured skin by enhancing migration and exosome secretion of dermal papilla cells. *Wound Repair Regen.* 30 (2), 245–257. doi:10.1111/wrr.12989

Zhao, B., Li, X., Shi, X., Shi, X., Zhang, W., Wu, G., et al. (2018). Exosomal MicroRNAs derived from human amniotic epithelial cells accelerate wound healing by promoting the proliferation and migration of fibroblasts. *Stem Cells Int.* 2018, 1–10. doi:10.1155/2018/5420463

Zhou, L., Wang, H., Jing, J., Yu, L., Wu, X., and Lu, Z. (2018). Regulation of hair follicle development by exosomes derived from dermal papilla cells. *Biochem. Biophys. Res. Commun.* 500 (2), 325–332. doi:10.1016/j.bbrc.2018.04.067

Zifkos, K., Dubois, C., and Schafer, K. (2021). Extracellular vesicles and thrombosis: Update on the clinical and experimental evidence. *Int. J. Mol. Sci.* 22 (17), 9317. doi:10.3390/ijms22179317

frontiers | Frontiers in Bioengineering and Biotechnology

TYPE Original Research
PUBLISHED 10 April 2023
DOI 10.3389/fbioe.2023.1139426

OPEN ACCESS

EDITED BY
Donglin Xia,
Nantong University, China

REVIEWED BY
Chao Zhang,
Southern Medical University, China
Chuan Ding,
Changzhou Institute of Technology, China

*CORRESPONDENCE
Zhilei Mao,
mao598808386@126.com
Huaiyan Wang,
huaiyanwang@njmu.edu.cn

†These authors have contributed equally to this work

SPECIALTY SECTION
This article was submitted to Biomaterials, a section of the journal Frontiers in Bioengineering and Biotechnology

RECEIVED 07 January 2023
ACCEPTED 06 March 2023
PUBLISHED 10 April 2023

CITATION
Zhang L, Zhu P, Wan T, Wang H and Mao Z (2023), Glutamine coated titanium for synergistic sonodynamic and photothermal on tumor therapy upon targeted delivery.
Front. Bioeng. Biotechnol. 11:1139426.
doi: 10.3389/fbioe.2023.1139426

Glutamine coated titanium for synergistic sonodynamic and photothermal on tumor therapy upon targeted delivery

Lina Zhang[1†], Pengfeng Zhu[1†], Ting Wan[1], Huaiyan Wang[1*] and Zhilei Mao[1,2,3*]

[1]Changzhou Maternal and Child Healthcare Hospital, Changzhou Medical Center, Nanjing Medical University, Changzhou, China, [2]State Key Laboratory of Reproductive Medicine, Center for Global Health, Nanjing Medical University, Nanjing, China, [3]Key Laboratory of Modern Toxicology of Ministry of Education, School of Public Health, Nanjing Medical University, Nanjing, China

Introduction: The application of titanium dioxide nanoparticles (TiO_2 NPs) for cancer therapy has been studied for decades; however, the targeted delivery of TiO_2 NPs to tumor tissues is challenging, and its efficiency needs to be improved.

Method: In this study, we designed an oxygen-deficient TiO_{2-x} coated with glutamine layer for targeted delivery, as well as the enhanced separation of electrons (e-) and holes (h+) following the joint application of sonodynamic therapy (SDT) and photothermal therapy (PTT).

Results: This oxygen-deficient TiO_{2-x} possesses relatively high photothermal and sonodynamic efficiency at the 1064 nm NIR-II bio-window. The GL-dependent design eased the penetration of the TiO_{2-x} into the tumor tissues (approximately three-fold). The *in vitro* and *in vivo* tests showed that the SDT/PTT-based synergistic treatment achieved more optimized therapeutic effects than the sole use of either SDT or PTT.

Conclusion: Our study provided a safety targeted delivery strategy, and enhanced the therapeutic efficiency of SDT/PTT synergistic treatment.

KEYWORDS

TiO_{2-x}@GL, sonodynamic (SDT), photothermal (PTT), synergistic tumor therapy, glutamine addiction

Introduction

Owing to its remarkable biocompatibility, high photoactivity, excellent stability, and low toxicity, titanium dioxide nanoparticles (TiO_2 NPs) were regarded as a promising anticancer material and were studied in-depth (Cesmeli and Biray Avci, 2019; Ziental et al., 2020). Being a typical emerging photochemical sensitizer, TiO_2 NPs were highly effective in tumor therapy, and generated reactive oxygen species (ROS) in numerous types of cancer cells resulting in cell death upon illumination with light, majorly ultraviolet (UV) light (Fujiwara et al., 2015; Lee et al., 2018). In addition, TiO_2 NPs were considered to be a promising acoustic sensitizer in tumor therapy owing to their remarkable stability compared to that of the organic acoustic sensitizer (Li et al., 2021). However, the ROS production of TiO_2 NPs is relatively low because of the rapid recombination of their electron (e-) and hole (h+) (Dai et al., 2022). Therefore, the

application of TiO_2 NPs as a photochemical or acoustic sensitizer would necessitate prolonged illumination of UV light and yield low efficiency in ROS production (Gao et al., 2019; Kim et al., 2022). To resolve this challenge, researchers reformed the physicochemical features of TiO_2 NPs to realize easier ROS release near the infrared-II biowindow, and proposed a SDT (sonodynamic therapy)/PTT (photothermal therapy)-based synergistic strategy for cancer therapy (Han et al., 2018).

SDT/PTT-based synergistic cancer therapy is a promising strategy, particularly considering TiO_2 NPs, which respond to both sound and light simultaneously (Behnam et al., 2018; Chu et al., 2019). Therefore, SDT/PTT synergistic therapy can shorten the illumination duration for activation, thus compensating for the deficiency in ROS generation. The accumulation of sufficient nanoparticles in the tumor tissues is an essential premise for all nanomedicne treatments, therefore, the target delivery of TiO_2 NPs to the cancer cells should be enhanced to the extent possible to improve efficacy and prevent adverse side effects (Kim et al., 2020; Liang et al., 2021). Therefore, a modified delivery method should be proposed to achieve this goal.

A previous study suggested that most of the cancer cells exhibited the phenomenon of glutamine (GL) addiction, that is, the tumor cells actively absorb and accumulate GL in tumor tissues for growth (Altman et al., 2016). Although *in vitro* research indicated that GL stimulated cancer cell growth (Knox et al., 1969), certain studies indicated that the GL supplementation did not stimulate tumor tissue growth in tumor-bearing mice models (Klimberg et al., 1996). Therefore, this unique feature of tumor cells provided a potential and safe strategy for the targeted delivery of TiO_2 NPs.

This study aimed to synthesize the TiO_{2-x}@GL NPs based on the "sugar coated bullet" theory in this study. We synthesized TiO_{2-x} NPs and coated them with GL for the targeted delivery of nanoparticles to cancer cells *via* the tumor cells' active uptake of GL, thus increasing the accumulation of TiO_{2-x}@GL in tumor tissues, which consequently meant to treat the breast cancer, a common and severe cancer disease that affecting women health. Therefore, the 4T1 cancer cells and the tumor-bearing nude-mice mice were applied for the functional verification.

Methods

Synthesis of TiO_{2-x}@GL NPs

TiO_{2-x} NPs were prepared through a an aluminum (Al) reduction method reported in a previous study (Wang et al., 2013; Han et al., 2018). To improve the tumor-targeting capability of TiO_{2-x} NPs, GL (#J61560, Thermos Scientific) was harnessed to modify the surface of TiO_{2-x} NPs. Categorically, 50 mg GL was added to TiO_{2-x} NPs solution (1 mg/ml, 10 ml) and then subjected to 4-h sonication in an ice bath. The resulting TiO_{2-x}@GL NPs were acquired through centrifugation (10000 r/min, 10 min) three times and washing with deionized water.

Characterization of TiO_{2-x}@GL NPs

Transmission electron microscopy (TEM) was used to observe the morphology of TiO_{2-x} and TiO_{2-x}@GL; X-ray diffraction (XRD) patterns were obtained using the Rigaku D/MAX-2200 PX XRD system; and the parameters were set as Cu Kα, 40 mA, and 40 kV. Elements of Ti, O, and N were detected by sectional energy-dispersive spectroscopy (EDS) with corresponding color mapping. The size distribution and ζ potential measurements of the particles were conducted on a Zetasizer system (Nano ZS90, Malvern Instrument Ltd.). The UV-vis-NIR absorption spectrum was used to record *via* Shimadzu UV-3600 UV-vis-NIR spectrometer. The irradiation source for photothermal hyperthermia was the 1064 nm multimode pump laser (Shanghai Connect Fiber Optics Co. Ltd.), and the ultrasound irradiation for sonodynamic therapy was conducted using an Intelect Transport Ultrasound (Chattanooga Group, United States). The Agilent 725 inductively coupled plasma-optical emission spectrometer (Agilent Technologies) was used to confirm the quantitative analysis of the contents of nanoparticles. The intracellular uptake of nanoparticles and cell apoptosis levels were detected by flow cytometry (Becton, Dickinson and Company, United States), and confocal laser scanning microscopy images were recorded using FV1000 (Olympus Company, Japan).

Cell culture

The 4T1 cells were purchased from the American Type Culture Collection: The Global Bioresource Center (#CRL-2539). The cells were cultured with RPMI-1640 medium, supplemented with 10% fetal bovine serum (FBS) (#10100147C, GIBICO), in a 5% CO_2 atmosphere at 37°C. The cell culture medium was replaced daily and the cells were treated upon reaching 60% confluence.

In vitro sonodynamic and photothermal treatment

The commercial Cell Counting Kit-8 (CCK-8) assay kit (#C0037, Beyotime Biotechnology) was used to evaluate the sonocatalytic and photothermal treatment for killing cancer cells. 4T1 cells were seeded in 96-well plates and cultured with RPMI-1640 medium containing 10% FBS for 12 h at a proper density, and then TiO_{2-x}@GL (Ti concentration 50 ppm) was added for co-incubation. The cell viabilities in each group were determined by comparison with the control group. The laser power intensities were set as 1.5 W/cm2, and the US irradiation parameters as 1 MHz, 50% duty cycle, 1.0 W/cm2, and 200 s.

Reactive oxygen species detection

4T1 cells were planted and co-incubated with TiO_{2-x}@GL at 37°C for 4 h. After incubation, the medium was removed and the cells were washed three times with PBS. To measure the ROS production by flow cytometry, the DCFH- DA (#S0033S, Beyotime Biotechnology) was added and incubated for 1 h. The cells were treated by US radiation for 5 min. After different treatments, the cells were collected to determine the intracellular fluorescence intensity of DCF.

Evaluation of *in vitro* photothermal effect of TiO_{2-x}@GL

The infrared thermal image recorder (FLIR TM A325SC camera) was used to evaluate the photothermal effects of TiO_{2-x}@GL by recording the temperature changes during laser irradiation in the NIR-II biowindow (1064 nm). TiO_{2-x}@GL were dispersed in deionized water at different Ti concentrations (0, 6.25, 12.5, 25, 50, 100 and 300 ppm) and exposed to 1064 nm pump laser irradiation at a laser power density of 1.5 W/cm2. In addition, the temperature increase of TiO_{2-x}@GL at a Ti concentration of 400 ppm as irradiated by a 1064 nm laser at different power intensities (0, 0.5, 1.0 and 1.5 W/cm2) was determined.

Evaluation of cell migration ability

The 4T1 cells were re-suspended with serum free medium, then 100 ml of the cell suspension was added to the upper chamber of the transwell plate at a proper density, after which the chamber was placed into the well filled with a serum-containing medium. After culturing for an additional 12 h, cells were fixed with 4% paraformaldehyde (#C104188, Aladdin), and then stained with 0.1% crystalviolet (#C0121, Beyotime Biotechnology) for 15 min at room temperature (22°C). Upon erasure of the cells on the bottom of the upper chamber, the well was observed and the migrated cells were counted under the light microscope. The cell number was collected from four independent fields from different directions.

Distinction between living and dead cells

The living and dead cells were distinguished using a commercial Calcein-AM/PI assay kit (#04511, Sigma-Aldich). The living cells were indicated with Calcein-AM (green) and the dead cells were stained red with PI. After staining, the cells were observed using a confocal laser scanning microscope (CLSM).

Establishment of tumor-bearing model and *in vivo* synergistic cancer therapy

The animal study was approved by the animal ethnic committee of Nanjing Medical University. To establish the tumor bearing model, 4T1 cells (1×10^6 cells) were suspended in 100 μl of PBS and injected into the right side of the back of mice (C57BL/6). Finally, 40 female 4T1 tumor-bearing mice were successfully established and fed at the Laboratory Animal Center. After the tumors grew to nearly 50 mm^3, the mice were divided into 5 groups (n = 8) as follows: 1) Control group (treated with saline), 2) TiO_{2-x}@GL only group, 3) TiO_{2-x}@GL + laser group (injected with TiO_{2-x}@GL followed by 1064 nm laser), 4) TiO_{2-x}@GL + US group (treated with TiO_{2-x}@GL + US irradiation), and 5) TiO_{2-x}@GL + laser + US group (injected with TiO_{2-x}@GL followed by laser and US irradiation). The injection dose of TiO_{2-x}@GL was 15 mg/ml. The injection of 4T1 cells was recorded as day −7, and the mice received treatment on day 0. After intravenous injection of TiO_{2-x}@GL for 4 h, the 1064 nm laser (1.5 W/cm^2, 10 min) or the US irradiation (1 MHz, 50% duty cycle, and 1.0 W/cm^2, 240 s) were administered to carry out the therapeutic plan. For the synergistic treatment, the mice received laser and US irradiation treatment on day 0, and the following US treatment was administered on days 3 and 5. The body weight and length and width of tumors were measured every 2 days using the digital scale and caliper, respectively. The tumor volume was calculated as follows: tumor volume (mm^3) = $ab^2/2$, a = the maximum length (mm), b = the minimum width (mm).

Contribution to SDT/PTT-based synergistic cancer therapy

The inhibitory rate of cell growth was calculated using the equation: % Growth inhibition = [(1 − OD extract treated)/(OD negative control)] × 100. The percentage contribution of each element (TiO_{2-x}@GL, US and NIR) to the SDT/PTT-based synergistic cancer therapy was calculated by % contribution= (% Growth inhibition/total growth inhibition) × 100.

Biodistribution of TiO_{2-x}@GL in tumor tissues

To verify that TiO_{2-x}@GL could penetrate barriers and accumulate in tumor tissues, the bio-distributions of TiO_{2-x} and TiO_{2-x}@GL in tumor tissues were determined in 4T1 female breast tumor bearing mice (n = 5); they were randomly divided into three groups and intravenously injected with TiO_{2-x} and TiO_{2-x}@GL in saline at a dosage of 50 ppm. The mice were euthanized after 4 h of injection and dissected to collect the tumors. These tissues were weighed, homogenized, and dissolved in aqua regia. Then the Ti element content in tumor tissue was measured using Inductively Coupled Plasma Optical Emission spectroscopy (ICP-OES), and the distribution was calculated using the original dose per gram of tissue.

Pathological changes, cell apoptosis, and cell proliferation after different treatments

Pathological changes, cell apoptosis, and cell proliferation were revealed by hematoxylin and eosin (H&E) staining (#C0105S, Beyotime Biotechnology), tunel assay (#25879, Cell Signal), and Ki-67 antibody (#9129, Cell Signal), respectively. The H&E staining was carried out according to a previous study (Yuan et al., 2022), and Tunel staining was performed using a commercially available assay kit according to the manufacturer's instructions. Cell proliferation was revealed by immunohistochemistry with an anti-Ki-67 antibody combined with a goat-anti-rabbit secondary antibody.

Statistical analysis

The data were presented as mean ± standard deviation (SD), and the difference between two groups was analyzed on the basis of the two-tailed t-test (*, $p < 0.05$; **, $p < 0.01$; ***, $p < 0.001$).

10.3389/fbioe.2023.1139426

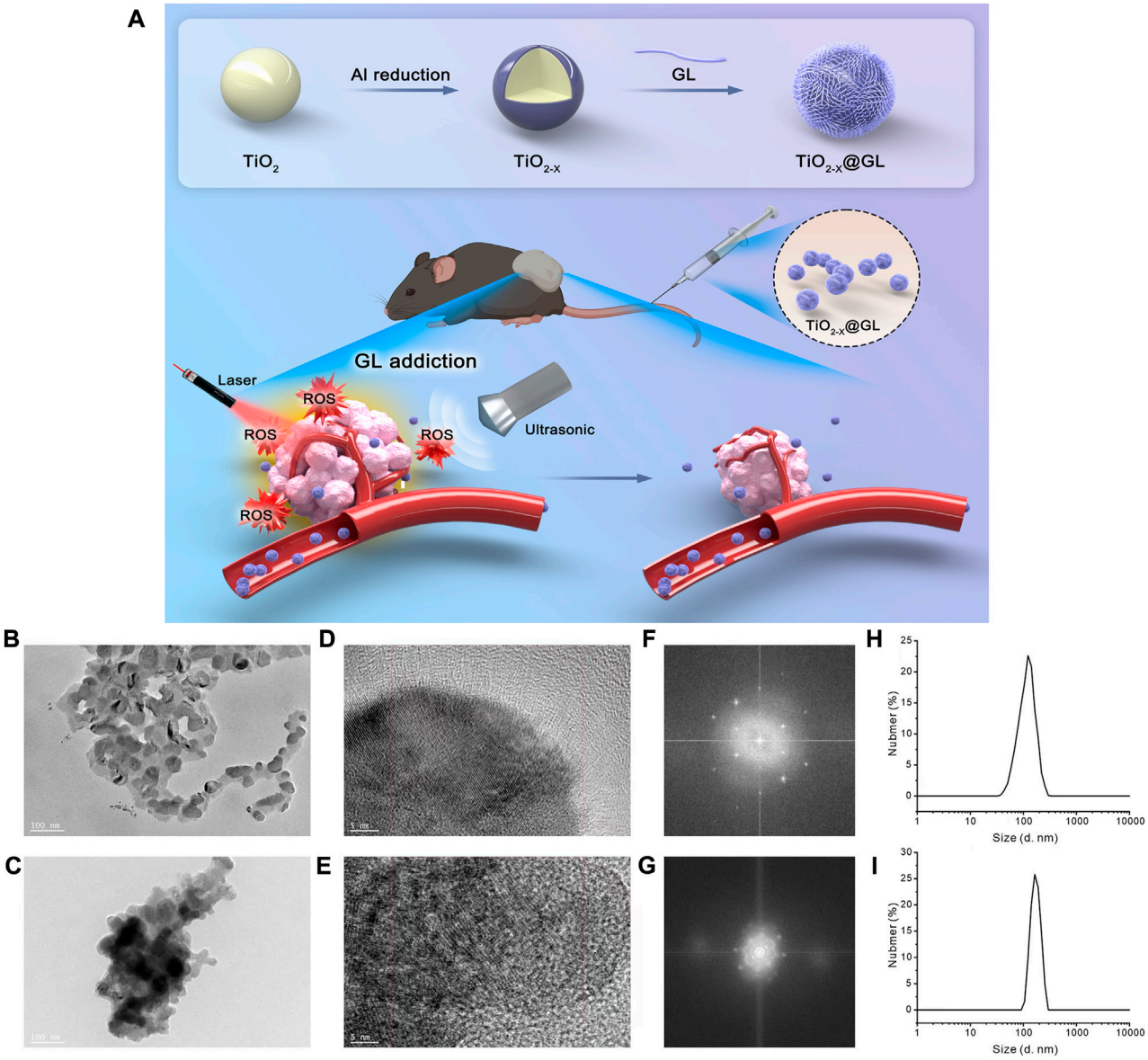

FIGURE 1
Characteristics of TiO_{2-x} NPs and TiO_{2-x}@GL NPs **(A)** Graphical information of the synthesis of TiO_{2-x} NPs and the synergistic SDT/PTT cancer therapy. **(B, C)** Low-magnification TEM images of TiO_{2-x} NPs **(B)**; and TiO_{2-x}@GL NPs **(C, D, E)** High-resolution TEM images of TiO_{2-x} NPs **(D)**; and TiO_{2-x}@GL NPs **(E, F, G)** SAED pattern images of TiO_2-x NPs **(F)**; and TiO_{2-x}@GL NPs **(G, H, I)** DLS of TiO_{2-x} NPs **(H)**; and TiO_{2-x}@GL NPs **(I)**.

Results

Synthesis and characterization of TiO_{2-x} NPs and TiO_{2-x}@GL NPs

The synthesis progress of TiO_{2-x}@GL NPs and the synergistic SDT/PTT therapy are indicated in Figure 1A. TEM were employed to identify the morphology of TiO_{2-x} NPs and TiO_{2-x}@GL NPs. As indicated in Figure 1B, TiO_{2-x} displayed a uniform, spherical structure with a mean size of 50 nm. After loading into GL, there was no apparent change in the morphology of the fabricated TiO_{2-x}@GL NPs compared with TiO_{2-x} NPs (Figure 1C). Based on the high-resolution TEM imaging results and corresponding SAED patterns of TiO_{2-x} NPs and TiO_{2-x}@GL NPs (Figures 1D–G), the encasement of GL did not change the crystalline structure of TiO_{2-x} NPs. The DLS results indicated the surface encasement of GL increased hydrodynamic particle size of TiO_{2-x} NPs from 122.4 to 164.2 nm (Figures 1H, I). There was a remarkable elevation of nitrogen (N) in the TiO_{2-x}@GL NPs group compared with the TiO_{2-x} NPs group as revealed in the SEM images (Figures 2A, B) and EDS results (Figures 2C, D), suggesting the successful loading of TiO_{2-x} NPs into GL. Despite the changes in ζ potential (Figure 2E) before and after GL encasement (from −36.1 to −9.1 mV), the crystal peaks of TiO2-x NPs and TiO_{2-x}@GL NPs in XRD measurement matched the standard crystal structure of TiO_{2-x} NPs (JCPDS No. 21-1272), suggesting the structure of TiO_{2-x} NPs is well preserved after the surface encasement of GL (Figure 2F). Additionally, the UV-Vis-NIR

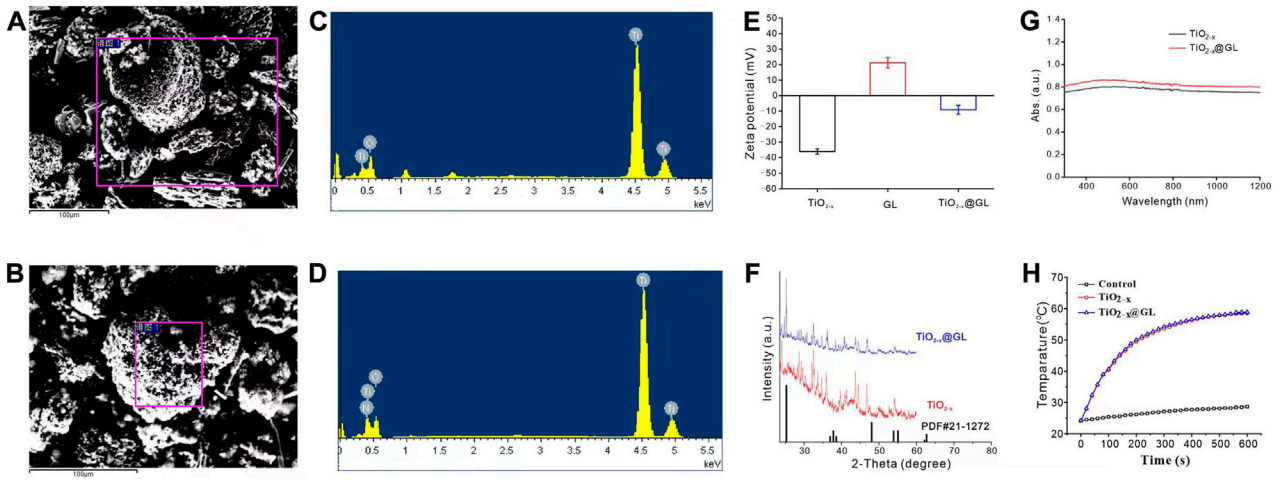

FIGURE 2
Characteristics of TiO_{2-x} NPs and TiO_{2-x}@GL NPs **(A, B)** SEM images of TiO_{2-x} NPs **(B)**; and TiO_{2-x}@GL NPs **(C, C, D)** EDS of TiO_2-x NPs **(C)** obtained based on the purple rectangle area in **(A)**; and TiO_{2-x}@GL NPs **(D)** obtained based on the purple rectangle area in **(B, E–G)** Zeta potentials **(E)**; XRD **(F)**; UV-Vis-NIR spectra **(G)**; photothermal heating curves **(H)** of TiO_{2-x} NPs and TiO_{2-x}@GL NPs.

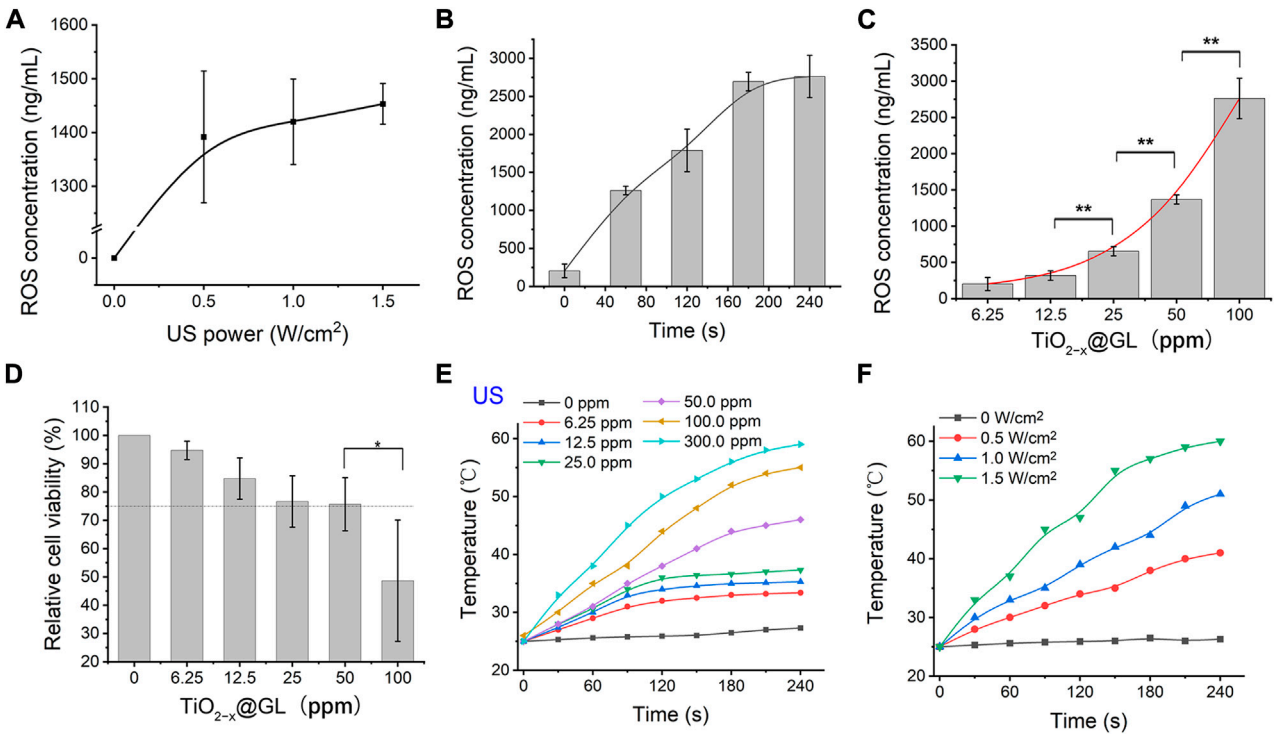

FIGURE 3
In vitro sonodynamic and photothermal effects of TiO_{2-x}@GL. **(A)** ROS generation behavior of TiO_{2-x}@GL under different ultrasonic intensities *in vitro*. **(B)** Cumulative ROS concentration curve of TiO_{2-x}@GL subjected to continuous ultrasound irradiation (1.5 W/cm^2). **(C)** Comparison of the effects of different particle concentrations on the ROS generation. **(D)** Cytotoxicities of various concentration of TiO_{2-x}@GL to normal epithelial cells. **(E)** Elevated concentrations (0, 6.25, 12.5, 25, 50, 100, and 300 ppm) of TiO_{2-x}@GL irradiated by NIR-II (1064 nm) at a power intensity of 1.5 W/cm^2. **(F)** Photothermal heating curves of 50 ppm TiO_{2-x}@GL irradiated at varied power densities (0, 0.5, 1.0, and 1.5 W/cm^2).

optical absorption curves (Figure 2G) and the photothermal heating curves (Figure 2H) of TiO_{2-x} NPs and TiO_{2-x}@GL NPs show that the NIR wave-absorbing capability and the photothermal performance were not compromised, and collectively demonstrated that both TiO_{2-x} NPs and TiO_{2-x}@GL NPs could serve as PTT agents for tumor treatment.

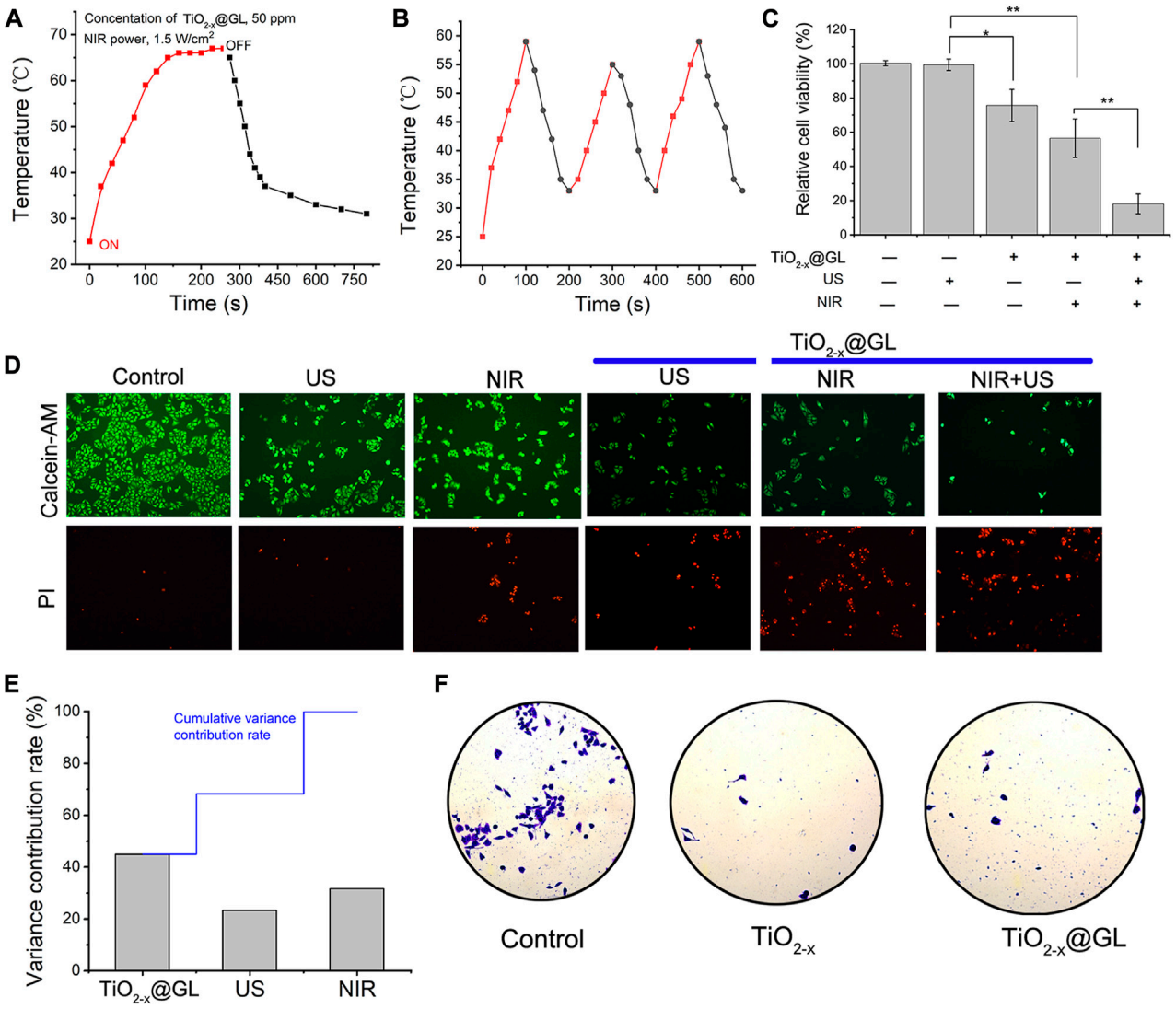

FIGURE 4
In vitro SDT/PTT-based synergistic cancer therapy. **(A)** Photothermal performance of the aqueous dispersion of TiO_{2-x}@GL (50 ppm) under NIR irradiation at a power intensity of 1.5 W/cm^2 for periods after US, and the temperature tended to stabilize when the laser cut off; **(B)** Heating curve of TiO_{2-x}@GL dispersed in water for three cycles at a power intensity of 1.5 W/cm^2; **(C)** Relative cell viability of 4T1 cells after different treatments, including control (without treatment), TiO_{2-x}@GL only, US only, TiO_{2-x}@GL combined with NIR, TiO_{2-x}@GL combined with US irradiation, and TiO_{2-x}@GL combined with NIR/US coirradiation. **(D)** CLSM images of 4T1 cells after different treatments, which were stained by PI (red fluorescence) and calcein-AM (green fluorescence). The scale bar is 40 μm; **(E)** Variance contribution rate of TiO_{2-x}@GL, US and NIR; **(F)** Plate counting experiments of control, TiO_{2-x}, and TiO_{2-x}@GL.

In vitro sonodynamic and photothermal effects of TiO_{2-x}@GL

The generation of ROS could be influenced by numerous factors, such as US irradiation, duration, and the sonosensitizer concentration. First, generation of ROS increased as ultrasound intensity increased; the ultrasound power duration was 180 s and the TiO_{2-x}@GL concentration 50 ppm (Figure 3A). To determine the influence of 40-kHz ultrasound in ROS generation kinetics, we determined the cumulative ROS generation from the 50 ppm TiO_{2-x}@GL (Figure 3B). Sustained INS release from TiO_{2-x}@GL was achieved through ultrasound irradiation at 1.0 W/cm2. As shown in Figure 3C, the increased particle concentration treatment led to a slight increase in ROS generation 180 s after the 1.0 W/cm2 ultrasound irradiation treatment. Conversely, TiO_{2-x}@GL at high concentration (>100 ppm) suppressed cell growth (<75%). Given the aforementioned results, an optimized procedure (1.0 W/cm2 of US power, 180 s, and 50 ppm TiO_{2-x}@GL) was adopted to achieve high ROS generation. Furthermore, the photothermal performance of TiO_{2-x}@GL aqueous solution was further evaluated at different concentrations (0, 6.25, 12.5, 25, 50, 100, and 300 ppm) and 1.5 W/cm2. The temperature could reach as high as 59.2°C (300 ppm), which is sufficient to kill cancer cells by hyperthermia. The laser power dependent photothermal effect (0, 0.5, 1.0 and 1.5 W/cm2) was also demonstrated (Figure 3F).

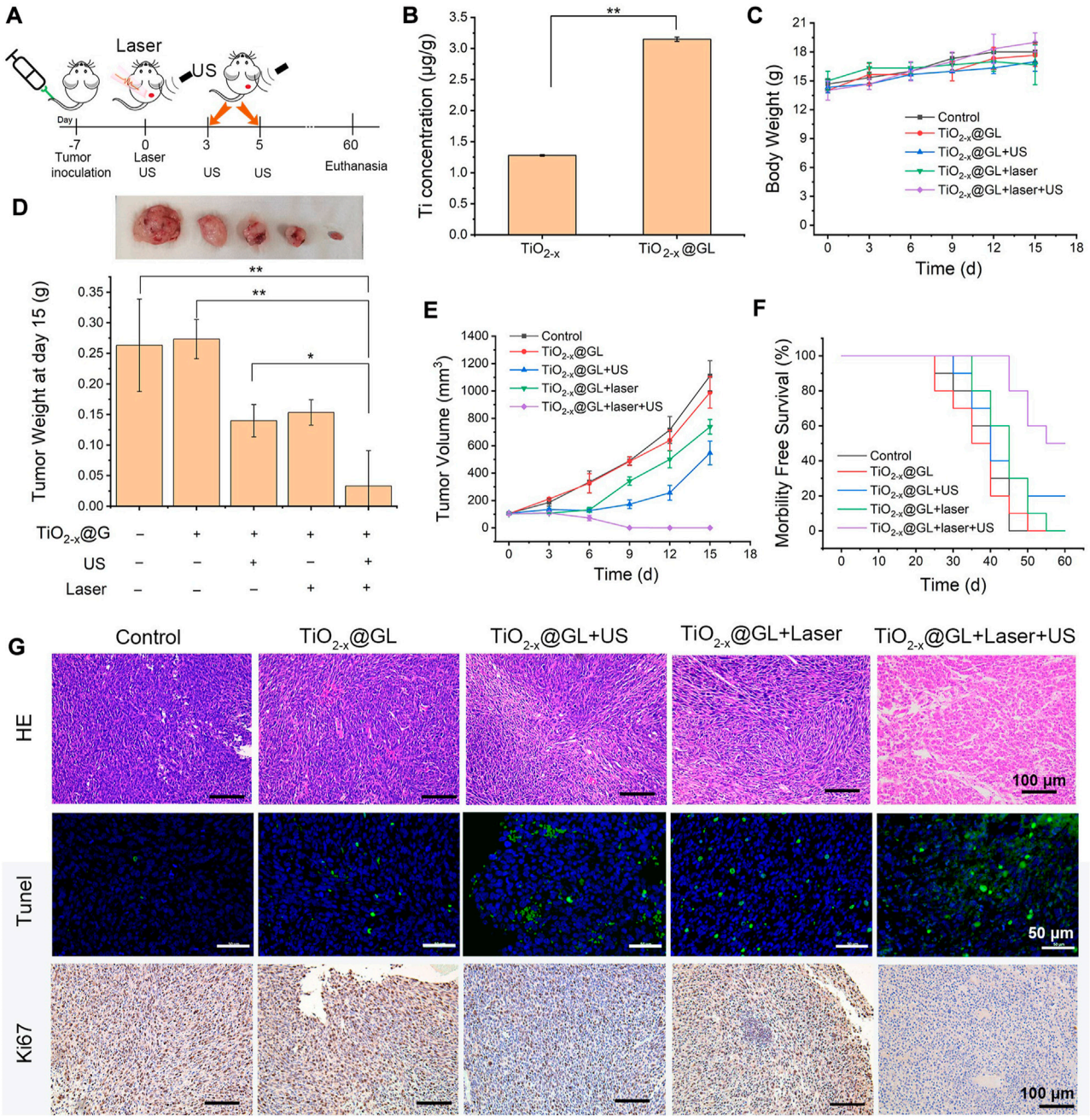

FIGURE 5
In vivo synergistic SDT/PTT on tumor suppression in the NIR-II biowindow. **(A)** Schematic of synergistic SDT and PTT as assisted by TiO_{2-x}@GL for tumor eradication. **(B)** Accumulated Ti in the tumor after the intravenous injection of TiO_{2-x} or TiO_{2-x} @GL for 4 h. **(C)** Time-dependent body-weight curves of 4T1 tumor-bearing mice in groups of control group, TiO_{2-x}@GL group, TiO_{2-x}@GL combined with US group, TiO_{2-x}@GL combined with laser group and TiO_{2-x}@GL combined with the laser and US therapy group. **(D)** Tumor weight of different groups on day 15. **(E)** Time-dependent tumor-volume curves during the 15 days. **(F)** Survival curves of 4T1 tumor-bearing mice after different treatments. **(G)** H&E staining, Tunel staining, and Antigen Ki-67 immunohistochemistry staining in tumor region of each group after the treatments. *$p < 0.05$, **$p < 0.01$, and ***$p < 0.001$.

In vitro SDT/PTT-based synergistic cancer therapy

In this study protocol, the 4T1 cells were treated by SDT and PTT (sequential treatment). Categorically, 4T1 cancer cells were incubated with TiO_{2-x}@GL nanoparticles for 4 h after US irradiation and NIR-II laser. The parameters of US irradiation were set as 1 MHz, 50% duty cycle, and 1.0 W/cm^2, 200 s. The NIR-II laser was set at a power density of 1.5 W/cm^2. The temperature rose quickly, and reached as high as 66°C (300 ppm), which was sufficient to kill cancer cells by hyperthermia (Figure 4A). As the laser is switched off, the temperature decreased rapidly. Notably, the extremely high temperature generated an obvious ablation and smoking phenomenon under NIR-laser irradiation. There was no obvious deterioration during three laser on/off cycles for the

photothermal performance of TiO_{2-x}@GL nanoparticles, showing the high photothermal stability of TiO_{2-x}@GL nanoagents for photothermal hyperthermia (Figure 4B). The standard CCK-8 assay was initially conducted to investigate the *in vitro* 4T1 cell killing efficacy of TiO_{2-x}@GL exposed to 1064 nm laser, TiO_{2-x}@GL irradiated by US activation, and TiO_{2-x}@GL combined with US and 1064 nm laser irradiations. In the SDT and PTT treated group, the cancer-cell viability incubated with TiO_{2-x}@GL as PTT agent for 4 h decreased with a cell-viability rate of 19.2% (Figure 4C). Furthermore, after various treatments, the cell-killing effect was directly observed by CLSM, where the live and dead cells were stained by calcein-AM (green) and PI (red), respectively. A host of dead cells were observed in the TiO_{2-x}@GL combined with US and laser group, indicating that the extensive occurrence of cell apoptosis and death for synergistic SDT and PTT (Figure 4D). From the average contribution rate of inter-regional differences, the TiO_{2-x}@GL had an enormous contribution rate, with an average contribution rate of 44.95%. The US and NIR variance contribution rates were 23.33% and 31.72%, respectively (Figure 4E). As reported earlier, the TiO_2 could inhibit tumor cell migration. Transwell experiments showed that the viable cells in TiO_{2-x}@GL and TiO_{2-x} groups were significantly less than those in the control group. This indicates that the TiO_{2-x}@GL could inhibit tumor cell migration, like TiO_2 (Figure 4F).

In vivio SDT/PTT-based synergistic cancer therapy

The synergistic therapeutic schedule is shown in Figure 5A, the establishment of the tumor-bearing model was recorded as day −7, and the laser and US irradiation treatment was applied after 4 h of TiO_{2-x}@GL injection on day 0. The subsequent US treatment was administered on the 3rd and 5th days. Ti element concentrations were significantly increased in tumor tissues after the intravenous injection of TiO_{2-x} NPs or TiO_{2-x}@GL. The GL increased the accumulation of TiO_{2-x} NPs nearly 3-fold compared to that of the TiO_{2-x} group (Figure 5B). The body weight of the mice showed no significant change during the treatment among all groups (Figure 5C). The tumor weight in the TiO_{2-x}@GL + laser + US group was decreased significantly ($p < 0.01$) compared to control and TiO_{2-x}@GL groups, and the decrease was significant ($p < 0.05$) compared to those of TiO_{2-x}@GL + laser and TiO_{2-x}@GL + US groups, respectively on day 15 (Figure 5D). Meanwhile, the tumor volume exhibited no growth in the TiO_{2-x}@GL + laser + US group (Figure 5E), and the synergistic therapy contributed to prolonged morbidityfree survival (Figure 5F). H&E staining showed obvious pathological changes in the TiO_{2-x}@GL + laser + US group as the tumor cells swelled, and Tunel assay showed increased apoptosis in the TiO_{2-x}@GL + laser + US group. The expression of Ki-67 was significantly down-regulated in xenograft tumors after TiO_{2-x}@GL + laser + US treatment. These data show that TiO_{2-x}@GL + laser + US suppressed tumor growth *in vivo*.

Safety evaluation of TiO_{2-x}@GL

The safety evaluation of TiO_{2-x}@GL was revealed by the pathological changes of important organs and key blood and biochemicial parameters. H&E staining showed that the heart, liver, kidney, and lung showed no obvious changes on days 1, 7, and 28 (Figure 6A). The blood markers, including white blood cells (WBC), platelets (PLT), and hemoglobin (HGB) showed no significant change among different groups. Meanwhile, the biochemicial parameters, including urea nitrogen (BUN), C-reactive protein (Cr), and globulin (GLB) did not change compared to the control group (Figure 6B).

Discussion

As a traditional nanomaterial, titanium dioxide nanoparticles (TiO_2 NPs) have been extensively applied in the field of anti-bacteria (Esteban Florez et al., 2018), particularly in cancer therapy (Rodriguez-Barajas et al., 2022), owing to their unique characteristics of low toxicity, remarkable biological compatibility, and SDT and PDT activity. TiO_2 NPs is a semiconductor material, the energy gap of the anatase type is 3.23 eV, and that of the rutile type 3.06 eV (Nosaka and Nosaka, 2016). The molecules of TiO_2 NPs would go into an excited state upon absorbing a photon with energy above or equal to the gap energy, and created negative electrons (e-) in the conduction, leaving a positive charged hole (h+) (George et al., 2011). This allowed them to induce reactive oxygen species (ROS), which was the key factor used by the researchers to kill cancer cells in other cancer therapy studies (Ganji et al., 2022).

Studies indicated that TiO_2 NPs have relatively low efficiency with respect to inducing ROS, which is mostly stimulated by UV light (Wang et al., 2022), which is harmful to cells to a certain degree (Haney et al., 2022). To improve the efficiency of TiO_2 NPs in ROS induction, Han et al. (2018) used the aluminum (Al) formed an oxygen-deficient TiO_{2-x} layer on the surface of the TiO_2 nanocrystals, which promoted and enhanced the separation of e- and h+ from the band structure under ultrasound irradiation, and significantly improved the effect of sonodynamic therapy on tumors. On this basis, we designed the TiO_{2-x} to enhance their ability to generate ROS, and tumor therapy efficacy. Our results showed that TiO_{2-x} was nearly 50 nm with the spherical morphology and 100 nm of DLS diameter, and the characteristic results were consistent with those of a previous study, indicating that synthesis was successful and is suitable for subsequent research (Li et al., 2022).

The application of TiO_2 NPs for PTT and SDT on cancer treatment had unique advantages and obvious disadvantages. This technology requires high concentrations of TiO_2 NPs and sufficient duration of illumination, and exhibits low target-killing ability, making it a focal point in numerous studies on drug delivery systems (Zhang et al., 2012; Torres-Romero et al., 2020). To enhance the targeting ability and stimulation of nanoparticles in cancer tissues, we used the GL as the guideline. Previous studies showed that the tumor cells would actively uptake GL for their growth. Despite being an abundant amino acid, GL is lacking in the tumor-bearing body (Chen et al., 1990), and the exogenous GL supplementation is preferentially transported to tumor tissues. Further, the tumor-bearing model study indicated that GL supplementation would not stimulate tumor growth (Fahr et al., 1994), indicating that the addition of GL is safe for tumor-bearing individuals. Based on the above studies, we designed a TiO_{2-x} (TiO_{2-x}@GL) coated with GL to achieve this goal. Our results indicated that

10.3389/fbioe.2023.1139426

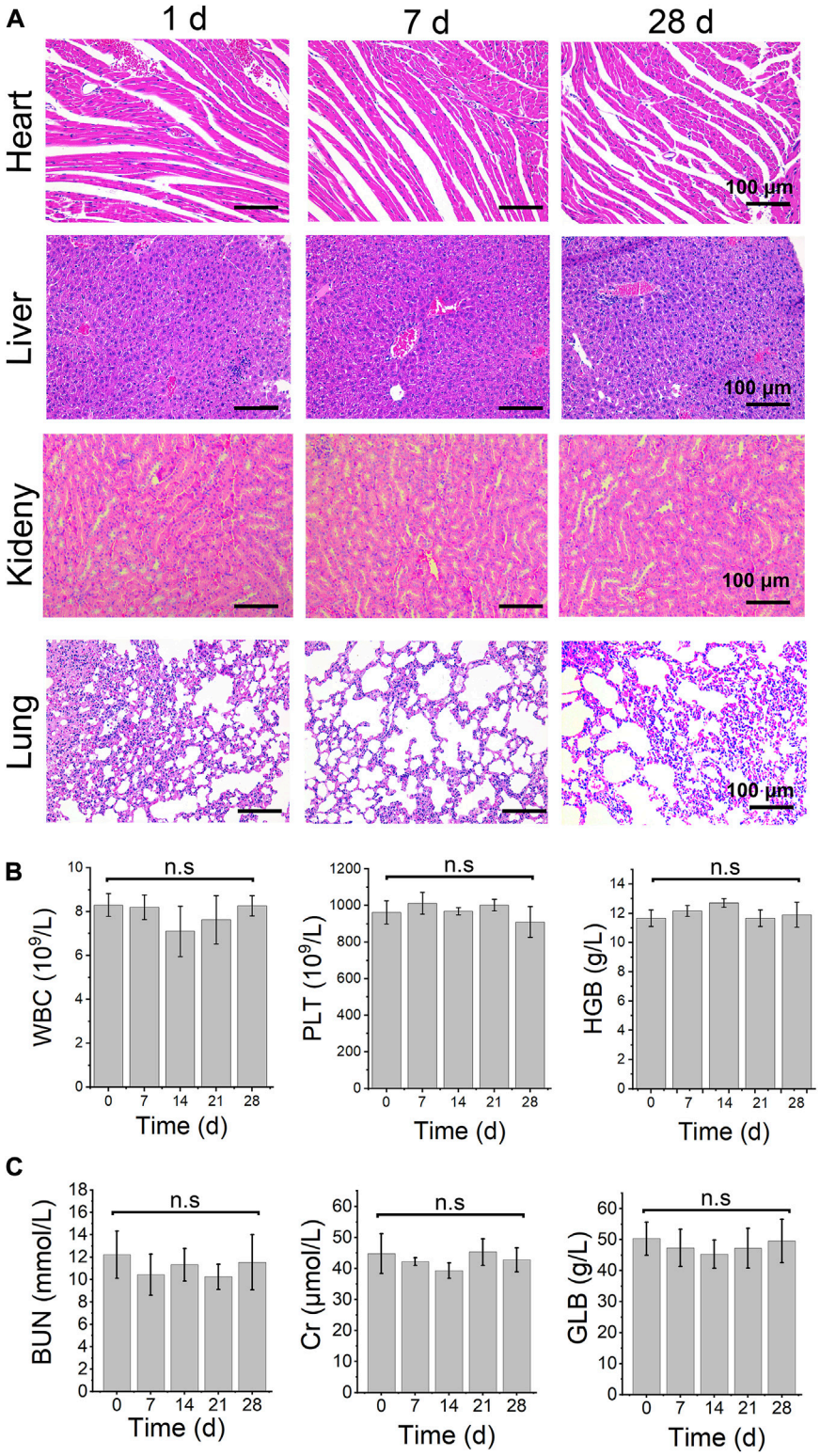

FIGURE 6
safety evaluation. **(A)** H&E staining images in main organ tissues of TiO_{2-x}@GL combined with laser and US irradiation on days 1, 7, and 28. Blood routine examination **(B)** and biochemical parameters **(C)** of TiO_{2-x}@GL combined with laser and US therapy from day 0 to day 28. WBC: white blood cell; PLT: platelet; HGB: Hemoglobin; BUN: urea nitrogen; Cr: Cr-reactive protein; GLB: Globulin.

TiO_{2-x} was successfully embedded with GL, and with a hydrodiameter of approximately 100 nm, which is consistent with the findings of numerous previous studies (Kim et al., 2022; Salah et al., 2022). In addition, TiO_{2-x}@GL can be activated at 1064 nm NIR-II bio-window, thus circumventing the potential challenge caused by UV illumination. Meanwhile, the concentration, US irradiation energy, and the light type and intensity for ROS generation by TiO_{2-x}@GL is prior to many nanoparticles previously reported (Zhang and Sun, 2004; Chun-Hui et al., 2009).

SDT and PTT had different mechanisms in killing tumor cells, including ROS generation and high temperature. This design of TiO_{2-x} with oxygen defects in the crystalline structure had been demonstrated to improve the separation efficacy of electrons and holes and subsequently enhance photocatalytic efficacy. TiO_{2-x} also also proved to enhance the temperature in tumor atmosphere response under NIR irradiation in the NIR-II biowindow, which assist hyperthermia for killing tumor cells. Therefore, the TiO_{2-x}@GL could inhibit tumor growth *via* inducing ROS under both US and laser irradiation, and enhance temperature to assist killing tumor cells after laser irradiation.

Despite the many advantages of nanoparticles in tumor treatment, it is difficult for them to penetrate barriers, particularly the tumor capsule. Studies indicate that only ≤1% nanomedicine doses can reach tumor tissues and exert their functions (Nakamura et al., 2016). Our results showed that with the help of GL, the concentration of TiO_{2-x}@GL increased approximately three-fold in the tumor tissues, which significantly improved their killing efficacy.

Although the joint application of SDT and PTT has been considerably successful in tumor therapy, the sole application of either form of therapy is less efficient in inducing ROS. Therefore, recent studies mainly focused on the synergistic sonodynamic and photothermal treatment (Gao et al., 2019; Cao et al., 2022; Du et al., 2022). Tan used TiO_2 NPs as the core to build a nano-sonosensitizer, combining it with the PD-1 checkpoint blockade therapy strategy, and found it effectively inhibited tumor cell proliferation and stopped tumor metastasis (Tan et al., 2021). In addition, Xue et al. designed a TIO_2@PT/GOX (TPG)-mediated sonodynamic therapy (SDT) and starvation therapy (ST) that promotes systemic tumor suppression (Zhao et al., 2022). Therefore, in this study, we carried out a SDT/PTT synergistic strategy for evaluation.

Our results showed that the TiO_{2-x}@GL + SDT + PTT yielded more optimized performance than the TiO_{2-x}@GL + SDT/PTT. The joint application of the aforementioned treatments had no effects on the weights of the tumor-bearing mice, but significantly reduced the tumor weight and prolonged the duration of morbidity-free survival. Further mechanical research showed that combination treatment inhibited tumor cell proliferation, and triggered cell apoptosis to anticancer, which is consistent with the elevated ROS induced bio-effects (Wei et al., 2022). In addition, we found that TiO_{2-x} and TiO_{2-x}@GL can inhibit cell migration, which is consistent with the results we previously found in studies onTiO_2 NPs study (Mao et al., 2018), suggesting that TiO_{2-x}@GL may have the ability to inhibit tumor metastasis and prolong survival time. To evaluate the safety of the combination treatment, we observed the pathological changes of main organs and the key biochemical parameters. All the results showed no significant change, indicating that TiO_{2-x}@GL had low toxicity to normal cells similar to TiO_2 NPs (Javed et al., 2022).

Conclusion

Our study reported a GL coated oxygen-deficient TiO_{2-x} to enhance their sonocatalytic and photothermal efficiency in tumor therapy. The oxygen-deficient TiO_{2-x} structure enhanced the separation efficiency of e− and h+, and endowed the nanoparticle with high photothermal-conversion in the 1064 nm NIR-II biowindow. The GL shell guided the target delivery of nanoparticles and enhanced their accumulation in the cancer tissues, which improved their anticancer efficiency considerably. This study presents a nanomedicine and high efficacy of a combined treatment plan for cancer therapy, and proposes a strategy for designing an anticancer nanomedicine.

Data availability statement

The original contributions presented in the study are included in the article/supplementary material, further inquiries can be directed to the corresponding authors.

Ethics statement

The animal study was reviewed and approved by the ethics committee of nanjing medical university.

Author contributions

LZ wrote the manuscript. PZ carried out the animal study. TW was responsible for the synthesis of nanomaterials. ZM and HW designed the study and provided funding support.

Funding

The study was supported by the National Natural Science Fund of China (81703256); Jiangsu Provincial Medical Youth Talent (QNRC2016307); Youth Talent Support Project of Changzhou Science and Technology Association; Youth Talent Support Project of Jiangsu Provincial Science and Technology Association; Social developmental project of Changzhou Science and Technology Bureau (CE20215037); Top Talent of Changzhou "The 14th Five-Year Plan" High-Level Health Talents Training Project.

Acknowledgments

We thanked LZ for the guidance of the material synthesis.

Conflict of interest

The authors declare that the research was conducted in the absence of any commercial or financial relationships that could be construed as a potential conflict of interest.

Publisher's note

References

Altman, B. J., Stine, Z. E., and Dang, C. V. (2016). From krebs to clinic: Glutamine metabolism to cancer therapy. *Nat. Rev. Cancer* 16, 619–634. doi:10.1038/nrc.2016.71

Behnam, M. A., Emami, F., Sobhani, Z., and Dehghanian, A. R. (2018). The application of titanium dioxide (TiO(2)) nanoparticles in the photo-thermal therapy of melanoma cancer model. *Iran. J. Basic Med. Sci.* 21, 1133–1139. doi:10.22038/IJBMS.2018.30284.7304

Cao, Z., Yuan, G., Zeng, L., Bai, L., Liu, X., Wu, M., et al. (2022). Macrophage-targeted sonodynamic/photothermal synergistic therapy for preventing atherosclerotic plaque progression using CuS/TiO(2) heterostructured nanosheets. *ACS Nano* 16, 10608–10622. doi:10.1021/acsnano.2c02177

Cesmeli, S., and Biray Avci, C. (2019). Application of titanium dioxide (TiO(2)) nanoparticles in cancer therapies. *J. Drug Target* 27, 762–766. doi:10.1080/1061186x.2018.1527338

Chen, M., Austgen, T., and Klimberg, V. (1990). Tumor glutamine use exceeds intestinal glutamine use in cachectic tumor-bearing rats. *Surg. Forum* 41, 12–14.

Chu, X., Mao, L., Johnson, O., Li, K., Phan, J., Yin, Q., et al. (2019). Exploration of TiO(2) nanoparticle mediated microdynamic therapy on cancer treatment. *Nanomedicine* 18, 272–281. doi:10.1016/j.nano.2019.02.016

Chun-Hui, X., Wen-Xue, Y., and Bai-Qi, W. (2009). Damaging effects of photoexcited TiO2 nanoparticles on gastric cancer SGC-7901 cells. *Chem. J. Chin. UNIVERSITIES-CHINESE* 30, 2123–2126.

Dai, L., Sun, F., Fu, P., and Li, H. (2022). Enhanced photocatalytic hydrogen evolution and ammonia sensitivity of double-heterojunction g-C(3)N(4)/TiO(2)/CuO. *RSC Adv.* 12, 13381–13392. doi:10.1039/d2ra01918c

Du, W., Chen, W., Wang, J., Cheng, L., and Zhang, H. (2022). Oxygen-deficient titanium dioxide-loaded black phosphorus nanosheets for synergistic photothermal and sonodynamic cancer therapy. *Biomater. Adv.* 136, 212794. doi:10.1016/j.bioadv.2022.212794

Esteban Florez, F. L., Hiers, R. D., Larson, P., Johnson, M., O'Rear, E., Rondinone, A. J., et al. (2018). Antibacterial dental adhesive resins containing nitrogen-doped titanium dioxide nanoparticles. *Mater Sci. Eng. C Mater Biol. Appl.* 93, 931–943. doi:10.1016/j.msec.2018.08.060

Fahr, M. J., Kornbluth, J., Blossom, S., and Harry, M. (1994). Glutamine enhances immunoregulation of tumor growth. *JPEN J. Parenter. Enter. Nutr.* 18, 471–476. doi:10.1177/0148607194018006471

Fujiwara, R., Luo, Y., Sasaki, T., Fujii, K., Ohmori, H., and Kuniyasu, H. (2015). Cancer therapeutic effects of titanium dioxide nanoparticles are associated with oxidative stress and cytokine induction. *Pathobiology* 82, 243–251. doi:10.1159/000439404

Ganji, C., Muppala, V., Khan, M., Purnachandra Nagaraju, G., and Farran, B. (2022). Mitochondrial-targeted nanoparticles: Delivery and therapeutic agents in cancer. *Drug Discov. Today* 28, 103469. doi:10.1016/j.drudis.2022.103469

Gao, F., He, G., Yin, H., Chen, J., Liu, Y., Lan, C., et al. (2019). Titania-coated 2D gold nanoplates as nanoagents for synergistic photothermal/sonodynamic therapy in the second near-infrared window. *Nanoscale* 11, 2374–2384. doi:10.1039/c8nr07188h

George, S., Pokhrel, S., Ji, Z., Henderson, B. L., Xia, T., Li, L., et al. (2011). Role of Fe doping in tuning the band gap of TiO2 for the photo-oxidation-induced cytotoxicity paradigm. *J. Am. Chem. Soc.* 133, 11270–11278. doi:10.1021/ja202836s

Han, X., Huang, J., Jing, X., Yang, D., Lin, H., Wang, Z., et al. (2018). Oxygen-deficient black titania for synergistic/enhanced sonodynamic and photoinduced cancer therapy at near infrared-II biowindow. *ACS Nano* 12, 4545–4555. doi:10.1021/acsnano.8b00899

Haney, A. M., Sanfilippo, J. E., Garczarek, L., Partensky, F., and Kehoe, D. M. (2022). Multiple photolyases protect the marine cyanobacterium synechococcus from ultraviolet radiation. *mBio* 13, e0151122. doi:10.1128/mbio.01511-22

Javed, R., Ain, N. U., Gul, A., Arslan Ahmad, M., Guo, W., Ao, Q., et al. (2022). Diverse biotechnological applications of multifunctional titanium dioxide nanoparticles: An up-to-date review. *IET Nanobiotechnol* 16, 171–189. doi:10.1049/nbt2.12085

Kim, C. H., You, D. G., Han, K. H., Um, W., and Lee, J. (2022). Self-immolative nanosensitizer for glutathione depletion-assisted sonodynamic therapy. *Theranostics* 12, 7465–7475. doi:10.7150/thno.75007

Kim, S., Im, S., Park, E. Y., Lee, J., Kim, C., Kim, T. i., et al. (2020). Drug-loaded titanium dioxide nanoparticle coated with tumor targeting polymer as a sonodynamic chemotherapeutic agent for anti-cancer therapy. *Nanomedicine* 24, 102110. doi:10.1016/j.nano.2019.102110

Klimberg, V. S., Kornbluth, J., Cao, Y., Dang, A., Blossom, S., and Schaeffer, R. F. (1996). Glutamine suppresses PGE2 synthesis and breast cancer growth. *J. Surg. Res.* 63, 293–297. doi:10.1006/jsre.1996.0263

Knox, W. E., Horowitz, M. L., and Friedell, G. H. (1969). The proportionality of glutaminase content to growth rate and morphology of rat neoplasms. *Cancer Res.* 29, 669–680.

Lee, J., Lee, Y. H., Jeong, C. B., Choi, J. S., Chang, K. S., and Yoon, M. (2018). Gold nanorods-conjugated TiO(2) nanoclusters for the synergistic combination of phototherapeutic treatments of cancer cells. *J. Nanobiotechnology* 16, 104. doi:10.1186/s12951-018-0432-4

Li, L., Lin, H., Li, D., Zeng, Y., and Liu, G. (2021). Ultrasound activated nanosensitizers for sonodynamic therapy and theranostics. *Biomed. Mater* 16, 022008. doi:10.1088/1748-605x/abd382

Li, Z., Pan, Y., Du, S., Li, Y., Chen, C., Song, H., et al. (2022). Tumor-microenvironment activated duplex genome-editing nanoprodrug for sensitized near-infrared titania phototherapy. *Acta Pharm. Sin. B* 12, 4224–4234. doi:10.1016/j.apsb.2022.06.016

Liang, X., Xie, Y., Wu, J., Wang, J., Petkovic, M., Stepic, M., et al. (2021). Functional titanium dioxide nanoparticle conjugated with phthalocyanine and folic acid as a promising photosensitizer for targeted photodynamic therapy *in vitro* and *in vivo*. *J. Photochem Photobiol. B* 215, 112122. doi:10.1016/j.jphotobiol.2020.112122

Mao, Z., Yao, M., Li, Y., Fu, Z., Li, S., Zhang, L., et al. (2018). miR-96-5p and miR-101-3p as potential intervention targets to rescue TiO(2) NP-induced autophagy and migration impairment of human trophoblastic cells. *Biomater. Sci.* 6, 3273–3283. doi:10.1039/c8bm00856f

Nakamura, Y., Mochida, A., Choyke, P. L., and Kobayashi, H. (2016). Nanodrug delivery: Is the enhanced permeability and retention effect sufficient for curing cancer? *Bioconjug Chem.* 27, 2225–2238. doi:10.1021/acs.bioconjchem.6b00437

Nosaka, Y., and Nosaka, A. Y. (2016). Reconsideration of intrinsic band alignments within anatase and rutile TiO2. *J. Phys. Chem. Lett.* 3, 431–434. doi:10.1021/acs.jpclett.5b02804

Rodriguez-Barajas, N., Anaya-Esparza, L. M., Villagran-de la Mora, Z., and Sanchez-Burgos, J. A. (2022). Review of therapies using TiO(2) nanomaterials for increased anticancer capability. *Anticancer Agents Med. Chem.* 22, 2241–2254. doi:10.2174/1871520622666211228112631

Salah, M., Akasaka, H., Shimizu, Y., Morita, K., Nishimura, Y., Kubota, H., et al. (2022). Reactive oxygen species-inducing titanium peroxide nanoparticles as promising radiosensitizers for eliminating pancreatic cancer stem cells. *J. Exp. Clin. Cancer Res.* 41, 146. doi:10.1186/s13046-022-02358-6

Tan, X., Huang, J., Wang, Y., He, S., Jia, L., Zhu, Y., et al. (2021). Transformable nanosensitizer with tumor microenvironment-activated sonodynamic process and calcium release for enhanced cancer immunotherapy. *Angew. Chem. Int. Ed. Engl.* 60, 14170–14178. doi:10.1002/ange.202102703

Torres-Romero, A., Cajero-Juarez, M., Nunez-Anita, R. E., and Contreras-Garcia, M. E. (2020). Ceria-Doped titania nanoparticles as drug delivery system. *J. Nanosci. Nanotechnol.* 20, 3971–3980. doi:10.1166/jnn.2020.17206

Wang, H., Xing, Z., Sun, Y., Jing, Y., Zhang, J., Li, X., et al. (2022). UV-irradiating synthesis of cyclodextrin-silver nanocluster decorated TiO(2) nanoparticles for photocatalytic enhanced anticancer effect on HeLa cancer cells. *Front. Chem.* 10, 995261. doi:10.3389/fchem.2022.995261

Wang, Z., Yang, C., Lin, T., Yin, H., Chen, P., Wan, D., et al. (2013). Visible-light photocatalytic, solar thermal and photoelectrochemical properties of aluminium-reduced black titania. *Energy & Environ. Sci.* 6, 3007–3014. doi:10.1039/c3ee41817k

Wei, B., Hao, Z., Zheng, H., Qin, Y., Zhao, F., and Shi, L. (2022). Brevilin A inhibits VEGF-induced angiogenesis through ROS-dependent mitochondrial dysfunction. *Oxid. Med. Cell Longev.* 2022, 1–18. doi:10.1155/2022/5888636

Yuan, X., Liu, W., Li, Y., Chen, K., Li, H., Tang, H., et al. (2022). CCL3 aggravates intestinal damage in NEC by promoting macrophage chemotaxis and M1 macrophage polarization. *Pediatr. Res.* doi:10.1038/s41390-022-02409-w

Zhang, A. P., and Sun, Y. P. (2004). Photocatalytic killing effect of TiO2 nanoparticles on Ls-174-t human colon carcinoma cells. *World J. Gastroenterol.* 10, 3191–3193. doi:10.3748/wjg.v10.i21.3191

Zhang, H., Wang, C., Chen, B., and Wang, X. (2012). Daunorubicin-TiO2 nanocomposites as a "smart" pH-responsive drug delivery system. *Int. J. Nanomedicine* 7, 235–242. doi:10.2147/IJN.S27722

Zhao, Y., Liu, J., He, M., Dong, Q., Zhang, L., Xu, Z., et al. (2022). Platinum-Titania Schottky junction as nanosonosensitizer, glucose scavenger, and tumor microenvironment-modulator for promoted cancer treatment. *ACS Nano* 16, 12118–12133. doi:10.1021/acsnano.2c02540

Ziental, D., Czarczynska-Goslinska, B., and Mlynarczyk, D. T. (2020). Titanium dioxide nanoparticles: Prospects and applications in medicine. *Nanomater. (Basel)* 10, 387. doi:10.3390/nano10020387

Frontiers in
Bioengineering and Biotechnology

Accelerates the development of therapies, devices, and technologies to improve our lives

A multidisciplinary journal that accelerates the development of biological therapies, devices, processes and technologies to improve our lives by bridging the gap between discoveries and their application.

Discover the latest Research Topics

See more →

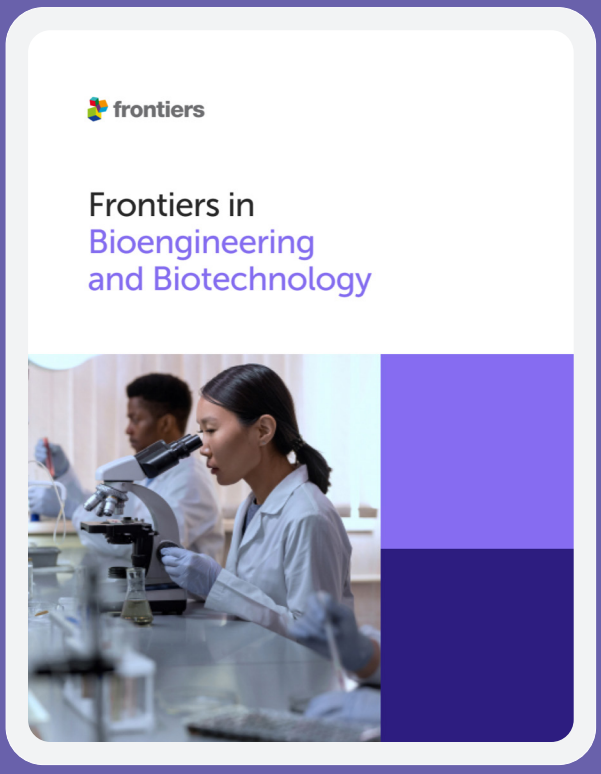

Frontiers

Avenue du Tribunal-Fédéral 34
1005 Lausanne, Switzerland
frontiersin.org

Contact us

+41 (0)21 510 17 00
frontiersin.org/about/contact